

Diese Dissertation haben begutachtet:

.....



DISSERTATION

A search for supersymmetry with a single lepton in the final state using hadronic variables

ausgeführt zum Zwecke der Erlangung des akademischen Grades eines
Doktors der technischen Wissenschaften unter der Leitung von

Univ.-Doz. Dipl.-Ing. Dr. Claudia-Elisabeth Wulz

E141

Atominstitut der Österreichischen Universitäten

eingereicht an der Technischen Universität Wien
Fakultät für Physik

von

Dipl.-Ing. Wolfgang Kiesenhofer

Matrikelnummer: 0125645
Schönbrunnerstraße 26/6, 1050 Wien

Wien, am 23. Oktober 2013

Kurzfassung

Supersymmetrie (SUSY) ist eine Theorie, die das Standardmodell (SM) der Teilchenphysik erweitert und versucht, diverse Defizite dieses Modells zu beheben. Sie postuliert eine Symmetrie zwischen Bosonen und Fermionen und liefert dadurch einen Mechanismus zur Lösung des Hierarchieproblems, welches in engem Zusammenhang zur Stabilität der Higgs-Boson-Masse steht. Dieser Mechanismus erfordert jedoch Schranken für die Massen der supersymmetrischen Partner der SM Teilchen. Im Besonderen werden die Massen der leichteren Squarks der dritten Generation auf maximal 700 GeV beschränkt, die Neutralino-Masse darf 350 GeV nicht überschreiten und die Gluino-Masse muss kleiner als 1.5 TeV sein. SUSY Theorien, die innerhalb dieser Massenschranken realisiert sind, werden gemeinhin als „natürliche“ SUSY bezeichnet. Die Suche nach neuer Physik, im Besonderen nach SUSY, ist eines der Hauptziele des Large Hadron Colliders (LHC), innerhalb dessen Reichweite der Massenbereich von natürlicher SUSY liegt.

Die Dissertation präsentiert Resultate einer Suche nach Gluino-Paarproduktion, wobei jedes der beiden Gluinos über ein Top-Squark in zwei Top-Quarks und ein Neutralino zerfällt. Dabei ist das Top-Squark entweder virtuell oder auf der Massenschale. „Simplified Models“ erlauben es, diese Topologie als Funktion der supersymmetrischen Teilchenmassen $m_{\tilde{g}}$, $m_{\tilde{\chi}^0}$ und $m_{\tilde{t}}$ zu beschreiben. Die Topologie ist durch die Massenhierarchie von natürlicher SUSY motiviert.

Die verwendeten Datensätze stammen von Proton-Proton Kollisionen, welche durch das CMS Experiment in den Jahren 2011 und 2012 bei einer Schwerpunktsenergie von 7 TeV beziehungsweise 8 TeV aufgezeichnet wurden. Die integrierte Luminosität der Datensätze entspricht 4.98 fb^{-1} (2011) und 19.4 fb^{-1} (2012). Diese Dissertation konzentriert sich auf die Analyse des größeren Datensatzes, die Resultate werden aber mit Ergebnissen aus dem Jahr 2011 verglichen, die auf einer ähnlichen Analysestrategie basieren.

Die Selektion von Kollisionen wurde auf hohe Signaleffizienz optimiert, während gleichzeitig so viel SM Untergrund wie möglich verworfen wird. Die ausgewählten Kollisionen sind charakterisiert durch ein einzelnes isoliertes Elektron oder Myon, fehlenden transversalen Impuls, hadronische Aktivität sowie mindestens sechs rekonstruierte Jets, wovon wenigstens einer als b -Quark Jet identifiziert werden muss. Die dominante SM Untergrundkomponente in dieser Selektion stammt von $t\bar{t}$ Produktion, gefolgt von kleinen Beiträgen aus W +Jets und single- t Ereignissen. Die Bedingung des Auftretens eines einzelnen isolierten Elektrons oder Myons in Verbindung mit fehlendem transversalen Impuls ermöglicht eine starke Reduktion von rein hadronischem SM Untergrund, erhält aber die hohe Signaleffizienz. Die Signaltopologie mit vier Top-Quarks im Endzustand produziert eine hohe Jet-Multiplizität mit bis zu vier b -Quark Jets. Die durch mindestens drei identifizierte b -Quark Jets definierten Signalregionen sind daher am sensitivsten.

Da die hochenergetischen Bereiche im Spektrum des fehlenden transversalen Impulses der SM Untergrundbeiträge durch die Simulation nicht notwendigerweise gut beschrie-

ben werden, wird ein Modell für das Spektrum entwickelt, um eine Schätzung aus Daten zu ermöglichen. Die Modellkomponente für $t\bar{t}$ Zerfälle wird als Funktion der hadronischen Aktivität und der Anzahl der identifizierten b -Quark Jets parametrisiert. Sie wird durch eine statische Komponente ergänzt, die den kleinen Beitrag von W +Jets Produktion miteinbezieht. Weiters berücksichtigt das Modell die Detektorauflösung für die Messung des fehlenden transversalen Impulses, die aus Daten bestimmt wird.

Die Modellparameter werden mittels der Maximum-Likelihood-Methode in untergrunddominierten Kontrollregionen gemessen. In einem zweiten Schritt wird das Modell zu Signalregionen mit hohem fehlenden transversalen Impuls und hoher hadronischer Aktivität extrapoliert, um den SM Untergrund für Kollisionen mit zwei identifizierten b -Quark Jets in diesen Bereichen zu schätzen. Eine weitere Extrapolation zu Signalregionen mit mindestens drei b -Quark Jets basiert auf diesen Vorhersagen und benützt Skalierungsfaktoren die mittels Simulation unter der Berücksichtigung von Unterschieden zu Daten bestimmt werden.

Im Vergleich zu den Erwartungen für das SM tritt kein Überschuss auf. Nur die im Jahr 2011 gewonnen Resultate werden im Kontext des „constrained Minimal Supersymmetric Standard Models“ interpretiert, während die Ergebnisse von 2011 und 2012 im Kontext der schon erwähnten Simplified-Model Topologie interpretiert werden. Die oberen Schranken für den Produktionswirkungsquerschnitt von Gluinopaaren aus der Analyse des Datensatzes von 2012 erweitern die ausgeschlossenen Massenbereiche in $m_{\tilde{g}}$, $m_{\tilde{\chi}^0}$ und $m_{\tilde{t}}$ signifikant, verglichen mit der Analyse des Datensatzes von 2011. Legt man die SUSY Vorhersage für den Produktionswirkungsquerschnitt von Gluinopaaren zugrunde, können Gluino-Massen bis zu 1.2 TeV für Neutralino-Massen unter 300 GeV ausgeschlossen werden. Für den Fall von schweren Neutralinos mit einer Masse über 300 GeV sind Gluino-Massen über 600 GeV immer noch erlaubt.

Abstract

Supersymmetry (SUSY) is a theory for physics beyond the Standard Model (SM), which attempts to eliminate some of its shortcomings. It postulates a symmetry between bosons and fermions and thereby provides a mechanism to solve the hierarchy problem, which is closely related to the stability of the Higgs boson mass. However, this mechanism imposes constraints on the mass spectra of the supersymmetric partners of SM particles. In particular, the masses of the lighter 3rd generation squarks should be smaller than 700 GeV, one of the neutralinos is expected to be lighter than 350 GeV and the gluino mass must not exceed 1.5 TeV. SUSY theories that are realized within these mass limits are commonly referred to as “natural” SUSY. The search for new physics, in particular for SUSY, is one of the primary goals of the Large Hadron Collider (LHC), where the allowed mass ranges of natural SUSY are within reach.

This thesis presents results from a search for gluino-pair production, with each gluino decaying to two top quarks and a neutralino via virtual or on-shell top squarks. “Simplified models” are used to describe this topology as a function of the supersymmetric particle masses $m_{\tilde{g}}$, $m_{\tilde{\chi}^0}$ and $m_{\tilde{t}}$. This topology is well motivated by the mass hierarchy of natural SUSY.

Events are selected from samples of proton-proton collisions, recorded by the CMS experiment at $\sqrt{s} = 7$ TeV during 2011 and $\sqrt{s} = 8$ TeV during 2012. The size of the samples corresponds to 4.98 fb^{-1} (2011) and 19.4 fb^{-1} (2012). This thesis focuses on the analysis of the larger dataset and the results are compared to those obtained from the sample collected in 2011, where a similar analysis strategy was used.

The event selection of the analysis is designed to retain a high efficiency for the targeted signal, while rejecting as much SM background as possible. Selected events are characterized by the presence of a single isolated electron or muon, missing transverse momentum, hadronic activity and a minimum of six reconstructed jets, of which at least one must be identified as a b -quark jet. The dominant SM background component in this selection is $t\bar{t}$ production, followed by a small contribution of W +jets and single- t events. The requirement of a single isolated electron or muon, together with missing transverse momentum, provides a strong suppression of backgrounds from multijet production, but preserves a high efficiency for signal events. The signal topology, with four top quarks in the final state, produces high jet multiplicities including up to four b -quark jets. Therefore, the most sensitive signal regions are those defined by a minimum of three identified b -quark jets.

Since the tails of the missing transverse momentum spectra of the SM background contributions are not necessarily well described by simulation, a model for the spectrum is developed to perform an estimation from data. The model component for $t\bar{t}$ decays is parametrized as function of the hadronic activity and the number of identified b -quark jets. It is complemented by a static component to account for the small contribution of W +jets production. This component is extracted from simulation, but its relative normalization is estimated from data as function of the hadronic activity and the

multiplicity of identified b -quark jets. Furthermore, the model accounts for the detector resolution of the missing transverse momentum, as measured in data.

The model parameters are estimated using an unbinned likelihood-fit to background-dominated control regions. Subsequently, the model is extrapolated to signal regions at high missing transverse momentum and high hadronic activity to predict the SM background in events with two identified b -quark jets. These predictions are further extrapolated to signal regions with a minimum of three identified b -quark jets using scale factors, which are derived from simulation and corrected for differences to data.

No excess with respect to the SM expectation is observed. Only the results obtained in 2011 are interpreted in terms of the constrained Minimal Supersymmetric Standard Model (cMSSM), while the results of 2011 and 2012 are both interpreted in terms of the aforementioned “simplified model” topology. The upper limits on the gluino-pair production cross section, based on the dataset collected during 2012, significantly extend the excluded mass regions in $m_{\tilde{g}}$, $m_{\tilde{\chi}^0}$ and $m_{\tilde{t}}$, compared to the upper limits based on the analysis of the 2011 dataset. Using the SUSY prediction for the production cross section of gluino-pairs as reference, gluino masses up to 1.2 TeV are excluded for neutralino masses up to 300 GeV, while in case of low mass splittings and a high neutralino mass above 300 GeV, a gluino mass as low as 600 GeV is still allowed.

Acknowledgments

First of all I want to thank my supervisor Claudia-Elisabeth Wulz for her experienced advice and professional support during the last years. Furthermore, I want to thank Prof. Walter Grimus for reviewing this thesis.

Special thanks go to Wolfgang Adam for giving me the chance to work in the CMS Collaboration, for his indispensable guidance through all aspects of data analysis and particle physics and for his patience during many discussions.

I would also like to thank Robert Schöffbeck for investing countless hours in discussions about the gory details of technical implementation, as well as for sharing his detailed knowledge about the theoretical background related to this work.

Further thanks go to all colleagues at HEPHY, especially to those who shared the office with me during the last years for their readiness to help and for providing a productive and pleasant work environment. Within the CMS collaboration I would like to thank the members of the SUSY group and its conveners. Their valuable comments and reviews substantially helped to improve my work.

I have to thank all my friends for their understanding of my frequent absence when I was occupied with work and for enduring long stories about high-energy physics I had to tell.

Eventually, I can truly claim the discovery of a superpartner in my life. Thank you Birgit for being there whenever I need you.

Finally, I want to thank my parents Herbert and Emma for their unconditional support, their encouragement to pursue my goals and for putting things into perspective when it was necessary.

Contents

1. Theoretical foundations of supersymmetry	1
1.1. The Standard Model of particle physics	1
1.1.1. Formulation of the Standard Model	1
1.1.2. Deficiencies of the Standard Model and their relation to supersymmetry	5
1.2. Supersymmetry	8
1.2.1. Particle content of the MSSM	9
1.2.2. The MSSM Lagrangian	10
1.2.3. R-parity	11
1.2.4. The mass spectrum of the MSSM	12
The Higgs sector and electroweak symmetry breaking	12
The neutralino and chargino sector	14
Gluinos	15
Sleptons and squarks	15
1.2.5. Naturalness and its implications	16
1.2.6. Constrained SUSY models	16
1.2.7. Simplified models	18
T1tttt	20
T1t1t and T5tttt	20
2. Experimental setup	21
2.1. The Large Hadron Collider	21
2.2. The Compact Muon Solenoid	23
2.2.1. Coordinate system	24
2.2.2. Silicon pixel detector	25
2.2.3. Silicon strip detector	26
2.2.4. Electromagnetic calorimeter	27
2.2.5. Hadronic calorimeter	28
2.2.6. Superconducting magnet	29
2.2.7. Muon system	30
2.2.8. Data acquisition and the trigger system	32
3. Data analysis	35
3.1. Analysis strategy	35
3.2. Data samples and simulation	37
3.2.1. Data samples	37
3.2.2. Simulation	38

3.3.	Analysis objects, selection requirements and efficiencies	40
3.3.1.	Analysis objects	40
	Muons	40
	Electrons	42
	Jets	43
	Missing transverse energy	44
	Identification of b -quark jets	46
3.3.2.	Event selection and SM backgrounds	47
3.3.3.	Lepton and trigger efficiencies	51
	Muon reconstruction and selection	51
	Electron reconstruction and selection	53
	Leptonic trigger leg	55
	Hadronic trigger leg	55
3.4.	Estimation of the SM Background	58
3.4.1.	Background estimation in the 2 b -tag category	58
3.4.2.	Modelling genuine- \cancel{E}_T	61
	The inclusive \cancel{E}_T model	61
	Parametrizing the impact of H_T selections	63
	Correcting the \cancel{E}_T model for b -jet acceptance effects	68
	The full \cancel{E}_T model for $t\bar{t}$	70
3.4.3.	Estimation of the W +jets background	71
3.4.4.	\cancel{E}_T -resolution templates	73
3.4.5.	Estimation of the \cancel{E}_T spectrum from data	79
3.4.6.	Systematic effects in the background estimation	85
	Jet and \cancel{E}_T scale	85
	b -tag efficiency and misidentification rates.	86
	W polarization in	86
	Lepton efficiencies	87
	Pileup	87
	Background cross sections	88
	\cancel{E}_T model	88
	Error functions	89
	Closure	89
3.4.7.	Background estimation in the ≥ 3 b -tag category	91
4.	Results and interpretation	96
4.1.	Summary of predicted and measured event yields	96
4.2.	Interpretation in terms of simplified models	99
4.2.1.	Observed and expected limits	99
4.2.2.	Signal contamination	100
4.2.3.	Treatment of uncertainties and their correlations	101
4.2.4.	Limits	102
4.3.	Comparison with results obtained from the analysis of the 7 TeV dataset	105
4.3.1.	Interpretation of the 7 TeV results in terms of the cMSSM . . .	106
4.3.2.	Interpretation of the 7 TeV results in terms of T1tttt	107

5. Summary	109
A. Data, simulated samples and trigger paths	112
B. Toy MC study	115
C. QCD estimation	118
D. Results using a fine binning	121
E. Signal contamination, efficiencies and acceptance uncertainties	124
E.1. Signal contamination	124
E.2. Signal efficiency	128
E.3. b -tagging efficiency uncertainty	132
E.4. Jet energy scale uncertainty	142
E.5. ISR uncertainty	147
List of Figures	152
List of Tables	158
Bibliography	160

1. Theoretical foundations of supersymmetry

1.1. The Standard Model of particle physics

Since its formulation over 40 years ago, the Standard Model (SM) of particle physics [1, 2, 3] has proven to successfully describe the fundamental constituents of matter and their interactions. Despite some deficiencies, which indicate the necessity for an extension of the theory at higher energy scales, the SM's predictions could be experimentally verified to a high level of precision [4]. A famous example is the anomalous magnetic moment of the electron, which has been calculated to 4th loop order [5] and agrees with the experimentally measured value up to 10 significant figures [6], turning it into one of the most accurately verified predictions in physics. Another impressive success of the SM was the prediction of several new particles, including the W and Z boson, two heavy quarks (charm, top), the τ -neutrino and the Higgs boson. After the discovery of the τ -neutrino in the year of 2000 [7], the Higgs boson was the final piece of the SM that was not experimentally verified. This changed in 2012 when the ATLAS and CMS collaborations at CERN jointly announced the discovery of a new boson with a mass of ~ 125 GeV [8, 9]. Although all preliminary measurements undoubtedly identify this particle as a Higgs boson, the final decision whether it is the Higgs boson predicted by the SM or only the lightest representative of a family of Higgs bosons as predicted by some extensions of the SM, is still missing. In this section I'll briefly summarize the formulation of the SM and discuss its deficiencies. The concept of supersymmetry offers an elegant solution to some of these problems and is subject of the next section.

1.1.1. Formulation of the Standard Model

A detailed summary of the SM would exceed the scope of this thesis and is subject of many text books (e.g. [10]). Therefore the following section only gives a brief description of the foundations of the SM.

The SM is a Yang-Mills gauge theory with the group structure $SU(3)_C \times SU(2)_L \times U(1)_Y$. Elementary particles are described as excitations of relativistic quantum fields. Matter particles with spin $\frac{1}{2}$ are called fermions and represented as spinor fields. There are three generations of fermions, each with an isospin-doublet of two leptons and two quarks, as well as one leptonic and two quark isospin-singlets.

$SU(3)_C \times SU(2)_L \times U(1)_Y$		
leptons	$L_i = \begin{pmatrix} \nu_e \\ e \end{pmatrix}_L, \begin{pmatrix} \nu_\mu \\ \mu \end{pmatrix}_L, \begin{pmatrix} \nu_\tau \\ \tau \end{pmatrix}_L$ $e_i = e_R, \mu_R, \tau_R$	$(\mathbf{1}, \mathbf{2}, -\frac{1}{2})$ $(\mathbf{1}, \mathbf{1}, 1)$
quarks	$Q_i = \begin{pmatrix} u \\ d \end{pmatrix}_L, \begin{pmatrix} c \\ s \end{pmatrix}_L, \begin{pmatrix} t \\ b \end{pmatrix}_L$ $u_i = u_R, c_R, t_R$ $d_i = d_R, s_R, b_R$	$(\mathbf{3}, \mathbf{2}, \frac{1}{6})$ $(\mathbf{3}, \mathbf{1}, -\frac{2}{3})$ $(\mathbf{3}, \mathbf{1}, \frac{1}{3})$
gauge bosons	G W^\pm, Z^0 γ	$(\mathbf{8}, \mathbf{1}, 0)$ $(\mathbf{1}, \mathbf{3}, 0)$ $(\mathbf{1}, \mathbf{1}, 0)$
Higgs boson	H	$(\mathbf{1}, \mathbf{2}, \frac{1}{2})$

Table 1.1.: Partices of the SM. The first two components of the tuple in the last column denote the group representation of the particle field, while the 3rd component is the weak hypercharge.

Interactions between fermions are mediated by exchanges of gauge bosons with spin-1, represented as vector fields in the theory. Three out of four fundamental interactions observed in nature, the strong, the weak and the electromagnetic interaction, are thereby included in the SM, while gravity is not described. The three fundamental interactions of the SM arise as a direct consequence of the invariance of its Lagrangian density under the local gauge transformations.

While leptons are only subjected to the electroweak interaction, which is accomplished under the symmetry group $SU(2)_L \times U(1)_Y$, quarks carry color charge and interact also via the strong force. The theory of the strong interaction is called quantum chromodynamics (QCD) and based on the symmetry group $SU(3)_C$ (C ... color) [11, 12, 13]. The quark fields are color triplets under the $SU(3)_C$ group while leptons are color singlets. The group has 8 generators, consequently, there exist 8 gluon fields G^i ($i = 1 \dots 8$), which carry combinations of two color charges. Because of the non-abelian structure of the group, self-interaction among gluons is possible. This is the reason for characteristic features, such as the confinement of quarks and the asymptotic freedom [14].

The remaining factor of the SM symmetry group, $SU(2)_L \times U(1)_Y$, accounts for the electroweak interaction, the unified weak and electromagnetic force, which was first introduced by Glashow, Weinberg and Salam in 1967 [1, 2, 3]. The charges associated to these two symmetries are the weak isospin (T) and the weak hypercharge (Y). Transformations under $SU(2)_L$ act only on left-handed chiral eigenstates of the fermions, which are expressed as isospin doublets ($T_3 = \pm \frac{1}{2}$), while right-handed states are isospin singlets ($T_3 = 0$). The associated gauge bosons fields of the electroweak symmetry are the isospin fields W^1, W^2 and W^3 , while the hypercharge field is commonly denoted as

B. All particle fields, their representations under $SU(3)_C$ and $SU(2)_L$, as well as their hypercharge are summarized in Tab. 1.1.

These fields must be massless since an explicit mass term in the Lagrangian (e.g. $m_W^2 W_\mu W^\mu$) breaks the local gauge symmetry. Moreover, explicit mass terms for the leptons are forbidden since left and right handed leptons transform differently under $SU(2)$. Nonetheless, it is of course necessary to incorporate the concept of mass in the SM. Implicit mass terms for the electroweak bosons, can be generated by adding a complex doublet of scalar fields to the theory, known as the Higgs field [15, 16, 17].

$$\phi = \begin{pmatrix} \phi^+ \\ \phi^0 \end{pmatrix} = \begin{pmatrix} \phi^1 + i\phi^2 \\ \phi^3 + i\phi^4 \end{pmatrix} \quad (1.1)$$

Adding ϕ to the Lagrangian preserves the local invariance under $SU(3)_C \times SU(2)_L \times U(1)_Y$. The Lagrangian density of the SM can be written as:

$$\begin{aligned} \mathcal{L}_{SM} = \mathcal{L}_g + \mathcal{L}_f + \mathcal{L}_H + \mathcal{L}_y = & \\ -\frac{1}{4}B_{\mu\nu}B^{\mu\nu} - \frac{1}{4}W_{\mu\nu}^a W^{a\mu\nu} - \frac{1}{4}G_{\mu\nu}^A G^{A\mu\nu} & (\mathcal{L}_g \dots \text{gauge terms}) \\ + \bar{L}_i \gamma^\mu i D_\mu L_i + \bar{e}_i \gamma^\mu i D_\mu e_i & \\ + \bar{Q}_i \gamma^\mu i D_\mu Q_i + \bar{d}_i \gamma^\mu i D_\mu d_i + \bar{u}_i \gamma^\mu i D_\mu u_i & (\mathcal{L}_f \dots \text{fermion dynamical terms}) \\ + (D_\mu \phi)^\dagger (D^\mu \phi) - V(\phi) & (\mathcal{L}_H \dots \text{Higgs dynamical and potential term}) \\ - y_{ij}^e \bar{L}_i \phi e_j - y_{ij}^u \bar{Q}_i \phi u_j - y_{ij}^d \bar{Q}_{ia} \epsilon^{ab} \phi_b^\dagger d_j + (h.c.) & (\mathcal{L}_y \dots \text{Yukawa terms}) \end{aligned} \quad (1.2)$$

D_μ denotes the covariant derivative. Its action on the fermions fields depends on the representation under the symmetry groups. For the left and right handed leptons the covariant derivative is given by

$$\begin{aligned} D_\mu \Psi_L &= \left(\partial_\mu + i g_1 Y B_\mu + i g_2 \frac{\tau_a}{2} W_\mu^a \right) \Psi_L, \\ D_\mu \Psi_R &= (\partial_\mu + i g_1 Y B_\mu) \Psi_R. \end{aligned} \quad (1.3)$$

whereas the derivative for the quark fields contains also a term for the gluons.

$$\begin{aligned} D_\mu \Psi_L &= \left(\partial_\mu + i g_1 Y B_\mu + i g_2 \frac{\tau_a}{2} W_\mu^a + i g_s \frac{\lambda_A}{2} G_\mu^A \right) \Psi_L \\ D_\mu \Psi_R &= \left(\partial_\mu + i g_1 Y B_\mu + i g_s \frac{\lambda_A}{2} G_\mu^A \right) \Psi_R \end{aligned} \quad (1.4)$$

The index i in Eq. 1.2 extends over the three fermion generations while τ_a and λ_A are the generators of $SU(2)$ and $SU(3)$. Finally, g_1 , g_2 and g_s denote the coupling constants for the three fundamental forces.

By means of an appropriately chosen Higgs potential

$$V(\phi) = \mu^2 \phi^\dagger \phi + \frac{\lambda^2}{2} (\phi^\dagger \phi)^2 \quad (1.5)$$

with real coefficients λ and $\mu^2 < 0$, the Higgs field acquires a non zero vacuum expectation value (VEV)

$$\langle 0 | \phi | 0 \rangle = \sqrt{\frac{-\mu^2}{\lambda^2}} = \frac{v}{\sqrt{2}} \quad (1.6)$$

with a value of $v \sim 246 \text{ GeV}$. It is reasonable to expand the field around the new ground state

$$\phi = \frac{1}{\sqrt{2}} e^{\frac{i\xi^a \tau^a}{v}} \begin{pmatrix} 0 \\ v + H \end{pmatrix} \quad (1.7)$$

The three massless Goldstone bosons ξ^a and the Higgs field H reflect the four degrees of freedom present in Eq. 1.1. Choosing the unitary gauge, defined by the requirement that the fields ξ vanish, only the scalar field component $(v + H)$ remains. Inserting the ground state of the Higgs field into the kinetic component of \mathcal{L}_H then yields:

$$\begin{aligned} (D_\mu \phi_0)^\dagger (D^\mu \phi_0) &= \left| \left(\partial_\mu + ig_1 Y B_\mu + ig_2 \frac{\tau_a}{2} W_\mu^a \right) \frac{1}{\sqrt{2}} \begin{pmatrix} 0 \\ v \end{pmatrix} \right| \\ &= \frac{v^2}{8} \left| \begin{pmatrix} g_2 W_\mu^1 - ig_2 W_\mu^2 \\ -g_2 W_\mu^3 + g_1 B_\mu \end{pmatrix} \right| \\ &= \frac{v^2}{8} \left[g_2^2 (W_\mu^1 W^{1\mu} + W_\mu^2 W^{2\mu}) + (g_2 W_\mu^3 - g_1 B_\mu)^2 \right] \end{aligned} \quad (1.8)$$

The formerly massless gauge fields W^1 and W^2 mix to the massive vector bosons W^\pm according to

$$W_\mu^\pm = \frac{1}{\sqrt{2}} (W_\mu^1 \mp i W_\mu^2). \quad (1.9)$$

Their mass can be extracted from the coefficients in the last line of Eq. 1.8 and reads

$$m_W = \frac{g_2 v}{2}. \quad (1.10)$$

The two remaining gauge fields B and W^3 mix to the neutral fields Z^0 and A , defined as

$$\begin{aligned}
Z_\mu^0 &= \frac{1}{\sqrt{g_2^2 + g_1^2}} (g_2 W_\mu^3 - g_1 B_\mu) \\
A_\mu &= \frac{1}{\sqrt{g_2^2 + g_1^2}} (g_2 W_\mu^3 + g_1 B_\mu)
\end{aligned}
\tag{1.11}$$

Equation 1.8 contains only a mass term for the Z^0 but none for the photon field A . With the proper normalization the mass of the Z^0 becomes

$$m_Z = \frac{v}{2} \sqrt{g_2^2 + g_1^2}. \tag{1.12}$$

The non-zero energy of the Higgs field's ground state breaks the electroweak symmetry, as can be seen by applying the generators of the groups on this state ($\tau^a \phi_0 \neq 0$, $Y \mathbf{I} \phi_0 \neq 0$). The fact that the photon field remains massless implies that a part of the electroweak symmetry is preserved. Indeed the ground state is invariant under $U(1)_Q$ with $Q = T_3 + Y$.

$$(\tau^a/2 + Y \mathbf{I}) \phi_0 = \begin{pmatrix} 1 & 0 \\ 0 & 0 \end{pmatrix} \begin{pmatrix} 0 \\ v/\sqrt{2} \end{pmatrix} = 0 \tag{1.13}$$

The tree level Higgs boson mass follows from Eq. 1.5 and is

$$m_H = \lambda v. \tag{1.14}$$

The value of v (~ 246.22 GeV) can be inferred from its relation to the Fermi constant G_F , which in turn is most precisely determined from measurements of the muon lifetime [18]. The second parameter λ is a free constant in the potential V_H and cannot be related to any other measurable quantity than the Higgs boson mass itself. Of course, any observation of the mass also includes loop corrections from particles that couple to the Higgs boson.

The masses of the fermions are introduced by adding Yukawa terms, coupling the fermions and the Higgs field. In Eq. 1.2 these terms are denoted by \mathcal{L}_y .

1.1.2. Deficiencies of the Standard Model and their relation to supersymmetry

Although the SM is a very successful theory and has been confirmed by experiments to a high level of precision up to the electroweak energy scale [4], it must be an effective theory that is not valid up to arbitrarily high energies. This section lists some of the open questions in the SM and motivates supersymmetric extensions.

- **Gravity**

One of the most obvious shortcoming of the SM is that gravity cannot be in-

cluded. This is no immediate problem at low energies where gravity can be neglected, since it is extremely weak in comparison to the other forces. For energies approaching the Planck scale ($m_p \sim 2.4 \times 10^{18}$ GeV) the strength of gravity is believed to be comparable to the other forces, rendering the SM invalid. Several theories beyond the SM (BSM) aim to unify quantum theory with general relativity. The most prominent extensions are loop quantum gravity and superstring theory.

- **Gauge coupling unification**

The strength of the gauge couplings depends on the energy scale at which they are observed. Renormalization group equations allow to calculate this dependence. In case of the SM, the extrapolation of the couplings to high energy scales does not result in their unification. However in supersymmetric models this unification is realized with a satisfactory accuracy because of contributions from additional supersymmetric particles to the evolution. In this case the unification occurs at $\sim 2 \times 10^{16}$ GeV which is referred to as the GUT scale (Grand Unified Theory). (Fig. 1.1).

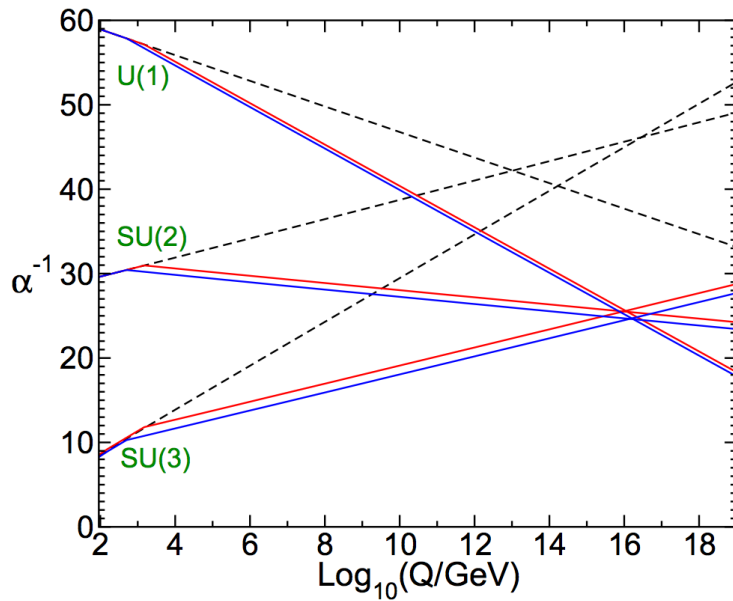


Figure 1.1.: Evolution of the inverse gauge couplings $\alpha^{-1}(Q)$. The SM renormalization group evolution (dashed lines) is compared to the evolution in the Minimal Supersymmetric Standard Model (solid lines). For the latter, the masses of the supersymmetric particles as well as $\alpha_3(m_Z)$ are varied, resulting in the blue and red lines. [19]

- **Hierarchy problem**

The hierarchy problem of particle physics [20] relates to the fact that the ratio of the GUT energy scale to the electroweak energy scale is huge. The bare Higgs boson mass, which is a free parameter in the SM, receives quadratically divergent loop corrections from all particles that couple to the Higgs field [19]. The 1st order

loop correction to m_H^2 from a fermion f that couples to the Higgs boson via the Lagrangian term $-\lambda_f H \bar{f} f$ is

$$\Delta m_H^2 = -\frac{|\lambda_f|^2}{8\pi^2} \Lambda_{UV}^2 \dots \quad (1.15)$$

where λ_f denotes the coupling and Λ_{UV} is the cut-off scale. The largest correction comes from the top-quark which has strongest coupling to the Higgs boson (see Fig. 1.2(a)). Under the assumption that the SM is valid up to the Planck scale ($\Lambda_{UV}^2 = m_p^2$), Δm_H will be many times larger than the bare Higgs boson mass m_H (Eq. 1.14), thus an unnatural level of fine tuning of the Higgs mass counter term would be required to achieve a cancellation between the quadratically divergent corrections and the bare Higgs boson mass. Several solutions have been proposed to this problem. Among these, supersymmetry is a particularly elegant one. In its minimal setting it postulates a bosonic, scalar counterpart for every fermionic SM particle. The 1st order loop correction from a scalar particle (see Fig. 1.2(b)), equivalent to Eq. 1.15 is given by

$$\Delta m_H^2 = \frac{\lambda_S}{16\pi^2} [\Lambda_{UV}^2 - 2m_S^2 \ln(\Lambda_{UV}/m_S) + \dots]. \quad (1.16)$$

Thus the Λ_{UV}^2 contributions of fermionic and bosonic partners cancel in supersymmetric models.

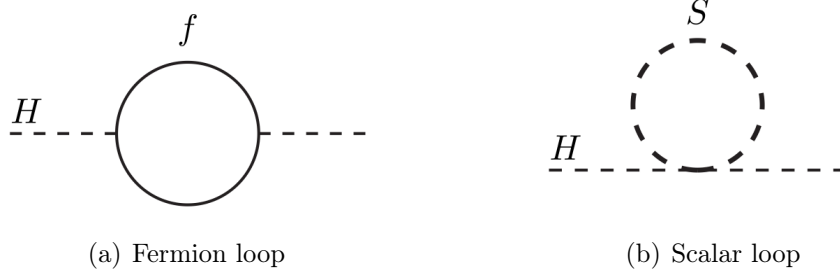


Figure 1.2.: One-loop corrections to the Higgs boson mass, for (a) a Dirac fermion f , and (b) a scalar S .

- **Origin of electroweak symmetry breaking**

The electroweak symmetry of the SM is broken by introducing a potential term $V(\phi)$ for the Higgs field (Eq. 1.5) with a negative parameter μ^2 . This potential does not follow from first principles and it is not understood why this particular form is realized in nature.

- **Dark matter**

Strong evidence from astrophysical observations, especially of the cosmic microwave background, indicate that baryonic matter constitutes only a small fraction ($\sim 5\%$) of the total mass and energy in the universe. About $\sim 27\%$ are attributed to the so called “dark matter” and the remaining $\sim 68\%$ are referred

to as “dark energy” [21]. The nature of the latter two components is to date unknown. Popular candidates for dark matter constituents are weakly interacting massive particles (WIMP), interacting only gravitationally and via the weak force. WIMPs follow from many supersymmetric models in case R-parity is conserved (see Sec. 1.2.3).

1.2. Supersymmetry

Over the last decades, supersymmetry (SUSY) [19, 22, 23, 24, 25, 26] has become one of the most popular extensions of the SM. It postulates a symmetry between bosonic and fermionic fields, relating particles with integer spin to particles with half integer spin and vice versa. This transformation is generated by an anti-commuting fermionic operator Q and can schematically be written as

$$Q |\text{Fermion}\rangle = |\text{Boson}\rangle, \quad Q |\text{Boson}\rangle = |\text{Fermion}\rangle. \quad (1.17)$$

The supersymmetry algebra is defined as

$$\begin{aligned} \{Q_\alpha, Q_\alpha^\dagger\} &= -2\sigma_{\alpha\dot{\alpha}}^\mu P_\mu \\ \{Q_\alpha, Q_\beta\} &= 0, \quad \{Q_\alpha^\dagger, Q_\beta^\dagger\} = 0 \\ [Q_\alpha, P^\mu] &= 0, \quad [Q_\alpha^\dagger, P^\mu] = 0 \end{aligned} \quad (1.18)$$

where σ^μ denotes the Pauli matrices with the spinor index α ($\dot{\alpha}$) for the first (last) two components of a Dirac spinor. From the fact that Q is a fermionic operator follows that supersymmetry must be a spacetime symmetry. This is visible from the anti-commutation relation in Eq. 1.18, where P_μ is the generator of spacetime translations. The relation of SUSY to a symmetry of spacetime is an appealing property of the theory, which allows to circumvent the theorem of Coleman and Mandula from 1967 [27]. It states under general assumptions, which guarantee a physically meaningful theory, that any Lie algebra of symmetry generators must be the direct product of the Poincaré group and an internal symmetry group. Thus, space-time and internal symmetries can only be combined in a trivial way. However, after Wess and Zumino provided the first example of a supersymmetric, renormalizable quantum field theory in 1974, Haag, Lopuszanski and Sohnius generalized the Coleman-Mandula theorem and thereby showed that supersymmetry, comprising fermionic generators, allows for a non-trivial extension of the Poincaré algebra. Moreover it was shown that this is the only non-trivial combination of spacetime and internal symmetries [28].

Particles related by a supersymmetry transformation are commonly referred to as superpartners and can be arranged in supermultiplets, which are irreducible representations of the supersymmetry algebra. Supersymmetric partners of the SM fermions

usually carry the same name with a prefix “s” for scalar, e.g. slepton or squark, while for superpartners of SM bosons it is common to add the suffix “ino”, e.g. gaugino.

Superpartners have identical mass and quantum numbers, except for the spin. The fact that no superpartner for any SM particle has so far been experimentally observed, implies that SUSY must be a broken symmetry in case it is realized in nature and consequently, the superpartners of SM particles must be considerably heavier. The origin of the supersymmetry breaking mechanism is unknown and often assumed to result from physics at a higher energy scale.

In the following sections I will briefly discuss the simplest and best studied version of a realistic supersymmetric SM extension, the Minimal Supersymmetric Standard Model (MSSM).

1.2.1. Particle content of the MSSM

Similar to the SM, its minimal supersymmetric extension, the MSSM [19, 29] is a $SU(3)_C \times SU(2)_L \times U(1)_Y$ gauge theory. It is a minimal extension with respect to the particle content, which is kept as small as possible.

Each fermionic matter field of the SM is extended to a chiral supermultiplet by adding spin-0 scalar superpartners (see Tab. 1.2). It is important to note that the isospin structure of the SM is preserved in the MSSM. Hence, for every left-handed fermionic isospin doublet there is a supersymmetric isospin doublet, while SM isospin singlets have singlet supersymmetric counterparts.

The bosonic gauge fields of the SM are extended to gauge supermultiplets with fermionic superpartners carrying spin $\frac{1}{2}$ (see Tab. 1.3). The extension is straightforward for the gluons G^A ($A = 1 \dots 8$), which are paired with gluinos \tilde{G}^A to form supermultiplets. Gluinos are color octet fermions, therefore they cannot mix with any other particle in the MSSM since there are no other fermionic color octets. The situation is slightly more complicated for the superpartners of the electroweak gauge bosons, the winos (\tilde{W}^a) and binos (\tilde{B}). Like their SM counterparts, they mix because of the broken electroweak symmetry. But in contrast to the SM vector bosons, these states additionally mix with the fermionic components of the Higgs supermultiplets. The resulting mass eigenstates, which might be light enough to be produced and observed at the LHC, are called charginos and neutralinos.

While the particle content for the matter and the gauge fields doubles in the MSSM, two Higgs supermultiplets, one with hypercharge $+\frac{1}{2}$ and another with $-\frac{1}{2}$, are necessary to obtain a consistent theory. A theory with only one supermultiplet would lead to triangular gauge anomalies. These anomalies cancel in the case of two supermultiplets with opposite hypercharge. The second reason lies in the structure of the supersymmetric Lagrangian which prohibits complex conjugates of the fields as they appear for example in Eq. 1.2. Hence, one Higgs supermultiplet (H_u) gives mass to up-type quarks, while the other (H_d) gives mass to down-type quarks and charged

leptons. The Higgs fields can again be arranged in isospin doublets. The weak isospin components of H_u are denoted as (H_u^+, H_u^0) , while H_d is defined as (H_d^0, H_d^-) with weak isospin components $T_3 = (\frac{1}{2}, -\frac{1}{2})$ for both multiplets.

Chiral superfields		spin- $\frac{1}{2}$	spin-0	$SU(3)_C \times SU(2)_L \times U(1)_Y$
quarks, squarks $\times 3$ families	\hat{Q}	$\begin{pmatrix} u_L \\ d_L \end{pmatrix}$	$\begin{pmatrix} \tilde{u}_L \\ \tilde{d}_L \end{pmatrix}$	$(\mathbf{3}, \mathbf{2}, -\frac{1}{6})$
	\hat{U}^c	\bar{u}_R	\tilde{u}_R^*	$(\bar{\mathbf{3}}, \mathbf{1}, -\frac{2}{3})$
	\hat{D}^c	\bar{d}_R	\tilde{d}_R^*	$(\bar{\mathbf{3}}, \mathbf{1}, \frac{1}{3})$
leptons, sleptons $\times 3$ families	\hat{L}	$\begin{pmatrix} \nu_L \\ e_L \end{pmatrix}$	$\begin{pmatrix} \tilde{\nu}_L \\ \tilde{e}_L \end{pmatrix}$	$(\mathbf{1}, \mathbf{2}, -\frac{1}{2})$
	\hat{E}^c	\bar{e}_R	\tilde{e}_R^*	$(\bar{\mathbf{1}}, \mathbf{1}, 1)$
Higgs bosons, higgsinos	\hat{H}_u	$\begin{pmatrix} \tilde{H}_u^+ \\ \tilde{H}_u^0 \end{pmatrix}$	$\begin{pmatrix} H_u^+ \\ H_u^0 \end{pmatrix}$	$(\mathbf{1}, \mathbf{2}, \frac{1}{2})$
	\hat{H}_d	$\begin{pmatrix} \tilde{H}_d^0 \\ \tilde{H}_d^- \end{pmatrix}$	$\begin{pmatrix} H_d^0 \\ H_d^- \end{pmatrix}$	$(\mathbf{1}, \mathbf{2}, -\frac{1}{2})$

Table 1.2.: Chiral supermultiplets in the MSSM. The first two components of the tuple in the last column denote the group representation of the particle field, while the 3rd component is the weak hypercharge.

Gauge superfields	spin-1	spin- $\frac{1}{2}$	$SU(3)_C \times SU(2)_L \times U(1)_Y$
Gluons, gluinos	G^A	\tilde{g}^A	$(\mathbf{8}, \mathbf{1}, 0)$
W-bosons, winos	W^i	\tilde{W}^i	$(\mathbf{1}, \mathbf{2}, 0)$
B-boson, bino	B	\tilde{B}	$(\mathbf{1}, \mathbf{1}, 0)$

Table 1.3.: Gauge supermultiplets in the MSSM. The first two components of the tuple in the last column denote the group representation of the particle field, while the 3rd component is the weak hypercharge.

1.2.2. The MSSM Lagrangian

In general, the effective Lagrangian of the MSSM can be written in the form

$$\mathcal{L} = \mathcal{L}_{\text{SUSY}} + \mathcal{L}_{\text{soft}}. \quad (1.19)$$

$\mathcal{L}_{\text{SUSY}}$ is invariant under supersymmetry transformations and contains all gauge and Yukawa interactions among the fields listed in Tab. 1.2 and Tab. 1.3. This part of the Lagrangian contains 19 parameters, the same number as in the SM [30]. A rigorous derivation of the general structure of $\mathcal{L}_{\text{SUSY}}$ is given in [19]. A complete list of all terms of the MSSM Lagrangian, can be found in [31].

From a theoretical perspective, it is reasonable to assume that supersymmetry is spontaneously broken, thus its Lagrangian is invariant under supersymmetry transformations while the ground state is not. A mechanism that destroys the invariance of the ground state requires the existence of new particles at a high unobservable mass scale, which is commonly referred to as the hidden sector. In this context, the MSSM resides in the visible sector, which must be coupled to the hidden sector by an interaction that mediates the symmetry breaking.

However, since the nature of the breaking mechanism is unknown, its effects are parametrized by the contributions in $\mathcal{L}_{\text{soft}}$ that break supersymmetry. “Soft” refers to the requirement to preserve the cancellation of the divergent Higgs mass corrections, the main motivation to introduce SUSY. A general recipe to construct all possibly allowed soft breaking terms is given in [19]. For the particle content of the MSSM the most general expression for $\mathcal{L}_{\text{soft}}$, compatible with gauge invariance and R-parity conservation is

$$\begin{aligned} \mathcal{L}_{\text{soft}} = & -\frac{1}{2} \left(M_3 \tilde{g} \tilde{g} + M_2 \tilde{W} \tilde{W} + M_1 \tilde{B} \tilde{B} + \text{c.c.} \right) \\ & - \left(\tilde{u} \mathbf{a}_u \tilde{Q} H_u - \tilde{d} \mathbf{a}_d \tilde{Q} H_d - \tilde{e} \mathbf{a}_e \tilde{L} H_d + \text{c.c.} \right) \\ & - \tilde{Q}^\dagger \mathbf{m}_Q^2 \tilde{Q} - \tilde{L}^\dagger \mathbf{m}_L^2 \tilde{L} - \tilde{u}^\dagger \mathbf{m}_u^2 \tilde{u} - \tilde{d}^\dagger \mathbf{m}_d^2 \tilde{d} - \tilde{e}^\dagger \mathbf{m}_e^2 \tilde{e} \\ & - m_{H_u}^2 H_u^* H_u - m_{H_d}^2 H_d^* H_d - (b H_u H_d + \text{c.c.}) . \end{aligned} \quad (1.20)$$

The first line contains the gluino, wino and bino mass terms with the mass parameters M_3 , M_2 and M_1 respectively, the second line contains the scalar cubic couplings \mathbf{a}_u , \mathbf{a}_d and \mathbf{a}_e , which are complex 3×3 matrices. The squark and slepton squared masses \mathbf{m}_Q^2 , \mathbf{m}_u^2 , \mathbf{m}_d^2 , \mathbf{m}_L^2 and \mathbf{m}_e^2 appear in the third line and are hermitian 3×3 matrices. The last line consists of the squared Higgs mass terms $m_{H_u}^2$, $m_{H_d}^2$ and b .

From Eq. 1.20, it is obvious that this general form of soft SUSY breaking introduces many new parameters. Although the parameter count can be reduced by considering the flavor symmetry of the gauge sector, a total of 105 new parameters remain [30, 32]. Of course this seemingly arbitrary parameterization is severely constrained by experimental results on flavor mixing or CP violating processes. A common restriction on $\mathcal{L}_{\text{soft}}$ is to assume flavor blind sfermion mass matrices (e.g. $\mathbf{m}_Q^2 = m_Q^2 \mathbf{1}$, $\mathbf{m}_L^2 = m_L^2 \mathbf{1}$, ...). Furthermore, flavor mixing can be induced by the cubic scalar couplings \mathbf{a}_u , \mathbf{a}_d and \mathbf{a}_e . A common approach to suppress large flavor mixings is to set these couplings proportional to the corresponding Yukawa matrices, ensuring at the same time that only 3^{rd} generation sfermions have large cubic scalar couplings [19].

1.2.3. R-parity

Without further assumptions, the MSSM Lagrangian would contain terms that allow lepton (L) and baryon number (B) violating processes, like the decay of the proton to a lepton and a meson via a squark (e.g. $p^+ \rightarrow e^+ \pi^0$). The proton decay has never been

observed experimentally and the lower limit on the lifetime is 6×10^{33} years [33]. Other physical processes that constrain lepton and baryon number violation, directly or indirectly, are reviewed in [34]. In the SM, there are no possible renormalizable Lagrangian terms that explicitly violate B or L conservation, thus it is not necessary to introduce any new fundamental symmetry as protection against such effects. Furthermore, it would be problematic to explicitly impose exact B or L conservation, since it is known that both are violated by non-perturbative electroweak effects, although these effects are negligibly small [19, 35]. In order to protect the conservation of B and L in the MSSM, a new symmetry called R-parity is introduced [36, 37, 38, 39, 40], which is a multiplicatively conserved quantum number and defined as

$$P_R = (-1)^{3B+L+2s}, \quad (1.21)$$

where s denotes the spin. P_R is equal to 1 for all SM particles and -1 for SUSY particles.

Besides the stability of the proton, R-parity conservation has the phenomenological consequence that only even numbers of sparticles can be produced in collider experiments. Furthermore, the decay products of sparticles must always comprise an odd number of lighter sparticles. This implies that the Lightest Supersymmetric Particle (LSP) cannot decay solely to SM particles and is therefore stable. If the LSP is also electrically neutral, it can only interact weakly and gravitationally and thus matches all characteristics that are required of a dark matter candidate. An LSP could be observed indirectly by collider experiments through the momentum imbalance it causes when escaping the detector volume without interaction (see Sec. 3.1 and 3.3.1). Many searches for supersymmetry, including the one presented in this thesis, exploit this imbalance and are therefore mainly sensitive to R-parity conserving models.

Despite these phenomenologically attractive implications, it has to be noted that R-parity conservation is no mandatory requirement. In fact, it can be replaced by other mechanisms that allow to fulfill the experimental constraints on B or L conservation. Such R-parity violating (RPV) models can exhibit decay topologies, substantially different to those considered in this thesis and therefore require dedicated search strategies.

1.2.4. The mass spectrum of the MSSM

The Higgs sector and electroweak symmetry breaking

Compared to the SM, electroweak symmetry breaking is complicated by the fact that there are two complex Higgs $SU(2)_L$ doublets in the MSSM.

$$H_u = \begin{pmatrix} H_u^+ \\ H_u^0 \end{pmatrix}, \quad H_d = \begin{pmatrix} H_d^0 \\ H_d^- \end{pmatrix} \quad (1.22)$$

The Higgs potential of the MSSM is given by

$$V_H = m_u^2 |H_u|^2 + m_d^2 |H_d|^2 + b \left(H_u H_d + H_u^\dagger H_d^\dagger \right) + \frac{1}{8} (g_1^2 + g_2^2) (|H_u|^2 - |H_d|^2)^2 + \frac{g_2^2}{2} |H_u^\dagger H_d|^2 \quad (1.23)$$

with $m_{u/d}^2 = |\mu|^2 + m_{H_{u/d}}^2$ and contains supersymmetric as well as soft breaking terms. Without loss of generality, $SU(2)_L$ transformations can be used to choose a gauge where the VEVs of the charged isospin components vanish and only the neutral isospin components acquire non-zero VEVs. This happens if the parameters of V_H fulfill the conditions $2b < m_u^2 + m_d^2$ and $b^2 > m_u^2 m_d^2$.

$$\langle 0 | H_u^0 | 0 \rangle = v_u, \quad \langle 0 | H_d^0 | 0 \rangle = v_d. \quad (1.24)$$

It is not possible to measure v_u and v_d directly, but they can be related to the VEV of the SM Higgs field defined in Eq. 1.6, which in turn is related to the tree-level mass m_Z of the Z -boson (Eq. 1.12).

$$v_u^2 + v_d^2 = \frac{v^2}{2} = \frac{2m_Z^2}{g_2^2 + g_1^2} \approx (174 \text{ GeV})^2 \quad (1.25)$$

The ratio of v_u and v_d is usually expressed as

$$\tan \beta = \frac{v_u}{v_d} \quad (1.26)$$

Requiring Eq. 1.25 to hold at the minima of V_H , leads to

$$\begin{aligned} m_u^2 - b \cot \beta - (m_Z^2/2) \cos(2\beta) &= 0 \\ m_d^2 - b \tan \beta + (m_Z^2/2) \cos(2\beta) &= 0. \end{aligned} \quad (1.27)$$

These are necessary conditions to reproduce the electroweak phenomenology of the SM after electroweak symmetry breaking.

The two complex $SU(2)_L$ Higgs doublets deliver eight degrees of freedom. Due to $v_u > 0$ and $v_d > 0$ the electroweak symmetry is broken and three degrees of freedom are absorbed as longitudinal components of the electroweak gauge bosons, which thereby acquire mass. The remaining 5 degrees of freedom mix to five mass eigenstates, which are the two neutral scalars h^0 and H^0 , one neutral pseudo scalar A^0 and two charged scalars H^\pm , with masses given by

$$\begin{aligned} m_{A^0}^2 &= \frac{2b}{\sin 2\beta} = m_u^2 + m_d^2 \\ m_{h^0, H^0}^2 &= \frac{1}{2} \left(m_{A^0}^2 + m_Z^2 \mp \sqrt{(m_{A^0}^2 - m_Z^2)^2 + 4m_Z^2 m_{A^0}^2 \sin^2(2\beta)} \right) \\ m_{H^\pm}^2 &= m_{A^0}^2 + m_W^2 \end{aligned} \quad (1.28)$$

All masses in Eq. 1.28, except m_{h^0} , can become arbitrarily large. It can be shown that the tree-level mass m_{h^0} is bounded above by $m_Z |\cos 2\beta|$. However, it receives potentially large quantum corrections, which can lift its mass to the measured value of ~ 125 GeV. The largest among these corrections comes from top quark and top squark loops in case of incomplete cancellation due to soft symmetry breaking, but also 2 loop gluino contributions can have sizable effects. The implications of the measured Higgs mass and its couplings in the context of the MSSM can be found in [41]. Given the current measurements, it is not yet possible to distinguish the SM Higgs boson from its MSSM counterpart.

The neutralino and chargino sector

Because of electroweak symmetry breaking, the gauge eigenstates of higgsinos and electroweak gauginos with identical quantum numbers in general mix. The resulting mass eigenstates of neutral higgsinos ($\tilde{H}_u^0, \tilde{H}_d^0$) and neutral gauginos (\tilde{B}, \tilde{W}^0) are called neutralinos ($\tilde{\chi}^{0i}, i = 1, 2, 3, 4$), while the charged higgsinos ($\tilde{H}_u^+, \tilde{H}_d^-$) and charged gauginos (\tilde{W}^1, \tilde{W}^2) mix to mass eigenstates called charginos ($\tilde{\chi}_i^\pm, i = 1, 2$).

The neutralino mass terms of the MSSM Lagrangian can be written in the gauge-eigenstate basis $\psi^0 = (\tilde{B}, \tilde{W}^0, \tilde{H}_d^0, \tilde{H}_u^0)$ as

$$\mathcal{L}_{\psi^0} = -\frac{1}{2}(\psi^0)^T \mathbf{M}_{\tilde{\chi}^0} \psi^0 + \text{c.c.}, \quad (1.29)$$

where the neutralino mass matrix $\mathbf{M}_{\tilde{\chi}^0}$ is given by

$$\mathbf{M}_{\tilde{\chi}^0} = \begin{pmatrix} M_1 & 0 & -c_\beta s_W m_Z & c_\beta s_W m_Z \\ 0 & M_2 & c_\beta s_W m_Z & -c_\beta s_W m_Z \\ -c_\beta s_W m_Z & c_\beta s_W m_Z & 0 & -\mu \\ s_\beta s_W m_Z & -s_\beta s_W m_Z & -\mu & 0 \end{pmatrix}. \quad (1.30)$$

M_i are the gaugino mass parameters in the soft part of the Lagrangian (Eq. 1.20) while μ is the higgsino mass parameter of the supersymmetric part. The sine and cosine of β and the Weinberg angle Θ_W are abbreviated by $s_\beta, c_\beta, s_{\Theta_W}$ and c_{Θ_W} .

The mass eigenstates result from diagonalizing $\mathbf{M}_{\tilde{\chi}^0}$ and its eigenvalues give the tree-level masses of the four neutralinos, which can receive potentially large loop corrections.

In a similar way, one can obtain the mass eigenstates of the charginos. Here the gauge-eigenstate basis ψ^\pm is defined as $(\tilde{W}^+, \tilde{H}_u^+, \tilde{W}^-, \tilde{H}_d^-)$. The chargino mass terms of the Lagrangian are given by

$$\mathcal{L}_{\psi^\pm} = -\frac{1}{2}(\psi^\pm)^T \mathbf{M}_{\tilde{\chi}^\pm} \psi^\pm + \text{c.c.}, \quad (1.31)$$

where $\mathbf{M}_{\tilde{\chi}^\pm}$ can be arranged in 2×2 block form,

$$\mathbf{M}_{\tilde{\chi}^\pm} = \begin{pmatrix} 0 & \mathbf{X}^T \\ \mathbf{X} & 0 \end{pmatrix}, \quad (1.32)$$

with

$$\mathbf{X} = \begin{pmatrix} M_2 & \sqrt{2}s_\beta m_W \\ \sqrt{2}c_\beta m_W & \mu \end{pmatrix}. \quad (1.33)$$

In contrast to the neutralinos, the block diagonal structure of the chargino sector makes it easier to transform to the mass eigenstates basis and express the chargino tree-level masses explicitly.

$$m_{\chi^\pm} = \frac{1}{2} \left(|M_2|^2 + |\mu|^2 + 2m_W^2 \mp \sqrt{(|M_2|^2 + |\mu|^2 + 2m_W^2)^2 - 4|\mu M_2 - m_W^2 \sin 2\beta|^2} \right) \quad (1.34)$$

Gluinos

Gluinos have no mixing partners, since they are the only color octet fermions in the MSSM. In models where boundary conditions are imposed at the GUT scale (see e.g. Sec. 1.2.6), the gluino mass parameter M_3 can become large when its evolution down to experimentally accessible energy scales of order 1 TeV is calculated, since its running with the energy scale depends on the strong coupling. Even without boundary conditions, the gluino is often heavier than the other supersymmetric particles in many models [19].

Sleptons and squarks

Unlike sleptons, squark masses ($m_{\tilde{Q}_i}^2$, $m_{\tilde{u}_i}^2$, $m_{\tilde{d}_i}^2$) receive contribution from the heavy gluino (M_3) in the evolution under the renormalization group (RG), thus squarks tend to be heavier than sleptons. The Yukawa and soft couplings also contribute to the RG evolution, with the effect that third generation sfermions have in general smaller masses than sfermions of the first two generations. While large Yukawa couplings of the third generation allow significant mixing, the mixing angles for the 1st and 2nd generation squarks are small. Furthermore universality prevents sizable mixings among different flavor contributions (see Sec. 1.2.2).

The relevant terms of the MSSM Lagrangian that contribute to the top squark mass can be expressed in the chiral basis as

$$\mathcal{L}_{\tilde{t}} = - \begin{pmatrix} \tilde{t}_L^* & \tilde{t}_R^* \end{pmatrix} \mathbf{m}_{\tilde{t}}^2 \begin{pmatrix} \tilde{t}_L \\ \tilde{t}_R \end{pmatrix}. \quad (1.35)$$

with the squared mass matrix

$$\mathbf{m}_{\tilde{t}}^2 = \begin{pmatrix} m_{\tilde{Q}_3}^2 + m_t^2 + \Delta_{\tilde{u}_L} & v(a_t^* \sin \beta - \mu y_t \cos \beta) \\ v(a_t \sin \beta - \mu^* y_t \cos \beta) & m_{\tilde{u}_3}^2 + m_t^2 + \Delta_{\tilde{u}_R} \end{pmatrix} \quad (1.36)$$

and $\Delta_\phi = (T_3^\phi - Q^\phi \sin^2 \theta_W) \cos(2\beta) m_Z^2$. The eigenvalues $m_{\tilde{t}_1}$ and $m_{\tilde{t}_2}$ of $\mathbf{m}_{\tilde{t}}^2$ are the masses of the eigenstates $(\tilde{t}_1^* \ \tilde{t}_2^*)$. Since RG evolution effects lead to $m_{\tilde{Q}_3} > m_{\tilde{u}_3}$, \tilde{t}_1 is usually the lightest squark and predominantly right handed. Similar arguments hold for sleptons, thus the $\tilde{\tau}_1$ is usually the lightest charged sparticle in many SUSY models.

1.2.5. Naturalness and its implications

One benefit of SUSY is to provide a solution to the hierarchy problem, by stabilizing the Higgs boson mass under radiative corrections, without requiring any fine tuning of the parameters (see. 1.1.2). However, only the quadratically divergent corrections cancel among superpartners. In order to avoid large sub-leading logarithmic contributions, the masses of the superpartners are required to be relatively small.

A related issue that arises in the MSSM is the so called μ -problem. The squared Higgs boson mass at tree level depends directly on the supersymmetric contribution $|\mu|^2$, as well as on contributions of the soft terms (b , $m_{H_u}^2$, $m_{H_d}^2$). There is no underlying principle that explains why these parameters should be on the same scale. However they are related to m_Z by Eq. 1.27. In order to fulfill this condition, again a large amount of fine tuning would be necessary. This motivates the common assumption $|\mu| \lesssim 200 \text{ GeV}$.

Despite the rough nature of these requirements, they allow to set approximate upper limits on the higgsino, gluino and stop masses. Both top squarks and one of the bottom squarks should be lighter than 700 GeV. The gluino mass, contributing to the Higgs boson mass via second order loop effects, should not exceed 1.5 TeV. Furthermore, the mass of the higgsinos is directly determined by $|\mu|$. Since naturalness requires $|\mu|$ to be small, the lightest two neutralinos and the lighter chargino tend to be higgsino-like and their mass can be expected below 350 GeV [42, 43]. However, (co)-annihilation rates for purely higgsino-like neutralinos are too high to explain the dark matter relic density, measured by WMAP and PLANCK [44].

These mass limits are of course neither strict, nor mandatory. Nonetheless they give a strong indication that SUSY might be within reach at energies that can be probed by the LHC.

1.2.6. Constrained SUSY models

The Lagrangian $\mathcal{L}_{\text{soft}}$ (Eq. 1.20) denotes the most general form of supersymmetry breaking terms in the MSSM and adds a large number of new parameters to the theory,

complicating phenomenological predictions. It is therefore reasonable to introduce simplifying assumptions about the SUSY breaking mechanism. A particularly popular simplification is the constrained MSSM (cMSSM), often referred to as minimal supergravity (MSUGRA). This model assumes that supersymmetry breaking is mediated by flavor blind gravitational interactions from a hidden sector at the Planck scale M_P . The parameters of Eq. 1.20 are fixed by boundary conditions at M_P .

$$\begin{aligned}
 M_3 &= M_2 = M_1 = m_{1/2}, \\
 m_Q^2 &= m_{\bar{u}}^2 = m_{\bar{d}}^2 = m_L^2 = m_{\bar{e}}^2 = m_0^2 \mathbf{1}, \\
 m_{H_u}^2 &= m_{H_d}^2 = m_0^2, \\
 \mathbf{a}_u &= A_0 \mathbf{y}_u, \quad \mathbf{a}_d = A_0 \mathbf{y}_d, \quad \mathbf{a}_e = A_0 \mathbf{y}_e.
 \end{aligned} \tag{1.37}$$

This approach allows to reduce the additional parameters of the MSSM to only 4 and the choice of a sign:

- a common gaugino mass $m_{1/2}$
- a common scalar mass m_0
- the ration of the Higgs field VEVs, $\tan \beta$
- the trilinear coupling parameter A_0
- the sign of the Higgs boson mass parameter μ

The trilinear coupling parameter A_0 relates the cubic scalar couplings \mathbf{a}_x to the SM Yukawa couplings \mathbf{y}_x and thus allows large couplings only for the third generation of squarks and sleptons. Using renormalization group equations, these parameters can be evolved from the GUT scale to the electroweak scale. The electroweak symmetry must of course be broken in the correct way, an additional requirement that determines the absolute value of μ and leaves only its sign open. Figure 1.3 shows an example for such an evolution. The evolution starts at the GUT scale at 2×10^{16} GeV, and the parameter of the Higgs potential $m_u^2 = \mu^2 + m_{H_u}^2$ turns negative around ~ 1 TeV and thereby causes the electroweak symmetry to break.

Because of its simplicity and predictive power, the cMSSM has been heavily used to interpret early LHC results. A set of benchmark points, split into low mass points (LM) and high mass points (HM), was chosen. While the LM points were defined to be accessible within the first years of LHC operation, the HM points will need substantially more data. Fig 1.4 shows the plane spanned by m_0 and $m_{1/2}$ at $\tan \beta = 10$, $A_0 = 0$ and $\mu > 0$ together with several LM and HM benchmark points.

However, the assumption of universality at the GUT scale is a simplification that might prevent the realization of the correct particle mass spectrum. An example for an alternative approach is the phenomenological MSSM (pMSSM) [29] which does not assume any particular model for SUSY breaking. By neglecting all complex phases in $\mathcal{L}_{\text{soft}}$ it eliminates new sources of CP-violation. To avoid flavor changing neutral currents (FCNC) only diagonal sfermion mass matrices and trilinear couplings are considered. In addition the pMSSM only assumes universality of the first and second

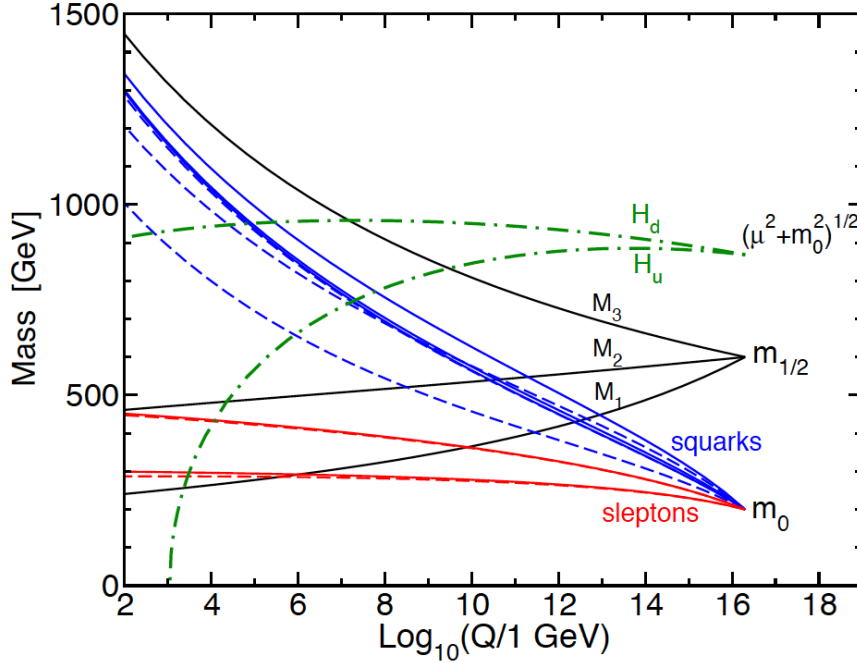


Figure 1.3.: Renormalization group evolution with MSUGRA boundary conditions $m_0 = 200 \text{ GeV}$, $m_{1/2} = -A_0 = 600 \text{ GeV}$, $\tan \beta = 10$ and $\mu > 0$. [19]

sfermion generations. Thereby, the number of parameters can be reduced to 19. An interpretation of results obtained from data collected by CMS during the year 2011 in terms of the pMSSM can be found in [46].

1.2.7. Simplified models

Theories beyond the SM (BSM) are typically defined by exact Lagrangians that describe a full set of particles and their interactions at a possibly high energy scale. This usually involves new parameters with complicated relations to experimentally accessible observables at an experimentally accessible energy scale. The interpretation of experimental results in these high dimensional parameter spaces can become complicated. On the other hand, imposing constraints on the parameter space can result in overly strong constraints on the kinematics of decay topologies and thereby increase the model dependence of the interpretation, as it is the case for the cMSSM.

The concept of simplified models spectra (SMS) [47] is an alternative approach, that aims to facilitate the task of interpreting experimental results. In contrast to a fundamental BSM theory, SMS use a low energy effective Lagrangian to describe single signatures that involves only a small number of particles and interactions. All other particles are decoupled from the model. Thereby a signature can be described by a few free parameters, which are directly related to experimental observables. Examples are particle masses, decay widths, production cross sections or branching ratios. Of course

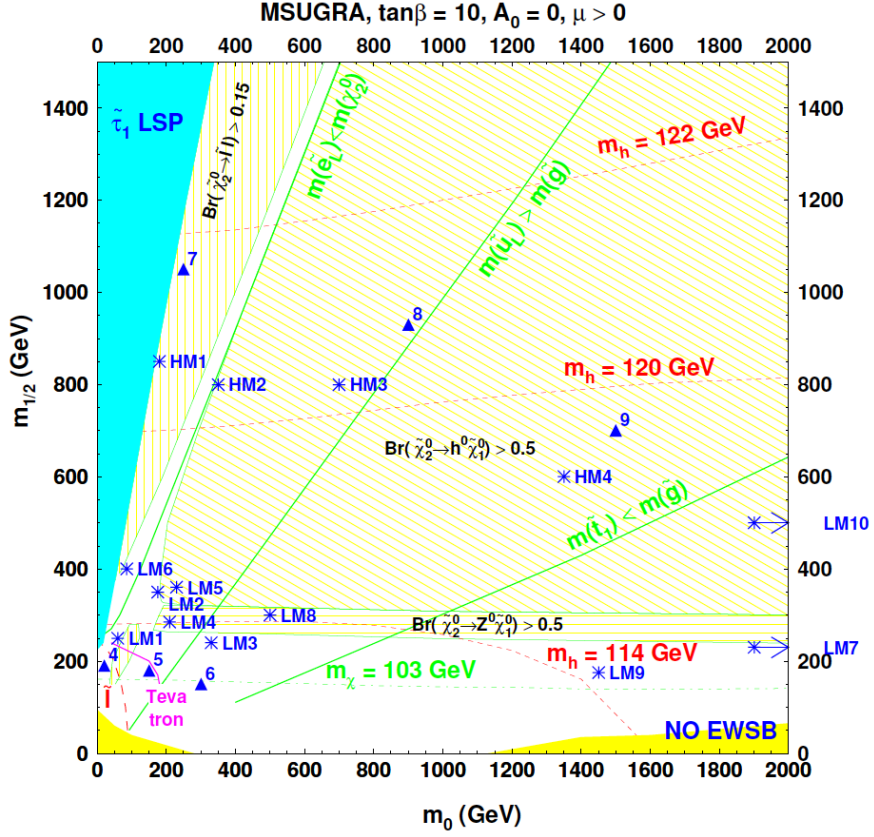


Figure 1.4.: Location of the CMS benchmark points in the m_0 vs. $m_{1/2}$ plane of the cMSSM for $\tan \beta = 10$, $A_0 = 0$ and $\mu > 0$. [45]. The shaded regions indicate excluded regions, where either the electroweak symmetry is not broken or the stau is the LSP. The red dashed lines show the LEP exclusions, the pink line shows the Tevatron exclusion limit as of 2006.

this approach is not completely model-independent either, since SMS still require assumptions about the parameterization of the production and decay matrix elements. However, for many cases the moderate required accuracy allows the kinematics to be parametrized primarily by the mass scales, while remaining independent of the details of the matrix elements [48, 49].

Simplified models spectra have to be validated to accurately reproduce topologies of complex models. For instance it can be shown that a few simplified model topologies are sufficient to reproduce the kinematics of most of the cMSSM parameter space [50]. It has also been demonstrated that pMSSM parameter space can be decomposed into simplified model topologies and that they help identifying regions of the parameter space that were previously overlooked [46]. A summary of interpretations of $\sqrt{s} = 7$ TeV results by CMS in terms of SMS can be found in [51].

A variety of SMS have been defined, reflecting various experimentally interesting topologies (e.g. [47]). Three topologies that model the production of gluino pairs,

decaying via top squarks to final states with top quarks and neutralinos, are discussed in the following. The analysis described in Sec. 3 is designed to target these topologies.

T1tttt

The topology labelled **T1tttt** [51] describes the production of two gluinos, each decaying to $t\bar{t}\tilde{\chi}^0$ via a virtual \tilde{t} (Fig. 1.5(a)). Since the top quark predominantly decays to a bottom quark and a W boson ($t \rightarrow bW^+$, $\bar{t} \rightarrow \bar{b}W^-$), this topology is particularly b -rich and additionally comprises leptons and neutrinos from leptonic W boson decays. **T1tttt** is therefore well suited for the interpretation of the results presented in this thesis. Free parameters of **T1tttt** are the gluino mass $m(\tilde{g})$ and the neutralino mass $m(\tilde{\chi}^0)$. The decay width of the gluino is set to 1 GeV.

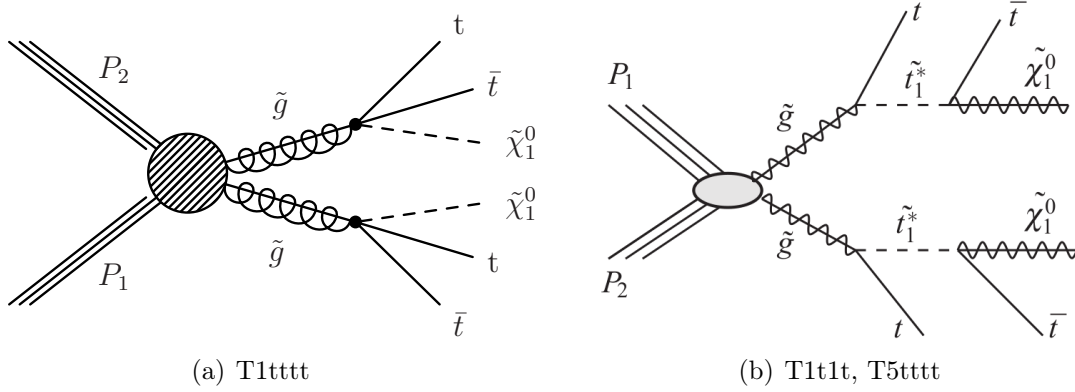


Figure 1.5.: Topologies of the simplified models **T1tttt** (a) and **T1t1t** and **T5tttt** (b) [51].

T1t1t and T5tttt

T1tttt has no dependence on the mass of the top squark which is assumed virtual in this model. In order to study the dependence on $m_{\tilde{t}}$ the models **T1t1t** and **T5tttt** are defined (Fig. 1.5(b)). Each gluino decays to a top quark and an intermediate on-shell top squark, requiring $m_{\tilde{t}}$ to be smaller than $m_{\tilde{g}}$. The top squark subsequently decays to a top quark and a neutralino. Hence, these models have the same final state as **T1tttt**. The free parameters of **T1t1t** are $m_{\tilde{t}}$ and $m_{\tilde{\chi}^0}$, while $m_{\tilde{g}}$ is fixed to 1 TeV. **T5tttt** has $m_{\tilde{g}}$ and $m_{\tilde{t}}$ as free parameters, while $m_{\tilde{\chi}^0}$ is fixed to 50 GeV.

2. Experimental setup

2.1. The Large Hadron Collider

The Large Hadron Collider (LHC) [52, 53, 54, 55] is a two-ring particle accelerator built by the European Organization for Nuclear Research (CERN) at the French-Swiss border near Geneva, Switzerland. With a circumference of ~ 27 km it has become the world's largest particle accelerator after replacing LEP (Large Electron Positron collider). LEP had been installed in the same tunnel before it was dismantled in the year 2000. Currently the LHC hosts 7 experiments, measuring the products of proton-proton and heavy ion collisions at four collision points (Fig. 2.1)

- The two largest experiments, ATLAS [56] and CMS [57], were designed as general-purpose detectors to investigate a wide range of SM phenomena and BSM theories.
- ALICE [58] is an experiment specialized to measure products of heavy ion collisions at extreme energies, to study the formation and properties of quark-gluon plasma.
- The LHCb [59] experiment is focused on precision measurements of b -hadron decays, which allow to study CP-violation and might help to explain the matter-antimatter asymmetry of the universe.
- LHCf [60] is a special purpose experiment, measuring collision products at very small angles with respect to the LHC's beam. These particles resemble particle showers produced by cosmic rays in the earth's atmosphere. Insights gained by this experiment will help to interpret and calibrate large-scale cosmic ray experiments. The two detectors of LHCf are placed at 140 m distance from the ATLAS collision point.
- The TOTEM [61] experiment studies forward particles like LHCf. Its main goals are to measure the total proton-proton cross section and to deliver accurate measurements of the LHC's luminosity at the interaction point 5, where CMS is located.
- MoEDAL [62] is the latest experiment at the LHC and shares its cavern with LHCb. MoEDAL will search for magnetic monopoles.

Before being injected into the LHC, protons have to be pre-accelerated to 450 GeV by an injector chain, depicted in Fig. 2.1.

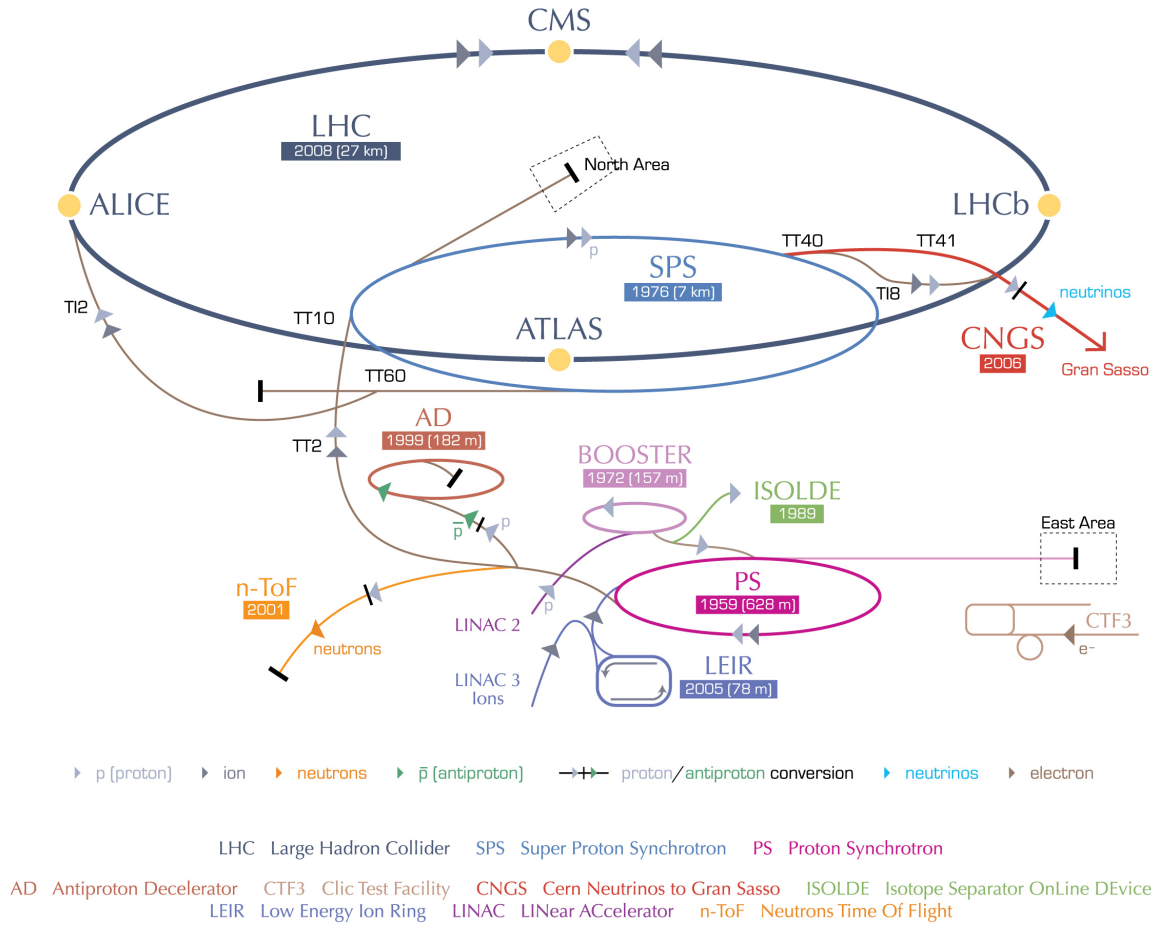


Figure 2.1.: Accelerator complex of CERN [63]

The LHC comprises 1232 superconducting dipole and 858 superconducting quadrupole magnets, operated at a temperature of 1.9 K, which keep the particle beams on track and focused. The limiting factor for the LHC's energy is the maximum field strength of the dipole magnets, which is 8.36 T and allows an acceleration of protons up to 7 TeV, thus a center-of-mass energy of 14 TeV. Proton beams in the LHC are not continuous but structured into proton packets, called bunches with an approximate length of 8 cm. When completely filled, each beam consists of up to 2808 bunches, with a bunch spacing of 25 ns. The design value for the instantaneous luminosity for proton-proton collisions is $\mathcal{L} = 10^{34} \text{ cm}^{-2} \text{ s}^{-1}$. \mathcal{L} is determined by the beam parameters and given by

$$\mathcal{L} = \frac{N_b^2 n_b f_{rev} \gamma}{4\pi \epsilon_n \beta^*} F, \quad (2.1)$$

where N_b denotes the number of particles per bunch, n_b the number of bunches per beam, f_{rev} the revolution frequency, γ the relativistic gamma factor, ϵ_n the normalized transverse beam emittance, β^* the beta function at the collision point and F the

geometric luminosity reduction factor related to the crossing angle at the interaction point [53]. The rate dN/dt of a production process with a cross section σ is given by

$$\frac{dN}{dt} = \mathcal{L} \cdot \sigma. \quad (2.2)$$

It is therefore common to quantify the number of collisions by the integrated luminosity

$$L = \int \mathcal{L} dt = \frac{N}{\sigma}, \quad (2.3)$$

which allows to calculate the actual expectation for the event count of any process from its cross section. Latest measurements by TOTEM determined the total inelastic cross section for proton-proton collisions to be 72.9 ± 1.5 mb at $\sqrt{s} = 7$ TeV and 74.7 ± 1.7 mb at $\sqrt{s} = 8$ TeV [64, 65].

Since the LHC became fully operational in November 2009, its performance has continuously been increased towards the design values. In 2010 the center-of-mass energy was increased to $\sqrt{s} = 7$ TeV and the LHC delivered an integrated luminosity of 47 pb^{-1} . For 2011 the LHC continued to operate at $\sqrt{s} = 7$ TeV and delivered an integrated luminosity of 6.1 fb^{-1} . The peak instantaneous luminosity during 2011 reached $4.0 \text{ nb}^{-1} \text{ s}^{-1}$, which is about a third of the design value. A further improvement of the performance could be achieved in 2012 at $\sqrt{s} = 8$ TeV. During this year, the LHC accumulated an integrated luminosity of 23.3 fb^{-1} and reached a peak instantaneous luminosity of $7.7 \text{ nb}^{-1} \text{ s}^{-1}$. Figure 2.2 and 2.3 show the integrated and instantaneous luminosities delivered to the CMS experiment over the first three years of LHC operation.

As of February 2013, the LHC entered a two-year shutdown period, which will be used to upgrade and improve the accelerator as well as the experiments.

2.2. The Compact Muon Solenoid

The Compact Muon Solenoid (CMS) is one of two multi-purpose experiments at the LHC. A detailed description of the detector design, its physics goals and the computing environment that is necessary for its operation, can be found in the Technical Design Reports [67, 45] and in [57]. This section aims to give a brief summary of the design and the performance of CMS and omits repeated references to these documents.

CMS is located in a cavern, approximately 100 m below ground, at the LHC's interaction point 5. It comprises various subdetector systems arranged in layers around the interaction region. The detector has a cylindrical shape with a length of 21.6 m and a diameter of 14.6 m. A central component of the detector is its superconducting solenoidal magnet, which surrounds the silicon tracker as well as the electromagnetic

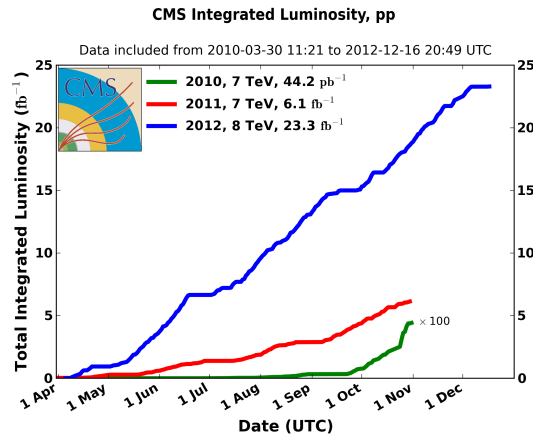


Figure 2.2.: Integrated luminosity versus time for 2010, 2011, 2012 (p - p collisions only) [66]

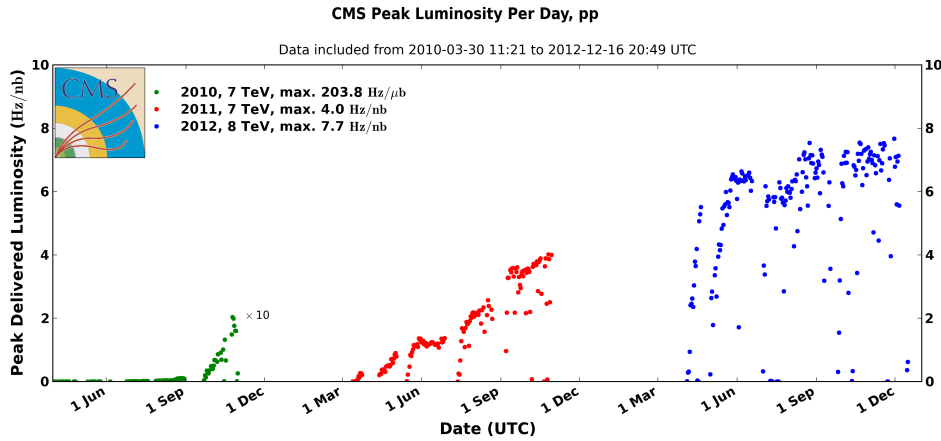


Figure 2.3.: Peak instantaneous luminosity per day for 2010, 2011, 2012 (p - p collisions only) [66]

and the hadronic calorimeters. The magnet itself is surrounded by a support structure made of steel, which also serves as return yoke to ensure an homogeneous magnetic field outside the coil. This steel support structure holds the muon chambers which are mounted outside the calorimeters and the magnet and thereby shielded from all interacting particles except for muons. A schematic view of the detector is shown in Fig. 2.4.

2.2.1. Coordinate system

CMS uses a right handed coordinate system which has its origin at the geometric center of the detector, also referred to as the nominal beam spot. The true beam spot does not necessarily coincide with the nominal beam spot. The x-axis points towards the center of the LHC, the y-axis points upwards, thus the z-axis points in the direction

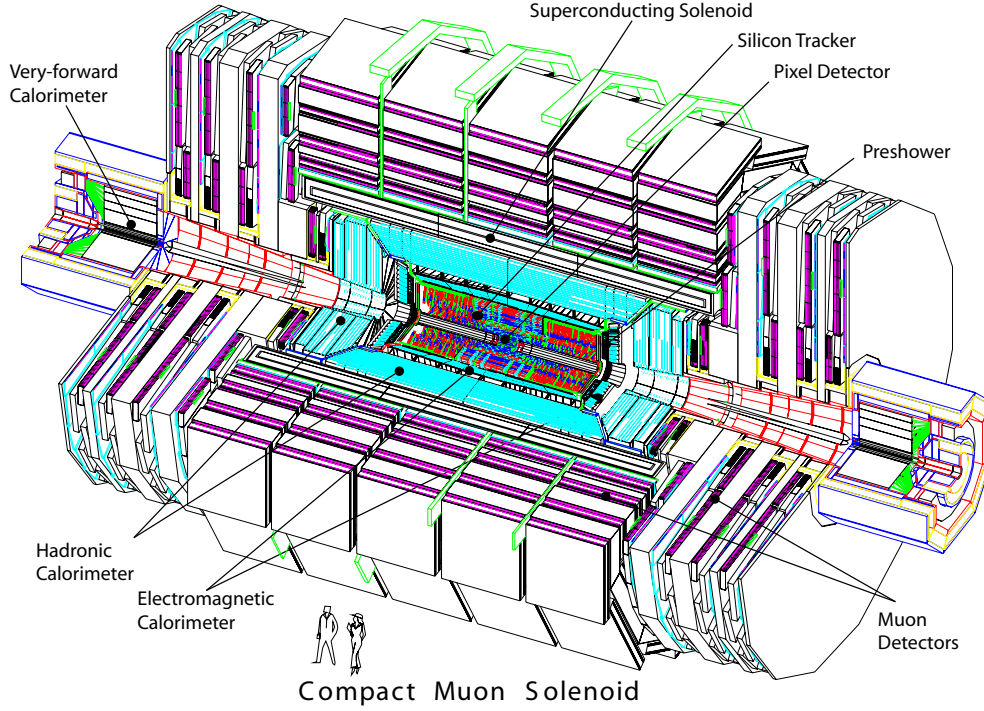


Figure 2.4.: The CMS detector [68]

counterclockwise with respect to the LHC viewed from above. The azimuthal angle ϕ and the polar angle θ are measured with respect to the x and the z-axis respectively. Instead of the polar angle it is usually convenient to use the pseudorapidity

$$\eta = -\ln \left[\tan \left(\frac{\theta}{2} \right) \right] = \frac{1}{2} \ln \left(\frac{|\mathbf{p}| + p_z}{|\mathbf{p}| - p_z} \right), \quad (2.4)$$

a quantity that is numerically close to the relativistic rapidity in the limit of high particle momenta $|\mathbf{p}| \gg m$. Therefore it has the advantage to be additive under Lorentz boosts. It is common to define a pseudo-angular distance between two directions by

$$\Delta R = \sqrt{\phi^2 + \eta^2}. \quad (2.5)$$

2.2.2. Silicon pixel detector

The innermost detector system of CMS is the pixel detector. In the barrel region it consists of 3 cylindrical layers with a length of 53 cm at distances of 4.4 cm, 7.3 cm and 10.2 cm from the beam spot. These cylindrical layers are closed by 2 discs on each side positioned at $z = \pm 34.5$ cm and $z = \pm 46.5$ cm (Fig. 2.4).

The pixel detector comprises 1440 sensor modules covering an active area of $\sim 1 \text{ m}^2$. With a pixel size of $100 \times 150 \mu\text{m}^2$ it has therefore ~ 66 million readout channels. The fine granularity is essential to ensure a maximum occupancy of 10^{-4} per pixel and bunch

crossing at the LHC design luminosity. The spatial resolution of $10 - 20 \mu\text{m}$ allows precise tracking of charged particles, an important ingredient for secondary vertex reconstruction and track seeding. An accurate and efficient reconstruction of secondary vertex positions facilitates the identification heavy flavor production, a capability which is crucial for the analysis of many physics processes, including those studied in this thesis.

Because of the proximity to the beam spot, the sensors and readout chips are exposed to a high particle flux and are therefore designed to be radiation hard. Nonetheless, the lifetime of the innermost pixel layer is limited to about 2-3 years, depending on the LHC's run conditions while the outermost layer is expected to operate for at least 10 years.

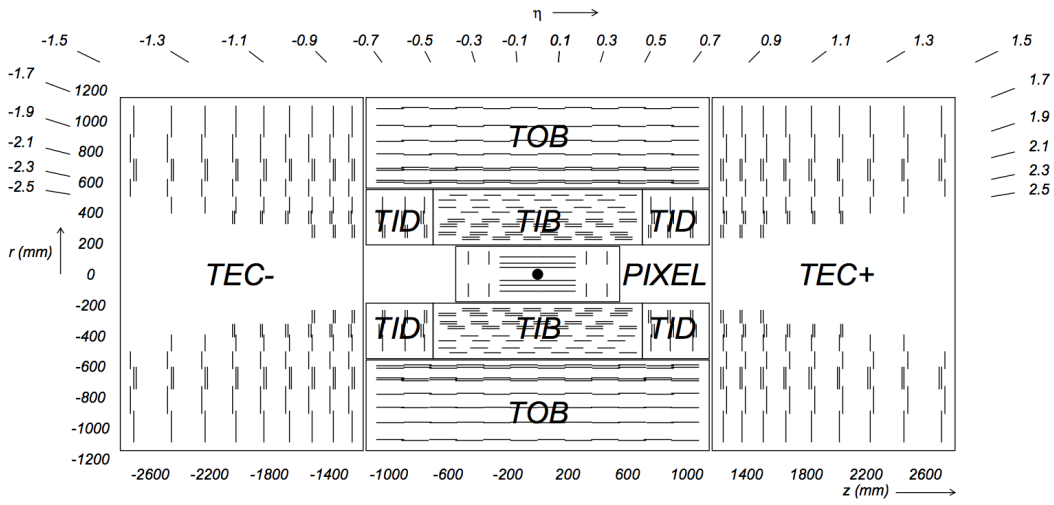


Figure 2.5.: Schematic cross section through the CMS silicon tracker [57]

2.2.3. Silicon strip detector

The outer part of the CMS tracker consists of layers of silicon strip detectors. They are arranged in 4 sections. The Tracker Inner Barrel (TIB) has 4 cylindrical layers at radii ranging from 25.5 to 49.8 cm. Towards the forward regions, the TIB is closed by the Tracker Inner Disks (TID). On each side, three discs are positioned between $|z| = 80 \text{ cm}$ and $|z| = 90 \text{ cm}$. Together these two sections ensure a hermetical coverage up to $|\eta| = 2.2$.

The outer two sections of the strip tracker are the Tracker Outer Barrel (TOB), comprising 6 cylindrical detector layers and the Tracker End Caps (TEC) with 9 discs on each end. The TEC increase the coverage to $|\eta| < 2.5$.

Several layers carry so called stereo modules, made of 2 sensors mounted back to back with an stereo angle of 100 mrad . These allow a measurement of the second coordinate (which is z for the barrel and r for the end cap sensors). The spatial resolution of the

TIB is $23 - 35 \mu\text{m}$ in ϕ and $230 \mu\text{m}$ in z . The TOB achieves resolutions of $35 - 52 \mu\text{m}$ in ϕ and $530 \mu\text{m}$ in z .

Like the pixel modules, the strip modules are radiation hard and operated at a temperature of -10°C to minimize the effects of radiation damage. Nonetheless, the lifetime of the tracker is limited to ~ 10 years.

The tracker was designed to achieve a relative momentum resolution of less than 2% within $|\eta| < 1.6$ for muons at $100 \text{ GeV}/c$. For higher pseudo rapidities the momentum resolution degrades, because of the reduced lever arm. This has been confirmed by measurements, using collision data [69].

2.2.4. Electromagnetic calorimeter

CMS has a hermetic homogeneous electromagnetic calorimeter (ECAL), which uses lead tungstate crystals (PbWO_4) as scintillator material. It comprises a barrel ($|\eta| < 1.479$) and two endcap regions ($1.479 < |\eta| < 3.0$) which are complemented by the so called preshower. Avalanche photo diodes (APD) are used to detect the scintillation photons in the barrel region, while vacuum photo triodes (VPT), being more radiation hard than the silicon based APDs, are used for the endcaps. Lead tungstate was chosen as scintillator material, because it combines several favorable properties. Its high density (8.28 g/cm^3), the short radiation length (0.89 cm) and its small Molière radius (2.2 cm) allow a fine granularity and a compact design of the calorimeter. The crystals in the barrel part have a depth of 23 cm , providing ~ 26 radiation lengths (X_0). Their front faces measure $22 \times 22 \text{ mm}^2$ corresponding to $\Delta\eta \times \Delta\phi = 0.0175 \times 0.0175$ in the barrel region. The endcaps crystal size varies between 0.0175×0.0175 and 0.05×0.05 . Another favorable property of PbWO_4 is that it emits 80% of the scintillation photons within 25 ns and is therefore suitable for the high bunch crossing rates of 40 MHz .

The aim of the additional sampling calorimeter, called Preshower, is to facilitate the identification of neutral pions and electrons. It is positioned in front of the endcaps and covers the pseudorapidity range $1.653 < |\eta| < 2.6$. It comprises 2 layers of lead and silicon strip sensors with a total thickness of 20 cm . The preshower adds $\sim 3X_0$ to the total radiation length of the ECAL endcaps.

Radiation damage also affects the performance of the ECAL. Ionizing radiation causes oxygen vacancies and lattice impurities, which change the transparency of the crystals, whereas the photon yield is not sensitive to irradiation. The loss of transparency is regularly measured by injecting laser light and accounted for in the ECAL calibration.

A major design criteria for the ECAL was its ability to discover the Higgs boson in one of the most promising decay channels $H \rightarrow \gamma\gamma$. This requires a good mass resolution which is determined by the energy resolution of the ECAL. The energy resolution can be parametrized by

$$\frac{\sigma_E}{E} = \frac{S}{\sqrt{E(\text{GeV})}} \oplus \frac{N}{E(\text{GeV})} \oplus C \quad (2.6)$$

up to energies of 500 GeV, where the shower leakage starts to become significant. The contributions to the resolution are parametrized by a stochastic term ($S = 2.8\%$), a noise term ($N = 0.12\%$) and a constant term ($C = 0.3\%$), dominant at high energies. Their values were determined from test beam measurements [70] and fulfill the design goals.

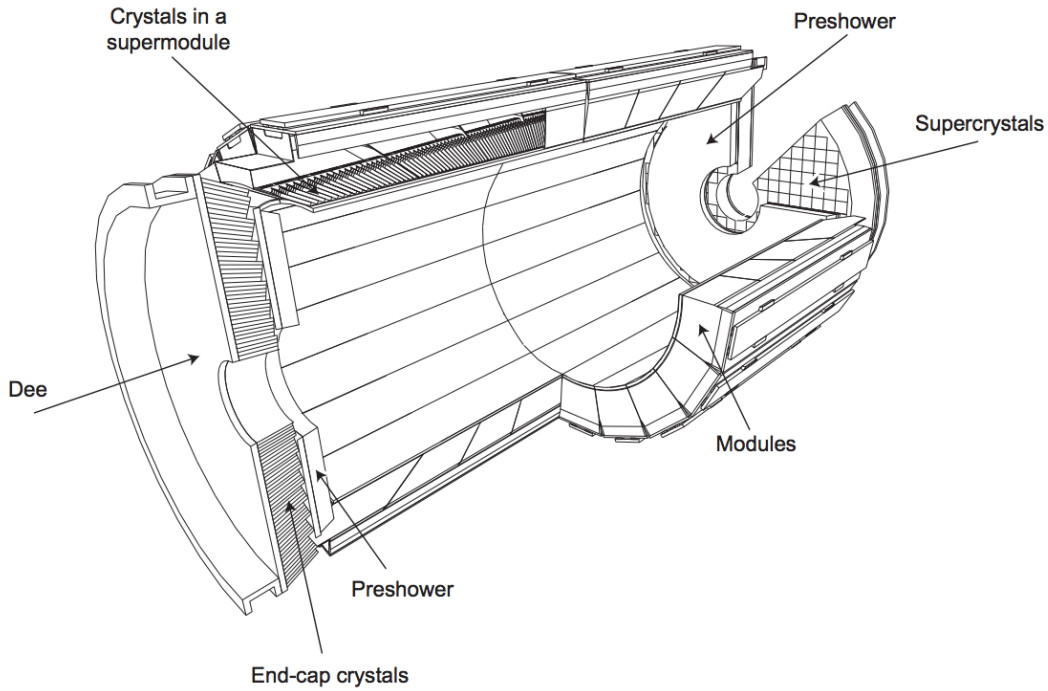


Figure 2.6.: Schematic view of the electromagnetic calorimeter [71]

2.2.5. Hadronic calorimeter

The hadronic calorimeter (HCAL) of CMS was built as non-compensating sampling calorimeter and consists of four elements. The barrel part (HB), fully contained inside the magnet coil, covers the pseudorapidity range $|\eta| < 1.3$. The endcaps (HE) cover $1.3 < |\eta| < 3$ and an additional forward calorimeter (HF) positioned at $|z| = 11.2$ m increases the calorimeter's acceptance up to $|\eta| < 5$. Additional layers are mounted outside the magnet. These layers are called HCAL Outer (HO) serve as “tail-catcher” to ensure the containment of high energetic hadronic showers in the region of $|\eta| < 1.3$. The HB alone provides only $5.82/\sin\theta$ interaction lengths (λ_I). Together with the ECAL barrel (providing $\sim 1.1\lambda_I$), the solenoid coil and the HO, the total depth of

the calorimeter system is extended to a minimum of $11.8\lambda_I$ in the barrel region. A schematic view of the hadronic calorimeter is shown in Fig. 2.7.

Except for the HF, where radiation hardness is of prime importance, the HCAL consists of 5 cm thick layers of brass absorbers and plastic scintillators, which are read out with wave length shifting fibers connected to multichannel hybrid photodiodes. Only the first and the last layer of the HB are made of steel to increase the structural strength. The scintillators of the HB and the HO are divided into segments, covering $\Delta\eta \times \Delta\phi = 0.087 \times 0.087$, what corresponds to a 5×5 cell of ECAL crystals. The same granularity is used in the HE for pseudo rapidities $|\eta| < 1.6$ while for $|\eta| > 1.6$ a coarser scintillator segmentation of $\Delta\eta \times \Delta\phi = 0.17 \times 0.17$ is used.

As already stated, the HF will suffer from the extremely high flux of high energy particles. It is estimated that its central part (at $|\eta| = 5$) will be exposed to ~ 10 MGy during 10 years of LHC operation. To withstand these harsh conditions, absorber plates made of steel were chosen and quartz fibers are used as active material. They emit Cherenkov light when transversed by charged shower particles. Since the magnetic field strength in the forward region is smaller compared to the barrel region, conventional photomultiplier tubes are used for the HF to convert the optical signals.

The HCAL energy response and resolution, its linearity, the e/π ratio and the shower leakage probability were studied in various test beams and validated by comparison to simulation. The raw energy resolution measured for pions with momenta between 30 GeV/ c and 300 GeV/ c can be parametrized as

$$\frac{\sigma_E}{E} = \frac{120\%}{\sqrt{E(\text{GeV})}} \oplus 6.9\%. \quad (2.7)$$

It can be substantially improved by exploiting the fine granularity of the calorimeter through cluster-based response compensation [72].

2.2.6. Superconducting magnet

The large solenoidal magnet, with a bore measuring 5.9 m in diameter and 12.9 m in length, is one of the detector's central components. The magnetic flux density (B) within the bore is 3.8 T. The strength of B is one of the factors that determine the transverse momentum resolution (Δp_T) and the charge misidentification rate of high energetic muon tracks. Both quantities, p_T and the charge q , are measured via the radius of curvature R of the x - y projection of a particle track since

$$R = k \frac{p_T}{qB}. \quad (2.8)$$

The factor $k = c/10^9$ accounts for the units commonly used in high-energy physics, thus p_T has the unit [GeV/ c] and q is measured in multiples of the elementary charge, delivering radii in [m]. A design goal of CMS was to achieve a relative momentum resolution of 10% at 1 TeV/ c . In order to reach such a high magnetic flux, it is necessary

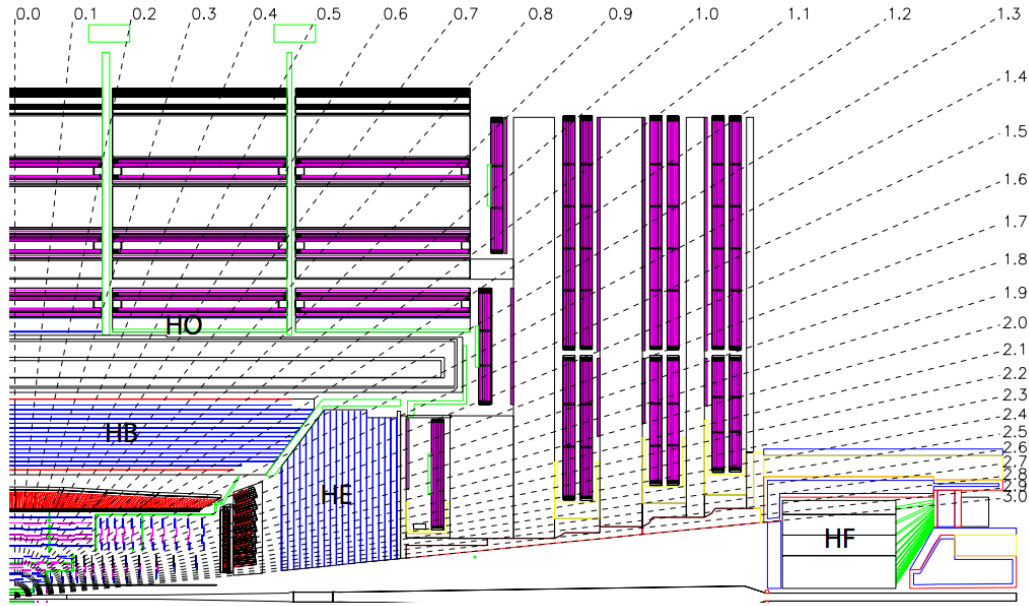


Figure 2.7.: Schematic view of the hadronic calorimeter and other subdetectors of CMS [57].

to use a superconducting coil, operated at a temperature of 4.6 K. The maximum energy, stored by the magnet during operation, is approximately 2.6 GJ.

2.2.7. Muon system

Muon identification is an important task, since muonic decays provide a clear signature for many SM processes and for many models of physics beyond the SM. Distinct interaction properties allow their identification despite a high background rate and large track multiplicities, resulting from pileup of secondary collisions. Furthermore muons are less affected by multiple scattering than electrons and emit less bremsstrahlung, resulting in a better mass resolution for dimuon resonances.

The muon system is the outermost detector system of CMS. The hermetic calorimeters and the magnet provide a good shielding from other charged particles, therefore muons can be reliably identified by the muon system with a relatively low misidentification rate. In general, measurements from the silicon tracker and the muon system are combined to improve the momentum resolution. For low energy muons, the momentum resolution of the standalone muon system is limited, because of multiple scattering in the inner detector systems. Therefore, the combined resolution is driven by the tracker measurements for $p_T < 200 \text{ GeV}/c$ (Fig. 2.8).

The muon system uses 3 kinds of gaseous detectors (Fig. 2.9).

- **Drift Tubes (DT)** are used in the barrel region (MB) since the magnetic field strength is low (the flux is captured by the return yoke), the neutron induced

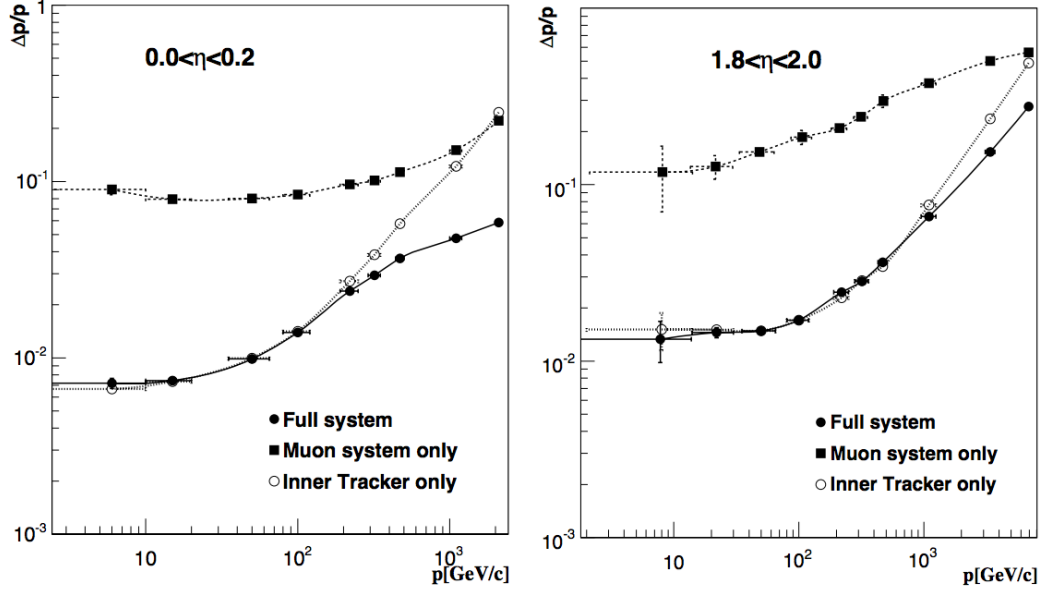


Figure 2.8.: Muon momentum resolution as function of p . For $p < 200 \text{ GeV}/c$ the resolution is determined by the tracker measurement, while at higher momentum the combination of tracker and muon system improves the performance considerably. [67]

background is small and muon rates are moderate. A total of 250 DT chambers are organized in 4 cylindrical layers mounted in the return yoke of the magnet at radii of approximately 4.0, 4.9, 5.9 and 7.0 m. They cover a pseudorapidity range of $|\eta| < 1.2$. The layers are staggered to guarantee that high p_T muons transverse at least 3 out of 4 chambers.

A DT chamber usually consists of 3 superlayers. The wires of the 2 outer superlayers are parallel to the beam line and provide a $r - \phi$ measurement while the wires of the central superlayer are orthogonal to the beam line and measure the z coordinate. In the outermost chambers of layer MB4 (see Fig. 2.9), the central superlayer is missing.

- **Cathode Strip Chambers (CSC)** are deployed in the endcaps (ME), where the magnetic field is stronger and the occupancy is higher compared to the barrel region. In the pseudorapidity range $1.2 < |\eta| < 2.4$ muons cross at least 3 CSC chambers, while the range $0.9 < |\eta| < 1.2$ is covered by a combination of CSCs and DTs.

CMS comprises 468 CSC chambers, each consisting of 6 planes with radial cathode strips, measuring the ϕ direction and anode wires running perpendicular to the strips, measuring r . Via charge interpolation a spatial point resolution ranging between $75 - 150 \mu\text{m}$ in the $r - \phi$ plane can be achieved.

- **Resistive Plate Chambers (RPC)** are used in both the barrel and the endcap regions over the pseudorapidity range of $|\eta| < 1.6$. In the barrel region they are

mounted on both sides of the 2 innermost layers of DTs, while they are only mounted on the inner side of the 2 outer DT layers. Only 3 layers of RPCs are used for the endcaps to support the CSCs

RPCs are very fast detectors and provide time resolutions of ~ 1 ns. Their timing information is therefore used by the trigger and to associate muons to the correct bunch crossing. However, RPCs have a coarser spatial resolution than the DTs and CSCs.

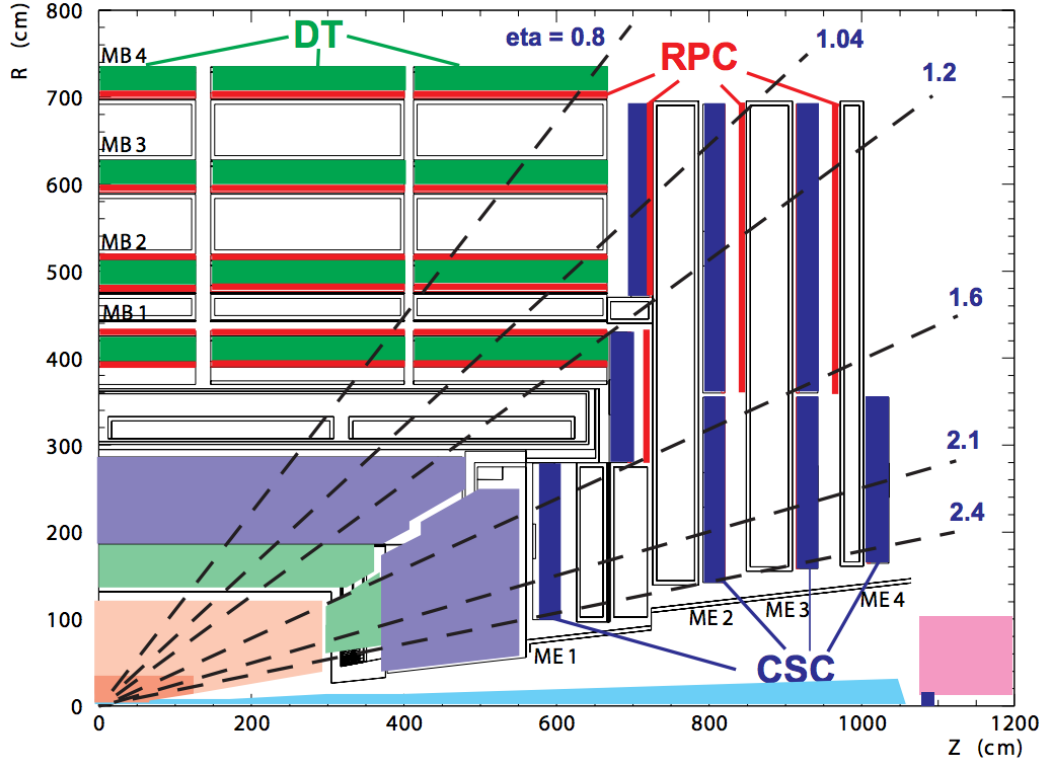


Figure 2.9.: Schematic view of the muon system of CMS [67].

2.2.8. Data acquisition and the trigger system

The nominal LHC design luminosity of $10^{34} \text{ cm}^{-2} \text{ s}^{-1}$ results in an expected proton-proton interaction rate of order 10^9 s^{-1} . Although the actual event rate during the 2011 and 2012 runs was reduced to 20 MHz, online data selection is still an extremely difficult task and determines the overall performance of the experiment.

The average size of an event is approximately 1 MB and the maximum bandwidth for storing data on disks or tape is at the order of $O(100) \text{ MB/s}$ [73]. Thus the trigger system of CMS has been designed to reduce an event rate of 40 MHz to $O(100 \text{ Hz})$. In CMS this task is split into two steps.

- **Level-1 Trigger (L1)**

The L1 Trigger [74] is implemented using custom-designed electronics, such as

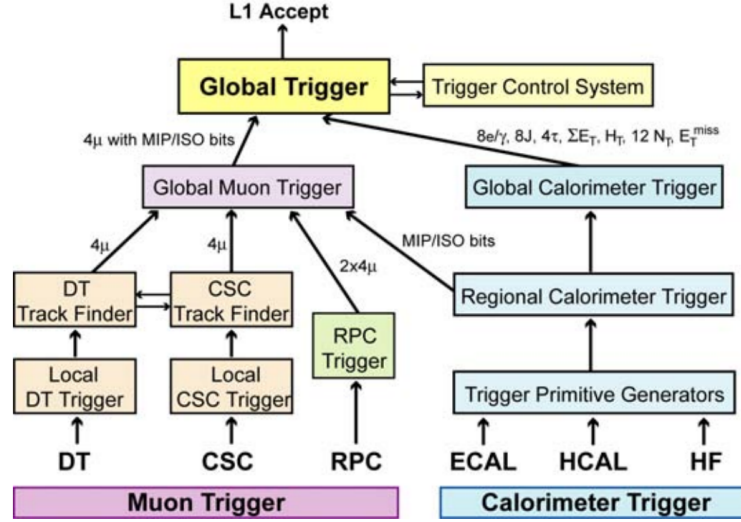


Figure 2.10.: Architecture of the Level-1 Trigger system. [57]

FPGAs, ASICs and programmable memory lookup tables (LUT), which allow flexibility but also fulfill speed requirements. It is designed to achieve a rate reduction of the order of 10^3 , resulting in a maximal output rate of 100 kHz.

The schematic overview of the system is shown in Fig. 2.10. It uses coarse segmented data from the muon system and from the calorimeters, while the complete raw data is pipelined in the front-end electronics until being rejected or accepted for further processing by the High-Level Trigger. The allowed latency between the bunch-crossing and the L1 Trigger decision is $3.2 \mu\text{s}$.

The calorimetric trigger branch combines signals from the ECAL and the HCAL to provide information about jet related quantities like multiplicities, individual energies or their total energy, as well as the missing transverse energy of the event. It can pass information about the energy deposit in the vicinity of muons to the muonic trigger branch.

The muonic branch combines information of all three muon systems, the DTs, the CSCs and the RPCs. It delivers up to four final muon candidates, sorted by their transverse momentum to the Global Trigger (GT).

The GT calculates the final L1 trigger decision based on information from both branches. Up to 128 programmable algorithms can be executed in parallel. Additionally 64 so called technical triggers can be considered based on direct signals from subdetectors or the TOTEM experiment.

- **High-Level Trigger (HLT)**

After being accepted by the L1 trigger, the full event data stored in the various front-end buffers of the subdetectors has to be collected by the data acquisition system (Fig. 2.11). At this stage, the data acquisition has to handle a data flow of

~ 100 GB/s, which is distributed to the software based filter system of the high-level trigger HLT [75]. The HLT runs on a computer farm and uses fast versions of the same algorithms that are used in the offline reconstruction. The main strategy to speed up the event processing is to reject events as early as possible. Typically, the reconstruction starts with information from the calorimeters and the muon detectors before tracker information is added. Because of the high number of channels and the complex pattern recognition, the full reconstruction of trajectories in the tracker is expensive in CPU time. Therefore, a partial reconstruction, involving only information from the pixel detector, is used for trigger decisions.

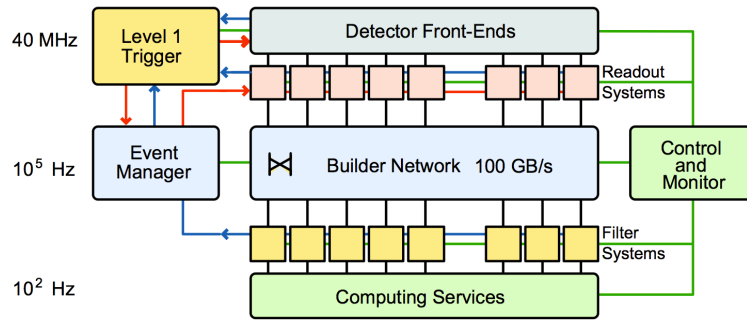


Figure 2.11.: Architecture of the data acquisition system. [57]

3. Data analysis

3.1. Analysis strategy

The analysis presented in this thesis searches for gluino-pair production in proton-proton collisions with a center-of-mass energy of 8 TeV. The data sample was recorded during the year 2012 and corresponds to an integrated luminosity of 19.4 fb^{-1} . The search focuses on events with a single isolated lepton, high hadronic activity, large missing transverse momentum and jets originating from b-quarks. This signature is well motivated for the following reasons.

- **Large missing transverse momentum:**

As already argued in Sec. 1.1.2 and 1.2.3 the conservation of R-parity implies the stability of the LSP and is motivated by astrophysical evidence for dark matter as well as by constraints from the proton decay. In many SUSY models, the LSP is the lightest neutralino which interacts only weakly and therefore escapes undetected, potentially producing a large momentum imbalance in the plane transverse to the beam axis. This observable is referred to as missing transverse momentum (\cancel{E}_T). Neglecting measurement errors and detector effects, the only source of \cancel{E}_T in background events is the production of neutrinos in weak decays of SM particles. \cancel{E}_T is therefore well suited to discriminate SUSY production from SM processes.

- **Lepton isolation:**

Isolated leptons are predominantly produced in weak decays of SM and SUSY particles. In this context “isolation” refers to the energy deposited in the vicinity of the lepton. It allows to discriminate prompt leptons, produced in hard interaction processes, from non-prompt leptons that are produced in jets or via photon conversions. Also misidentified leptons, e.g. mesons that are reconstructed as leptons, are rejected by requiring isolation.

- **High hadronic activity:**

High hadronic energy arises in signal events from complex decay chains of the heavy, colored particles. Besides the total hadronic energy, the multiplicity of jets is typically larger in SUSY decay chains, compared to those in the SM. A good example is the simplified model topology $T1tttt$ with four top quarks in the final state. A sensitive selection for this topology, which keeps as many signal events as possible, while rejecting the maximum amount of SM background events, requires a minimum of six reconstructed jets. An important quantity for this analysis is the sum of the transverse hadronic energy in the event, denoted

as H_T . It is defined as the scalar sum of all jet momenta that pass the criteria described in 3.3.1.

$$H_T = \sum_{i \in \text{jets}} p_{T,i} \quad (3.1)$$

- **b -quark jets:**

In many SUSY models, at least one of the two mass eigenstates of the left- and right-handed top squarks is among the lightest charged sparticles (see Sec. 1.2.4). Their decays lead to an enhanced fraction of events with 3rd generation quarks in the final state. Therefore, the identification of jets originating from the fragmentation of b -quarks (b -jets) is an important tool in the discrimination between signal and SM background processes.

The details of the preselection requirements and the properties of the selected sample are presented in Sec. 3.3.2. This selection is suitable for targeting gluino-pair production, with four top quarks and two neutralinos in the final state.

The important SM backgrounds, contributing to the event selection with at least 6 reconstructed jets, 2 of them identified as b -jets, arise either from true single-leptonic decays or from feed down from dilepton topologies due to unidentified leptons. The most important background source is the pair production of top quarks ($t\bar{t}$), followed by smaller contributions from W boson production in association with jets (W +jets), single top quark production (single- t) and multijet production (QCD). A purely dileptonic background source of minor importance is Drell-Yan production. These SM backgrounds are all characterized by a rapidly falling E_T spectrum.

In order to estimate SM background event yields from data, a model describing the E_T spectrum as function of H_T and the b -tag multiplicity (number of identified b -quark jets) is developed. The model parameters are estimated using a maximum likelihood fit, including only events from kinematic regions with low E_T , low H_T and one or two b -tagged jets. These control regions are expected to be dominated by SM background processes. Subsequently the model is extrapolated to signal regions defined by the requirement of two b -tagged jets, high E_T or high H_T to predict the SM background yield. Background predictions for signal regions comprising events with at least three b -tagged jets are obtained by extrapolating the results from the two b -tag regions, exploiting precise measurements of the b -tagging algorithm's efficiencies and misidentification probabilities for light partons and charm quarks. These signal regions with more than two b -tagged jets are particularly sensitive to signal models predicting four top quarks in the final state (Sec. 1.2.7).

Data and simulated event samples are described in Sec. 3.2. The reconstruction and selection of the objects that are relevant for this analysis (electrons, muons, jets, E_T and b -jet identification) are discussed in Sec. 3.3. Section 3.4 describes the background estimation for signal regions with two b -tagged jets and the extrapolation of these estimates to signal regions with at least three b -tagged jets. In Sec. 4 the results are presented and interpreted in terms of the simplified model topologies **T1ttttt**, **T1t1t** and **T5ttttt**.

A methodically very similar analysis strategy has been applied for the data sample recorded during the year 2011. Besides the lower center-of-mass energy and a smaller sample size, the preselection required four or more reconstructed jets instead of six. This changes the background composition compared to the 2012 analysis and enhances the importance of the W +jets background. The 2011 analysis results are interpreted in terms of the cMSSM and $T1tttt$. A description of the 2011 analysis is not part of this thesis and can be found in [76, 77]. Nonetheless, a summary of the results obtained in 2011 is included in Sec. 4.3 and compared with the recent results.

3.2. Data samples and simulation

3.2.1. Data samples

During the year 2012, data has been recorded in 4 periods, *Run2012A*, *Run2012B*, *Run2012C* and *Run2012D*. Although the maximum instantaneous luminosity increased over the year, the conditions were more stable compared to the significant increase of instantaneous luminosity during 2011.

Within the CMS collaboration, the longest, uninterrupted period of data-taking is called a run. It can extend over the duration of an LHC fill (up to 12 h). A run is subdivided into luminosity sections, which correspond to 2^{18} orbits of the LHC's beam (~ 23 s). Trigger thresholds and prescales do not change during this period. Within a luminosity section, each event can be uniquely identified by its event number. Before being released for physics analysis, the data is validated and certified for each luminosity section. This ensures that all CMS subdetector systems work within the required specifications. Only runs and luminosity sections passing the certification, are used for physics analysis. Thereby, approximately 10% of the recorded data is rejected.

As discussed in Sec. 2.2.8, only events that pass the L1 trigger and the HLT are stored by the DAQ. They are sorted in dedicated data streams which group trigger decisions from similar topologies. The output of each data stream constitutes a primary dataset. Data used in this analysis is extracted from the *MuHad* and *ElectronHad* primary datasets and has been reconstructed using the CMS software framework release *CMSSW_5_3_X*. The *MuHad* and *ElectronHad* datasets contain events that pass trigger requirements based on lepton momenta (electrons or muons only), H_T and \cancel{E}_T . Such triggers that base their decision on attributes of several reconstructed objects, are commonly referred to as cross triggers. The names of the datasets and run ranges are summarized in Tab. A.1 in Appendix A.

The relative integrated luminosity recorded by CMS is estimated by counting clusters, which were reconstructed from signals measured by the pixel detector. The absolute calibration is inferred from Van der Meer scans [78, 79]. An alternative method exploits HF measurements, instead of the pixel detector and is used as validation [80]. The systematic uncertainty on the estimate of the integrated luminosity recorded by CMS during the year 2012 was found to be 4.4%.

3.2.2. Simulation

The Monte Carlo simulation of proton-proton collisions and the interaction of the collision products with the detector is performed in three steps. As a first step, the hard scattering process is calculated using an event generator such as PYTHIA 6 [81], MADGRAPH [82] or POWHEG [83]. In a second step the showering of the intermediate parton states from the hard scatter is provided by PYTHIA for all simulated samples. Finally the interactions with the CMS detector are simulated, using a detailed model of the detector implemented in GEANT4 [84]. This software framework simulates interactions of the generated particles with the detector material, as well as the response of the detector electronics to these interactions.

The output of this simulation process comprises all the information that would be stored by the DAQ from measurements of real particle collisions. Simulated events are therefore reconstructed using the same software tools as for real data. Of course, the information about the simulated physics process (i.e. the initial, intermediate and final particle states and their four-momenta) is retained.

In order to simulate large samples (e.g. scans over the parameter space of a SUSY model), the CMS collaboration has developed a dedicated framework for fast parametric simulation, called FASTSIM. This framework increases the production rate by a factor of ~ 100 , compared to GEANT4. A description of FASTSIM and further references can be found in [85].

For the simulation of the SM background, we use MADGRAPH to generate W +jets and Drell-Yan events, while POWHEG is used for the single- t and $t\bar{t}$ events. For the two latter samples, decays of tau leptons are simulated by TAUOLA [86]. QCD production was simulated using only PYTHIA. In order to better match the requirements of a leptonic analysis, the QCD sample was enriched by events with electrons and muons at the generator level.

The event yields of the simulated samples are scaled to match the integrated luminosity L of the data. The weight factor for N simulated events of a physics process with cross section σ is

$$w = \frac{\sigma L}{N}. \quad (3.2)$$

For $t\bar{t}$ production, the next-to-leading order (NLO) cross section of 225.2 pb [87, 88] is used for the normalization. The production of W +jets is restricted to leptonic decay modes and to $H_T > 250$ GeV. The next-to-next-to-leading order (NNLO) cross section for inclusive decays to $\ell\nu$ of 36.3 nb is used [89]. Drell-Yan production with decays to e, μ or τ pairs is simulated for lepton pair masses larger than 10 GeV. A cross section of 1.92 nb is used for the normalization of each decay channel. The background from single t -quark production in the s -, t - and tW channels has cross sections of 5.55, 87.1 and 22.2 pb.

The high instantaneous luminosities achieved during 2012 results in 21 collisions per bunch crossing on average (Fig. 3.1). The physics process of interest that actually

triggered the recording of the event, usually originates from a single high energetic collision, while the residual collisions are low energetic. These residual collisions are commonly called “pileup”.

In the simulation this is accounted for by adding minimum bias interactions to the event. Since the simulation is usually completed before the end of the data-taking, the distribution of the number of pileup collisions has to be guessed beforehand and does not exactly match the actual distribution in data. Therefore, all simulated samples are reweighted, in order to reproduce the pileup distribution in data. The reweighting procedure follows the recommended procedure by CMS, based on the true number of pileup interactions which is known for the simulation. For data it is estimated for each bunch crossing from HF measurements.

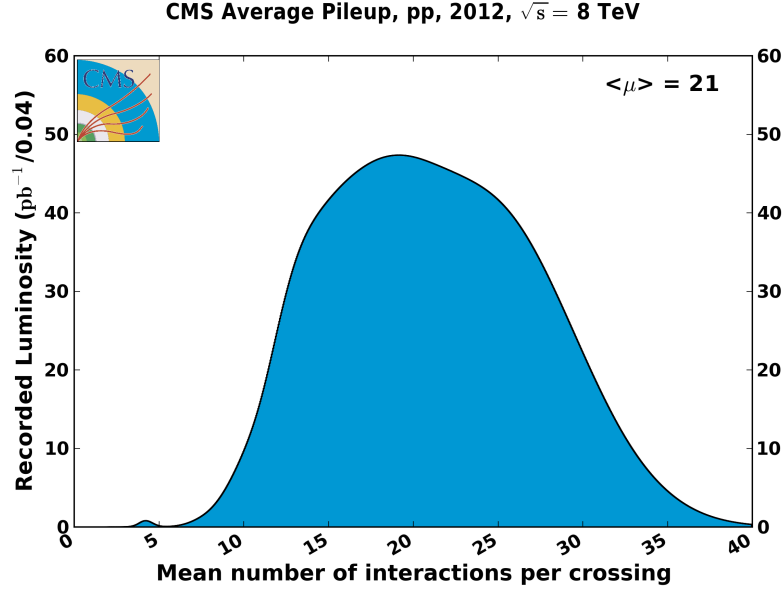


Figure 3.1.: Distribution for the number of interactions per bunch crossing [66]

The signal scans of the three simplified model topologies are generated using MADGRAPH for the hard scattering processes and PYTHIA for particle decays and hadronization, followed by the FASTSIM detector simulation. The scan of $T1tttt$ extends over the mass ranges $400 \leq m_{\tilde{g}} \leq 1400$ GeV and $m_{\tilde{\chi}^0} \leq m_{\tilde{g}} - 200$ GeV. The $T5tttt$ scan includes the mass ranges $800 \leq m_{\tilde{g}} \leq 1400$ GeV and $m_{\tilde{t}} \leq m_{\tilde{g}} - 175$ GeV. For the third scan of $T1t1t$, signal samples in the mass ranges $200 \leq m_{\tilde{t}} \leq 825$ GeV and $m_{\tilde{\chi}^0} \leq m_{\tilde{t}} - 100$ GeV are generated. Step sizes for the scan of the gluino, neutralino and top-squark masses range between 25 and 50 GeV. The NLO+NLL (next-to-leading logarithmic) gluino production cross sections and their theoretical uncertainties are taken from [90].

The names of all simulated background and signal samples used for this work are listed in Tab. A.2 in Appendix A.

3.3. Analysis objects, selection requirements and efficiencies

The reconstruction of analysis objects and the preselection requirements on events have been synchronized among two other analysis groups that participate in the CMS wide effort to search for supersymmetric topologies with a single lepton in the final state and the analysis presented in this thesis. This allows for a common evaluation of object efficiencies and facilitates the comparison of individual results and their interpretations. The two other analysis are documented in [91].

The event reconstruction is based on the particle flow (PF) algorithm [92, 93, 94]. This algorithm combines information from all sub-detectors, in order to identify and reconstruct all stable particles in the event, such as electrons, muons, photons, charged hadrons and neutral hadrons. The resulting list of particle candidates is then used to construct various higher-level objects (e.g. jets, H_T , \cancel{E}_T , ...). This section briefly describes the reconstruction methods, the selection requirements and the resulting efficiencies as well as the performance of the analysis objects used in this work.

3.3.1. Analysis objects

Muons

The standard reconstruction of muons [95, 96] is done prior to the PF event reconstruction. In a first step, a Kalman filter algorithm [97] is used to build tracks either from silicon tracker measurements (“tracker tracks”), or from muon chamber measurements (“standalone muons”). To improve the momentum resolution for standalone muons, the position of the beams spot is used to constrain the muon track.

The silicon tracker and muon chamber measurements are then combined in two ways. The first approach searches the best matching tracker track for each standalone muon and reapplies the Kalman filter on the combined set of measurements. The resulting muon object is called “global muon”. Figure 2.8 shows the momentum resolution for global muons. It is driven by tracker measurements for momenta smaller than 200 GeV/ c but substantially improved by the muon system for higher momenta.

The second approach extrapolates each tracker track to the muon chambers, considering energy loss and multiple scattering. If this extrapolation matches at least one muon segment (a short track stub made of DT or CSC hits), the tracker track is accepted as a “tracker muon”. The tracker muon collection is less pure compared to the global muon collection, but has the advantage of being more efficient at low momenta [98]. If a tracker muon and a global muon share the same tracker track, they are merged to a single muon object, shared by both collections.

The standard reconstruction is efficient and robust, but the resulting muon collections contain a significant amount of misidentified hadrons. Several sets of additional selection requirements, based on muon identification variables, are used to increase the

purity. These requirements determine the efficiency of the muon identification and therefore vary between analyses. In particular, it is important to preserve a high efficiency to identify muons within jets. Unidentified muons within jets would contribute to the charged jet component and thereby distort the energy estimate of the neutral jet component. The muon identification criteria used by the PF algorithm aim to find an optimal balance between high identification efficiency and purity [95]. A detailed description of the PF muon identification is given in [92].

The muon selection used in this analysis follows internal guidelines of CMS, which are documented in [95]. We start with muon candidates, reconstructed as global muons that pass the identification criteria of the PF algorithm. Due to the geometric acceptance of the muon spectrometer, only muons within $|\eta| < 2.4$ are selected and their transverse momentum has to exceed $20 \text{ GeV}/c$. Differences in the momentum assignment between the standard reconstruction and PF can result from reconstruction errors in pathological cases. To exclude such events, the difference in transverse momentum to the closest muonic PF candidate with $p_T > 10 \text{ GeV}/c$ must be smaller than $5 \text{ GeV}/c$.

The transverse (d_{xy}) and the longitudinal (d_z) impact parameters of the muon track with respect to the primary vertex are required to be smaller than $200 \mu\text{m}$ and 5 mm respectively. This serves as a protection against cosmic muons and suppresses non-prompt muons originating from hadronic decays. Vertices are reconstructed using an adaptive vertex fitter [99] and sorted by $\sum (p_T^{\text{track}})^2$. Further requirements, which suppress non-prompt muons or misidentified muons, originating from hadrons that are not absorbed by the HCAL and reach the muon system, are based on observables related to the quality of the track reconstruction. The global track fit must have a $\chi^2/\text{ndf} < 10$ and at least one hit in the muon chamber must be included in the fit. In addition, the tracker track must be matched to muon segments reconstructed in at least two different muon stations and hits from at least 5 different tracker layers are required, ensuring a precise measurement of the transverse momentum.

As stated previously, prompt and non-prompt leptons can also be discriminated by requiring the lepton to be isolated. To calculate the muon isolation, we use the sum of transverse momenta from reconstructed PF candidates, such as charged hadrons, neutral hadrons and photons, in a cone of $\Delta R < 0.3$ around the muon. Their energy deposits are denoted as E_T^\pm , E_T^0 and E_T^γ . To minimize the influence of pileup on the isolation, only charged hadrons that can be associated to the primary vertex are considered in the sum. Since neutral hadrons and photons do not leave any signals in the tracker, they cannot be matched to a vertex. The contribution from the neutral pileup component is therefore estimated by taking 50% of the sum over the deposits from charged hadrons that are not associated to the primary vertex. The fraction of 50% corresponds to the average ratio between neutral to charged energy deposits and has been measured in [93]. This analysis requires the relative isolation I_{rel} (with respect to the transverse momentum of the muon) to be smaller than 0.12.

$$I_{\text{rel}} = \frac{\sum E_{T,\text{PV}}^\pm + \max\left(0, \sum E_T^0 + \sum E_T^\gamma - 0.5 \sum E_{T,\text{PU}}^\pm\right)}{p_T} \quad (3.3)$$

Each event that is selected for this analysis must contain exactly one muon, passing all requirements just mentioned.

A looser selection is defined in order to veto events with more than one muon. The veto selection requires muons to be reconstructed either as global or as tracker muon which passes the PF identification criteria. The kinematic thresholds are relaxed to $15 \text{ GeV}/c$ and $|\eta| < 2.5$. The impact parameter requirements with respect to the primary vertex are loosened to $|d_{xy}| < 2 \text{ mm}$ and $|d_z| < 5 \text{ mm}$ and the relative isolation must not exceed 0.2.

Electrons

CMS uses two complementary approaches to identify electrons. The ECAL-driven reconstruction [100] builds clusters from energy deposits in the electromagnetic calorimeter within a narrow window in η , which extends over a wide range in the azimuthal ϕ direction in order to catch bremsstrahlung radiated by the electron when traversing the tracker material. These ECAL clusters are matched to track seeds, built from hits in the pixel detector. The electron tracks are then reconstructed, starting from matched seeds using a Gaussian Sum Filter (GSF) [101], which is able to cope with energy loss due to bremsstrahlung. This approach is well suited for isolated high- p_T electrons.

The ECAL-driven approach is complemented by the tracker-driven reconstruction, which is able to reconstruct low- p_T electrons starting from $2 \text{ GeV}/c$. Its efficiency is less dependent on the electron isolation. Since the GSF fit is CPU intensive, all tracks that are reconstructed by the fast Kalman filter are tested for their compatibility with the electron hypothesis, based on track quality criteria. The track quality is typically worse for electrons, because large bremsstrahlung emission cannot be handled by the Kalman filter. Compatible tracks are then used as seed for the GSF fit, which is extrapolated to the ECAL to find the energy deposit of the electron. Energy deposits from bremsstrahlung are associated to the electron candidate by extrapolating a tangent to the electron track from each tracker layer to the ECAL [92].

For this analysis, electrons with $p_T > 20 \text{ GeV}/c$ in the pseudorapidity range $|\eta| < 2.5$ are selected. Only the barrel-endcap transition region of $1.4442 < |\eta| < 1.566$ is excluded. The following criteria are used to differentiate prompt electrons from misidentified or non-prompt electrons, originating from meson decays or photon conversions. The ratio of energy deposits in the HCAL and the ECAL (H/E) must be smaller than 0.12 (0.10) for the barrel (endcap) region. The observables $\Delta\phi$ and $\Delta\eta$ measure the distance between the ECAL cluster and the extrapolation of the GSF-track to the ECAL. The allowed deviation in the barrel (endcap) is $|\Delta\phi| < 0.06$ (0.03) and $|\Delta\eta| < 0.004$ (0.007). The shape of the ECAL cluster with respect to η can be quantified by $\sigma_{i\eta i\eta}$, which is the energy-weighted sum over the squared η distances between the ECAL-cluster center and the ECAL crystals (in a 5×5 grid around the cluster center). For electrons this observable is small compared to misidentifications or jets. We require $\sigma_{i\eta i\eta} < 0.01$ (0.03) for the barrel (endcaps). Further, dedicated algorithms aim to identify photon conversions that are matched to the electron candidates. In

case a match is found, the electron is rejected. Furthermore, electrons that miss more than one hit on the inner tracker layers are excluded from the analysis. The impact parameter requirements with respect to the primary vertex are $|d_{xy}| < 200 \mu\text{m}$ and $|d_z| < 1 \text{ mm}$.

Similar to the muon isolation, the electron isolation is calculated from the transverse momenta of the reconstructed PF particles in a cone of $\Delta R < 0.3$. The method to correct for the neutral pileup component differs from the muon case. The correction for electrons uses the FASTJET algorithm [102] to estimate a pileup induced energy flux ρ [$\text{GeV}/\Delta\phi/\Delta\eta$] of the event. An effective area A_{eff} is calculated from $Z \rightarrow ee$ events in bins of η by

$$A_{\text{eff}} = \frac{dI_{\text{uncorr}}^0}{dn_{\text{vtx}}} / \frac{d\rho}{dn_{\text{vtx}}}, \quad (3.4)$$

where I_{uncorr}^0 is the uncorrected neutral component of the electron isolation and n_{vtx} denotes the number of reconstructed vertices. The relative electron isolation, corrected for pileup, is then given by

$$I_{\text{rel}} = \frac{\sum E_{\text{T,PV}}^{\pm} + \max(0, \sum E_{\text{T}}^0 + \sum E_{\text{T}}^{\gamma} - \rho A_{\text{eff}})}{p_{\text{T}}}, \quad (3.5)$$

and required to be smaller than 0.15. Similarly to the muon selection, we reject electrons when the transverse momentum differs more than $10 \text{ GeV}/c$ to that of the closest PF electron candidate.

The electron veto selection accepts all electrons with $p_{\text{T}} > 15 \text{ GeV}/c$ outside the barrel-endcap transition region. The requirements on I_{rel} and $\sigma_{i\eta i\eta}$ are unchanged with respect to the electron selection. H/E is relaxed to 0.15 for the barrel region and unconstrained for the endcaps. For the barrel (endcap) region we require $|\Delta\phi| < 0.8$ (0.7), $|\Delta\eta| < 0.007$ (0.01). The impact parameters $|d_{xy}|$ and $|d_z|$ must be smaller than $400 \mu\text{m}$ and 2 mm respectively.

Jets

Jets are showers of particles that result from the hadronization of quarks and gluons from the hard process. The narrow collimation of the constituent particles allows to use clustering algorithms to reconstruct the jet and assign a four-momentum. Nonetheless, particles might be lost or incorrectly assigned by the clustering algorithm, e.g. when jets overlap or merge.

In a first step, the PF event reconstruction aims to reconstruct all charged particle candidates from silicon tracker measurements and associates calorimeter deposits to these tracks. Neutral particle candidates are built from the remaining calorimeter deposits. The combined collection of PF candidates is used as input to the jet clusterizer. This analysis uses the anti- k_T jet clustering algorithm [103] with a size parameter (ΔR) of 0.5, operating on the output of the PF event reconstruction.

Energy measurements in the CMS calorimeters have a nonlinear dependence on the particle energy and on the pseudorapidity. Furthermore, particles originating from pileup collisions might be associated to the jets and thereby distort the measurements of the jet energy. The raw four-momenta of the jets are therefore subjected to several corrections. These corrections depend on the kinematic properties of the jet and aim to provide an unbiased energy estimate. This analysis uses all collaboration-wide recommended jet corrections [104, 105]:

- **Pileup corrections (L1)**

The FASTJET algorithm provides estimates of the jet areas (A) and the energy density (ρ) resulting from additional minimum bias collisions or electronic noise [106]. The product ρA gives an estimate of the contribution to the jet energy and is subtracted. Thereby, any dependence of the jet energy on the luminosity is removed.

- **Relative η correction (L2)**

This correction aims to achieve a flat jet response over the full η range. Jets are corrected relative to the response of central jets within $|\eta| < 1.3$. The correction factors are estimated from simulation.

- **Absolute p_T correction (L3)**

On top of the relative η correction, the jet response is also corrected to be flat over the momentum range. Again the correction factors are estimated from simulation.

- **Residual data/simulation correction (L2L3)**

Residual differences between data and simulation are corrected as function of p_T and η only for data.

Upon the application of these corrections, jets with $p_T \geq 40$ GeV and $|\eta| < 2.4$ are selected, which additionally fulfill a list of quality criteria in order to suppress noise and spurious energy deposits [107].

Jets are clustered from all PF candidates, including electrons and muons. To avoid double counting, all jets reconstructed within $|\Delta R| < 0.3$ from muons or electrons that pass the lepton veto selections, are excluded from the analysis.

Missing transverse energy

Prior to the collision, protons have negligible transverse momenta. Momentum conservation implies that the transverse momenta of the final state particles are balanced as well. Hence, a transverse momentum imbalance can therefore be used, to detect weakly interacting particles indirectly, such as neutrinos or hypothetical particles (e.g. $\tilde{\chi}^0$) that have not yet been discovered.

The missing transverse momentum is calculated from the same PF candidate collection that is used to cluster jets (see Sec. 3.3.1) by

$$\vec{E}_T = - \sum_i \vec{E}_{T,i}, \quad (3.6)$$

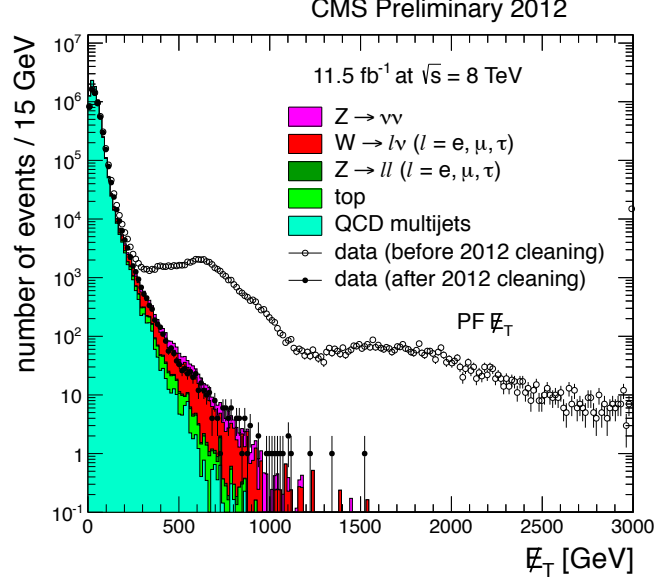


Figure 3.2.: PF \cancel{E}_T distribution for events passing a dijet selection without the 2012 cleaning algorithms applied (open markers), with the 2012 cleaning algorithms applied (filled markers), and simulated events (filled histograms) [109]

where $\vec{E}_{T,i}$ denotes the transverse energy of the i^{th} PF particle candidate. The performance of \cancel{E}_T has been extensively studied in [108, 109]. Of course, nonzero \cancel{E}_T is not necessarily related to undetected, weakly interacting particles, but can also result from instrumental causes or measurement errors such as

- particles hitting readout electronic components of the calorimeters,
- beam-halo particles, i.e. muons resulting from interactions of protons with residual gas or the structures of the accelerator,
- dead or miscalibrated calorimeter cells,
- noise from the detector electronics and
- failures of the tracking algorithm.

A variety of filter algorithms have been developed to reject such events [109]. These algorithms are applied in this analysis. A comparison of the cleaned and uncleaned PF \cancel{E}_T distribution in an inclusive dijet selection is shown in Fig. 3.2, to illustrate the effect of the \cancel{E}_T cleaning filters. In addition to the cleaning filters, two types of corrections are applied to \cancel{E}_T . The so called “type-I” correction propagates the jet energy corrections (see Sec. 3.3.1) to the calculation of \cancel{E}_T and thereby provides consistency between jet energies and \cancel{E}_T . An asymmetry of \cancel{E}_T with respect to ϕ due to a systematic shift in its x- and y-components, which depends linearly on the number of vertices, is also corrected in data and simulation.

Identification of b -quark jets

As discussed already in Sec. 3.1 the identification (tagging) of jets that originate from the fragmentation of b -quarks (b -jets) enhances the sensitivity of SUSY searches.

Several properties of b -hadrons allow to discriminate b -jets from light-flavored jets. Compared to light-flavored hadrons, b -hadrons have larger masses, longer lifetimes, larger leptonic branching fractions and daughter particles with harder momentum spectra [110]. The long lifetime of b -hadrons can lead to long flight distances prior to their decay, thus tracks associated to the jet have larger impact parameters with respect to the primary vertex. The impact parameter is defined as the distance between the vertex and the track at the point of closest approach. Furthermore, it is often possible to reconstruct a secondary vertex that allows to measure the flight distance and the vertex mass.

This analysis uses the combined secondary vertex (CSV) algorithm [110]. Compared to other b -tagging algorithms, which use solely information from the secondary vertex and therefore depend on the vertex reconstruction efficiency, the CSV algorithm reverts to track-based information in case no secondary vertex is found. Likelihood ratios are built from several track and vertex related observables and combined to a single discriminator value. The distribution of the discriminator's output is shown in Fig. 3.3. As can be seen in Fig. 3.4(a) and 3.4(b) the CSV algorithm achieves a good performance compared to several other b -tagging algorithms developed by the CMS collaboration. The medium working point of the CSV algorithm, with a misidentification rate for light-partons (c -quarks) of approximately 3% (15 – 20%) and a b -tag efficiency of 70%, is best suited for this analysis. The discriminator value corresponding to the medium working point is 0.679. A recent evaluation of the performance using 8 TeV data can be found in [111].

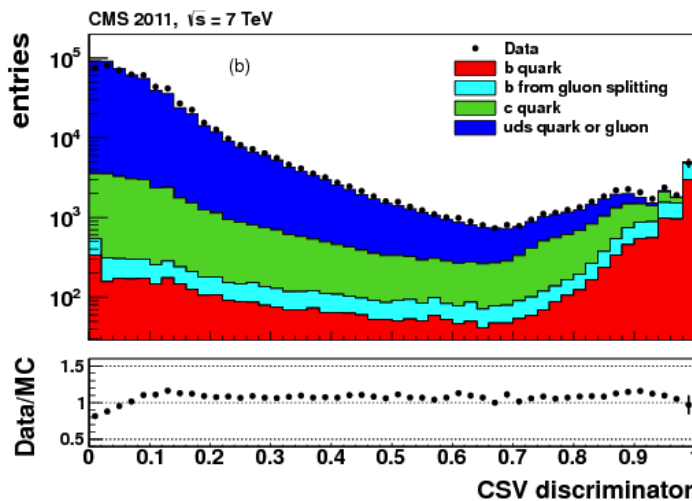


Figure 3.3.: CSV discriminator distribution [110].

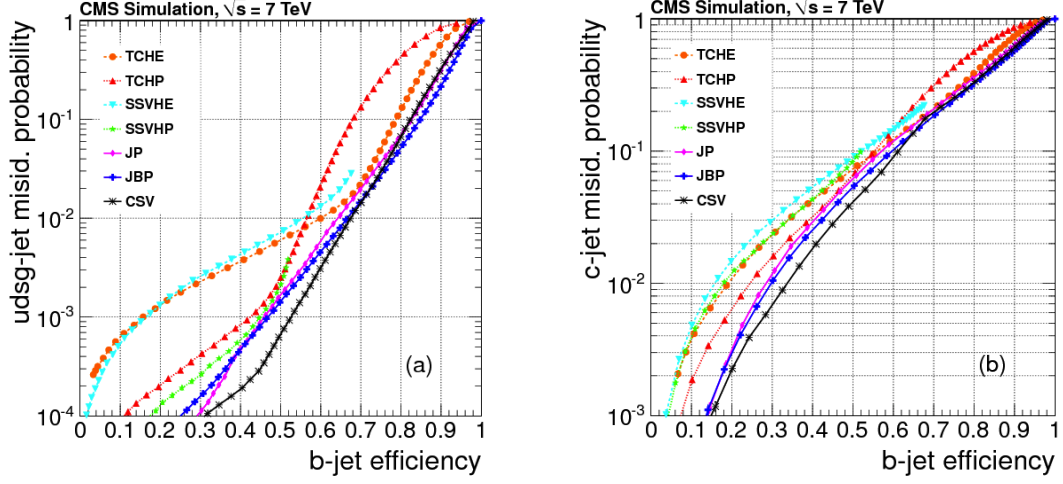


Figure 3.4.: Misidentification probability vs. b -jet efficiency of several b -tagging algorithms for jets from (a) u -, d - and s -quarks as well as gluons, and (b) c -quarks. [110]

3.3.2. Event selection and SM backgrounds

The selection at trigger level is implemented using a cross-trigger strategy, which exploits the presence of an electron or muon, high H_T and high \cancel{E}_T , as expected in signal events. This allows to keep the thresholds for the single objects sufficiently low, while maintaining an acceptable trigger rate. For electron channel cross-triggers, loose selection requirements are applied (e.g. on the electron isolation) in order to reduce the contamination with QCD multijet events. Furthermore, electron-jet ambiguities are resolved to further reduce the trigger rate. For data taken during run 2012C and 2012D, the particle flow H_T calculation at HLT-level was modified in order to suppress pileup effects. The HLT paths for the leptonic cross-trigger channels, as well as the purely hadronic trigger paths, used to obtain \cancel{E}_T -resolution templates for the estimation of the SM background (see Sec. 3.4.4), are listed in Tab. A.3 in Appendix A. Measurements of the trigger efficiencies from data are summarized in Sec. 3.3.3.

Several filters (Sec. 3.3.1), designed to reject events with known detector or reconstruction problems and machine-induced background, precede the analysis selection [109].

The preselection procedure is designed to select an event sample that is close to the characteristics of the signal. At the same time, the preselection must include control regions that are dominated by SM background events to allow for a validation of the main background features using simulation. As already stated in Sec. 3.1 these control regions are also used to extrapolate kinematic properties of the background to the signal regions in order to predict the SM event yield.

Events are required to have exactly one muon or electron that fulfill the previously defined tight lepton selection requirements (see Sec. 3.3.1). Events, which contain

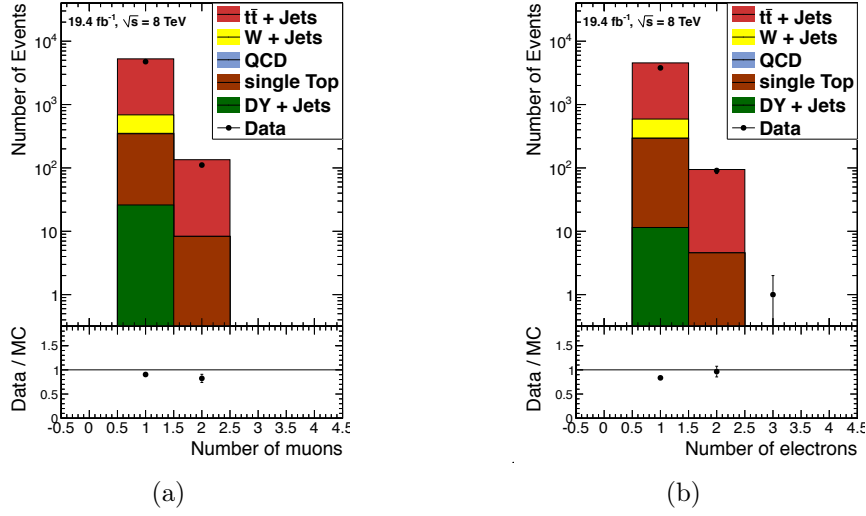


Figure 3.5.: Multiplicity distributions for data and simulation in the ≥ 4 -jet selection, requiring at least one b -tagged jet: (a) number of isolated muons and (b) number of isolated electrons. Data yields are shown as black points with error bars, while filled histograms are used for the simulation with the individual components stacked. The data/simulation ratio is displayed at the bottom of each subfigure. The simulation has been normalized to the integrated luminosity of the data sample.

additional leptons that pass the veto selection are rejected in order to minimize the overlap with multilepton searches (these usually implement looser lepton selection criteria) and to reduce the contamination with dilepton events, where the second lepton fails to pass the tight selection.

Furthermore, preselected events must contain at least 6 jets with $p_T > 40$ GeV and $|\eta| < 2.4$. However, for the evaluation of some systematic uncertainties, the jet multiplicity requirement is relaxed to 4 or more jets. The trigger selection is applied to observables that are calculated by HLT algorithms, which are optimized for CPU time consumption and therefore less accurate than the full reconstruction. In order to avoid dependencies on the resulting trigger efficiency turn-on, the preselection requirements must be tighter than the trigger selection. H_T has to exceed 400 GeV and \cancel{E}_T must be larger than 150 GeV.

Based on this preselection, the properties of the data sample can be compared with the simulation. The goal of this survey is not a detailed comparison of SM background yields, but a qualitative assessment of the sample composition. The comparison requires a minimum of four reconstructed jets, including at least one identified b -jet, together with the H_T and \cancel{E}_T selection mentioned above. Figure 3.5 shows the multiplicity distributions of isolated leptons. The fraction of events with multiple isolated muons (Fig. 3.5a) or electrons (Fig. 3.5b) matches the prediction and is dominated by

$t\bar{t}$ events. In Fig. 3.6, the multiplicity distributions of reconstructed primary vertices, jets and b -tagged jets are shown.

After pileup reweighting, good agreement is observed in the distribution of the number of reconstructed vertices, with a small trend to higher multiplicities in data. Finally, the distributions of the leading jet p_T , of H_T and E_T are shown in Fig. 3.7. In general, good agreement is observed between data and simulation, with a small trend to a shallower spectrum of H_T and jet p_T in simulation.

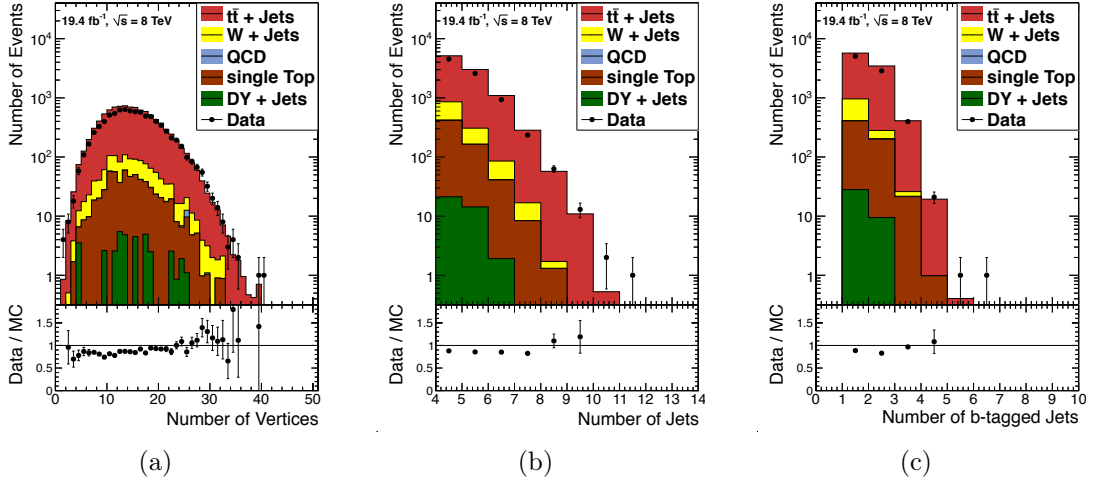


Figure 3.6.: Multiplicity distributions for data and simulation: (a) number of reconstructed primary vertices, (b) number of jets, and (c) number of b -tagged jets. Symbols and conditions are identical to Fig. 3.5.

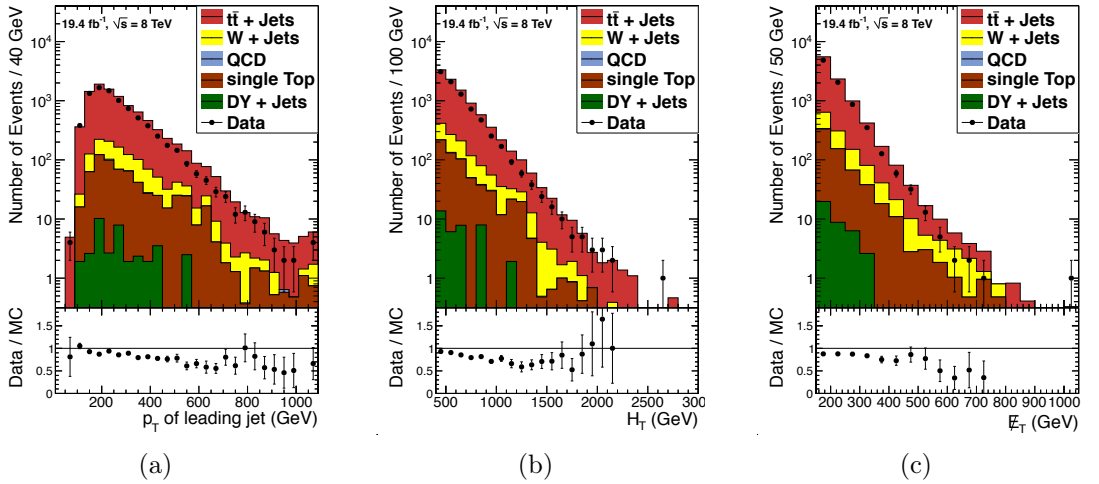


Figure 3.7.: Distributions of (a) p_T of the leading jet, (b) H_T and (c) E_T . Symbols and conditions are identical to Fig. 3.5.

To qualitatively assess the discriminative power of \cancel{E}_T and H_T between signals and the SM background, the \cancel{E}_T distribution from simulation is shown for the 1, 2 and more than 3 b -tag case for a low and a high H_T selection in Fig. 3.8. The figure shows three mass points of the topology, modeling gluino mediated top quark production with decoupled top squark mass (T1tttt). The best discrimination is achieved in the selection with more than 3 b -tags and high H_T .

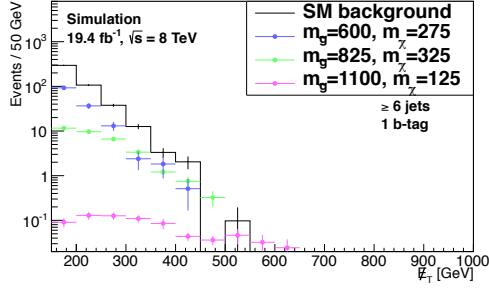
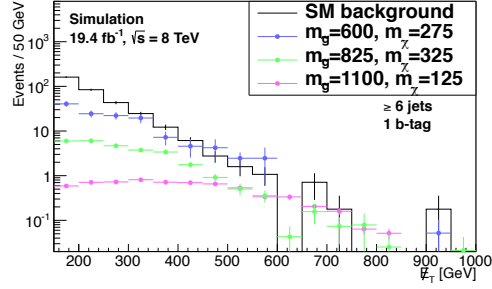
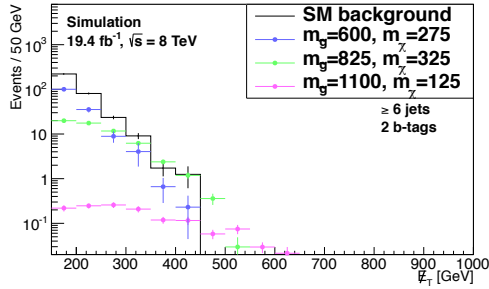
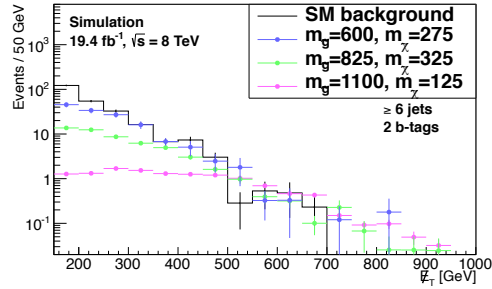
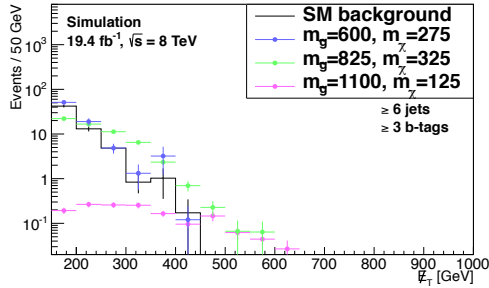
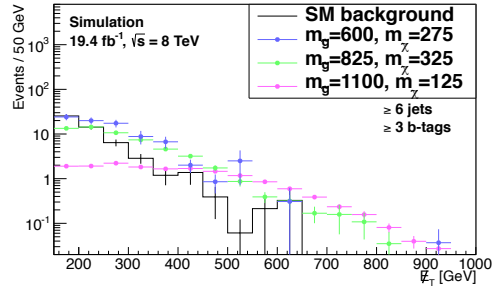
(a) $400 < H_T < 750$ GeV, 1 b -tag(b) $750 < H_T < 2500$ GeV, 1 b -tag(c) $400 < H_T < 750$ GeV, 2 b -tags(d) $750 < H_T < 2500$ GeV, 2 b -tags(e) $400 < H_T < 750$ GeV, ≥ 3 b -tags(f) $750 < H_T < 2500$ GeV, ≥ 3 b -tags

Figure 3.8.: Distribution of \cancel{E}_T for a selection of low H_T ($400 < H_T < 750$ GeV) (left) and high H_T ($750 < H_T < 2500$ GeV) (right) and 1 b -tag (a,b), 2 b -tags (c,d) or ≥ 3 b -tags (e,f). The black histogram shows the SM background while the colored histograms show three mass points of the topology, modeling gluino mediated top quark production with decoupled top squark mass (T1tttt)

3.3.3. Lepton and trigger efficiencies

The selection and reconstruction efficiencies for both, muons and electrons, as well as the efficiency of the leptonic cross-trigger legs, are estimated using the Tag and Probe method (T&P) [98]. The T&P lepton pairs are selected from a mass window ($60 < m_Z < 120 \text{ GeV}$) around the Z resonance. After subtracting the background from the invariant mass distribution, the ratio between the number of pairs that contain probe leptons, passing a set of selection requirements (“passing probes”), to the number of all pairs, gives the efficiency of a selection.

For the estimation of efficiencies in data a leptonically triggered sample is used, while Drell-Yan samples are used for efficiency estimates of “full” (GEANT4) and “fast” simulation (FASTSIM). The efficiencies of the hadronic trigger legs are measured from leptonically triggered samples in data. These estimates are used to assign systematic uncertainties on the SM background prediction and to correct the signal selection efficiencies for the limit setting procedure later on.

Muon reconstruction and selection

The total efficiency to reconstruct and select a muon, fulfilling the requirements described in Sec. 3.3.1, can be factorized by

$$\epsilon_{\text{reco}} = \epsilon_{\text{ID1}} \cdot \epsilon_{\text{ID2}} \cdot \epsilon_{\text{track}}. \quad (3.7)$$

The tracking efficiency ϵ_{track} has been studied for the 2011 analysis [76] and was found to be very close to 100% in the full kinematic range, a result also valid for this analysis.

The identification efficiencies ϵ_{ID1} and ϵ_{ID2} measure the impact of the muon selection cuts summarized in Sec. 3.3.1. The efficiency ϵ_{ID1} is calculated using trajectories measured only in the tracker with $p_T > 5 \text{ GeV}/c$ as probes. These are matched to all reconstructed muons that pass the full muon selection, except for the isolation requirement and the reco-PF arbitration. The efficiency ϵ_{ID2} of the two remaining cuts is measured using probes, passing the ID1 selection. The tag-muon selection requirements are in any case tighter than those of the passing probe.

Figure 3.9 shows both efficiencies for data and full simulation as function of p_T for $|\eta| < 2.4$ and as function η for $p_T > 20 \text{ GeV}$. Since ϵ_{ID2} includes the isolation cut it is also shown as function of n_{vtx} and n_{jets} . Obviously, the dependence on the number of pileup collisions has been largely reduced by the correction applied to the relative isolation. Table 3.1 (3.2) summarizes the average efficiencies and the data/simulation scale factor for full (fast) simulation. The systematic uncertainty on the average scale factor is approximated by the maximum deviation observed over the p_T and η range. As expected, the scale factors for fast simulation show larger deviations from unity and do not reproduce the data as well as the full simulation, resulting in a larger systematic uncertainty.

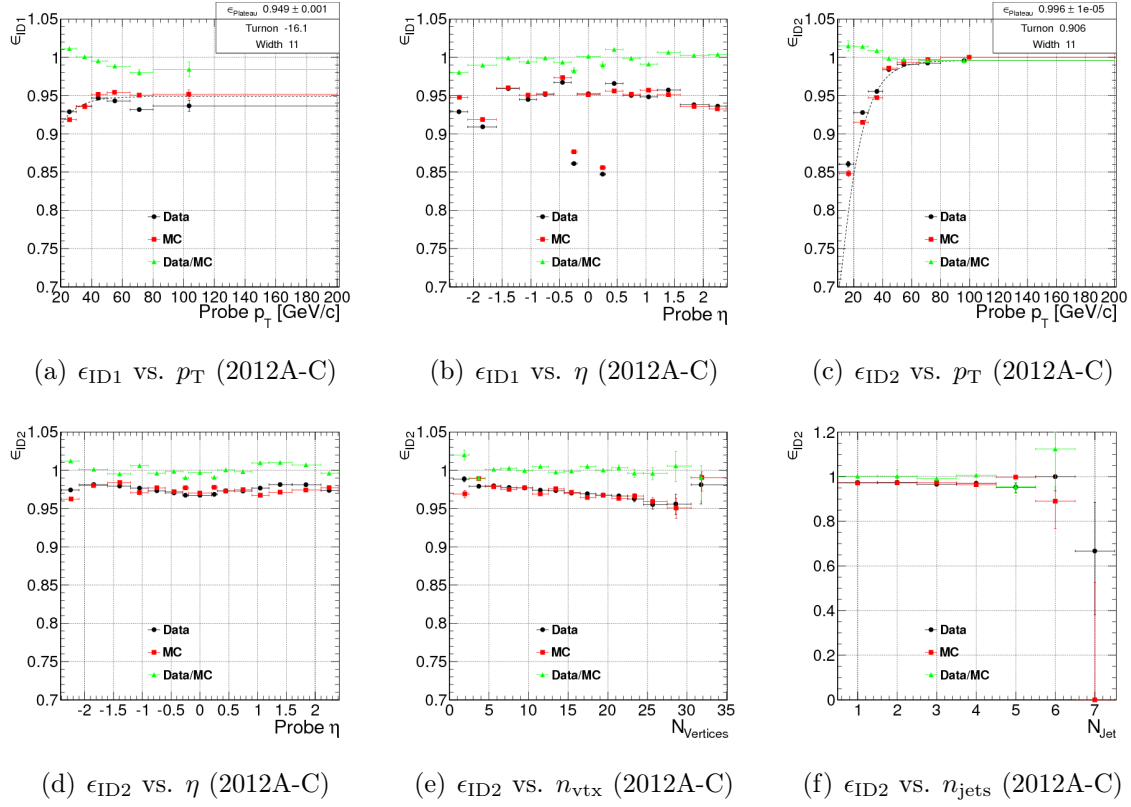


Figure 3.9.: The efficiency ϵ_{ID1} (a,b) and ϵ_{ID2} (c-f). Both efficiencies are shown as a function of p_T for $|\eta| < 2.1$ (a, c) and as a function of η for $p_T > 20$ GeV (b, d). Since ϵ_{ID2} includes the relative isolation requirement also the dependence on n_{vtx} (e) and n_{jets} (f) for $p_T > 20$ GeV and $|\eta| < 2.1$ is shown. Black circles correspond to data, red squares to full simulation and green triangles to their ratio.

Table 3.1.: Muon efficiencies in the kinematic region $p_T > 20$ GeV and $|\eta| < 2.4$.

ϵ	data	full simulation	data/full simulation
ID1	0.9422 ± 0.0006	0.9440 ± 0.0003	0.9981 ± 0.0007 (stat.) ± 0.02 (sys.)
ID2	0.9735 ± 0.0005	0.9720 ± 0.0002	1.0015 ± 0.0006 (stat.) ± 0.01 (sys.)

Table 3.2.: Muon efficiencies in the kinematic region $p_T > 20$ GeV and $|\eta| < 2.4$.

ϵ	data	fast simulation	data/fast simulation
ID1	0.9422 ± 0.0006	0.9886 ± 0.0002	0.9531 ± 0.0007 (stat.) ± 0.03 (sys.)
ID2	0.9735 ± 0.0005	0.9832 ± 0.0002	0.9902 ± 0.0005 (stat.) ± 0.01 (sys.)

Electron reconstruction and selection

The reconstruction and selection efficiency of electrons can be factorized to

$$\epsilon_{\text{reco}} = \epsilon_{\text{ID}} \cdot \epsilon_{\text{GSF}}, \quad (3.8)$$

where ϵ_{GSF} and ϵ_{ID} denote the GSF tracking and the electron identification efficiency. The probes for the tracking efficiency measurement are ECAL clusters with $E_T > 10 \text{ GeV}$ that are not associated to jets. A passing probe must have a match to an ECAL seeded GSF track. The measurement of ϵ_{ID} is based on GSF tracks that have to fulfill all requirements of the electron selection in Sec. 3.3.1. The requirements for tag electrons are in any case tighter than those of the passing probe.

The GSF tracking efficiency is shown in Fig. 3.10 and we observe good agreement between data and full simulation. The identification efficiency in data and full simulation is shown in Fig. 3.11 as a function of p_T for the central ($|\eta| < 1.2$) and forward regions, as a function of η for $p_T > 20 \text{ GeV}$ and as function of the jet multiplicity. It increases with p_T and saturates in data at about 92% (83%) in the central (forward) region, while its η dependence is flat in the central region and decreases in the forward region. These effects are reproduced well by the full simulation, resulting in a 2% systematic uncertainty on the inclusive data/simulation scale factor (Tab. 3.3). The differences in ϵ_{ID} observed for the forward region in fast simulation result in a larger systematic uncertainty of 7% for the scale factor in Tab. 3.4.

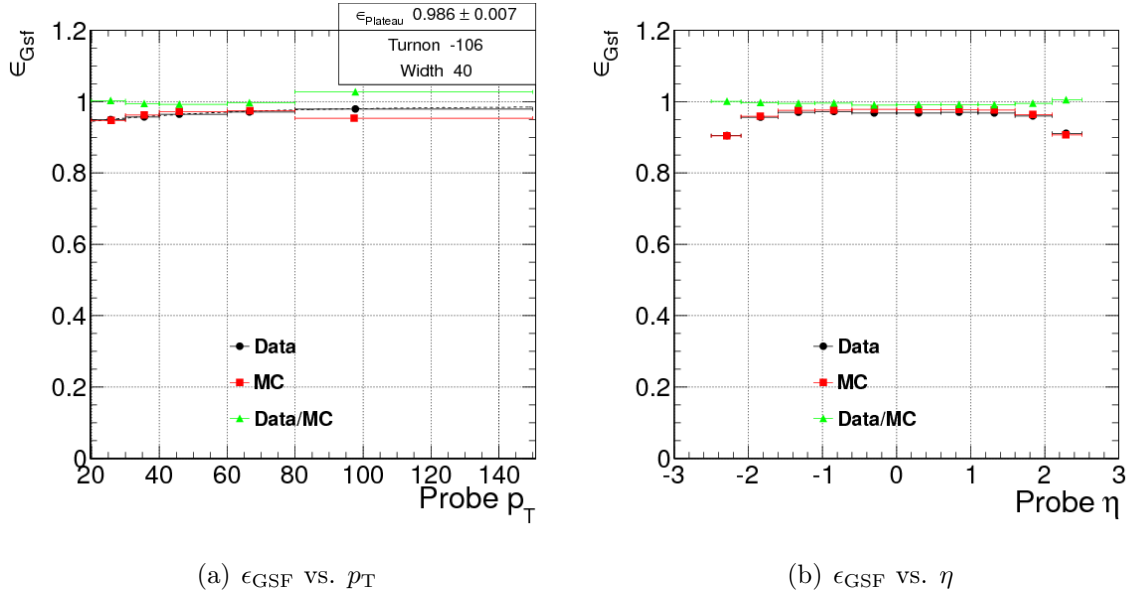


Figure 3.10.: ϵ_{GSF} as a function of p_T for $|\eta| < 2.5$ (left) and η for $p_T > 20 \text{ GeV}$ (right). Black circles correspond to data, red squares to full simulation and green triangles to the ratio data/full simulation.

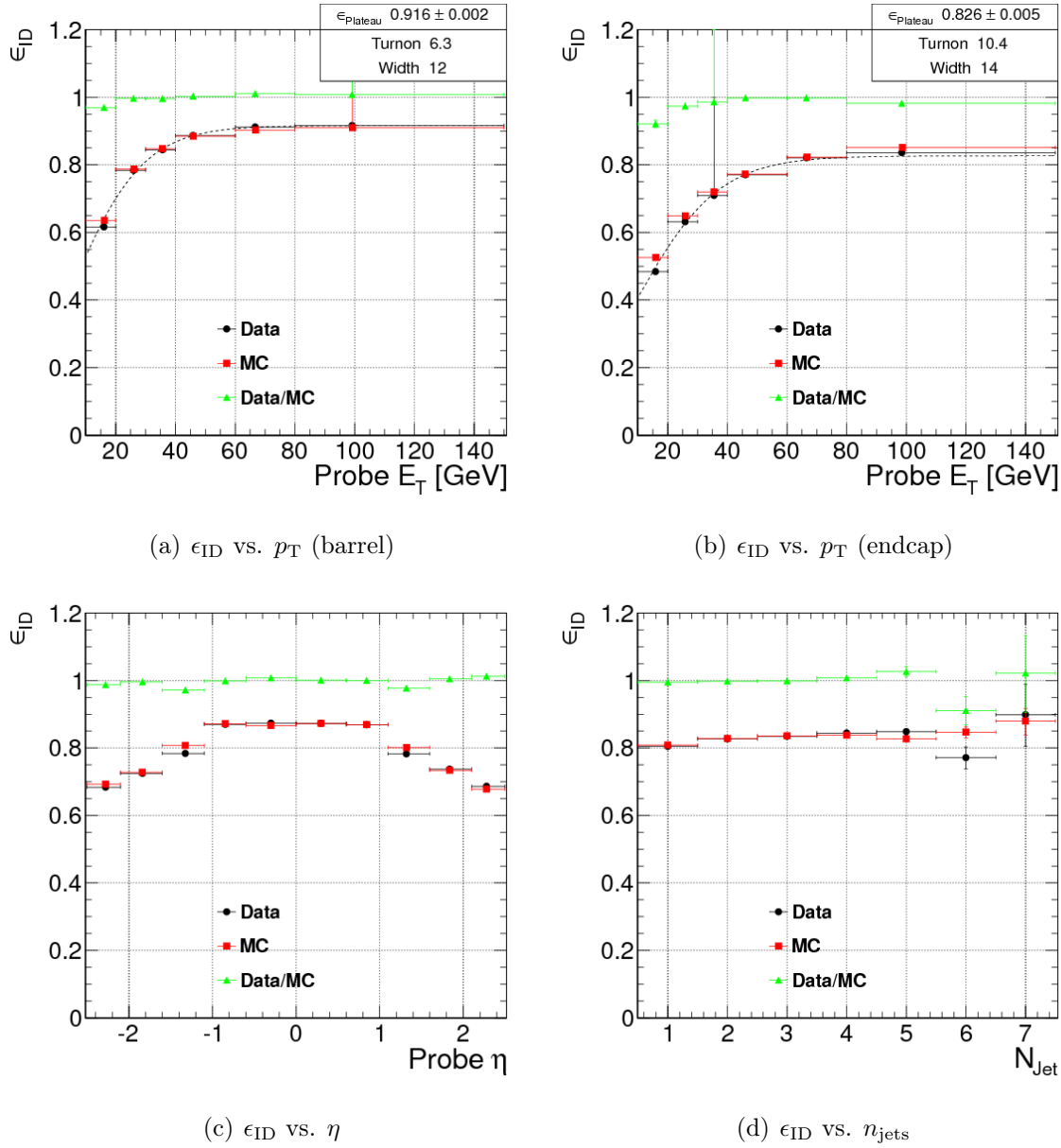


Figure 3.11.: Efficiency of the electron identification requirement (including isolation) as a function of p_T for $|\eta| < 1.2$ (a) and $1.2 < |\eta| < 2.5$ (b), as a function of η for $p_T > 20$ GeV (c) and as function of the number of jets ($p_{T,jet} > 40$ GeV) for $|\eta| > 2.5$ and $p_T > 20$ GeV (d). Black circles correspond to data, red squares to full simulation and green triangles to their ratio.

Table 3.3.: Electron efficiencies in the kinematic region $p_T > 20$ GeV and $|\eta| < 2.5$ for data and full simulation.

ϵ	data	full simulation	data/full simulation
ID	0.8193 ± 0.0011	0.8204 ± 0.0005	0.9987 ± 0.0015 (stat.) ± 0.02 (sys.)
GSF	0.9622 ± 0.0003	0.9676 ± 0.0002	0.9944 ± 0.0003 (stat.) ± 0.02 (sys.)

Table 3.4.: Electron efficiencies in the kinematic region $p_T > 20$ GeV and $|\eta| < 2.5$ for data and fast simulation.

ϵ	data	fast simulation	data/fast simulation
GSF	0.9622 ± 0.0003	0.9718 ± 0.0002	0.9902 ± 0.0004 (stat.) ± 0.01 (sys.)
ID	0.8193 ± 0.0011	0.8524 ± 0.0004	0.9613 ± 0.0014 (stat.) ± 0.08 (sys.)
$ID(EB)$	0.8579 ± 0.0004	0.8665 ± 0.0004	0.9900 ± 0.0007 (stat.) ± 0.03 (sys.)
$ID(EF)$	0.7078 ± 0.0009	0.8112 ± 0.0008	0.8725 ± 0.0014 (stat.) ± 0.07 (sys.)

Leptonic trigger leg

The efficiencies of the leptonic trigger legs are measured in events which pass the hadronic legs of the cross-trigger. Similar to the identification efficiencies the T&P method at the Z resonance is used, with probe-leptons that satisfy the full list of requirements of Sec. 3.3.1. To count as passing probe, the lepton must pass the criteria of the leptonic trigger leg. To avoid any bias the tag selection requirements are equal to those of the passing probe. The total efficiency of the cross trigger factorizes to the efficiency product of the leptonic and the hadronic legs.

Results for an electron cross trigger with a p_T threshold of 15 GeV are shown in Fig. 3.13 as function of p_T ($|\eta| < 2.5$) and as function of η ($p_T > 20$ GeV). The same results for muons are shown in Fig. 3.12 with $|\eta| < 2.4$. The leptonic trigger plateau efficiencies of the p_T turn-on curve for several cross trigger paths are summarized in Tab. 3.5. The efficiencies of the muon trigger legs exhibit significant differences between the central and forward regions. Two correction factors are defined to correct the average efficiency in order to take this effect into account (see Tab. 3.5).

Hadronic trigger leg

For the evaluation of the hadronic efficiencies, events are selected from a data sample triggered by the presence of a single lepton only, with online selection requirements at least as tight as those for the leptonic legs of our cross triggers. A minimum of 3 jets that pass the common jet selection requirements and $p_T \geq 40$ GeV is required. Furthermore the lepton has to pass the full set of requirements listed in Sec. 3.3.1.

The muon (electron) channel trigger efficiency of the H_T trigger leg with 350 GeV (300 GeV) online threshold is shown in Figure 3.14. The turn-on curves are modeled

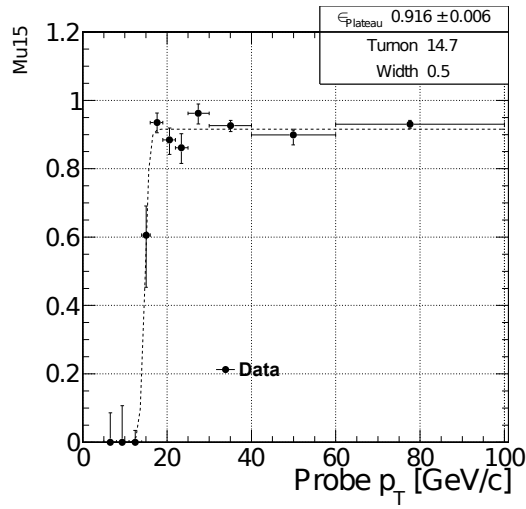
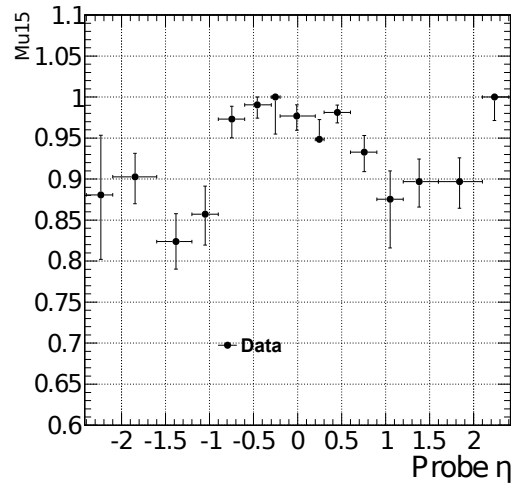
(a) p_T (b) η

Figure 3.12.: Efficiency of the $*_Mu15_*$ trigger leg as functions of the muon p_T and η . Only results obtained from data are shown in these plots. The p_T turn-on is well parameterized by an error function, which is used to estimate the plateau efficiency.

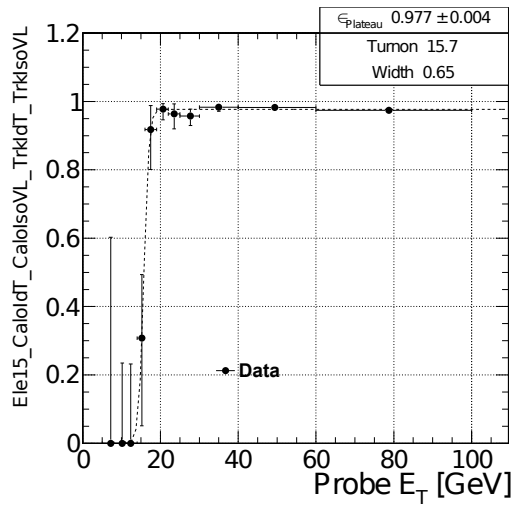
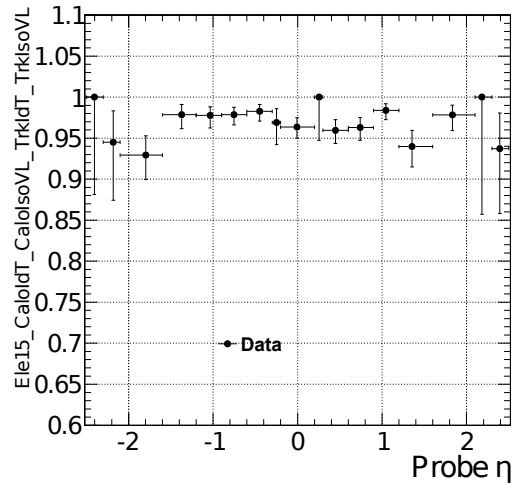
(a) p_T (b) η

Figure 3.13.: Efficiency of the $*_Ele15_*$ trigger leg as functions of the muon p_T and η . Only results obtained from data are shown in these plots. The p_T turn-on is well parameterized by an error function, which is used to estimate the plateau efficiency.

Table 3.5.: The lepton efficiencies for single-lepton cross-channel trigger paths with on-line trigger threshold of $p_T > 5 \text{ GeV}$ or $p_T > 15 \text{ GeV}$, in events that pass the hadronic trigger selection. The efficiency of muon triggers shows a significant difference between the central and forward regions. Two correction factors are defined to be applied on the average efficiency, in order to take this effect into account.

Electron trigger path		ϵ_{trig}^e
CleanPFHT350_Ele5_CaloIdT_CaloIsoVL_TrkIdT_TrkIsoVL_PFMET45		0.96 ± 0.04
CleanPFNoPUHT350_Ele5_CaloIdT_CaloIsoVL_TrkIdT_TrkIsoVL_PFMET45		0.94 ± 0.07
CleanPFHT300_Ele15_CaloIdT_CaloIsoVL_TrkIdT_TrkIsoVL_PFMET45		0.97 ± 0.07
CleanPFNoPUHT300_Ele15_CaloIdT_CaloIsoVL_TrkIdT_TrkIsoVL_PFMET45		0.98 ± 0.03
Muon trigger path		ϵ_{trig}^μ
PFHT400_Mu5_PFMET45		0.92 ± 0.05
PFNoPUHT400_Mu5_PFMET45		0.93 ± 0.04
PFHT350_Mu15_PFMET45		0.93 ± 0.05
PFNoPUHT350_Mu15_PFMET45		0.92 ± 0.04
Scale factor for $ \eta < 0.9$		1.076
Scale factor for $ \eta \geq 0.9$		0.928

by an error function and the fitted trigger efficiencies at plateau are denoted as ϵ in these figures. Across the run periods, the H_T efficiency at plateau varies between 98% and 99% and the application of pileup subtraction at trigger level, starting from run 2012C, has very little influence on the trigger turn-on.

Efficiencies with respect to E_T do not show any significant dependence on H_T . For the measurement of the E_T turn-on shown in Fig. 3.15, $H_T > 450 \text{ GeV}$ is required to saturate the H_T trigger leg. The fitted efficiency plateau for E_T varies again between 98% and 99%.

The plateau efficiencies for the hadronic trigger legs have been averaged over the first and the second half of the data taking period of 2012, as well as over the different trigger path, listed in Tab. A.3. These averages are listed in Tab. 3.6.

Given these measurements, the offline selection of $E_T > 150 \text{ GeV}$ and $H_T > 400 \text{ GeV}$ applied in this analysis, can be considered unbiased by the trigger.

Table 3.6.: The averaged efficiency plateau values by trigger types.

Trigger Type	Avg Plateau Eff (2012AB) (%)	Avg Plateau Eff (2012CD)
Ele_HT	98.6 ± 0.3	97.7 ± 0.3
Mu_HT	99.9 ± 0.1	99.7 ± 0.1
Ele_HT_PFMET	98.3 ± 0.5	98.1 ± 0.1
Mu_HT_PFMET	98.0 ± 0.3	98.2 ± 0.2

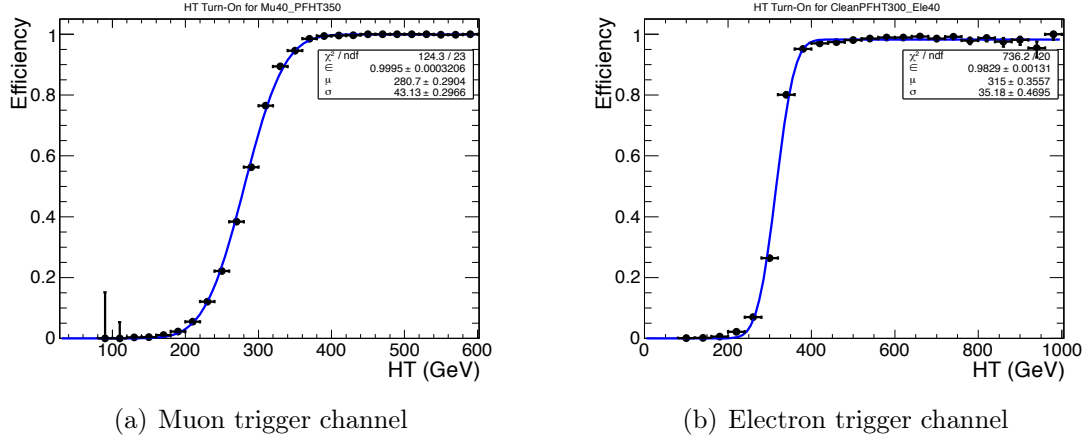


Figure 3.14.: The HT turn-on curves for (a) Muon + H_T and for (b) Electron + H_T cross triggers for the run 2012B.

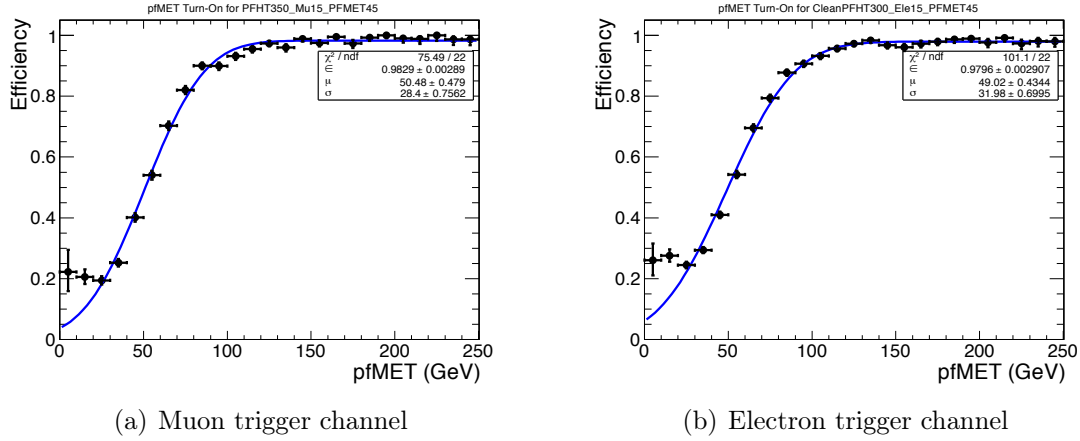


Figure 3.15.: The E_T turn-on curves for the (a) muon + H_T + E_T and (b) electron + H_T + E_T cross triggers for the run 2012B.

3.4. Estimation of the SM Background

3.4.1. Background estimation in the 2 b -tag category

In order to estimate the event yields of SM backgrounds at high H_T and E_T , a model for the shape of the genuine E_T spectrum of $t\bar{t}$ production, which is the leading SM contribution, is constructed. Therefore, the probability density function describing the inclusive E_T spectrum is corrected for the effects of H_T selections, as well as for b -jet acceptance effects.

In order to extract the fraction of W +jets/ $t\bar{t}$ in bins of the b -tag multiplicity, templates of the b -tag multiplicity distribution are constructed from simulated samples of these two backgrounds. These templates include corrections that account for differences in

the b -tag efficiency and misidentification probability between data and simulation. The W +jets/ $t\bar{t}$ fraction is subsequently estimated via a fit of the templates to the observed b -tag multiplicity distribution in data. Since the contribution of W +jets production to events with one or two b -tags is small ($< 10\%$ for 1 b -tag, $< 3\%$ for 2 b -tag), it is sufficient to extract the genuine \cancel{E}_T spectrum from a simulated sample for this background source.

Finally, the genuine \cancel{E}_T distributions of these background components (W +jets and $t\bar{t}$) are added according to the estimated fractions and the sum is convoluted with \cancel{E}_T resolution templates, measured from data. The parameters of the \cancel{E}_T model are then obtained from a likelihood fit to control regions in the 1 b -tag and in the 2 b -tag bin. The background yields in the 2 b -tag signal regions are predicted by an extrapolation of the fit results and normalized at low \cancel{E}_T . The main steps of the estimation procedure are summarized in Fig. 3.16.

The control region in the 1 b -tag bin is only restricted by the lower bounds $\cancel{E}_T > 150 \text{ GeV}$ and $H_T > 400 \text{ GeV}$, imposed by the preselection. It is important to provide a sufficiently large range in \cancel{E}_T to gain sensitivity for the estimation of the shape parameters of the \cancel{E}_T model.

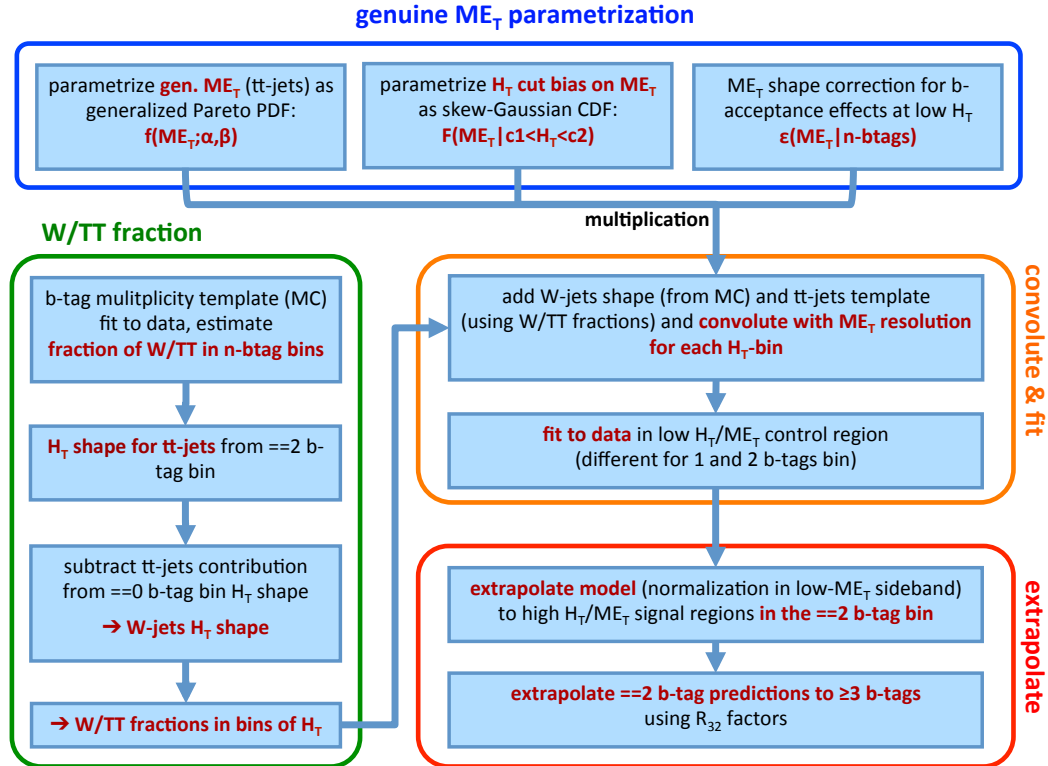


Figure 3.16.: Workflow of the estimation of the \cancel{E}_T spectrum to predict SM background yields in signal regions shown in 3.17.

All control, signal and normalization regions in \cancel{E}_T and H_T for the 2 b -tag bin are shown in Fig. 3.17(a). Here the control region is defined by $400 < H_T < 750$ GeV and $150 < \cancel{E}_T < 400$ GeV. The upper bounds on the 2 b -tag control region limit the effect of possible signal contamination in the likelihood fit. The normalization and the signal region have a lower bound of 750 GeV in H_T and are separated at 250 GeV in \cancel{E}_T .

Two sets of four signal regions in \cancel{E}_T are defined at high values of H_T . The two H_T selections are $750 < H_T < 2500$ GeV and $1000 < H_T < 2500$ GeV for the first and second set, respectively. For each of the H_T selections, four regions in \cancel{E}_T are defined, delimited by \cancel{E}_T values of 250, 350, 450 and 2500 GeV.

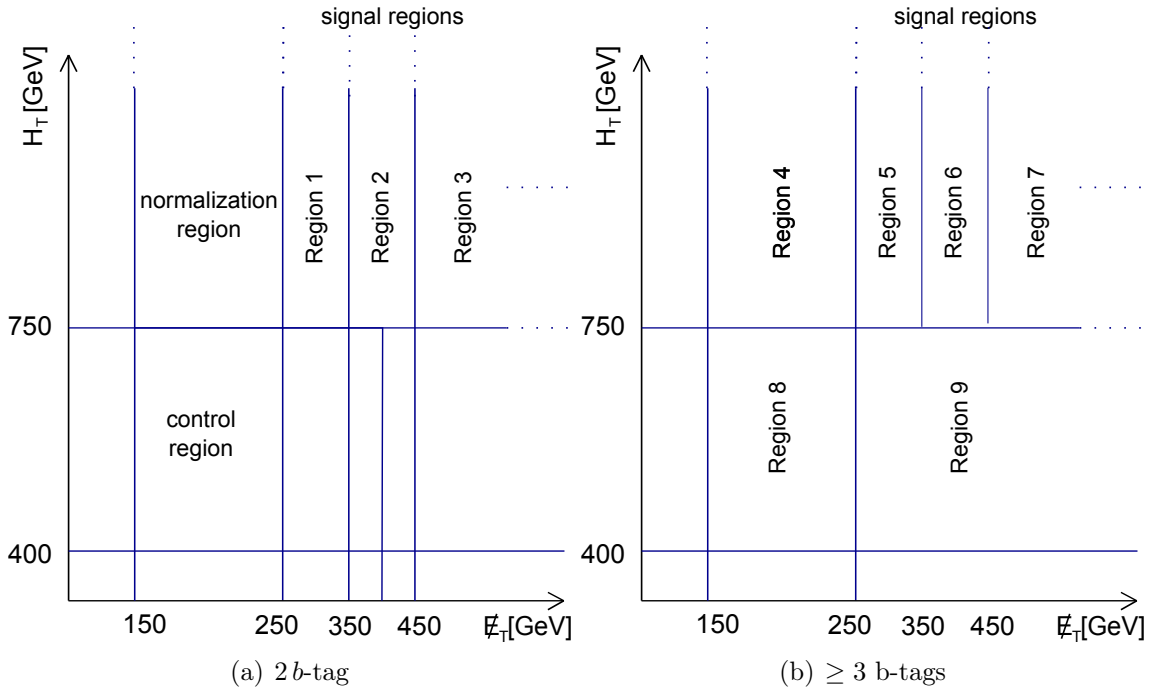


Figure 3.17.: Graphical representation of the different regions in \cancel{E}_T and H_T for events with (a) two and (b) at least three b -tagged jets.

The features of the genuine \cancel{E}_T distribution and the model for $t\bar{t}$ production are discussed in Sec. 3.4.2, followed by a procedure for the estimation of the fraction of W +jets and $t\bar{t}$ events, which is described in Sec. 3.4.3. The method used to obtain templates for the smearing of \cancel{E}_T , due to detector effects is explained in Sec. 3.4.4. Finally the results from a likelihood fit of the full background model to data and simulation is presented in Sec. 3.4.5, followed by a discussion of systematic uncertainties in Sec. 3.4.6.

3.4.2. Modelling genuine \cancel{E}_T

The inclusive \cancel{E}_T model

Genuine- \cancel{E}_T of the leading backgrounds results from neutrinos that are produced in leptonic decays of W bosons from top-quark decays or direct production. High transverse neutrino momenta that exceed the threshold of 150 GeV imposed by the preselection, require highly boosted W bosons because of the rest mass of only 80.4 GeV. The transverse momentum of the ℓ - ν system is always balanced by hadronic activity, resulting in a strong correlation of \cancel{E}_T and H_T . Thus, in a first step, a genuine- \cancel{E}_T model disregarding the effect of any H_T selection is built and the impact of H_T on this model will be investigated in the next section.

The neutrino transverse momentum spectrum for kinematic regions, comprising highly boosted W bosons, is characterized by a nearly exponentially falling distribution with an enhanced tail. The slope of this distribution and the size of its tail varies for the different production process, the W polarization and rapidity. Furthermore constraints imposed by the lepton or jet acceptance have an influence on the distribution of genuine- \cancel{E}_T since these objects are kinematically correlated with the neutrino momentum. Hence, it is difficult to construct a genuine- \cancel{E}_T model from first principles. Empirically, we find that the genuine- \cancel{E}_T distribution, above a threshold x_{\min} , can be parameterized well with the generalized Pareto distribution

$$f_P(x; x_{\min}, \alpha, \beta) = \frac{1}{\alpha} \left(1 + \frac{\beta(x - x_{\min})}{\alpha} \right)^{-\frac{1}{\beta}-1}, \quad (3.9)$$

where α is the scale parameter, controlling the steepness of the exponential decline and β is the shape parameter. The shape parameter determines the size of the tail. In the limit $\beta \rightarrow 0$, Eq. 3.9 approaches an exponential distribution, while $\beta > 0$ results in a polynomial tail.

This distribution has a statistically beneficial property. According to the Pickands-Balkema-de Haan theorem [112, 113] the generalized Pareto distribution can be used to approximate the conditional excess distribution, i.e. the tail above a high threshold, for a large class of underlying distribution functions.

The threshold parameter x_{\min} is set to 150 GeV, corresponding to the lowest \cancel{E}_T threshold used in the analysis, while the other two parameters α and β are determined by a maximum likelihood fit. In the analysis of 2011 data [76, 77] the functional form $x \exp(-\alpha x^\beta)$ has been used to parametrize the inclusive distributions within each sample ($t\bar{t}$, W^+ +jets and W^- +jets). Both models provide a numerically similar description of the genuine- \cancel{E}_T shape but the generalized Pareto distribution shows lower correlation of the free parameters α and β , resulting in a more robust fit.

In order to demonstrate the applicability of the generalized Pareto distribution beyond the 6-jets selection used for the final analysis, likelihood fits of Eq. 3.9 to the genuine- \cancel{E}_T

distributions of simulated $t\bar{t}$ events with a minimum requirement of 2 to 5 jets are shown in Fig. 3.18(a) to 3.18(d). Of course the preselection requirement of $H_T > 400$ GeV is not applied here, since it would distort the genuine- \cancel{E}_T spectrum. In all cases the model describes the data well.

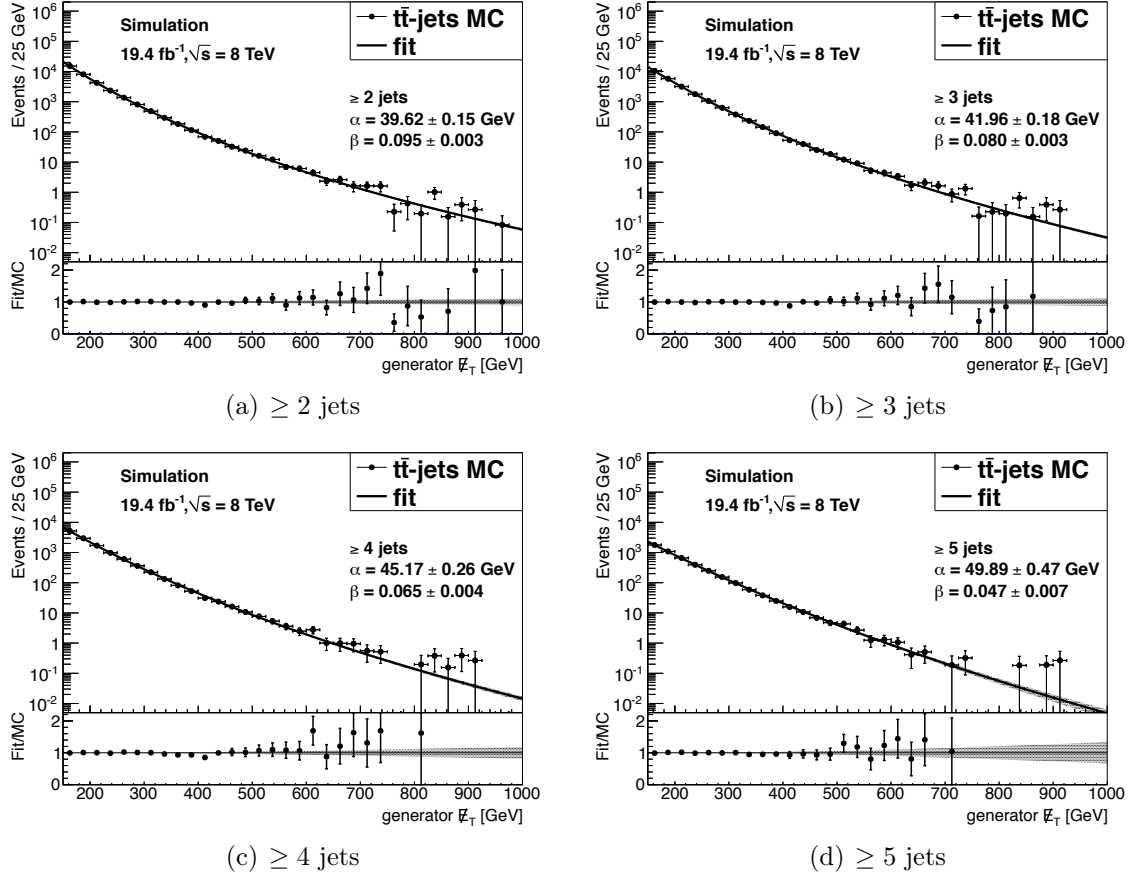


Figure 3.18.: Genuine- \cancel{E}_T distribution of simulated $t\bar{t}$ events with at least 2 jets (a), 3 jets (b), 4 jets (c) and 5 jets (d), with a fit of the generalized Pareto distribution (Eq. 3.9).

The result from a fit of Eq. 3.9 (with $x_{\min} = 150$ GeV) to the genuine- \cancel{E}_T distribution of simulated $t\bar{t}$ events with at least 6 reconstructed jets, corresponding to the selection used later in the estimation of the SM background, is shown in Fig. 3.19(a) together with a scan of the likelihood in Fig. 3.19(b). Again good agreement between model and simulation can be observed, together with a parabolic shape of the likelihood around its minimum, justifying the usage of symmetric gaussian errors. The estimated value of the Pareto parameters are $\alpha = 55.10 \pm 0.99$ GeV and $\beta = 0.034 \pm 0.014$.

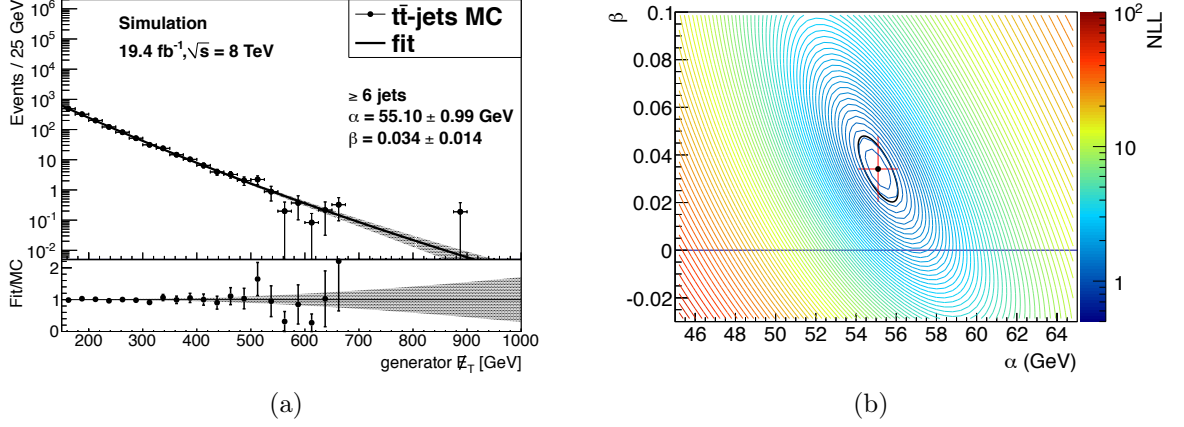


Figure 3.19.: (a) Genuine- \cancel{E}_T distribution of simulated $t\bar{t}$ events with at least 6 jets and a fit of the Parteto distribution (Eq. 3.9). (b) Corresponding likelihood scan of the scale and shape parameters α and β .

Parametrizing the impact of H_T selections

As already argued in the previous section, the selection of H_T intervals alters the genuine- \cancel{E}_T distribution, since the transverse momentum of the leptonically decaying W boson is balanced by the jet system. In order to asses the effect of a lower limit c on H_T , it is useful to investigate the ratio between the \cancel{E}_T distribution for events with $H_T > c$ and the inclusive \cancel{E}_T distribution

$$r_s(x; c) = \frac{f(x = \cancel{E}_T | H_T > c)}{f(x = \cancel{E}_T)}. \quad (3.10)$$

The single-sided ratio r_s can be well described by the cumulative distribution function (CDF) of a skew Gaussian density,

$$\epsilon_s(x; c) = \epsilon(x = \cancel{E}_T | H_T > c) = \Phi(y) - 2T(y, \xi) \quad \text{with} \quad y = \frac{x - \mu'(c)}{\sigma'(c)}, \quad (3.11)$$

where Φ is the standard normal CDF, T denotes the Owen's T function and μ' , σ' and ξ are the location, scale and shape (skewness) parameters.

The mean μ and variance σ^2 of the skew Gaussian distribution are related to its parameters by

$$\mu = \mu' + \sigma' \delta \sqrt{\frac{2}{\pi}} \quad \text{and} \quad \sigma^2 = \sigma'^2 \left(1 - \frac{2\delta^2}{\pi}\right), \quad \text{with} \quad \delta = \frac{\xi}{\sqrt{1 + \xi^2}}. \quad (3.12)$$

The combined effect of a lower and upper H_T limit on the \cancel{E}_T distribution ($c_1 < H_T < c_2$), is therefore given by

$$\epsilon_d(x; c_1, c_2) = \epsilon(x = \cancel{E}_T | c_1 < H_T < c_2) = \epsilon_s(x; c_1) - \epsilon_s(x; c_2) . \quad (3.13)$$

For the evolution of the moments μ and σ^2 a linear dependence on the H_T limit is assumed, while the skewness parameter ξ is kept constant:

$$\begin{aligned} \mu(c) &= \mu_1(c - c_0) + \mu_0 \\ \sigma^2(c) &= \sigma_1^2(c - c_0) + \sigma_0^2 \\ \xi(c) &= \text{const} . \end{aligned} \quad (3.14)$$

The constant c_0 is set to 400 GeV, corresponding to the lower H_T limit of the preselection.

In total, this parameterization introduces five parameters μ_0 , μ_1 , σ_0^2 , σ_1^2 and ξ . These parameters are determined from a simultaneous likelihood fit of ϵ_d to double-sided ratios r_d for a sequence of H_T limits c_i , using simulated $t\bar{t}$ events.

$$r_d(x; c_i, c_{i+1}) = \frac{f(x = \cancel{E}_T | c_i < H_T < c_{i+1})}{f(x = \cancel{E}_T)} . \quad (3.15)$$

The estimated parameter values are listed in the second column of Tab. 3.7. Examples of the ratios r_d and the corresponding fitted functions ϵ_d are shown in Fig. 3.20.

Table 3.7.: Parameters determining the evolution of the skew error functions according to Eq 3.14: values obtained from simulation in the ≥ 6 jet selection (second column) and a comparison of results from simulation and data for the ≥ 4 jet control region (last two columns).

	≥ 6 jets	≥ 4 jet control region	
parameter	$t\bar{t}$ (MC)	$t\bar{t}$ (MC)	≥ 2 b -tag (data)
μ_0 (GeV)	-29.7 ± 10.4	137.4 ± 1.4	132.8 ± 5.3
μ_1	0.77 ± 0.03	0.68 ± 0.01	0.73 ± 0.04
σ_0^2 (GeV ²)	$(12.0 \pm 2.3)10^3$	$(9.5 \pm 0.4)10^3$	$(10.3 \pm 1.4)10^3$
σ_1^2 (GeV)	58.1 ± 8.7	45.4 ± 2.2	39.2 ± 6.3
ξ	-0.85 ± 0.47	-0.92 ± 0.16	-1.45 ± 0.42

The evolution of the error function parameters μ' , σ' and ξ with H_T is summarized in Fig. 3.21. This figure shows also results for individual H_T cuts, which are obtained from additional likelihood fits where μ' and σ' float, while the skewness is restricted to the value in Tab. 3.7 and vice versa. These results confirm the linear evolution of mean and variance and the assumption of a constant skewness.

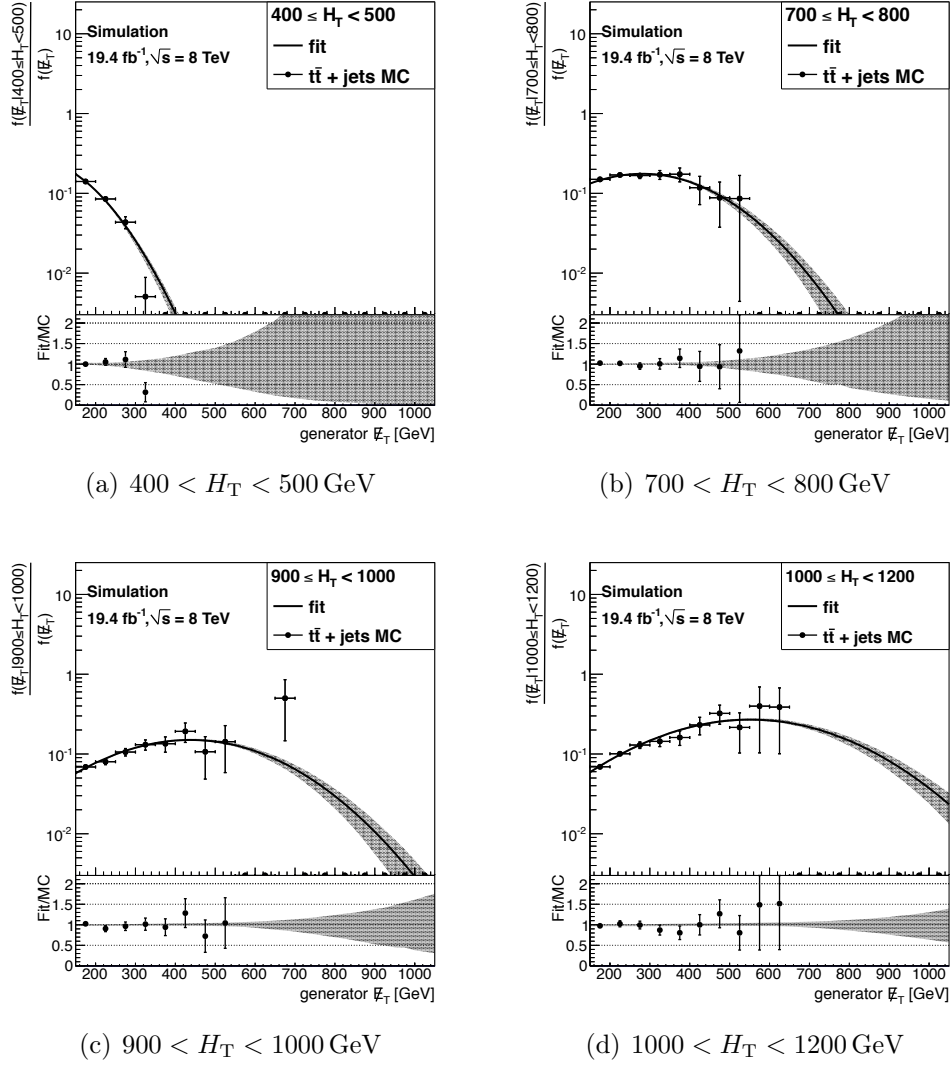


Figure 3.20.: Ratio of the genuine- \cancel{E}_T spectrum for simulated $t\bar{t}$ events after requiring (a) $400 < H_T < 500$ GeV, (b) $700 < H_T < 800$ GeV, (c) $900 < H_T < 1000$ GeV and (d) $1000 < H_T < 1200$ GeV. The filled circles indicate the ratio from simulation. The line and the shaded areas represent the result and the statistical uncertainty of the fit to a set of skew error functions with parameters according to Eq. 3.14. The lower panels show the ratios between the fitted functions and the simulation.

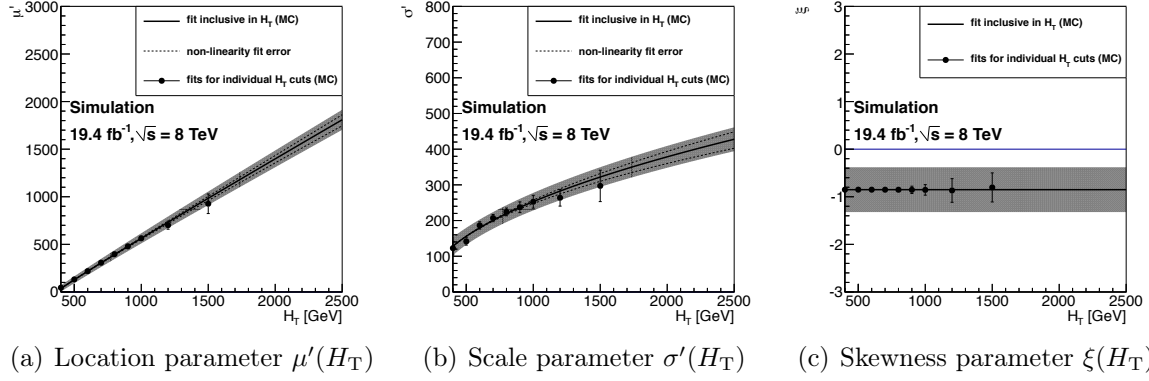


Figure 3.21.: Evolution of the error function parameters (a) μ' , (b) σ' and (c) ξ with H_T in simulated $t\bar{t}$ events. The line and the shaded areas represent the result and the statistical uncertainty of the fit to a set of skew error functions with parameters according to Eq. 3.14. The filled circles show the results obtained for individual H_T bins.

In order to assign a systematic uncertainty, the fits were repeated with a non-linear modification of the linear evolution in Eq. 3.14.

$$\begin{aligned}\mu(c) &= c_0(\mu_1/\mu_2)((c/c_0)^{\mu_2} - 1) + \mu_0, \\ \sigma^2(c) &= c_0(\sigma_1^2/\sigma_2^2)((c/c_0)^{\sigma_2^2} - 1) + \sigma_0^2\end{aligned}\tag{3.16}$$

This evolution introduces additional parameters μ_2 and σ_2^2 , that add a non-linear dependence. Linearity is restored for $\mu_2 = \sigma_2^2 = 1$. An additional likelihood fit with all parameters fixed to the values of Tab. 3.7, except for μ_2 and σ_2^2 , estimates $\mu = 0.99 \pm 0.03$ and $\sigma_2^2 = 0.98 \pm 0.10$. This result is perfectly compatible with the assumption of a linear H_T evolution. The estimated uncertainties of μ_2 and σ_2^2 are used as a variation of the linear model to derive a systematic uncertainty for the background prediction (see Sec. 3.4.6).

Since the H_T evolution is estimated from simulation, its consistency with data is evaluated using a control region with the requirement of at least 4 jets. To ensure that the data sample is dominated by $t\bar{t}$ events we require at least 2 b -tagged jets. To account for the $H_T > 400$ GeV cut, which cannot be avoided on data because of the cross trigger, we fit

$$\epsilon_d^{\text{corr}}(x; c_i, c_{i+1}) = \frac{\epsilon_d(x; c_i, c_{i+1})}{\epsilon_s(x; 400)},$$

and use the parameters estimated on simulation for $\epsilon_s(x; 400)$. The result of this likelihood fit on simulation is shown in Fig. 3.22 and the evolution of the model parameters with H_T is visualized in Fig. 3.23 for data and simulation. Table 3.7 lists both sets of parameters in the two last columns.

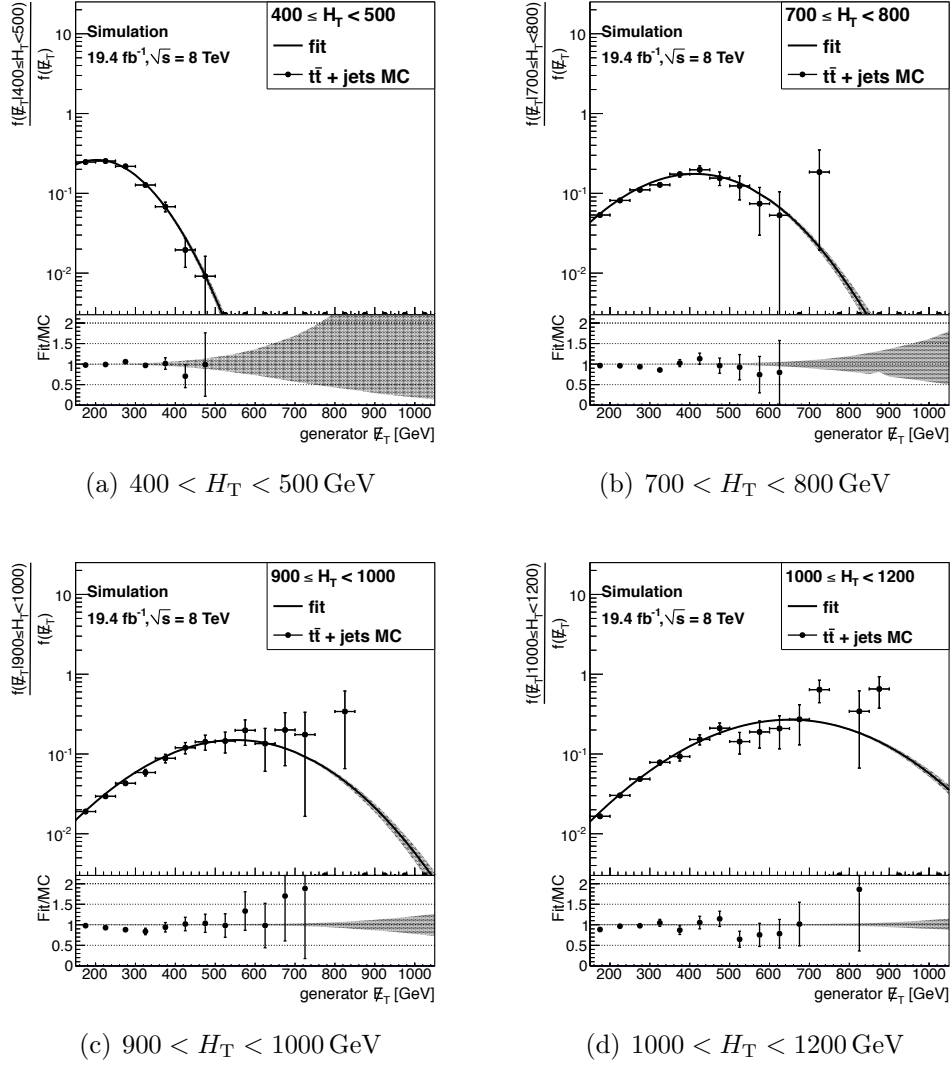


Figure 3.22.: Ratio of the genuine- E_T spectrum for simulated $t\bar{t}$ events and the ≥ 4 -jet selection after requiring (a) $400 < H_T < 500$ GeV, (b) $700 < H_T < 800$ GeV, (c) $900 < H_T < 1000$ GeV and (d) $1000 < H_T < 1200$ GeV. The filled circles indicate the ratio from simulation. The line and the shaded areas represent the result and the statistical uncertainty of the fit to a set of skew error functions with parameters according to Eq. 3.14. The lower panels show the ratios between the fitted functions and simulation.

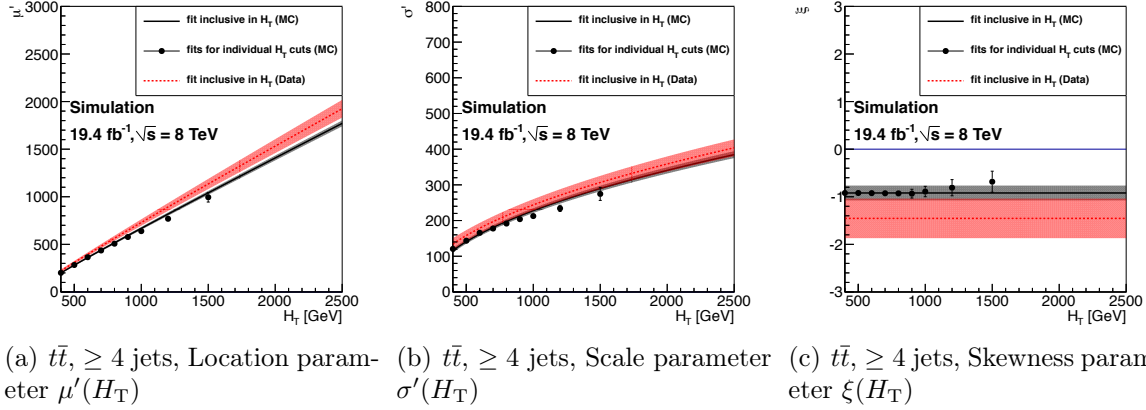


Figure 3.23.: Evolution of the error function parameters (a) μ' , (b) σ' and (c) ξ with H_T for a selection of at least 4 jets in the 2 b -tag bin compared with simulated $t\bar{t}$ events. The line and the shaded areas represent the result and the statistical uncertainty of the fit to (red) data and (black) simulation of a set of skew error functions with parameters according to Eq. 3.14. The filled circles show the results obtained for individual H_T bins for fits to simulation.

To set a systematic uncertainty that accounts for deviations between data and simulation, the difference of the parameters estimated in the 4-jets control region for data and simulation are added to the parameters estimated on simulation for 6-jets. This modified 6-jet parameterization is then used in the reevaluation of the entire background estimation process and the observed deviation of the predicted SM background yields is used as an estimate of the corresponding systematic uncertainty (see Sec. 3.4.6).

Correcting the \cancel{E}_T model for b -jet acceptance effects

Equation 3.13 models the impact of a H_T selection on the genuine- \cancel{E}_T spectrum without accounting for effects related to the b -jet selection. Such an additional modification of the genuine- \cancel{E}_T distribution is necessary in $t\bar{t}$ events. In $t\bar{t}$ events with low H_T ($\lesssim 750$ GeV) the momenta of the single top quarks, decaying to Wb , tend to be low. Subsequently, the neutrino momentum can only be high if the direction of the leptonically decaying W boson aligns with the top quark direction. This W - t alignment implies an anti-alignment of the bottom and the top quark, hence the bottom quark momenta are low and the probability that the corresponding b -jets will fail the jet- p_T threshold of 40 GeV increases. In sum, the b -jet acceptance decreases with increasing \cancel{E}_T for events with low H_T , while this effect disappears for high H_T because the top quarks are sufficiently boosted and the requirement of high \cancel{E}_T does not impose such tight kinematic constraints on the b -quark. This effect is specific for the $t\bar{t}$ topology and no related effect can be observed in a simulated $W+b\bar{b}$ sample. The b -jet acceptance

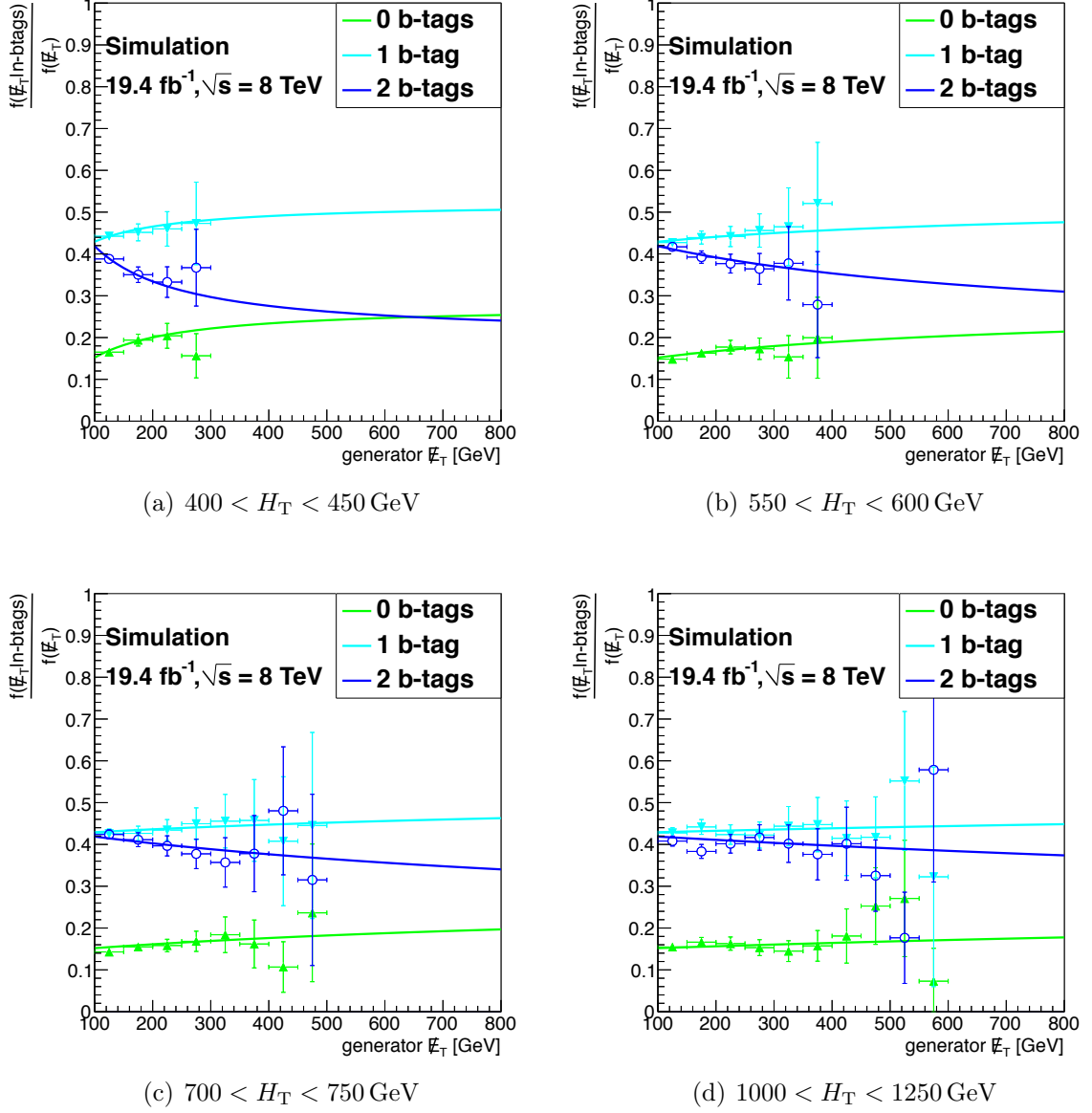


Figure 3.24.: Ratio of the genuine- E_T spectrum in b -jet multiplicity bins with respect to the inclusive spectrum for simulated $t\bar{t}$ events after requiring (a) $400 < H_T < 450$ GeV, (b) $550 < H_T < 600$ GeV, (c) $700 < H_T < 750$ GeV and (d) $1000 < H_T < 1250$ GeV. The circles show the values of the ratios in simulation, while the lines correspond to a simultaneous fit of the functions described by Eq. 3.17.

effect is illustrated in Fig. 3.24, where the ratio of the genuine- \cancel{E}_T spectrum of single b -tag categories (0, 1 and 2) to the inclusive spectrum is shown for selected H_T regions.

The ratios can be well parametrized by a model that interpolates between a linearly changing efficiency $\epsilon_{0,b}$ at x_0 and a constant efficiency $\epsilon_{1,b}$ at infinity:

$$\epsilon_b(x, i) = \epsilon_{0,b} + \frac{x - x_0}{x - x_0 + r(\overline{H}_{T,i})}(\epsilon_{1,b} - \epsilon_{0,b}), \quad r(\overline{H}_{T,i}) = r_0 + r_1(\overline{H}_{T,i} - \overline{H}_{T,1}) \quad (3.17)$$

The index b denotes the multiplicity of b -tagged jets and x_0 is set to 100 GeV. The parameter $r(\overline{H}_{T,i})$ in the denominator of Eq. 3.17 determines the point of transition from linearity to a constant function and is assumed to rise linearly with $\overline{H}_{T,i}$. The argument $\overline{H}_{T,i}$ is the average of the limits c_i and c_{i+1} that define the H_T bin i .

A reliable estimate of the parameters can be obtained from simulated $t\bar{t}$ events where the described acceptance effect is well modeled. For the estimation we use a simultaneous likelihood fit, taking into account events with 0, 1 and 2 b -tags in consecutive H_T categories with a 50 GeV step size between 400 and 800 GeV followed by a 200 GeV step and 250 GeV steps up to 2500 GeV. Furthermore, the constraints

$$\sum_{b=0}^2 \epsilon_{0,b} = \sum_{b=0}^2 \epsilon_{1,b} = 1,$$

must hold and are applied in the fit. The resulting parameters are

$$\begin{aligned} \epsilon_{0,0} &= 0.15 \pm 0.006, & \epsilon_{0,1} &= 0.43 \pm 0.006, & \epsilon_{0,2} &= 0.42 \pm 0.007 \\ \epsilon_{1,0} &= 0.28 \pm 0.004, & \epsilon_{1,1} &= 0.52 \pm 0.006, & \epsilon_{1,2} &= 0.20 \pm 0.01 \\ r_0 &= 158.7 \pm 123.0 \text{ GeV}, & r_1 &= 3.64 \pm 3.05. \end{aligned}$$

The parameters r_0 and r_1 are determined rather poorly since the functions $\epsilon_b(x)$ are already quite flat at medium H_T while for low H_T no simulated data for $\cancel{E}_T > 300$ GeV is available. Hence, these parameters are not constrained tightly. Nonetheless, their impact on the analysis is small for the same reasons and any residual systematic errors are certainly covered by the closure uncertainty (see. Sec. 3.4.6).

The full \cancel{E}_T model for $t\bar{t}$

The functions $\epsilon_b(x, i)$ and $\epsilon_d(x; c_i, c_{i+1})$ are used as multiplicative corrections of the inclusive \cancel{E}_T model $f_P(x, \alpha, \beta)$, to account for the selection of categories in H_T and b -tag multiplicity. The absolute scale of these corrections is absorbed by the normalization of the \cancel{E}_T model. The full model of genuine- \cancel{E}_T for $t\bar{t}$ production in a single H_T bin i , defined by $c_i < H_T < c_{i+1}$ and for a b -tag multiplicity b is given by

$$\mathcal{M}_{i,b}(x) \sim N f_P(x, \alpha, \beta) \times \epsilon_d(x; c_i, c_{i+1}) \times \epsilon_b(x, i) . \quad (3.18)$$

with N accounting for the normalization.

3.4.3. Estimation of the W +jets background

In order to measure the fraction of W +jets events in a control region we divide the preselected single-leptonic sample into three categories, based on the b -jet multiplicity in the event. The three subsamples are composed of events with 0, 1 and 2 b -tagged jets respectively, each with a different W +jets/ $t\bar{t}$ ratio. Simulation predicts W +jets fractions for a control region defined in the range $150 < \cancel{E}_T < 400$ GeV of 43.0%, 6.5% and 1.7% for the 0 b -tag, 1 b -tag and 2 b -tag subsamples.

The relative fraction of W +jets and $t\bar{t}$ events in each b -tag category is estimated using a template fit to the b -tag multiplicity distribution. To this end, templates of the b -tag multiplicity in $t\bar{t}$ and W +jets events are constructed from simulation. Differences in identification and misidentification rates of b , c or light-jets between data and simulation change the yield and the composition of the b -tag categories. To account for such differences, single-jet efficiencies are extracted from simulation and corrected by data/simulation scale factors which are externally provided by the b -tagging working group of the CMS collaboration [114].

Using the corrected single jet probabilities ϵ_i ($i = 1 \dots n$) the probability to find n_b b -tagged jets in an event with n jets can be calculated by

$$P(n_b|n) = \begin{cases} n_b = 0 : & \prod_{i=1}^n (1 - \epsilon_i) \\ n_b = 1 : & \sum_{i=1}^n P(0|n) \cdot \frac{\epsilon_i}{1 - \epsilon_i} \\ n_b = 2 : & \sum_{i=1}^n \sum_{j>i}^n P(0|n) \cdot \frac{\epsilon_i}{1 - \epsilon_i} \cdot \frac{\epsilon_j}{1 - \epsilon_j} \\ n_b = 3 : & \sum_{i=1}^n \sum_{j>i}^n \sum_{k>j}^n P(0|n) \cdot \frac{\epsilon_i}{1 - \epsilon_i} \cdot \frac{\epsilon_j}{1 - \epsilon_j} \cdot \frac{\epsilon_k}{1 - \epsilon_k} \\ n_b \geq 4 : & 1 - P(n_b < 4|n) \end{cases} \quad (3.19)$$

The efficiencies ϵ_i depend on the parton flavor, p_T and η of each jet. The corrected event yield in each b -tag category n_b is calculated by summing the probabilities $P(n_b|n)$ over the full sample, thus all events of the sample contribute to each b -tag category. Figure 3.25 shows the corrected templates for the $t\bar{t}$ and the W +jets sample after a fit to data in the control region $150 < \cancel{E}_T < 400$ GeV.

In a second step, the fitted fractions in each b -tag category are used to extract the H_T distribution of W +jets and $t\bar{t}$ events from data. The 2 b -tag category is dominated by $t\bar{t}$ and contains only a small contamination of other backgrounds. Therefore its H_T distribution can be used as a template for $t\bar{t}$. This shape is subtracted from the H_T shape of the 0 b -tag category, using the W +jets/ $t\bar{t}$ ratio determined from the inclusive fit, to obtain the H_T distribution for W +jets events. These two H_T templates are scaled for each b -tag category, according to the fractions obtained from the previous fit. This yields H_T dependent W +jets/ $t\bar{t}$ fractions. The H_T shapes for the W +jets and $t\bar{t}$ contribution in different b -tag categories are shown in Fig. 3.27 and agree well.

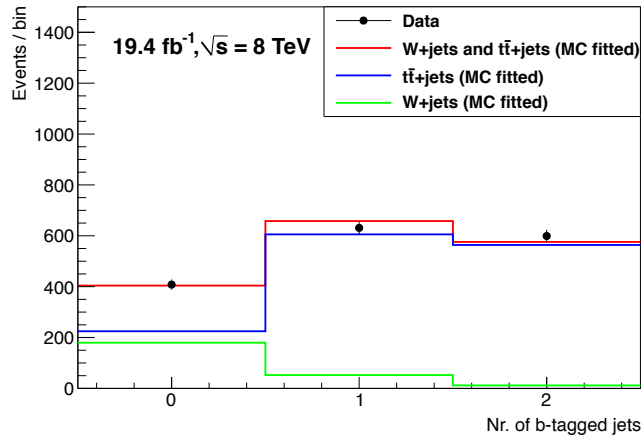


Figure 3.25.: Distribution of b -tag multiplicity. The black circles indicate data and the colored lines indicate the templates as obtained from simulation, normalized to the fit result.

The W +jets/ $t\bar{t}$ ratios obtained in this way show no significant trend as a function of H_T , neither in simulation nor in data, as shown in Fig. 3.26. In simulation, the fractions are well reproduced.

In order to account for the small W +jets contribution in the final \cancel{E}_T model, used to predict the SM background, the genuine- \cancel{E}_T distribution of each H_T category is extracted from the simulated W +jets sample and added as static component to the genuine- \cancel{E}_T model for $t\bar{t}$ (Eq. 3.18). For the relative sizes of the W and $t\bar{t}$ components, the estimated W +jets/ $t\bar{t}$ fractions are used.

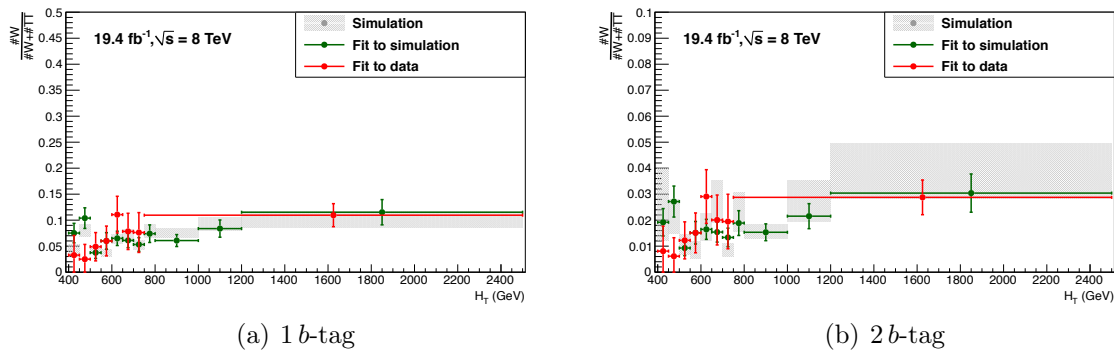


Figure 3.26.: Ratio of W +jets to $t\bar{t}$ for (a) 1 b -tag and (b) 2 b -tag as predicted by the fit to b -tag multiplicity in data and simulation. For comparison, the true fractions from simulation are also shown.

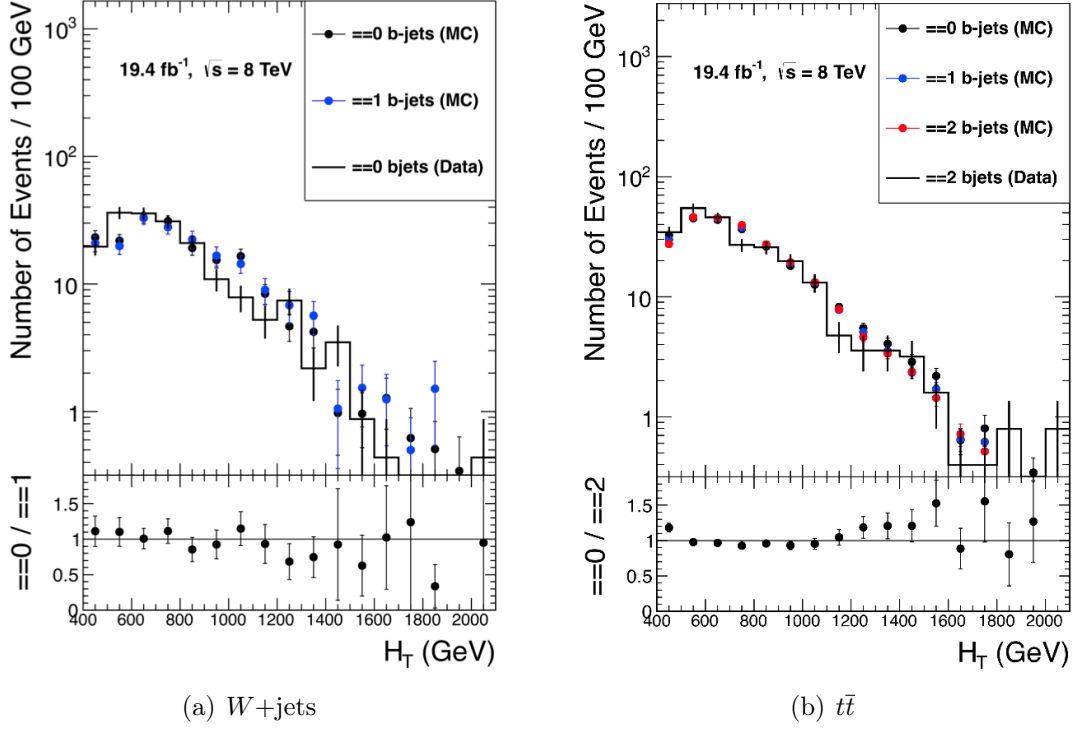


Figure 3.27.: Comparison of the simulated H_T distributions for W +jets (left) and $t\bar{t}$ (right) simulation for different b -tag multiplicities. Overlaid are the data distributions in the 0 b -tag (left) and 2 b -tag bin (right). Data and simulation have been normalized to the same content.

3.4.4. \cancel{E}_T resolution templates

So far, the \cancel{E}_T model was developed to describe the distribution of genuine- \cancel{E}_T . This section describes the measurement of \cancel{E}_T -resolution templates and their application in the analysis, to incorporate contributions due to detector or event reconstruction effects. The selections and methods to construct \cancel{E}_T resolution templates are shared with the “Lepton Spectrum” analysis [91] and have first been proposed in [115]. They were used in the same way in the analysis of the dataset collected during the year 2011 [76].

The observed \cancel{E}_T spectrum in data results from the vectorial addition of genuine- \cancel{E}_T and a contribution due to detector effects ($\cancel{E}_T^{\text{fake}}$). This source of \cancel{E}_T may not be accurately modeled in simulation because of additional noise, a slightly worsened jet resolution or time-dependent degradation of the detector material.

Therefore \cancel{E}_T -resolution templates are constructed separately for each H_T category, jet multiplicity and b -tag multiplicity from a data sample that is statistically independent from the single-lepton selection. The object definitions concerning \cancel{E}_T , jets and leptons correspond to the preselection described in Sec. 3.3, with the sole difference that any

event containing leptons, identified by the veto selection, is discarded. This control sample is dominated by multijet events without genuine- \cancel{E}_T . The datasets and run ranges used to collect this sample are listed in Tab. 3.8, the binning of H_T categories and the corresponding triggers are summarized in Tab. 3.9.

For each H_T category, a trigger with a threshold well below the lower H_T limit of the category is chosen. Trigger streams with low H_T thresholds are prescaled because of their high event rates, thus events recorded by such triggers have to be reweighted with the product of the L1 and HLT prescale factors in order to preserve possible time-dependent effects in the \cancel{E}_T reconstruction. Only the highest H_T trigger path, HLT_HT_750_v*, has not been prescaled during the full data taking period. After correcting for prescale factors, a smooth H_T spectrum is obtained, as shown in Fig. 3.28.

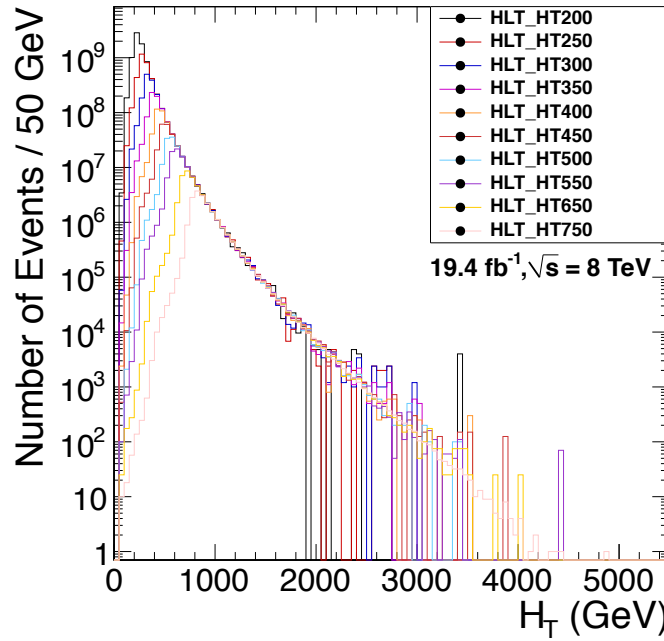


Figure 3.28.: Distribution of H_T obtained from different H_T triggers after correction for the trigger prescale factors.

These templates are normalized separately and added according to the jet and b-tag multiplicity, observed for the single-lepton selection in each H_T category. Figure 3.29 compares the resulting predictions for the \cancel{E}_T -resolution templates to templates that were constructed from simulated QCD events, as well as to the simulated \cancel{E}^{fake} distribution of the background components in the single-lepton selection. To obtain \cancel{E}^{fake} for the latter, genuine- \cancel{E}_T is subtracted from the reconstructed \cancel{E}_T , i.e. $\cancel{E}^{\text{fake}} = |\vec{\cancel{E}}^{\text{reco}} - \vec{\cancel{E}}^{\text{gen}}|$. The simulated QCD control regions model the \cancel{E}_T resolution in the single-lepton selection well, while the predicted \cancel{E}_T -resolution templates from data are slightly wider, as expected from a slightly degraded jet resolution in data.

Table 3.8.: Certification files and primary data sets used for the determination of \vec{E}_T -resolution templates, together with the run ranges and integrated luminosities for the data-taking periods.

Data sets	run range	$\int \mathcal{L} dt$
Certification: Cert_190456-196531_8TeV_13Jul2012ReReco_Collisions12_JSON/HT/Run2012A-13Jul2012-v1	190456 – 193621	0.8 fb ⁻¹
Certification: Cert_190456-196531_8TeV_13Jul2012ReReco_Collisions12_JSON/JetHT/Run2012B-13Jul2012-v1	193833 – 196531	4.4 fb ⁻¹
Certification: Cert_198022-198523_8TeV_24Aug2012ReReco_Collisions12_JSON/JetHT/Run2012C-24Aug2012-v1	198022 – 198913	0.5 fb ⁻¹
Certification: Cert_190456-203002_8TeV_PromptReco_Collisions12_JSON/JetHT/Run2012C-PromptReco-v2	198934 – 203746	6.4 fb ⁻¹
Certification: Cert_190456-208686_8TeV_PromptReco_Collisions12_JSON/JetHT/Run2012D-PromptReco-v1	203768 – 208686	7.3 fb ⁻¹

Table 3.9.: Triggers and H_T binning used for fake- \vec{E}_T templates.

$350 \leq H_T < 400$ HLT_HT_200_v*	$400 \leq H_T < 450$ HLT_HT_300_v*	$450 \leq H_T < 500$ HLT_HT_350_v*	$500 \leq H_T < 550$ HLT_HT_400_v*
$550 \leq H_T < 600$ HLT_HT_450_v*	$600 \leq H_T < 650$ HLT_HT_500_v*	$650 \leq H_T < 700$ HLT_HT_550_v*	$700 \leq H_T < 750$ HLT_HT_550_v*
$750 \leq H_T < 800$ HLT_HT_650_v*	$800 \leq H_T < 1000$ HLT_HT_650_v*	$1000 \leq H_T < 1200$ HLT_HT_750_v*	$1200 \leq H_T < 1500$ HLT_HT_750_v*
$1500 \leq H_T < 2500$ HLT_HT_750_v*			

Since \vec{E}_T is calculated from all PF candidates, the direction \vec{E}_T^{fake} tends to be anti-aligned with the jet system, which has usually the largest share in mismeasurements. On the other hand, the jet system recoils against the W boson and balances the $\ell\nu$ system, aligning the directions of \vec{E}_T^{gen} and \vec{E}_T^{fake} , as can be seen in Fig 3.31. This figure shows the distribution of $\Delta\phi$, the angle between \vec{E}_T^{gen} and \vec{E}_T^{fake} . For a majority of simulated $t\bar{t}$ events we find $\Delta\phi < \pi/2$.

The deviation of $\Delta\phi$ from a uniform distribution due to the recoiling jet system can be corrected by a shift of \vec{E}_T^{fake} in direction of \vec{E}_T^{gen} , as indicated in Fig. 3.30. An estimate of this shift can be obtained from the mean of \vec{E}_T^{fake} projected on \vec{E}_T^{gen} . This average shift, denoted as $\langle \vec{E}_{T,\parallel}^{\text{fake}} \rangle$, is shown in Fig. 3.32(a) and has a linear dependence on H_T . Accounting for this shift in the addition of \vec{E}_T^{gen} and \vec{E}_T^{fake} , results in an uniformly distributed $\Delta\phi_{\text{corr}}$, as can be seen in Fig. 3.31.

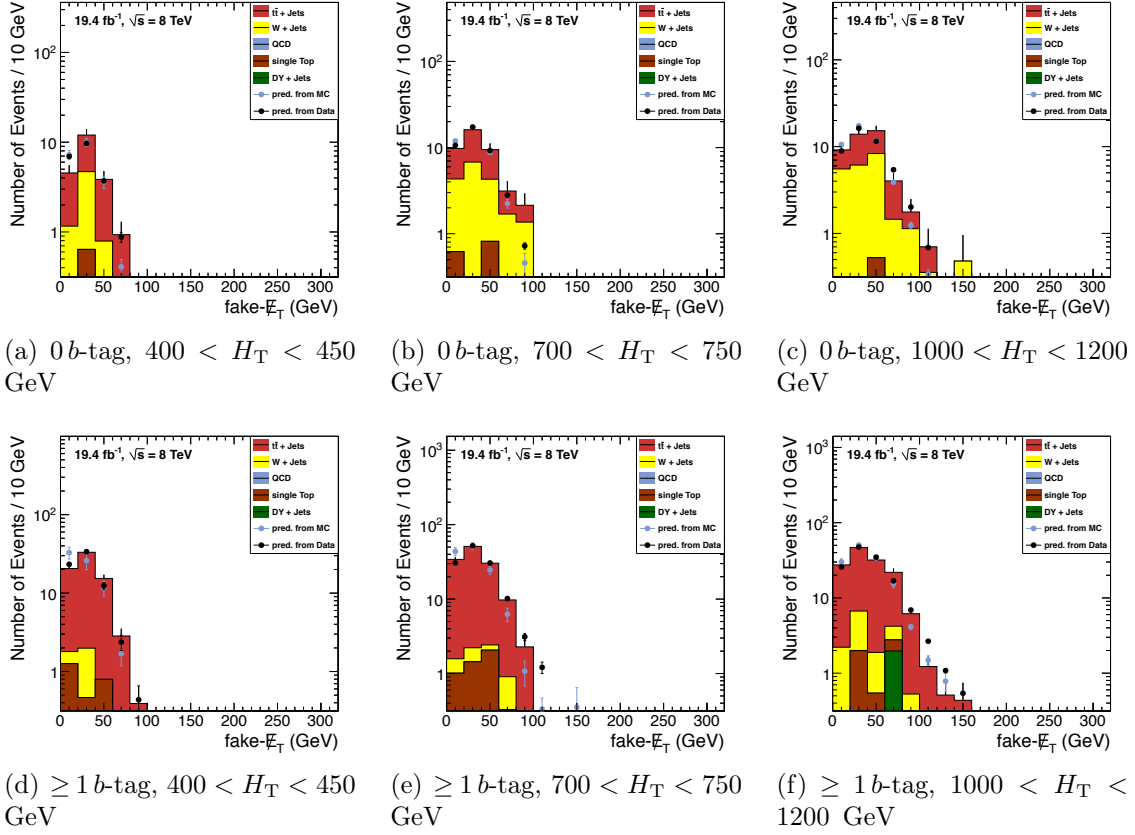


Figure 3.29.: E_T -resolution templates as measured in the QCD control region (dots) and E_T^{fake} in the single lepton channel for different H_T bins (left, center, right) and the 0 b -tag (top) and ≥ 1 b -tag (bottom) bin.

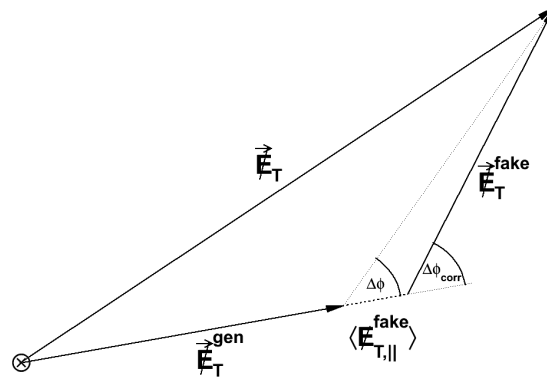


Figure 3.30.: Addition of \vec{E}_T^{gen} and \vec{E}_T^{fake} and the shift $\langle E_T^{\text{fake}} \rangle$ to correct for the effects from the hadronic recoil.

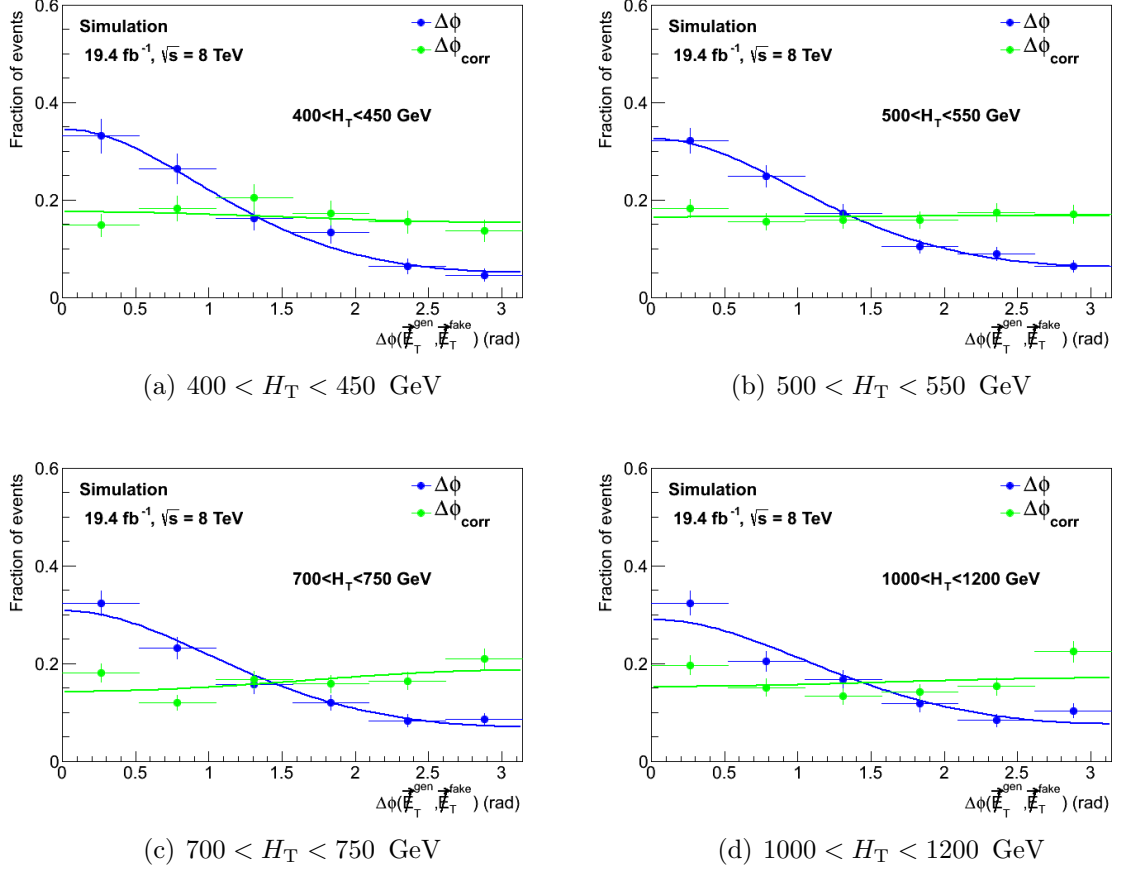


Figure 3.31.: Distribution of $\Delta\phi$ in the single-lepton selection of the simulated $t\bar{t}$ sample before and after correcting for the bias introduced by the recoiling jet system. In all H_T categories $\Delta\phi_{\text{corr}}$ is distributed uniformly within the required accuracy.

Figure 3.32(b) shows the distribution of $\cancel{E}_T^{\text{fake}}$ in bins of $\cancel{E}_T^{\text{gen}}$ for simulated $t\bar{t}$ events after correcting for the shift $\langle \cancel{E}_{T,\parallel}^{\text{fake}} \rangle$. Within statistical uncertainties, no significant dependence of $\cancel{E}_T^{\text{fake}}$ can be observed. It is therefore reasonable to assume that these two variables are uncorrelated. Residual correlations are mitigated, since the convolution procedure is performed for each H_T bin separately.

Consequently, the convolution can be implemented by sampling the uncorrelated joint probability distribution $f(\cancel{E}_T^{\text{gen}}, \cancel{E}_T^{\text{fake}}, \Delta\phi_{\text{corr}})$ of the full genuine- \cancel{E}_T model, the uniform distribution of $\Delta\phi_{\text{corr}}$ and the \cancel{E}_T -resoituon templates, for each H_T and b -tag category.

$\cancel{E}_T^{\text{fake}}$ can lead to observed values of $\cancel{E}_T > 150$ GeV for genuine- \cancel{E}_T that is smaller than this threshold, an analytic extension of the Pareto distribution for values of $\cancel{E}_T^{\text{gen}} < 150$ GeV of the form $x \exp(-\alpha'x)$ is used for the $t\bar{t}$ component. The parameter α' is fixed by the requirement that the first derivatives agree at $\cancel{E}_T^{\text{gen}} = 150$ GeV.

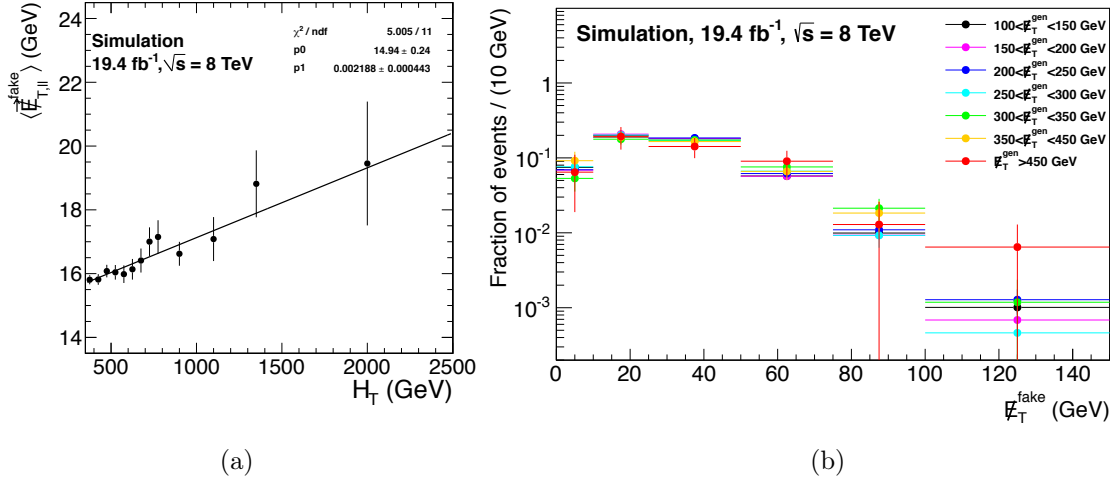


Figure 3.32.: (a) Evolution of the shift $\langle E_{T,\parallel}^{\text{fake}} \rangle$ with H_T due to the recoiling jet system. (b) Distribution of \vec{E}_T^{fake} in bins of \vec{E}_T^{gen} in $t\bar{t}$ events for $H_T > 400$ GeV.

Since the \vec{E}_T resolution templates are steeply falling, the details of this extension to low genuine- \vec{E}_T have very little impact on the results of the convolution. Omission of the extension would on the other hand lead to unpleasant edge effects in the convolution, which distort the estimation of the model parameters.

The joint distribution $f(\vec{E}_T^{\text{gen}}, \vec{E}_T^{\text{fake}}, \Delta\phi_{\text{corr}})$ is sampled on a fixed three dimensional grid over \vec{E}_T^{gen} , \vec{E}_T^{fake} and $\Delta\phi_{\text{corr}}$ and for each point of this grid, the addition

$$\begin{aligned} \vec{E}_T &= \left| \vec{E}_T^{\text{gen}} \left(1 + \frac{\langle E_{T,\parallel}^{\text{fake}} \rangle}{E^{\text{gen}}} \right) + \vec{E}_T^{\text{fake}} \right| \\ &= \left(E_T^{\text{gen}} + \langle E_{T,\parallel}^{\text{fake}} \rangle \right)^2 + E_T^{\text{fake}2} + 2 \left(E_T^{\text{gen}} + \langle E_{T,\parallel}^{\text{fake}} \rangle \right) E_T^{\text{fake}} \cos(\Delta\phi_{\text{corr}}) \end{aligned}$$

is evaluated and cached. The distribution of the resulting \vec{E}_T in each category is then obtained from a histogram of these cached values, weighted by probabilities, which are sampled from the joint distribution $f(\vec{E}_T^{\text{gen}}, \vec{E}_T^{\text{fake}}, \Delta\phi_{\text{corr}})$.

This procedure is applicable in the likelihood fit of the full model, comprising all categories of H_T and b -tag multiplicity. For each minimization step of the likelihood function, the convolution of the varied model can be reevaluated in each category solely by updating the weights.

3.4.5. Estimation of the \cancel{E}_T spectrum from data

All components described in the preceding sections are combined and convoluted with the detector resolution for each H_T category, separately for 1 and 2 b -tags. The H_T categories correspond to those listed in Tab. 3.9.

The control regions are chosen in order to ensure sufficient statistics to determine the model parameters and to limit signal contamination. Signal contamination can be mainly expected at high \cancel{E}_T and H_T , for selections with more than one b -tagged jet. Thus, for events with two tagged b -quark jets the control region is defined by $400 < H_T < 750$ GeV and $150 < \cancel{E}_T < 400$ GeV, as shown in Fig. 3.17, while the 1 b -tag category is used inclusively as control region, since otherwise no \cancel{E}_T -tail events would contribute to the likelihood. Nonetheless, we introduce high upper limits of 2500 GeV in \cancel{E}_T and H_T for technical reasons. No event passing the preselection exceeds these limits.

For each H_T and b -tag category, denoted by the indices i and b , likelihood functions $L_{i,b}$ are built from control region data and combined to a single likelihood function $L = \prod_{i,b} L_{i,b}$. The parameters of L that are allowed to float in the likelihood fit are the scale and shape parameters α and β of the Pareto distribution, as well as the five parameters of the error functions that model the impact of H_T selections (Tab. 3.7).

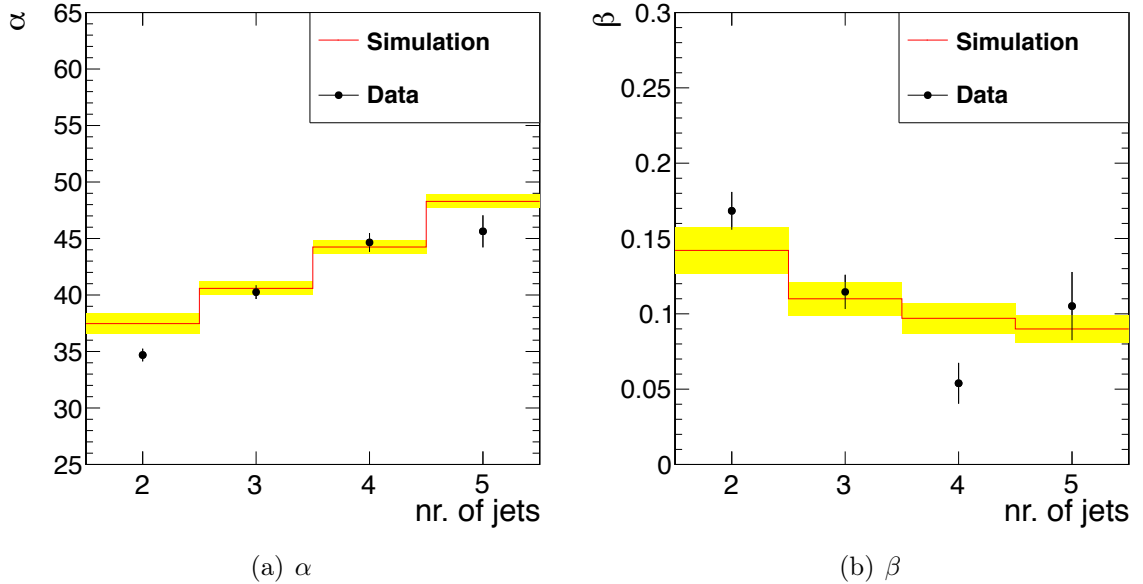


Figure 3.33.: Values of the parameter (a) α and (b) β of the Pareto distribution describing the \cancel{E}_T spectrum for control regions with two to five jets and a lepton p_T threshold of 30 GeV. Results from data are indicated by closed symbols and black error bars while simulation is shown as a red line with a shaded area representing the uncertainty.

Although all events of the 1 b -tag category above $H_T > 400$ GeV and $\cancel{E}_T > 150$ GeV are included in the Likelihood, the data sample size is not sufficient for a reliable estimation of the tail parameter β . Therefore, this parameter is constrained from simulation. The constraint is implemented by adding a Gaussian term to the likelihood function with mean $\mu_\beta = 0.034$ and standard deviation $\sigma_\beta = 0.014$, corresponding to the values estimated by the likelihood fit shown in Fig. 3.19(a). The quality of this constraint on β is validated by a comparison of simulation to data in control regions defined by lower jet multiplicities as shown in Fig. 3.33. In order to avoid a bias from restrictions on H_T , a data sample, which was recorded by a pure single lepton trigger is used. Due to a higher trigger threshold on the lepton momentum ($p_T^{\text{lep}} > 24$ GeV), the offline selection on the lepton momentum has to be tightened to $p_T^{\text{lep}} > 30$ GeV. The two sets of estimates for α and β are compatible and show the same trend with respect to the jet multiplicity. The maximum deviation of $\Delta\beta = 0.047$ is observed for the 4-jet selection. To establish a systematic uncertainty on the prediction, μ_β is varied by $\pm\Delta\beta$ in repeated fits (see Sec. 3.4.6).

The parameters of the error functions (Eq. 3.14) are also constrained in the final likelihood fit of the \cancel{E}_T model. This constraint is implemented as a multivariate Gaussian term reflecting the parameter estimates, their statistical uncertainties and correlations obtained from simulation. These parameter values are listed in Tab. 3.7. The results from fits of the full model to data and to simulation are summarized in Tab. 3.10. The estimated values of the error function parameters, reported in the lower part of the table, are dominated by the constraint on these parameters.

Table 3.10.: Fit results for data and simulation for the parameters of the generalized Pareto function describing the genuine \cancel{E}_T shape and of the error functions describing the effect of a selection in H_T on the \cancel{E}_T shape.

parameter	data	simulation
α (GeV)	54.2 ± 2.2	53.9 ± 1.4
β	0.032 ± 0.012	0.035 ± 0.012
μ_0 (GeV)	-27.4 ± 10.2	-27.6 ± 10.1
μ_1	0.76 ± 0.03	0.76 ± 0.03
σ_0^2 (GeV ²)	11658.6 ± 2257.1	11774.7 ± 2253.8
σ_1^2 (GeV)	57.2 ± 8.4	56.9 ± 8.4
ξ	-0.83 ± 0.45	-0.85 ± 0.46

For each H_T and b -tag category the model components are scaled to match the observed number of events in the normalization region $150 < \cancel{E}_T < 250$ GeV. The predicted event yields for the signal regions are then obtained by integrating over \cancel{E}_T and summing over the respective H_T categories. Statistical uncertainties on the predicted event yields are evaluated by sampling the parameters from a multivariate Gaussian distribution, with means according to the fit result and a covariance matrix, which is estimated from the shape of the likelihood minimum. Thereby, we account for all correlations between the uncertainties of the estimated parameter values. The calculation of the event

yields is reevaluated for each sampled parameter tuple and the central 68% quantiles of the resulting event yield distributions are reported as statistical uncertainties.

Figure 3.34 shows the true event yields, the predictions and the sampled distributions of the predictions for simulation above several lower limits defining the signal regions. The estimated \cancel{E}_T distributions in simulation and their statistical uncertainties are shown for three H_T categories in Fig. 3.35 for events with one and two b -tagged jets, respectively. Simulation and predictions agree well for all signal regions and the event counts for the 2 b -tag bin are summarized in Tab. 3.11. The observed and predicted \cancel{E}_T distributions for data are presented in Fig. 3.36. For these plots the statistical and systematic uncertainties are stacked.

A study with pseudo-experiments, randomly drawn from the full background model, was performed to confirm the statistical validity of the likelihood fit. This study confirms that no bias in the estimation of the central parameter values is present and that the sizes of the estimated uncertainties are correct. A description of the method and its results can be found in Appendix B.

Table 3.11.: Predicted and true event counts in simulation for 2 b -tags and different \cancel{E}_T and H_T signal regions. Uncertainties are statistical.

2 b -tag	750 < H_T < 2500 GeV					
	MC truth			MC pred.		
250 < \cancel{E}_T < 350 GeV	48.98	±	3.14	46.07	±	2.18
350 < \cancel{E}_T < 450 GeV	14.09	±	1.74	11.09	±	0.98
450 < \cancel{E}_T < 2500 GeV	4.56	±	0.96	3.42	±	0.48
2 b -tag	1000 < H_T < 2500 GeV					
	MC truth			MC pred.		
250 < \cancel{E}_T < 350 GeV	19.78	±	1.95	18.42	±	0.92
350 < \cancel{E}_T < 450 GeV	7.19	±	1.26	5.55	±	0.48
450 < \cancel{E}_T < 2500 GeV	3.22	±	0.81	2.27	±	0.38

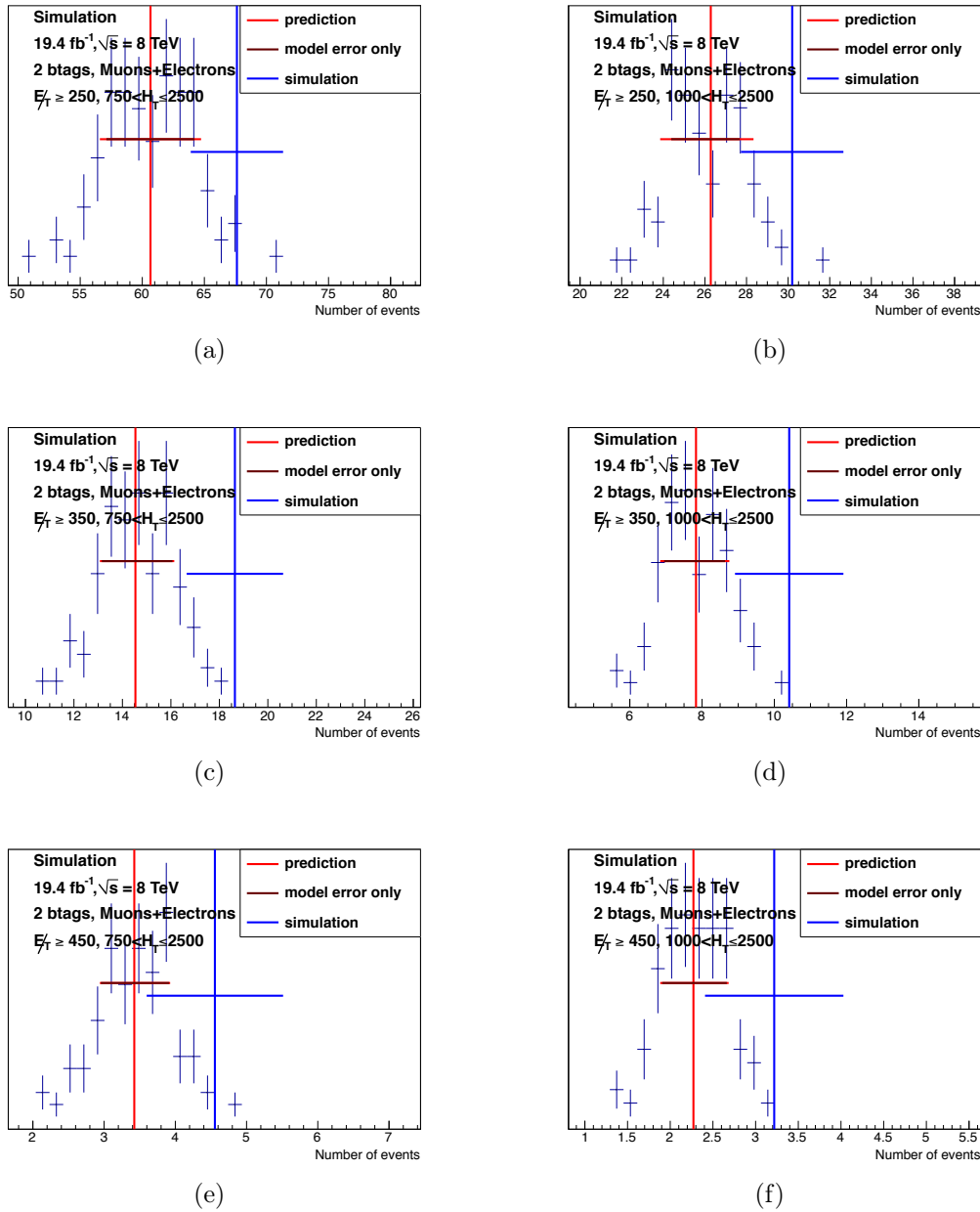


Figure 3.34.: Comparison of the predicted event yields with the counts from simulation for regions defined by (left) $750 < H_T < 2500$ GeV and (right) $1000 < H_T < 2500$ GeV, two b -tagged jets and (top) $250 < E_T < 2500$ GeV, (centre) $350 < E_T < 2500$ GeV and (bottom) $450 < E_T < 2500$ GeV. The widths of the sampled distributions and the dark red horizontal line reflect the statistical uncertainties on the model parameters only. The light red horizontal line includes also the uncertainty from statistical fluctuations of the normalization region.

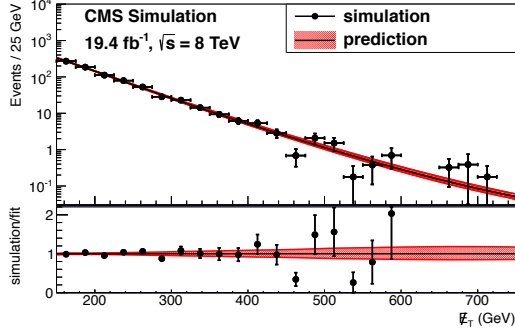
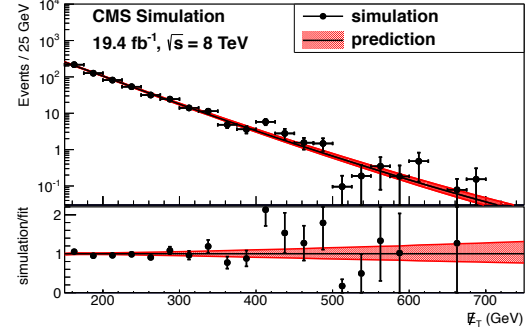
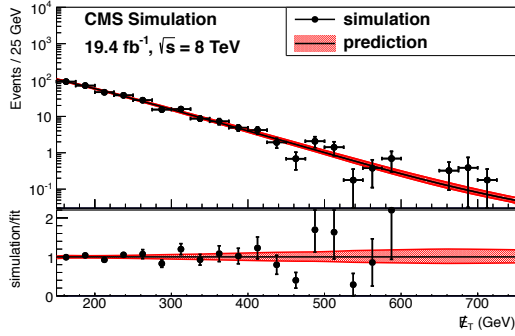
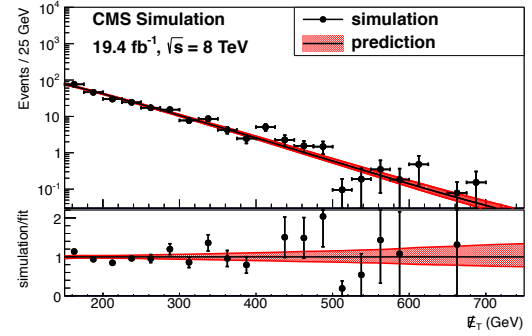
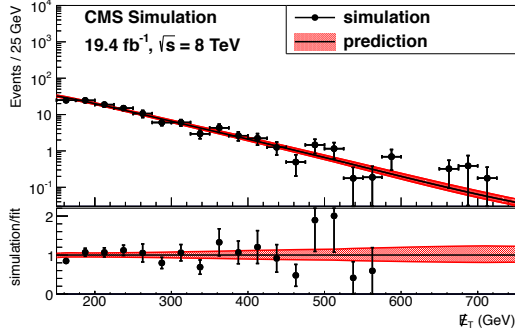
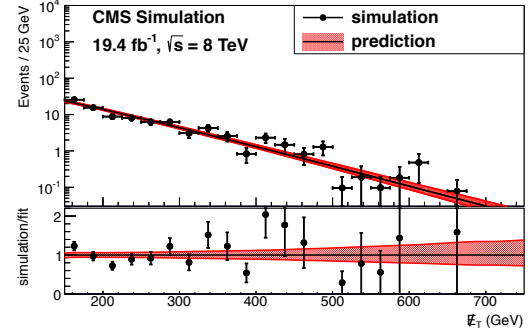
(a) MC, 1 b -tag, $H_T > 400$ GeV(b) MC, 2 b -tag, $H_T > 400$ GeV(c) MC, 1 b -tag, $H_T > 750$ GeV(d) MC, 2 b -tag, $H_T > 750$ GeV(e) MC, 1 b -tag, $H_T > 1000$ GeV(f) MC, 2 b -tag, $H_T > 1000$ GeV

Figure 3.35.: Results from fits to simulation for the (left) 1 b -tag and (right) 2 b -tag bins with (top) $H_T > 400$ GeV, (middle) $H_T > 750$ GeV and (bottom) $H_T > 1000$ GeV. The red error band reflects the statistical uncertainties on the shape parameters and on the event yield in the normalization region.

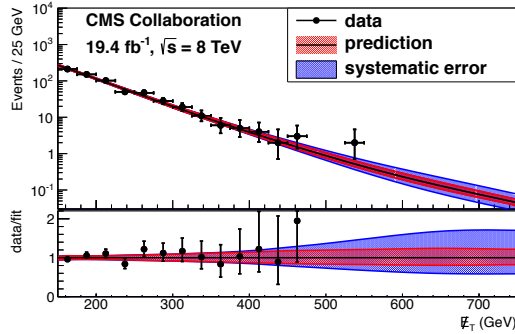
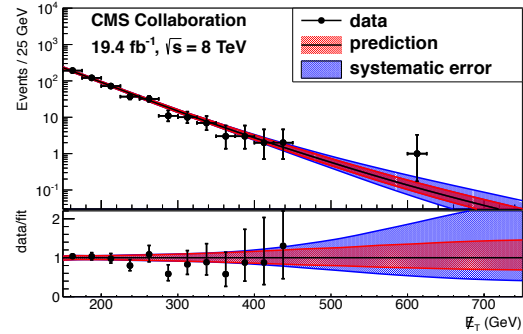
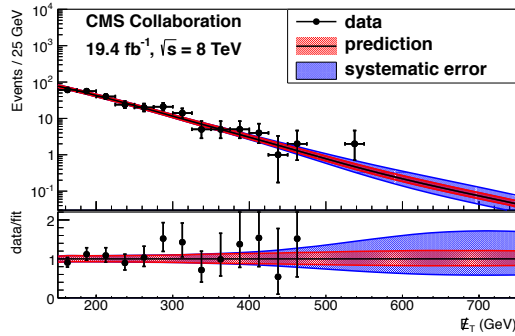
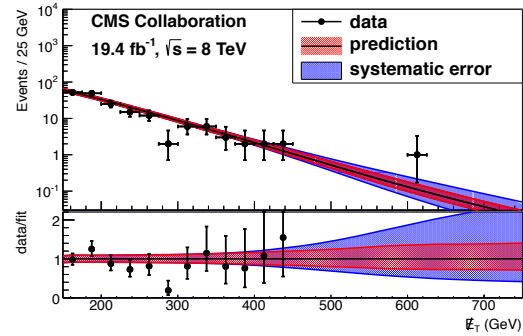
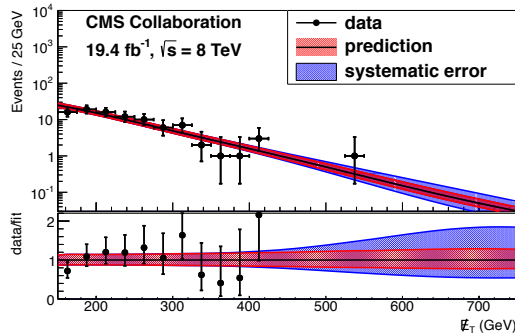
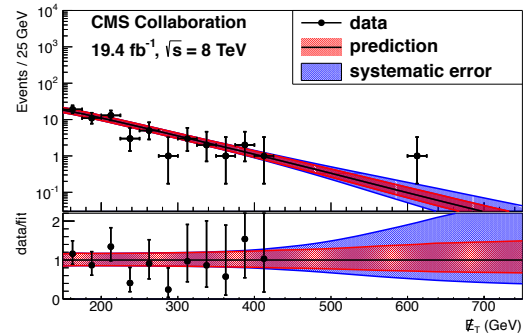
(a) Data, 1 b -tag, $H_T > 400$ GeV(b) Data, 2 b -tag, $H_T > 400$ GeV(c) Data, 1 b -tag, $H_T > 750$ GeV(d) Data, 2 b -tag, $H_T > 750$ GeV(e) Data, 1 b -tag, $H_T > 1000$ GeV(f) Data, 2 b -tag, $H_T > 1000$ GeV

Figure 3.36.: Results from fits to data for the (left) 1 b -tag and (right) 2 b -tag bins with (top) $H_T > 400$ GeV, (middle) $H_T > 750$ GeV and (bottom) $H_T > 1000$ GeV. The red error band reflects the statistical uncertainties on the shape parameters and on the event yield in the normalization region. The blue error band shows the systematic uncertainties.

3.4.6. Systematic effects in the background estimation

The results of the \cancel{E}_T model fit can be affected by several systematic uncertainties related to detector effects, assumptions made on the shape of the distribution as well as theoretical uncertainties and contributions from non-leading backgrounds. In order to estimate the size of these effects, we repeat the background estimation on simulation under changed conditions, implemented by either reweighting the sample or by a modification of the model.

The impact of these variations on the background predictions is quantified by the double-ratio

$$\delta\kappa = \frac{N'_{pred}/N'_{true}}{N_{pred}/N_{true}} - 1, \quad (3.20)$$

where N' denotes the predicted or observed event yields after the variation. The factor N'_{true}/N_{true} accounts for the fact that variations of the SM yield in the signal region should ideally be compensated by a corresponding change of the background prediction. Thus, $\delta\kappa$ measures the variation in closure, i.e. how well the prediction follows the change of events in the signal region. However, in rare cases where N_{true} is determined by a small number of simulated events, N'_{true}/N_{true} can introduce a large statistical uncertainty in the double-ratio $\delta\kappa$. In contrast, the change of the background prediction N'_{pred}/N_{pred} is not affected by signal region statistics. In such cases it is reasonable to revert to the more conservative expression

$$\delta\kappa = \frac{N'_{pred}}{N_{pred}} - 1. \quad (3.21)$$

For systematic uncertainties due to assumptions on the \cancel{E}_T model that do not change the true number of events in the signal region, Eq. 3.20 translates into Eq. 3.21.

The recipes to implement systematic variations that affect all three SUSY searches, participating in the CMS wide effort to investigate the single-lepton topology, have been synchronized. The other two analyses are documented in [91]. Descriptions of each contribution to the total systematic uncertainty for this analysis are given in the following paragraphs and a summary of the resulting uncertainties $\delta\kappa$ factors for all signal regions is presented in Tab. 3.13.

Jet and \cancel{E}_T scale

Miscalibration of the energy scales for jets or \cancel{E}_T are expected to be largely compensated by the fit to the \cancel{E}_T spectrum from data and the use of normalization regions. However, residual effects could remain. In order to assess their size, a standard procedure, recommended by the *JetMET* working group of the CMS collaboration, is applied. Thereby, the jet energies for all jets with $p_T > 10$ GeV are scaled up or down according to the uncertainty on the energy scale correction [104]. Jets with lower momenta are

scaled by 10%. This variation is propagated to the \cancel{E}_T scale and other quantities related to the jet momentum like H_T . Furthermore, the jet and b -tag multiplicities change, since jet momenta may be lifted above or drop below the jet- p_T threshold of the preselection. The resulting systematic uncertainties (denoted as JES in Tab. 3.13) are small, since the changes of the background event yields are captured by the fit to a large extent.

b -tag efficiency and misidentification rates

Variations in the b -tagging efficiency and purity can move events among the b -tag categories and thereby change the fractions of W +jets and $t\bar{t}$ events. As already noted in Sec. 3.4.3, b -tagging efficiencies and misidentification rates for single jets are extracted from simulation as function of p_T , η and parton flavor. To account for differences between data and simulation, scale factors are applied. The scale factors and their uncertainties are externally provided by the b -tagging working group of the CMS collaboration [114]. Again we use Eq. 3.19 of Sec. 3.4.3 to calculate event probabilities $P(n_b|n)$ from the scaled single jet efficiencies. Event yields for any selection requiring n_b b -tags, are obtained by summing $P(n_b|n)$ over all events that pass the respective selection requirements, disregarding the b -tagging information.

To assess the impact of the b -tag efficiencies on the prediction, the single jet scale factors are varied up and down by their uncertainty. These variation are performed independently for light-flavour jets and for c - or b -quark jets. The data/simulation scale factors and their uncertainties are only available for b and light-jets, thus c jets are treated as b jets, but their uncertainties are doubled as recommended by the b -tagging working group. As expected, the fit captures these modifications well. This can be attributed to the estimation of $W/t\bar{t}$ fractions based on fits to the b -tag multiplicity (see Sec. 3.4.3) and to the independent normalization of each b -tag category after the fit.

W polarization

An additional source of uncertainty arises from the W polarization in $t\bar{t}$ events. Variations of the W polarization alter the angular distributions of the lepton and the neutrino momenta and thereby also the \cancel{E}_T spectrum. Precise predictions of the W polarization in top-quark decays were calculated in [116] including NNLO QCD corrections and have been verified within experimental uncertainty by measurements at CDF [117] and D0 [118]. The calculated polarization fractions for the helicities $\lambda = 0$, $\lambda = -1$, $\lambda = 1$ are:

$$\begin{aligned} f_{\lambda=0} &= 0.6787 \pm 0.005 \\ f_{\lambda=-1} &= 0.311 \pm 0.005 \\ f_{\lambda=1} &= 0.0017 \pm 0.0001 \end{aligned} \tag{3.22}$$

Considering the decay $t \rightarrow bW^+ \rightarrow b\ell^+\nu_\ell$, the angular distribution of the positively charged lepton in the W^+ rest frame is given by

$$\frac{dN}{d\cos\theta_\ell^*} = f_{\lambda=1}\frac{3}{8}(1 + \cos\theta_\ell^*)^2 + f_{\lambda=-1}\frac{3}{8}(1 - \cos\theta_\ell^*)^2 + f_{\lambda=0}\frac{3}{4}\sin^2\theta_\ell^* \quad (3.23)$$

Here, θ_ℓ^* denotes the angle between the lepton and the reversed direction of the top-quark momentum in the W^+ rest frame. The helicity fraction $f_{\lambda=1}$ would be zero at LO with $m_b = 0$ because of angular momentum conservation, but receives corrections from gluon radiation at the per mil level at higher orders [116]. Since this prediction can be considered to be precise in the scope of the SM (in case no new physics contributes) and its influence on the angular distribution is rather small, $f_{\lambda=1}$ is not subjected to systematic variations. For the case of the anti-top-quark decay, the helicity fractions are identical to 3.22, only the helicity labels $\lambda = \pm 1$ are interchanged.

To obtain an estimate of the systematic uncertainty due to polarization effects, the two helicity fractions $f_{\lambda=0}$ and $f_{\lambda=-1}$ are each varied by $\pm 5\%$ in a correlated way and we use Eq. 3.23 to reweight the simulated $t\bar{t}$ sample by $N_{\lambda\pm 5\%}/N$ as function of $\cos\theta_\ell^*$. The size of this variation is ten times larger than the theoretical uncertainty, still the effects on the final prediction are small.

Lepton efficiencies

The preselection is chosen in such a way as to use only kinematic domains with stable trigger and reconstruction efficiencies. These efficiencies are summarized in Section 3.3.3 and good agreement between data and simulation can be observed. The impact on the background prediction is therefore expected to be small. In order to test the impact of possible deviations from the measured lepton efficiencies, the simulated sample is reweighted by the function

$$\epsilon(p_T) = \frac{\epsilon_0}{1 + e^{-\frac{p_T - \mu}{\sigma}}}, \quad (3.24)$$

which parametrizes the electron and muon identification efficiency as measured in data, using the parameter values in Tab. 3.12. There are two separate variations for muons and one variation for electrons, which differs between barrel and endcap. The largest effects on the background prediction, resulting from this variation is smaller than 2% for the highest E_T categories.

Pileup

As the maximum instantaneous luminosity per bunch crossing changed during 2012, also the average number of simultaneous minimum bias collisions (pileup) changed throughout the data taking period. For all results presented in this thesis, simulation has been reweighted to the pileup conditions observed in data, based on the expected

Table 3.12.: Parameters used for the evaluation of uncertainties due to variations of the lepton efficiencies.

	ϵ_0	μ	σ
μ (case 1)	0.949	-16.1	11.0
μ (case 2)	1.01	-3.8	14.0
e (barrel)	0.916	6.3	12.0
e (endcap)	0.962	10.4	14.0

average number of collisions for each luminosity section, calculated from the instantaneous luminosity and the minimum bias cross section.

The simulation therefore provides a satisfactory description of the dependence of several key observables on the number of pileup events. To account for possible residual effects a 5% uncertainty on the associated minimum bias cross section was propagated to the final prediction by reweighting the simulated samples. The reweighting procedure follows the recommendations of the responsible CMS working group.

Background cross sections

The background estimation procedure described in this thesis is designed to provide an estimate of the \cancel{E}_T spectrum from $t\bar{t}$ production, which is the dominant background, accounting also for contributions due to W +jets production. The possible influence of other subleading backgrounds, unexpected deviations of the background composition due to tau leptons or feed down from dileptonic decays, as well as uncertainties related to the $W+b\bar{b}$ cross section are tested by:

- varying the cross sections for $t\bar{t}$ and W +jets by 30%,
- varying the contributions of events with a tau lepton or with two leptons by 15%,
- increasing the cross section for $W+b\bar{b}$ production by 100% and
- varying the cross sections of all other non-leading backgrounds by 30%.

The highest impact on the prediction is observed when varying the cross section for $W+b\bar{b}$ production, with relative changes smaller than 3%.

\cancel{E}_T model

The parameter β of the Pareto distribution, controlling the tails of the \cancel{E}_T distribution, is varied by ± 0.047 according to the maximum difference between data and simulation, observed in control regions at lower jet multiplicity as described in Sec. 3.4.5. As expected, the resulting variation of the background prediction is relatively small for $250 < \cancel{E}_T < 350$ GeV, but becomes one of the leading systematic uncertainties for high \cancel{E}_T .

Error functions

In order to account for uncertainties arising from the assumption of a linear evolution of the parameters of the error functions with H_T (Eq. 3.14), we introduce additional parameters μ_2 and σ_2^2 , describing a possible non-linearity (Eq. 3.16). The result of a likelihood fit confirms the compatibility with the linear hypothesis. The uncertainties on the nonlinearity parameters are propagated through the background estimation and the change in prediction is taken as systematic uncertainty. Since μ_2 and σ_2^2 are correlated in the fit, they are not varied independently, but along the eigenvectors of the covariance matrix estimated from the shape of the likelihood minimum, denoted as EV_0 and EV_1 in Tab. 3.13.

A second uncertainty, due to possible differences of the error-function parameters (Tab. 3.7) between data and simulation in the 6-jet selection, is evaluated based on the difference of the same parameters, estimated by fits to data and simulation in a ≥ 4 -jet control region, as described in Sec. 3.4.2.

Closure

Conservatively, an additional systematic uncertainty is assigned based on the application of the method to simulation. It is determined by the maximum of the relative difference between prediction and true value (relative to the prediction) and the uncertainty on this quantity.

A summary of all systematic uncertainties for $400 < H_T < 750$ GeV, $H_T > 750$ and $H_T > 1000$ GeV is given in Tab. 3.13. The first of these H_T regions overlaps with the control region and is therefore not considered as a signal region in the 2 b -tag selection. It is only relevant for the background prediction in the ≥ 3 b -tag category, described in the following section. The upwards and downwards variations are typically almost symmetric, therefore the average of their absolute size has been used in order to decrease the effect of statistical fluctuations. The signs of the uncertainties in Tab. 3.13 indicate the relative directions of the variations and determine whether these uncertainties are assumed to be correlated or anti-correlated along different E_T bins in the limit-setting procedure (see Sec. 4.2).

The dominant contributions are due to uncertainties on the E_T model (≈ 1 –35%, depending on the H_T and E_T bin) and on closure (≈ 6 –40%).

Table 3.13.: Systematic uncertainties for the background estimation in different E_T regions defined for $400 < H_T < 750$ GeV, $750 < H_T < 2500$ GeV and $1000 < H_T < 2500$ GeV. The signs shown with the values are only relevant within each row, where they indicate the relative direction of the variations in different E_T bins.

	H_T	750–2500 GeV			1000–2500 GeV			
	E_T	250–2500 GeV	250–350 GeV	350–450 GeV	450–2500 GeV	250–350 GeV	350–450 GeV	450–2500 GeV
SF _{light}		0.1%	0.1%	0.2%	0.4%	0.1%	0.2%	0.4%
SF _{b,c}		0.3%	0.5%	0.5%	0.7%	0.7%	0.3%	0.8%
dilep. background		0.3%	<0.1%	-0.3%	0.6%	-0.9%	-0.1%	0.5%
JES		-0.5%	1.0%	0.4%	-4.9%	2.7%	2.6%	3.8%
tau background		-0.2%	0.7%	-0.1%	-0.1%	0.1%	0.2%	0.4%
μ efficiency ₁		0.3%	-0.4%	-0.2%	-0.8%	<0.1%	0.4%	-0.9%
μ efficiency ₂		-0.1%	<0.1%	<0.1%	0.1%	<0.1%	-0.1%	0.1%
e efficiency		-0.8%	0.5%	0.1%	1.5%	-0.1%	-0.8%	1.8%
W polarization		-0.1%	0.1%	-0.4%	-0.6%	0.1%	-0.3%	-0.9%
$t\bar{t}$ cross sec.		<0.1%	<0.1%	1.0%	-1.4%	-0.9%	1.5%	-0.7%
$W+b\bar{b}$ cross sec.		-0.2%	-0.4%	1.1%	2.6%	0.8%	1.4%	2.7%
W +jets cross sec.		0.5%	0.4%	0.4%	0.6%	0.1%	<0.1%	<0.1%
non-lead. cross sec.		-0.8%	0.5%	0.3%	0.1%	0.5%	0.4%	0.1%
pileup		-0.6%	-1.6%	0.2%	-2.4%	-1.9%	1.0%	-2.6%
E_T model ($\Delta\beta$)		-1.1%	-1.4%	7.8%	33.0%	-1.3%	8.0%	35.4%
ert nonlin. EV ₀		0.6%	-0.6%	-0.9%	-1.4%	-1.5%	-2.5%	-3.2%
ert nonlin. EV ₁		0.2%	-0.1%	-0.3%	-0.8%	-0.2%	-0.6%	-1.1%
ert data/MC		-1.7%	1.8%	4.2%	6.3%	-0.5%	1.1%	4.7%
closure		-8.9%	8.5%	27.0%	33.7%	11.9%	29.6%	42.9%

3.4.7. Background estimation in the ≥ 3 b -tag category

The previous sections describe the estimation of the SM background in signal regions at high H_T and \cancel{E}_T , for events with exactly two b -tagged jets. This section explains the methods to extrapolate this estimates to signal regions defined by ≥ 3 b -tagged jets. The ≥ 3 b -tag requirement reduces the SM background further, while retaining efficiency for our reference signals that are characterized by four b -quark jets in the final state.

The data-sample size in the ≥ 3 b -tag category is too small to estimate the \cancel{E}_T -model parameters in the same way as for the 2 b -tag case. Furthermore, the strong suppression of SM backgrounds would result in substantial signal contamination of control and normalization regions, in case these regions were defined in a similar manner as for the 2 b -tag category.

Therefore, the background for high b -tag multiplicities is estimated using “2 $\rightarrow \geq 3$ ” b -tag translation factors, referred to as R_{32} . On top of the extrapolation of the existing 2 b -tag signal regions to their ≥ 3 b -tag equivalents, R_{32} factors allow to define additional signal regions in the ≥ 3 b -tag bin at low H_T and/or low \cancel{E}_T as shown in Fig. 3.17(b). In the 2 b -tag category, these low H_T - \cancel{E}_T regions are used to fit or normalize the \cancel{E}_T model for the prediction of background event yields. Simultaneously, these regions can serve as a basis for a prediction in the ≥ 3 b -tag category. Of course, this introduces a correlation of the statistical uncertainties on the background predictions in both b -tag categories that is accounted for in the limit setting procedure later on.

The central values for the R_{32} factors are determined from simulation. In order to use the full statistical power of the simulation, the factors are calculated from the same combinatorial weights that have already been defined in Eq. 3.19, to correct the b -tag multiplicity templates in Sec. 3.4.3, as well as for the evaluation of the systematic uncertainties related to b -tagging efficiencies in Sec. 3.4.6. We then determine $R_{32} = \sum_i P_i(\geq 3|n_{jets}) / \sum_i P_i(2|n_{jets})$, where the sums extend over all simulated events in a given selection. This procedure reduces the statistical fluctuations, at the expense of a correlation between nominator and denominator. In order to estimate the statistical error on R_{32} in the presence of this correlation we apply a “jackknife” resampling method (see e.g. [119]).

Figure 3.37 shows the R_{32} factors as a function of H_T , for different bins of jet multiplicity, including the effects of the data/simulation b -tagging scale factors. Naturally, the probability to misidentify one or more jets increases with the jet multiplicity, but the scale factors do not show a strong dependence on H_T . Data is shown for comparison, for low jet multiplicities.

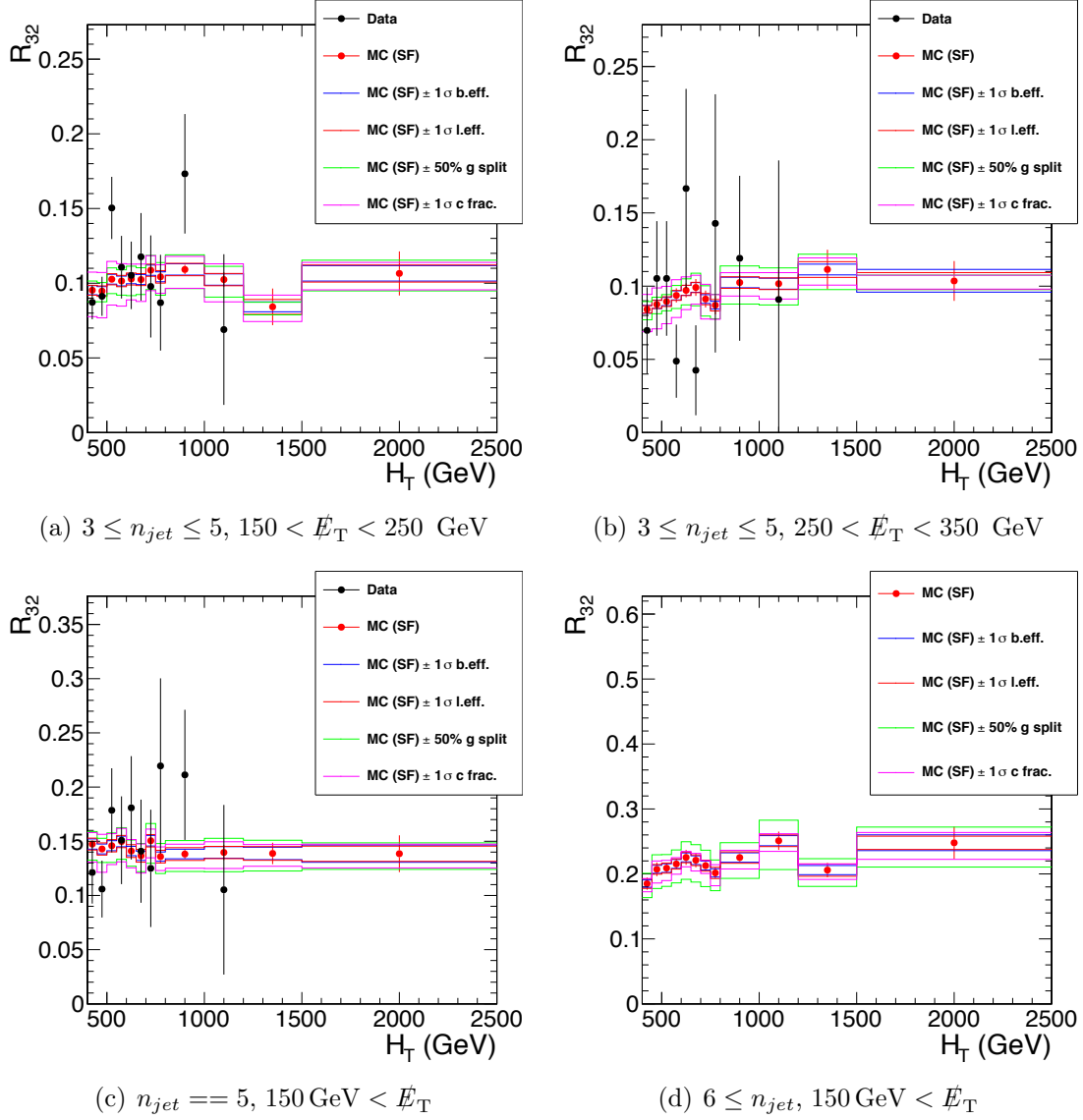


Figure 3.37.: The ≥ 3 b -tag to 2 b -tag scale factors R_{32} for events with (a) $3 \leq n_{jet} \leq 5$ and $150 < \cancel{E}_T < 250$ GeV, (b) $3 \leq n_{jet} \leq 5$ and $250 < \cancel{E}_T < 350$ GeV, (c) $n_{jet} = 5$ and $150 \text{ GeV} < \cancel{E}_T$ and (d) $6 \leq n_{jet}$ and $150 \text{ GeV} < \cancel{E}_T$. The values obtained from simulation are indicated by red symbols and include the data/simulation scale factors for b -tag efficiencies and misidentification rates. The uncertainties on the b -tag scale factors for heavy and light partons and the effect of changes in the c -quark content of the sample and of the $g \rightarrow b\bar{b}$, $c\bar{c}$ rate are indicated as bands around the symbols. For the selections with jet multiplicities smaller than 6 jets, the ratios obtained on data are shown as black symbols.

Table 3.14.: Systematic uncertainties for the impact of residual differences in the kinematics of light jets.

H_T range	400–2500 GeV	750–2500 GeV	1000–2500 GeV
$150 < \cancel{E}_T < 250$ GeV	0.1%	0.3%	4.6%
$250 < \cancel{E}_T < 350$ GeV	0.4%	0.4%	4.5%
$350 < \cancel{E}_T < 450$ GeV	1.5%	1.7%	15%
$450 < \cancel{E}_T < 2500$ GeV	16%	16%	16%

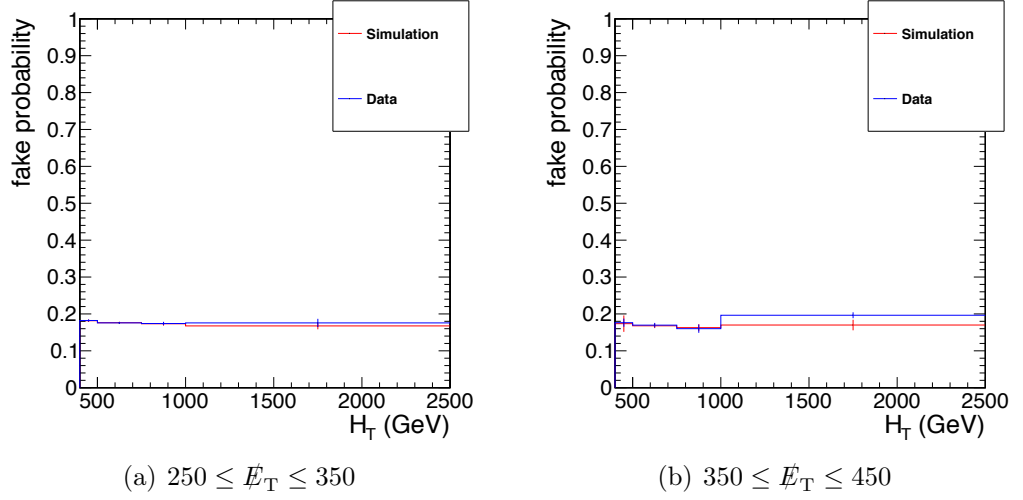


Figure 3.38.: Data/MC comparison of the estimation of the probability to find a third b -jet in the event for (a) $250 \leq \cancel{E}_T \leq 350$ GeV and (b) $350 \leq \cancel{E}_T \leq 450$ GeV and $3 \leq n_{jets} \leq 5$.

The effects of several experimental and theoretical uncertainties on R_{32} are visualized in Fig 3.37. These are estimated in the following way.

- The b -tagging (data/simulation) scale factors for the efficiencies and misidentification rates are varied according to the recommendations of the b -tagging working group of the CMS collaboration. (using the same scale factor uncertainties that have already been applied in Sec. 3.4.6).
- The c -quark fraction is varied by 50%. The size of the variation is motivated by the uncertainty, obtained from a fit of CSV-discriminator distributions of b -, c -, and light-quarks to data. Since most c -quarks in the events under consideration originate from the hadronically decaying W bosons from top quark decays, this estimate is conservative.
- Changes in the true heavy-quark content of the events are evaluated by varying the rate of gluon splitting to $b\bar{b}$ and $c\bar{c}$ by 50%. Events that are considered for this reweighting procedure either have a generated b - or c -quark stemming from a

gluon, more than two reconstructed jets matched to a b -parton or a reconstructed jet matched to a c -parton, excluding those from W decays. The variation of 50% coincides with the variation used by the b -tagging working group in the evaluation of systematic uncertainties on the data/simulation scale factors.

- Possible effects from differences in the characteristics of the system of light-quark jets between data and simulation, are tested in a data-driven way. Using events from data with two b -tagged jets, parton flavors are randomly assigned to all remaining jets. One jet is marked as a c -quark jet and all others are treated as light-quark jets. Based on this assignment, the R_{32} factor is reevaluated. This procedure can also be applied to simulation. The results are shown as a function of H_T in Fig. 3.38 for two example \cancel{E}_T regions in a control region defined by $3 \leq n_{jets} \leq 5$. The good agreement between data and simulation indicates that any residual differences in the light-jet system have little impact on R_{32} and the resulting uncertainties are shown in Tab. 3.14.

The total uncertainties from these sources on R_{32} add to $\sim 9\%$ -19% for the different signal regions.

A further check for additional sources of heavy flavor decays, which could change R_{32} in data with respect to the expectation from simulation, uses a control sample based on the single lepton triggers HLT_IsoMu24_eta2p1 and HLT_Ele27_WP80, requiring exactly 5 or ≥ 6 jets. The transverse momentum of the lepton must exceed 30 GeV and the H_T and \cancel{E}_T requirements are $0 < H_T < 400$ GeV and $100 < \cancel{E}_T < 250$ GeV. Thereby, this control regions do not overlap with any other region defined for this analysis. For ≥ 6 jets, we measure $R_{32} = 16/68 = 0.235 \pm 0.065(\text{stat.})$ in data, to be compared to a value from simulation of $R_{32} = 0.195 \pm 0.013(\text{stat.}) \pm 0.022(g\text{-split.}) \pm 0.006(\text{SF}_b) \pm 0.007(\text{SF}_l)$. The result in the 5 jet category is $R_{32} = 135/856 = 0.158 \pm 0.015(\text{stat.})$ for data and $R_{32} = 0.142 \pm 0.003(\text{stat.}) \pm 0.011(g\text{-split.}) \pm 0.005(\text{SF}_b) \pm 0.005(\text{SF}_l)$ for simulation. The values obtained from data and simulation are compatible within 1σ of the statistical uncertainty.

On top of the statistical and systematic uncertainties on R_{32} , the statistical and systematic uncertainties on the predictions in the 2 b -tag category are propagated to the ≥ 3 b -tag signal regions and treated fully correlated. For the new signal regions in the ≥ 3 b -tag category that correspond to the normalization region of the 2 b -tag category ($150 < \cancel{E}_T < 250$ GeV), no systematic uncertainties related to the 2 b -tag category have to be taken into account, since the estimate is directly based on the observed event count.

Results from the application of the procedure described in this section on simulation, are summarized in Tab. 3.15, where the uncertainties on the predictions contain all contributions from systematic sources that might influence R_{32} , as well as the statistical uncertainties of the predictions in the 2 b -tag category. Systematic uncertainties obtained in the 2 b -tag category are not included in this table, but are of course accounted for in the limit setting procedure later on. Since the same events from simulation were used for the prediction, as well as for the determination of the R_{32} factors, the quoted uncertainties should not be used to judge the closing of the method.

Table 3.15.: Predicted and true event counts in simulation for different \cancel{E}_T and H_T signal regions and for ≥ 3 b-tags. Note that the prediction is obtained from the same simulated sample which is also used for the determination of R_{32} . Uncertainties on the event yields from simulation are statistical, the uncertainties on the prediction include the uncertainties on R_{32} as well as the statistical uncertainty from the 2 b -tag category.

≥ 3 b-tags	$400 < H_T < 2500$ GeV					
	MC truth			MC pred.		
$150 < \cancel{E}_T < 250$ GeV	105.98	\pm	2.14	104.35	\pm	16.26
$250 < \cancel{E}_T < 350$ GeV	16.86	\pm	0.82	17.27	\pm	2.89
$350 < \cancel{E}_T < 450$ GeV	3.22	\pm	0.35	3.01	\pm	0.73
$450 < \cancel{E}_T < 2500$ GeV	0.85	\pm	0.16	0.84	\pm	0.23
≥ 3 b-tags	$750 < H_T < 2500$ GeV					
	MC truth			MC pred.		
$150 < \cancel{E}_T < 250$ GeV	40.35	\pm	1.26	39.31	\pm	5.91
$250 < \cancel{E}_T < 350$ GeV	10.09	\pm	0.67	10.36	\pm	1.83
$350 < \cancel{E}_T < 450$ GeV	2.42	\pm	0.31	2.23	\pm	0.47
$450 < \cancel{E}_T < 2500$ GeV	0.85	\pm	0.16	0.75	\pm	0.21
≥ 3 b-tags	$1000 < H_T < 2500$ GeV					
	MC truth			MC pred.		
$150 < \cancel{E}_T < 250$ GeV	13.68	\pm	0.77	13.39	\pm	2.18
$250 < \cancel{E}_T < 350$ GeV	4.35	\pm	0.47	4.35	\pm	0.91
$350 < \cancel{E}_T < 450$ GeV	1.11	\pm	0.20	1.05	\pm	0.30
$450 < \cancel{E}_T < 2500$ GeV	0.65	\pm	0.15	0.53	\pm	0.15

4. Results and interpretation

4.1. Summary of predicted and measured event yields

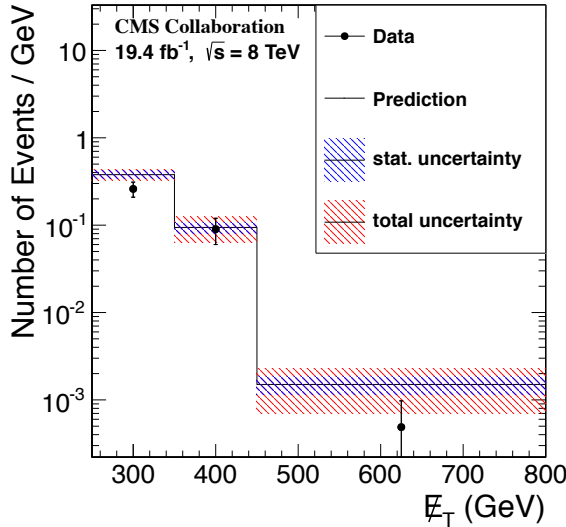
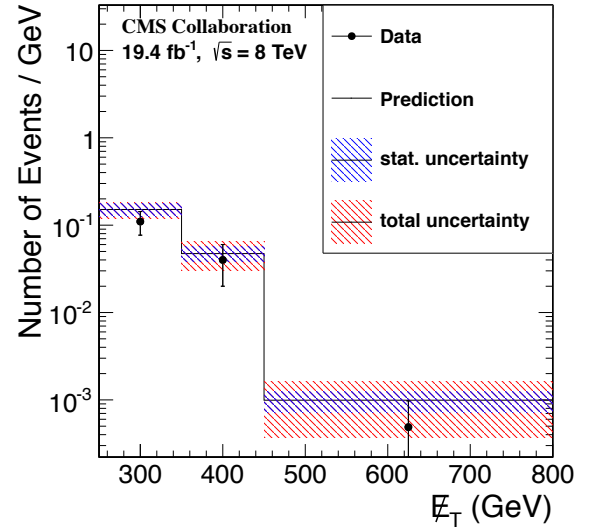
Final predictions for the SM background in each signal region are summarized in Tab. 4.1 for the 2 b -tag category and in Tab. 4.2 for ≥ 3 b -tags, together with the observed event yields in data. While the background predictions for the 2 b -tag signal regions are obtained from the fit of the \cancel{E}_T model to data in control regions as described in Sec. 3.4.1, the predicted background yields for the ≥ 3 b -tag signal regions result from extrapolating the 2 b -tag results, using the R_{32} factors described in Sec. 3.4.7. The quoted uncertainties on the background prediction are split into three contributions. The statistical uncertainty is determined by the number of events in the control and normalization regions. The systematic uncertainty includes all contributions described in the previous sections, excluding the uncertainties related to b -tagging, which are shown separately. All results that are summarized in the tables are also visualized in Fig. 4.1 and Fig. 4.2. A collection of tables and plots with a finer binning in \cancel{E}_T can be found in App. D. No significant excess of events beyond the SM prediction can be observed for any of the signal regions.

Table 4.1.: Predicted and measured event counts in data for the 2 b -tag signal regions.

2 b -tag	750 < H_T < 2500 GeV						
	obs.	pred.	stat.	b-tag	sys.	total	
250 < \cancel{E}_T < 350 GeV	26	37.87	± 4.04	± 0.21	± 3.44	± 5.31	
350 < \cancel{E}_T < 450 GeV	9	9.42	± 1.43	± 0.06	± 2.68	± 3.04	
450 < \cancel{E}_T < 2500 GeV	1	3.08	± 0.71	± 0.03	± 1.48	± 1.64	
2 b -tag	1000 < H_T < 2500 GeV						
	obs.	pred.	stat.	b-tag	sys.	total	
250 < \cancel{E}_T < 350 GeV	11	15.12	± 2.46	± 0.11	± 1.91	± 3.11	
350 < \cancel{E}_T < 450 GeV	4	4.73	± 0.92	± 0.02	± 1.47	± 1.73	
450 < \cancel{E}_T < 2500 GeV	1	2.03	± 0.54	± 0.02	± 1.14	± 1.27	

Table 4.2.: Predicted and measured event counts in data for the ≥ 3 b -tag signal regions.

≥ 3 b-tag	$400 < H_{\text{T}} < 2500$ GeV											
	obs.		pred.		stat.		b-tag		sys.		total	
$150 < \cancel{E}_{\text{T}} < 250$ GeV	94	92.46	\pm	4.50	\pm	14.38	\pm	1.42	\pm	15.14		
$250 < \cancel{E}_{\text{T}} < 350$ GeV	16	14.54	\pm	1.27	\pm	2.32	\pm	1.00	\pm	2.83		
$350 < \cancel{E}_{\text{T}} < 450$ GeV	2	2.55	\pm	0.38	\pm	0.56	\pm	0.49	\pm	0.83		
$450 < \cancel{E}_{\text{T}} < 2500$ GeV	0	0.77	\pm	0.18	\pm	0.16	\pm	0.34	\pm	0.42		
≥ 3 b-tag	$750 < H_{\text{T}} < 2500$ GeV											
	obs.		pred.		stat.		b-tag		sys.		total	
$150 < \cancel{E}_{\text{T}} < 250$ GeV	37	31.82	\pm	2.68	\pm	4.76	\pm	0.56	\pm	5.50		
$250 < \cancel{E}_{\text{T}} < 350$ GeV	12	8.54	\pm	0.91	\pm	1.40	\pm	0.77	\pm	1.84		
$350 < \cancel{E}_{\text{T}} < 450$ GeV	2	1.90	\pm	0.29	\pm	0.33	\pm	0.54	\pm	0.70		
$450 < \cancel{E}_{\text{T}} < 2500$ GeV	0	0.68	\pm	0.16	\pm	0.15	\pm	0.32	\pm	0.39		
≥ 3 b-tag	$1000 < H_{\text{T}} < 2500$ GeV											
	obs.		pred.		stat.		b-tag		sys.		total	
$150 < \cancel{E}_{\text{T}} < 250$ GeV	14	11.14	\pm	1.64	\pm	1.80	\pm	0.35	\pm	2.46		
$250 < \cancel{E}_{\text{T}} < 350$ GeV	4	3.60	\pm	0.58	\pm	0.67	\pm	0.46	\pm	1.00		
$350 < \cancel{E}_{\text{T}} < 450$ GeV	1	0.91	\pm	0.18	\pm	0.23	\pm	0.28	\pm	0.40		
$450 < \cancel{E}_{\text{T}} < 2500$ GeV	0	0.47	\pm	0.13	\pm	0.10	\pm	0.27	\pm	0.31		

(a) 2 b -tags, $750 < H_T < 2500$ GeV(b) 2 b -tags, $1000 < H_T < 2500$ GeVFigure 4.1.: Predicted and measured event counts in data for the 2 b -tag signal regions (a) $750 < H_T < 2500$ GeV and (b) $1000 < H_T < 2500$ GeV.

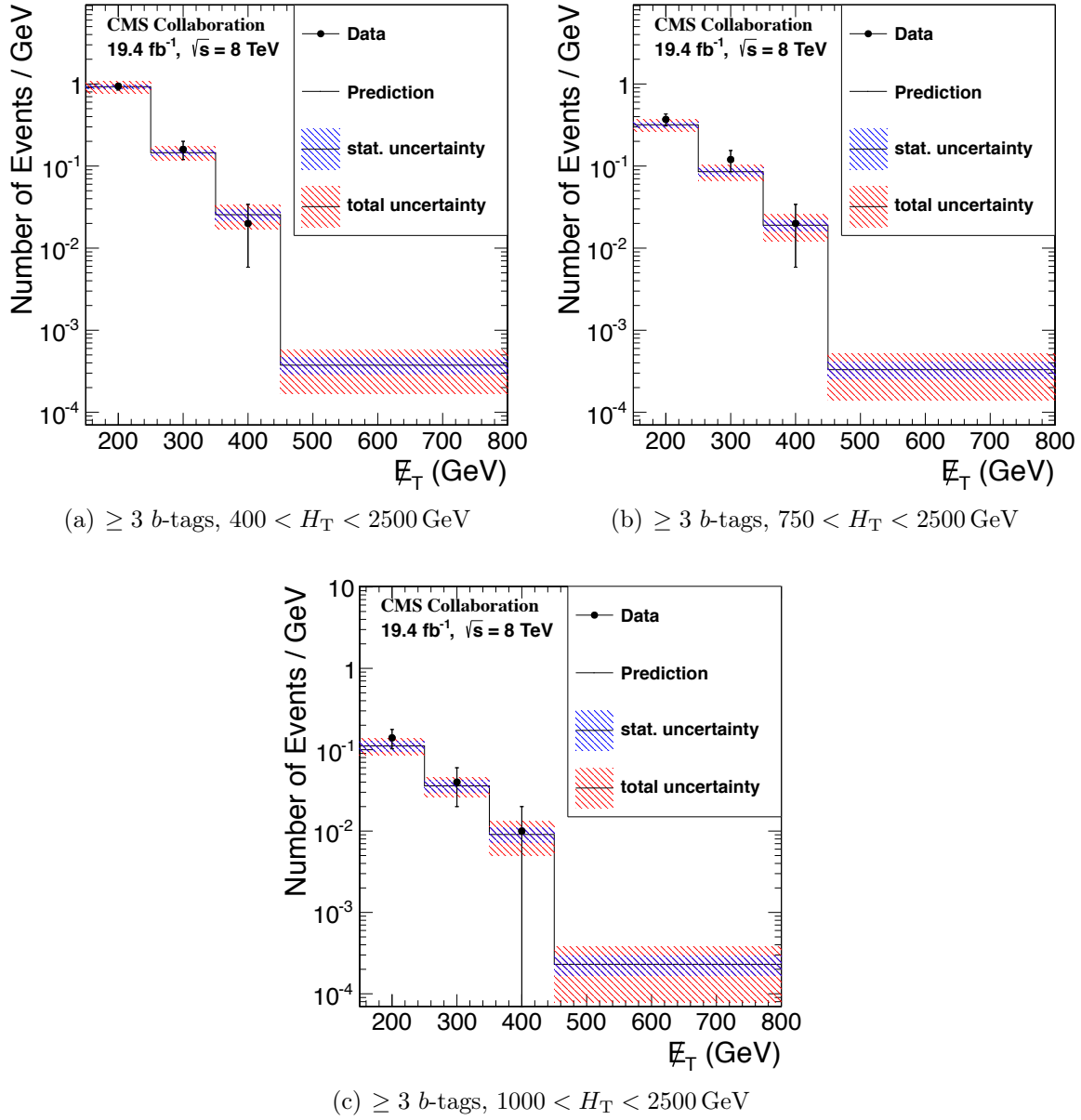


Figure 4.2.: Predicted and measured event counts in data for the ≥ 3 b -tag signal regions (a) $400 < H_T < 2500$ GeV, (b) $750 < H_T < 2500$ GeV and (c) $1000 < H_T < 2500$ GeV.

4.2. Interpretation in terms of simplified models

In order to interpret these results, the compatibility between observed and predicted event counts is used to set upper limits on the production cross section of three simplified models which were already introduced in Sec. 1.2.7. All three models describe pair production of gluinos. Each gluino decays to a final state with two top quarks and a neutralino via a top squark ($\tilde{g} \rightarrow t\bar{t}\tilde{\chi}^0$). While gluinos decay via virtual top squarks in the model T1ttttt (Fig. 1.5(a)), where $m_{\tilde{g}}$ and $m_{\tilde{\chi}^0}$ are free parameters, the gluino decays in the models T1t1t and T5ttttt are restricted to on-shell top squarks (Fig. 1.5(a)), thus top squarks must be lighter than the gluino ($\tilde{g} \rightarrow t\tilde{t} \rightarrow t\bar{t}\tilde{\chi}^0$). This permits to introduce $m_{\tilde{t}}$ as free parameter in these models. The second parameter in T1t1t is $m_{\tilde{\chi}^0}$ and $m_{\tilde{g}}$ is fixed to 1 TeV while T5ttttt has $m_{\tilde{g}}$ as second parameter and $m_{\tilde{\chi}^0} = 50$ GeV.

4.2.1. Observed and expected limits

Upper limits on the production cross section as function of the free masses are derived using the modified-frequentist CL_S method [120, 121, 122] with a one-sided profile likelihood test statistic following the recommendations of the LHC Higgs Combination Group [123].

Two kinds of limits are calculated as explained in the following paragraphs. The expected limit illustrates the potential reach under the background-only hypothesis, based on the integrated luminosity, the signal acceptance and efficiency, as well as all uncertainties related to background and signal, whereas the observed limit reflects the full information that can be obtained from the measured event counts.

The procedure to obtain the observed limit is based on the likelihood function

$$\mathcal{L}(n|\mu, \boldsymbol{\theta}) = \text{Poisson}(n|\mu \cdot s(\boldsymbol{\theta}) + b(\boldsymbol{\theta})) \cdot p(\tilde{\boldsymbol{\theta}}|\boldsymbol{\theta}), \quad (4.1)$$

where “Poisson” denotes the product over Poisson probabilities for each signal region with the observed event count n . The parameter μ is called signal strength modifier and scales the expected signal rate $s(\boldsymbol{\theta})$, which is extracted at each mass point of a simplified model scan. The signal rate is scaled to the observed integrated luminosity using the NLO + NLL gluino-pair production cross section and corrected to account for differences between lepton or trigger efficiencies in data and fast simulation. The predicted SM background yield is denoted as $b(\boldsymbol{\theta})$. Signal and background rates are functions of the nuisance parameters $\boldsymbol{\theta}$, which are introduced to model the corresponding uncertainties. The likelihood $p(\tilde{\boldsymbol{\theta}}|\boldsymbol{\theta})$ can be interpreted as the probability for a measurement $\tilde{\boldsymbol{\theta}}$ given true nuisance parameters $\boldsymbol{\theta}$ and is used as a constraint. Each nuisance parameter, reflecting an uncertainty, is assumed to be log-normal distributed, except for the statistical uncertainty from the normalization of the \cancel{E}_T model where a Poisson distribution is used.

The test statistic \tilde{q}_μ is given by the likelihood ratio

$$\tilde{q}_\mu = \frac{\mathcal{L}(n|\mu, \hat{\boldsymbol{\theta}}_\mu)}{\mathcal{L}(n|\hat{\mu}, \hat{\boldsymbol{\theta}})}, \quad \text{with } 0 \leq \hat{\mu} \leq \mu. \quad (4.2)$$

The profiled likelihood estimate of $\boldsymbol{\theta}$ for a given signal strength modifier μ is denoted by $\hat{\boldsymbol{\theta}}_\mu$, while the likelihood estimates $\hat{\mu}$ and $\hat{\boldsymbol{\theta}}$ follow from the global maximum of $\mathcal{L}(n|\mu, \boldsymbol{\theta})$. In a first step, the observed value of the test statistic $\tilde{q}_\mu^{\text{obs}}$ is calculated. Additionally, the sets of nuisances, $\hat{\boldsymbol{\theta}}_0^{\text{obs}}$ and $\hat{\boldsymbol{\theta}}_\mu^{\text{obs}}$ that provide the best description of the data in case of the background-only or the signal+background hypothesis, are determined by maximizing Eq. 4.1. Using these values, the distribution of the test statistic $f(\tilde{q}_\mu)$ under the two hypotheses can be constructed by Monte Carlo sampling. In case of the background-only hypotheses, μ is set to zero for generating pseudo data, but not for evaluating \tilde{q}_μ . The probabilities to observe $\tilde{q}_\mu \geq \tilde{q}_\mu^{\text{obs}}$ follow from

$$\begin{aligned} \text{CL}_{\text{s+b}}(\mu) &= \int_{\tilde{q}_\mu^{\text{obs}}}^{\infty} f(\tilde{q}_\mu|\mu, \hat{\boldsymbol{\theta}}_\mu^{\text{obs}}) d\tilde{q}_\mu \\ \text{CL}_{\text{b}}(\mu) &= \int_{\tilde{q}_\mu^{\text{obs}}}^{\infty} f(\tilde{q}_\mu|0, \hat{\boldsymbol{\theta}}_0^{\text{obs}}) d\tilde{q}_\mu, \end{aligned} \quad (4.3)$$

and $\text{CL}_{\text{s}}(\mu)$ is defined as the ratio of these two probabilities

$$\text{CL}_{\text{s}}(\mu) = \frac{\text{CL}_{\text{s+b}}(\mu)}{\text{CL}_{\text{b}}(\mu)}. \quad (4.4)$$

In case $\text{CL}_{\text{s}}(\mu) \leq \alpha$, a signal of strength μ is said to be excluded at a $(1 - \alpha)$ confidence level (CL). To find the signal strength that can be excluded at a 95% confidence level, μ is adjusted until $\text{CL}_{\text{s}}(\mu) \leq 0.05$.

To obtain the expected limit, a large pseudo-dataset of event counts under the background-only hypothesis $\mu = 0$ is generated, using Eq. 4.1. The distribution of the test statistic does not depend on the pseudo-data and has to be generated only once. Only the probabilities $\text{CL}_{\text{s+b}}(\mu)$ and $\text{CL}_{\text{b}}(\mu)$ have to be evaluated for each trial to determine $\mu^{95\%}$. The expected limit follows from the median of the distribution of $\mu^{95\%}$ over all trials and the 16% and 84% quantiles give the width of the $\pm 1\sigma$ experimental uncertainty.

4.2.2. Signal contamination

The predictions of the SM background from the fit of the \tilde{E}_{T} model could be affected by a possible contribution of a signal to the normalization or control regions. The size of the effect depends on the branching ratios and the cross section of the signal, which vary strongly as function of the mass parameters. In order to evaluate the signal contamination with a focus on the vicinity of the expected limit, we reweight the signal events at each point of the mass plane to the production cross section for a gluino mass

$m_{\tilde{g}} = 1100 \text{ GeV}$, i.e. by a factor $k = \sigma(m_{\tilde{g}} = 1100 \text{ GeV})/\sigma(m_{\tilde{g}})$, except for **T1t1t**, where the gluino mass is always fixed to 1 TeV. The effect of the signal contamination on the prediction is evaluated by repeating the full background estimation procedure on a simulated sample that includes the signal for the respective point of the mass plane. The change in prediction is quantified by $c = (N'/N - 1)/k$.

In the limit calculation, the contamination is taken into account by modifying the expected number of events for the signal+background hypothesis (at the nominal reference cross section) from $\mu \cdot s + b$ to $\mu \cdot s + b - (\mu c)/(1 + \mu c)b$. This procedure assures a reliable estimation of the signal contamination over the whole mass plane because it does not directly refer to the steeply falling reference cross section. We find that a contamination of 10% has no significant effect on the expected limit.

The size $N'/N - 1$ of the signal contamination evaluated for all models and signal regions is summarized in App. E.1.

4.2.3. Treatment of uncertainties and their correlations

All limits are calculated in a multichannel approach using 2 and ≥ 3 b -tag signal regions simultaneously. Several uncertainties related to the background predictions and the signal yields are correlated among these regions. This has to be taken into account in the limit setting.

For both b -tag categories, only the signal regions defined by $H_T > 750 \text{ GeV}$ are used with \cancel{E}_T -bin boundaries of 250 GeV, 350 GeV, 450 GeV, 2500 GeV. For ≥ 3 b -tags, also the signal regions limited by $400 < H_T < 750 \text{ GeV}$ are included. Since there are very few events predicted for $H_T \leq 750 \text{ GeV}$ and high \cancel{E}_T , the \cancel{E}_T regions above $\cancel{E}_T > 250 \text{ GeV}$ are collapsed to a single region, in order to evade large statistical uncertainties on the estimates of the systematic uncertainties. The $H_T > 1000 \text{ GeV}$ signal regions do not improve the expected limit, thus these regions are omitted.

The alignment of the 2 and ≥ 3 b -tag signal regions in H_T and \cancel{E}_T is helpful, since correlations of uncertainties must either be 100% or zero in the limit setting procedure. Moreover, aligned regions are desirable since this keeps the correlation pattern. Figure 3.17 illustrates the signal regions. The following uncertainties are taken into account for the limit setting:

- **Background prediction:** In both b -jet categories the statistical uncertainties on the background consist of two components. The statistical fluctuations of the normalization regions are modeled as Poisson distributions. They are fully correlated between the b -tag categories and the \cancel{E}_T bins while they are fully uncorrelated for different H_T bins.

To describe the second component of statistical uncertainty, related to the \cancel{E}_T model parameters, log-normal distributions are used. The correlations between these uncertainties between different signal regions are taken into account by a Cholesky decomposition of the 6-dimensional covariance matrix of the predicted

yields across all signal regions, which is calculated from the output of the sampling procedure described in Sec. 3.4.5.

Furthermore, all systematic uncertainties on the background prediction, listed in Sec. 3.4.6, are modeled as log-normal distributions. They are correlated or anti-correlated between the signal regions, depending on the signs in Tab. 3.13. For uncertainties related to the tagging efficiencies for heavy and light flavors, the correlation between the 2 and ≥ 3 b-tag category was taken into account as well.

- **Signal yields:** As already stated in Sec. 3.2, the uncertainty on the integrated luminosity was found to be 4.4%. The trigger, lepton reconstruction and identification efficiencies for data and fast simulation (FASTSIM) are summarized in Sec. 3.3.3. For each model point, an uncertainty on the total predicted yield was attributed, based on the quoted uncertainties for the data/fast simulation scale factors.

Uncertainties on the jet and \cancel{E}_T scales, as well as on the number of pileup vertices, are evaluated as a function of the model parameters, following the prescription in Sec. 3.4.6 and are treated fully correlated with the corresponding uncertainties on the background prediction and between b -tag, H_T and \cancel{E}_T bins. The effect of variations in the b -tagging efficiency on the yield is also taken to be fully correlated with the corresponding uncertainties of the background prediction. Furthermore the impact of initial-state radiation (ISR) is evaluated using a reweighting prescription, which involves the transverse momentum of the $\tilde{g}\tilde{g}$ system.

Finally, for evaluating the uncertainty due to the parametrization of the parton distribution functions, we employed Eq. 3 and Eq. 4 of [124] using the maximum deviations in the three sets CTEQ66, MSTW2008nlo68cl and NNPDF20 from a total of 181 different PDF weights. The uncertainties related to the parton distribution functions are sizable for model points with compressed spectra, but low if the predicted amount of visible energy is high.

Typical values for the total systematic uncertainty on the signal yield vary from 10–20% in a large part of the parameter regions to 60–70% for mass combinations with small mass differences between the gluino and the neutralino in the T1tttt model, and for high top squark and neutralino masses in T1t1t. A summary of signal efficiencies and their relative uncertainties can be found in App. E.

4.2.4. Limits

The 95% confidence upper limit on the production cross section is depicted in Fig. 4.3 as a function of the two mass parameters $m_{\tilde{g}}$ and $m_{\tilde{\chi}^0}$ of T1tttt. The observed (expected) mass limit based on a reference NLO+NLL gluino-pair production cross section is also included, together with the theoretical (experimental) uncertainties.

For $T1tttt$, the top squark mass does not enter the limit, since it is decoupled. The dependence of the limit on $m_{\tilde{t}}$ and $m_{\tilde{\chi}^0}$ is therefore shown in Fig. 4.4(a) for the topology $T1t1t$, where $m_{\tilde{g}}$ is fixed to 1 TeV. For high values of $m_{\tilde{t}}$, the limit approaches the $T1tttt$ limit for $m_{\tilde{g}} = 1$ TeV, as required by consistency. In Fig. 4.4(b), $m_{\tilde{\chi}^0}$ is fixed to 50 GeV and the limit is shown as a function of $m_{\tilde{g}}$ and $m_{\tilde{t}}$ ($T5tttt$). Again, for high values of $m_{\tilde{t}}$ the limit approaches the $T1tttt$ result for the appropriate value $m_{\tilde{\chi}^0} = 50$ GeV.

From Fig. 4.3 it follows that for a high mass splitting between gluino and neutralino, a gluino mass below 1.2 TeV can be excluded in case the neutralino mass is smaller than 300 GeV, while in case of low mass splittings and a neutralino mass above 300 GeV, a gluino mass as low as 600 GeV is still allowed. Figure 4.4(b) also indicates that gluino masses down to 1 TeV are still allowed for the case of light neutralino and light top squark masses.

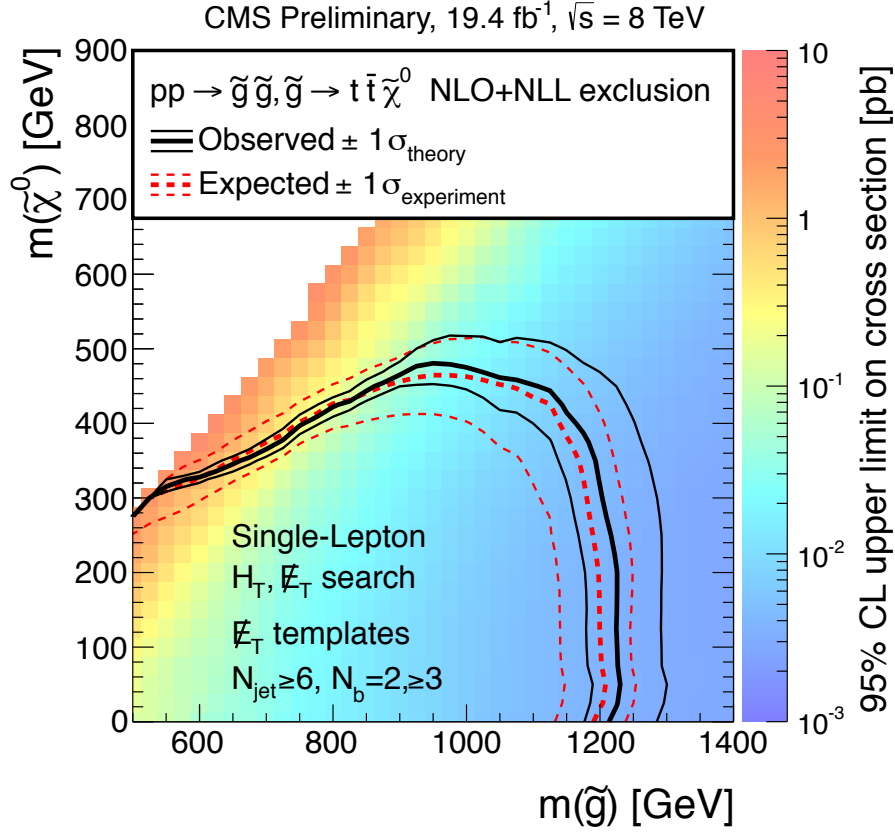
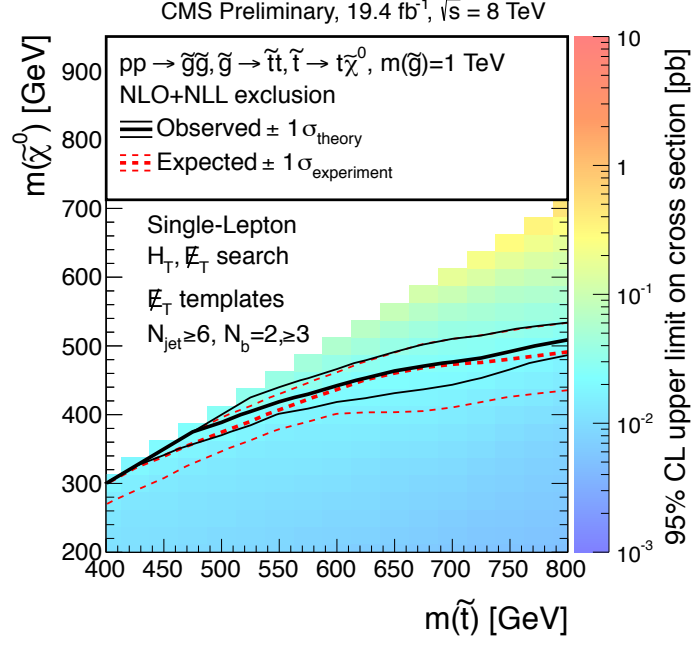
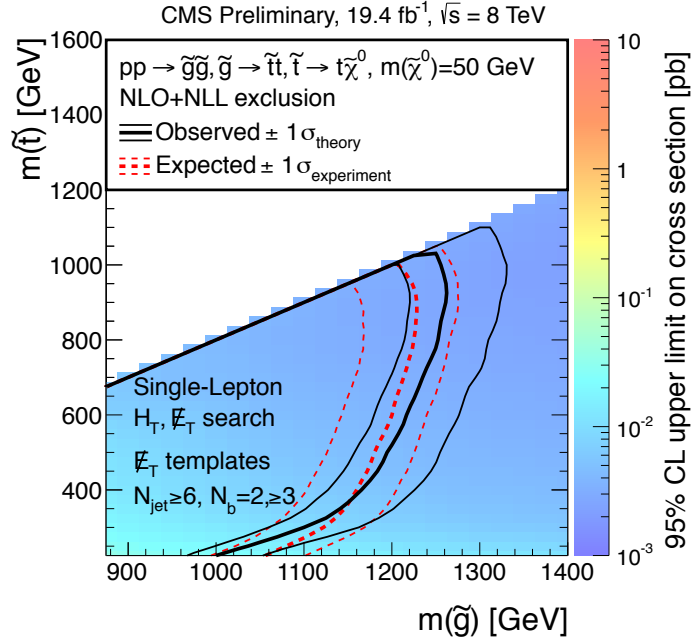


Figure 4.3.: Upper limits on the production cross section for $T1tttt$ as function of $m_{\tilde{g}}$ and $m_{\tilde{\chi}^0}$. The contour lines correspond to the expected upper limit (dashed red line) and the observed upper limit (solid black line) based on the NLO + NLL reference gluino-pair production cross section. The thin dashed (solid) lines show the $\pm 1\sigma$ experimental (theoretical) uncertainties on the expected (observed) limit.



(a) T1t1t



(b) T5tttt

Figure 4.4.: Upper limits on the production cross section for (a) T1t1t as function of $m_{\tilde{t}}$ and $m_{\tilde{\chi}^0}$ and for (b) T5tttt as function of $m_{\tilde{g}}$ and $m_{\tilde{t}}$. The contour lines correspond to the expected upper limit (dashed red line) and the observed upper limit (solid black line) based on the NLO + NLL reference gluino-pair production cross section. For T1t1t the gluino mass is fixed to 1 TeV, while for T5tttt the neutralino mass is fixed to 50 GeV. The thin dashed (solid) lines show the $\pm 1\sigma$ experimental (theoretical) uncertainties on the expected (observed) limit.

4.3. Comparison with results obtained from the analysis of the 7 TeV dataset

Although this thesis focuses on the analysis of the dataset recorded in 2012, the results obtained from data collected in 2011 should not be omitted. The methodology of this earlier analysis is very similar to what has been described in this thesis. Key differences between the two analyses and their justifications are highlighted in the following. The methods and results of 2011 are documented in [76].

- **Center-of-mass energy and data sample size**

The 2011 data sample comprises an integrated luminosity of 4.98 fb^{-1} , recorded at a center-of-mass energy of 7 TeV. In 2012, the performance of the LHC has been significantly improved, therefore the size of the collected data, recorded at a center-of-mass energy of 8 TeV is approximately 4 times larger.

- **Analysis target and data selection**

The main target of the 2011 analysis is the interpretation of results in the cMSSM, while the interpretation in the simplified model topology $T1tttt$, although of great interest, was not intended in the early stages of the analysis design. For that reason, the preselection of the 2011 analysis requires a minimum of 4 jets and the b -tag categories for which the SM background is predicted are 0, 1 and ≥ 2 b -tags. The 2012 analysis uses a ≥ 6 jet requirement in the preselection and introduces a ≥ 3 b -tags category to gain sensitivity for $T1tttt$ and the related simplified model topologies, while the W +jets dominated 0 b -tag category is completely omitted.

- **Inclusive \cancel{E}_T model**

The parametrization of the inclusive \cancel{E}_T models has been changed from $f(x = \cancel{E}_T^{\text{gen}}) = N \cdot x \cdot e^{-\alpha \cdot x^\beta}$ to a generalized Pareto distribution (Eq. 3.9). Although both distributions provide a good description of the genuine- \cancel{E}_T , the parameter estimation of the former distribution suffers from a redundancy between α and β , leading to correlations, which are small when using the generalized Pareto distribution.

- **W +jets model component**

The looser preselection of the 2011 analysis, including the 0 b -tag category, results in a significant increase of the W +jets component. Therefore, the distribution of genuine \cancel{E}_T from W +jets was modeled in a similar way as the $t\bar{t}$ component. This was neither necessary, nor possible in the 2012 analysis, where the W +jets component contributes at the percent level.

- **b -jet acceptance correction**

The b -jet acceptance correction (see Sec. 3.4.2) has not been used to correct the genuine- \cancel{E}_T model of the 2011 analysis, but the influence of the effect was investigated by excluding either the 1 or the 2 b -tag category from the likelihood fit. The effect on the predictions was found to be small compared to other systematic uncertainties.

The observed and predicted events counts, together with their statistical and systematic uncertainties are summarized in Tab 4.3

Table 4.3.: Overview of the predicted and observed yields with statistical and systematical uncertainties for different signal regions from the analysis of the 7 TeV dataset collected in 2011. Details on the methodology and the composition of the systematic uncertainties are described in [76].

	$H_T > 750 \text{ GeV}$					$H_T > 1000 \text{ GeV}$				
	predicted	stat.	sys.	obs.		predicted	stat.	sys.	obs.	
$\cancel{E}_T > 250 \text{ GeV}$										
total	145.82	± 9.28	± 23.73	137		37.54	± 3.73	± 8.85	36	
0 b -tags	98.95	± 7.54	± 18.11	97		27.02	± 3.19	± 7.01	30	
1 b -tag	34.62	± 2.76	± 7.54	35		7.51	± 1.18	± 2.58	5	
≥ 1 b -tags	46.87	± 3.09	± 10.18	40		10.52	± 1.33	± 3.61	6	
≥ 2 b -tags	12.26	± 1.38	± 2.68	5		3.01	± 0.61	± 1.03	1	
$\cancel{E}_T > 350 \text{ GeV}$										
total	53.55	± 4.54	± 11.75	44		15.49	± 1.73	± 4.94	13	
0 b -tags	38.72	± 3.59	± 9.52	32		11.66	± 1.55	± 4.15	11	
1 b -tag	11.51	± 1.03	± 3.5	11		2.87	± 0.46	± 1.36	2	
≥ 1 b -tags	14.83	± 1.11	± 4.5	12		3.83	± 0.5	± 1.81	2	
≥ 2 b -tags	3.32	± 0.4	± 1.02	1		0.96	± 0.2	± 0.46	0	
$\cancel{E}_T > 450 \text{ GeV}$										
total	19.62	± 2.05	± 6.19	20		6.58	± 0.86	± 2.77	7	
0 b -tags	14.93	± 1.7	± 5.18	14		5.15	± 0.76	± 2.31	6	
1 b -tag	3.84	± 0.4	± 1.5	5		1.14	± 0.2	± 0.67	1	
≥ 1 b -tags	4.69	± 0.42	± 1.83	6		1.43	± 0.21	± 0.86	1	
≥ 2 b -tags	0.85	± 0.12	± 0.33	1		0.29	± 0.07	± 0.19	0	

4.3.1. Interpretation of the 7 TeV results in terms of the cMSSM

The upper limit on the production cross section in the $m_{1/2}$ vs. m_0 cMSSM plane with parameters $\tan\beta = 10$, $A_0 = 0$ and $\mu > 0$, is calculated from the signal region defined by $H_T > 1000 \text{ GeV}$ and $\cancel{E}_T > 250 \text{ GeV}$ in Tab. 4.3. The same definitions of the test statistic and CL_s as described for the 2012 analysis are used and statistical and systematic uncertainties are modeled in the same way.

Similar to the 2012 analysis, a multichannel approach allows to combine all b -jet categories (0, 1 and ≥ 2). The observed and expected upper limits are shown in Fig. 4.5. Signal yields are calculated based on the NLO cross sections that were evaluated with PROSPINO [125] for each mass point.

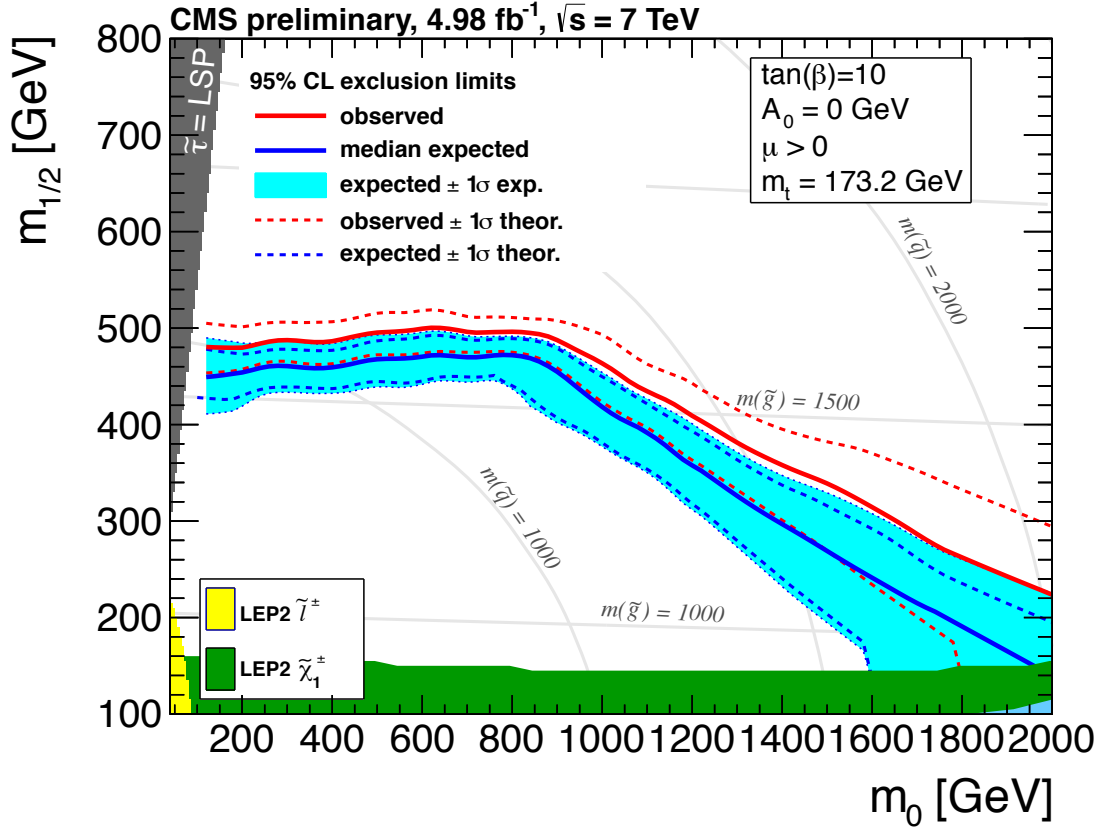


Figure 4.5.: Exclusion limits at 95% C.L. in the $m_{1/2}$ vs. m_0 cMSSM plane for $\tan\beta = 10$, $A_0 = 0$ and $\mu > 0$ using NLO cross sections and the multi-channel approach. Red and blue lines indicate the observed and expected limits, respectively. The solid lines correspond to the observed and expected limits, including all experimental uncertainties. The shaded region indicates the $\pm 1\sigma$ band around the expected limit. The dashed lines show the effect of a variation of the signal yields due to theoretical uncertainties.

4.3.2. Interpretation of the 7 TeV results in terms of T1tttt

Due to the presence of up to four b -quarks, the best limits for T1tttt are obtained from the ≥ 2 b -tag signal regions. The upper limits on the production cross section are calculated, using the signal region defined by $H_T > 750$ GeV and $\cancel{E}_T > 250$ GeV in the ≥ 2 b -tag category of Tab. 4.3. The choice of the lowest energetic signal region, results in high signal efficiencies also for low gluino masses and low mass splittings of the gluino and the LSP. The signal efficiency for the signal region is shown in Fig. 4.6(a). The nominal branching ratio into inclusive single-leptonic final states (not counting tau leptons) would be $\sim 40\%$.

The resulting upper limit on the production cross section is shown in Fig. 4.6(b). The contour lines reflect upper limits obtained for different choices of reference cross sections. For high mass splittings, gluino masses up to 950 GeV can be excluded, if the

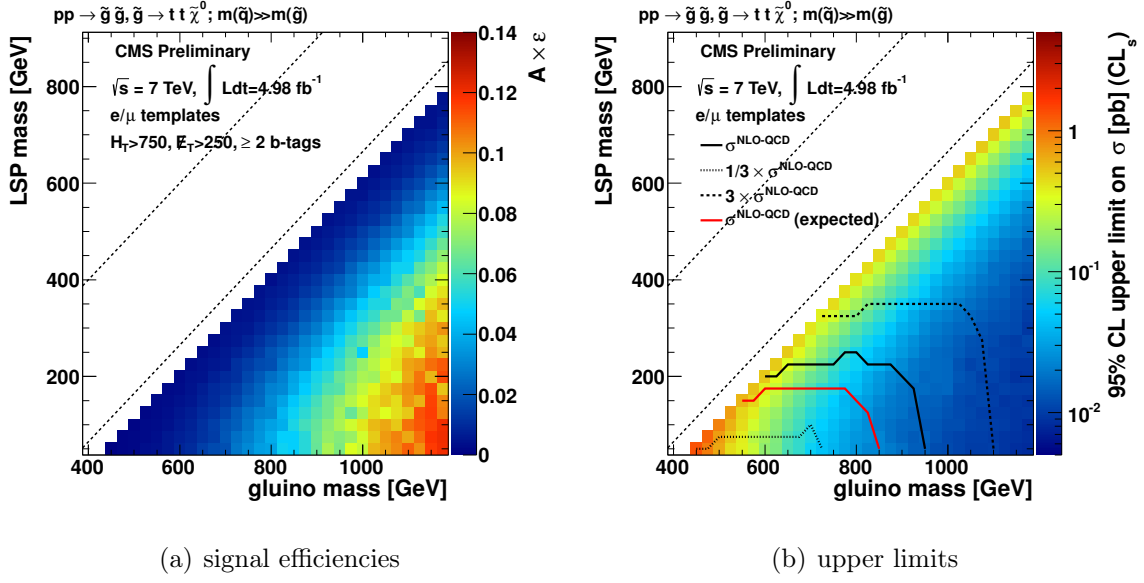


Figure 4.6.: Signal efficiencies (left) and exclusion limits at 95% CL (right) as a function of the two mass parameters of the T1tttt model. The contour lines correspond to different choices of the reference cross section, the red line shows the expected exclusion contour. Details on the selection are given in the text.

reference cross section is assumed. For low mass splittings, i.e. for higher LSP masses, this limit on the gluino masses is lowered to 600 GeV.

T1tttt is used to interpret both results obtained from the 2011 and the 2012 dataset. Compared to 2011, the excluded mass region can be significantly extended. For high mass splittings and neutralino masses below 250 GeV, the excluded gluino mass increases by ~ 250 GeV to 1200 GeV while the increase in the excluded neutralino mass ranges between 100 GeV and 300 GeV for gluinos lighter than 900 GeV. Low mass splittings, with neutralino masses above 250 GeV, still allow a gluino mass as low as 600 GeV. The improvements of the exclusion reach result from the increase in statistics, the higher center-of-mass energy and from the tuned selection of the 2012 analysis. Specifically, it can be shown that the split of the ≥ 2 b-tags category to 2 and ≥ 3 b-tags, considerably increases the sensitivity for b-rich models.

5. Summary

Although the Standard Model of particle physics provides a precise description of the fundamental constituents of matter and their interactions up to experimentally accessible energy scales it has several deficiencies that indicate the need for an extension of the theory. A particularly popular extension is supersymmetry, which offers solutions for several shortcomings of the Standard Model. Examples are the realization of gauge coupling unification, a candidate for dark matter and the cancellation of quadratically divergent radiative corrections to the Higgs boson mass, which avoids the need for fine-tuned parameters in the theory.

However, smaller logarithmic and higher-order quantum corrections to the Higgs boson mass remain and can become potentially large in case of high masses of the supersymmetric particles. Hence, retaining the Higgs boson mass parameters at the order of the electroweak scale, imposes constraints on supersymmetric mass spectra. In particular, it requires the masses of the lighter 3rd generation squarks to be smaller than 700 GeV, a neutralino mass below 350 GeV and a gluino with a mass below 1.5 TeV. Supersymmetric theories that are realized within these mass limits are commonly referred to as natural supersymmetry and are well suited to be targeted by LHC experiments, where these mass ranges are within reach.

Motivated by the mass hierarchy of natural SUSY, this thesis presents a search for gluino pair production, with each gluino decaying to two top quarks and one neutralino via an intermediate top squark, which is assumed to be either virtual or on-shell. “Simplified models” are used to describe this topology as a function of the supersymmetric particle masses $m_{\tilde{g}}$, $m_{\tilde{\chi}^0}$ and $m_{\tilde{t}}$.

The search selects events from samples of proton-proton collisions recorded by the CMS experiment at $\sqrt{s} = 7$ TeV during 2011 and $\sqrt{s} = 8$ TeV during 2012. The size of the samples corresponds to 4.98 fb^{-1} (2011) and 19.4 fb^{-1} (2012). This thesis focuses on the analysis of the larger dataset and the results are compared to those obtained from the sample collected in 2011, where a similar analysis strategy was used.

The selected events are characterized by the presence of a single isolated electron or muon, missing transverse momentum, hadronic activity and a minimum of 6 reconstructed jets, with at least one of them being tagged as a b -jet. The dominant SM background component in this selection is $t\bar{t}$ production, followed by a small contribution of W +jets and single- t events. The requirement of a single isolated electron or muon, together with missing transverse momentum provides a strong suppression of backgrounds from multijet production, but retains a large efficiency for signal events.

The 4 top quarks in the final state of the signal topology, result in high jet multiplicities with up to 4 b -jets, thus the most sensitive signal regions are those with at least 3 b -tagged jets.

To estimate the Standard Model background for the signal regions defined by the presence of 2 b -tags, high \cancel{E}_T and high H_T , a model for the genuine- \cancel{E}_T spectrum of $t\bar{t}$ events is developed, which provides a description in categories of H_T as well as b -tag multiplicity. The ratio of W +jets/ $t\bar{t}$ is measured in a low \cancel{E}_T sideband of the data and used to add a W +jets component extracted from simulation to the genuine- \cancel{E}_T model of $t\bar{t}$. The resulting distributions are convoluted with \cancel{E}_T -resolution templates, which are measured using a statistically independent data sample that is dominated by multijet production.

The parameters of the \cancel{E}_T model are estimated by an unbinned likelihood fit to control regions in the 1 and 2 b -tag category. The control region of the 2 b -tag category is restricted to low \cancel{E}_T and H_T to avoid overlaps with the signal regions. In order to predict the SM background for signal regions in the 2 b -tag category, the \cancel{E}_T model is normalized at low \cancel{E}_T and extrapolated. To further extrapolate the predicted event counts from the 2 b -tag category to more sensitive signal regions in the ≥ 3 b -tag category, translation factors are extracted from simulation and corrected for differences between data and simulation.

No excess beyond the SM expectation is observed. Therefore, the compatibility between the background predictions and the observation is used to set upper limits on the production cross section using three parametrizations of the aforementioned simplified model topology. Each parametrization uses two out of the three mass parameters $m_{\tilde{g}}$, $m_{\tilde{\chi}^0}$ and $m_{\tilde{t}}$. The third mass parameter is decoupled in case of the top squark or fixed for the other two cases ($m_{\tilde{g}} = 1$ TeV, $m_{\tilde{\chi}^0} = 50$ GeV). The limit calculation uses the modified-frequentist CL_S method with a one-sided profile likelihood test statistic and includes all statistical and systematic uncertainties, arising from experimental or theoretical sources on the background, as well as the signal prediction. Using the SUSY prediction for the production cross section of gluino-pairs as reference, gluino masses up to 1.2 TeV are excluded for neutralino masses up to 300 GeV, while in case of low mass splittings and a high neutralino mass above 300 GeV, a gluino mass as low as 600 GeV is still allowed. In case of very light neutralino and top squark masses, a gluino mass as low as 1 TeV is still allowed.

Compared to the upper limits on the gluino-pair production cross section based on the analysis of the 2011 dataset, the limits based on the dataset collected during 2012 significantly extend the excluded mass regions in $m_{\tilde{g}}$, $m_{\tilde{\chi}^0}$ and $m_{\tilde{t}}$. These limits start to challenge the hypothesis of natural SUSY as the mechanism that stabilizes the Higgs boson mass.

A. Data, simulated samples and trigger paths

Table A.1.: Certification files and primary data sets used for the muon and electron channels, together with the run ranges and integrated luminosities for the *rereco* and *prompt reco* periods.

Data sets	run range	$\int \mathcal{L} dt$
Certification: Cert_190456-196531_8TeV_13Jul2012ReReco_Collisions12_JSON /MuHad/Run2012A-13Jul2012-v1 /ElectronHad/Run2012A-13Jul2012-v1	190456 – 193621	0.8 fb ⁻¹
Certification: Cert_190456-196531_8TeV_13Jul2012ReReco_Collisions12_JSON /MuHad/Run2012B-13Jul2012-v1 /ElectronHad/Run2012B-13Jul2012-v1	193833 – 196531	4.4 fb ⁻¹
Certification: Cert_198022-198523_8TeV_24Aug2012ReReco_Collisions12_JSON /MuHad/Run2012C-24Aug2012-v1 /ElectronHad/Run2012C-24Aug2012-v1	198022 – 198913	0.5 fb ⁻¹
Certification: Cert_190456-203002_8TeV_PromptReco_Collisions12_JSON /MuHad/Run2012C-PromptReco-v2 /ElectronHad/Run2012C-PromptReco-v2	198934 – 203746	6.4 fb ⁻¹
Certification: Cert_190456-208686_8TeV_PromptReco_Collisions12_JSON /MuHad/Run2012D-PromptReco-v1 /ElectronHad/Run2012D-PromptReco-v1	203768 – 208686	7.3 fb ⁻¹

Table A.2.: Simulated event samples.

Sample name
/TT_CT10_TuneZ2star_8TeV-powheg-tauola/Summer12_DR53X-PU_S10_START53_V7A-v1/AODSIM
/TT_CT10_TuneZ2star_8TeV-powheg-tauola/Summer12_DR53X-PU_S10_START53_V7A-v2
/WJetsToLNu_TuneZ2star_8TeV-madgraph-tarball/Summer12_DR53X-PU_S10_START53_V7A-v1/AODSIM
/WJetsToLNu_HT-250To300_8TeV-madgraph/Summer12_DR53X-PU_S10_START53_V7A-v1/AODSIM
/WJetsToLNu_HT-300To400_8TeV-madgraph/Summer12_DR53X-PU_S10_START53_V7A-v1/AODSIM
/WJetsToLNu_HT-400ToInf_8TeV-madgraph/Summer12_DR53X-PU_S10_START53_V7A-v1/AODSIM
/DYJetsToLL_M-10To50filter_8TeV-madgraph/Summer12_DR53X-PU_S10_START53_V7A-v1
/DYJetsToLL_M-50_TuneZ2star_8TeV-madgraph-tarball/Summer12_DR53X-PU_S10_START53_V7A-v1
/T_tW-channel-DR_TuneZ2star_8TeV-powheg-tauola/Summer12_DR53X-PU_S10_START53_V7A-v1
/T_s-channel_TuneZ2star_8TeV-powheg-tauola/Summer12_DR53X-PU_S10_START53_V7A-v1
/T_t-channel_TuneZ2star_8TeV-powheg-tauola/Summer12_DR53X-PU_S10_START53_V7A-v3
/Tbar_t-channel_TuneZ2star_8TeV-powheg-tauola/Summer12_DR53X-PU_S10_START53_V7A-v1
/Tbar_s-channel_TuneZ2star_8TeV-powheg-tauola/Summer12_DR53X-PU_S10_START53_V7A-v1
/Tbar_tW-channel-DR_TuneZ2star_8TeV-powheg-tauola/Summer12_DR53X-PU_S10_START53_V7A-v1
/QCD_Pt-*MuEnrichedPt5_TuneZ2star_8TeV_pythia6/Summer12_DR53X-PU_S10_START53_V7A-v1
/QCD_Pt-*EMEnriched_TuneZ2star_8TeV_pythia6/Summer12_DR53X-PU_S10_START53_V7A-v1
/QCD_Pt_20_30_BCtoE_TuneZ2star_8TeV_pythia6/Summer12_DR53X-PU_S10_START53_V7A-v1
/SMS-MadGraph_Pythia6Zstar_8TeV_T1tttt_2J_mGo-*to*_mLSP-*to*_GeVX*GeV_Binning ...
.../Summer12-START52_V9_FSIM-v3
/SMS-T5tttt_mGo-800to1200_mStop-225to1025_mLSP_50_8TeV-Madgraph...
.../Summer12-START52_V9_FSIM_UFL
/SMS-MadGraph_Pythia6Zstar_8TeV_T1tt_2J_mGo-*to*_mLSP-*to*_GeVX*GeV_Binning...
.../Summer12-START52_V9_FSIM-v1

Table A.3.: HLT trigger path names for the signal selection (muon and electron channel) and for the fake E_T templates. Different versions of the same path have been added.

Muon trigger paths
HLT_PFHT350_Mu15_PFMET45_v*
HLT_PFHT350_Mu15_PFMET50_v*
HLT_PFHT400_Mu5_PFMET45_v*
HLT_PFHT400_Mu5_PFMET50_v*
HLT_PFNpUHT350_Mu15_PFMET45_v*
HLT_PFNpUHT350_Mu15_PFMET50_v*
HLT_PFNpUHT400_Mu5_PFMET45_v*
Electron trigger paths
HLT_CleanPFHT300_Ele15_CaloIdT_CaloIsoVL_TrkIdT_TrkIsoVL_PFMET45_v*
HLT_CleanPFHT300_Ele15_CaloIdT_CaloIsoVL_TrkIdT_TrkIsoVL_PFMET50_v*
HLT_CleanPFHT350_Ele5_CaloIdT_CaloIsoVL_TrkIdT_TrkIsoVL_PFMET45_v*
HLT_CleanPFHT350_Ele5_CaloIdT_CaloIsoVL_TrkIdT_TrkIsoVL_PFMET50_v*
HLT_CleanPFNpUHT300_Ele15_CaloIdT_CaloIsoVL_TrkIdT_TrkIsoVL_PFMET45_v*
HLT_CleanPFNpUHT350_Ele5_CaloIdT_CaloIsoVL_TrkIdT_TrkIsoVL_PFMET45_v*
HLT_CleanPFNpUHT350_Ele5_CaloIdT_CaloIsoVL_TrkIdT_TrkIsoVL_PFMET50_v*
HT trigger paths
HLT_HT200_v* ... HLT_HT750_v*
HLT_PFHT350_v* ... HLT_PFHT700_v*

B. Toy MC study

In order to verify that the likelihood fit does not introduce any bias on the central values and gives correct error estimates we use the full model described in section 3.4.5 to generate 250 datasets comprising the same number of events as predicted by the simulation. For each fit to a toy dataset, random values for the constraints on the parameters β , μ_0 , μ_1 , σ_0^2 , σ_1^2 and ξ were chosen according to their covariance matrix. The distributions of the parameters from fits to this 250 datasets are shown in Fig. B.1-B.3. Since the folding of the \cancel{E}_T model with the fake- \cancel{E}_T templates is rather time consuming it was omitted for these fits.

The mean and standard deviations of the resulting parameter distributions as well as the normalized residuals indicate that the parameter estimation is unbiased and returns correct errors.

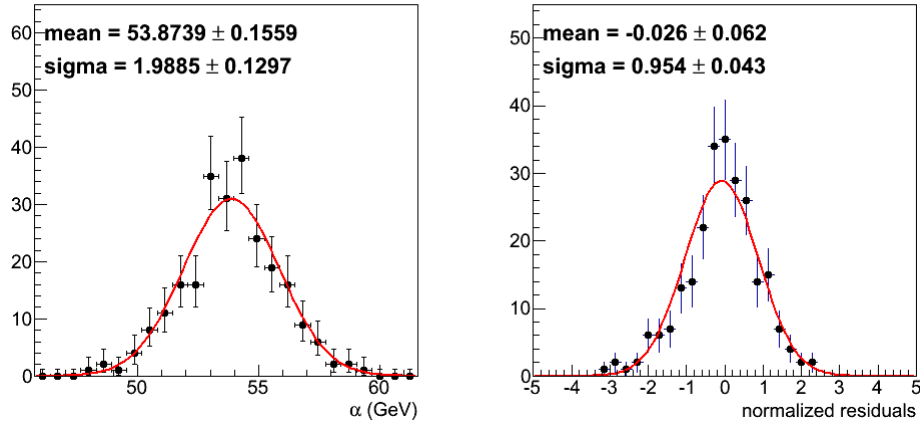


Figure B.1.: Distribution of the parameter α and its normalized residuals for 250 toy experiments.

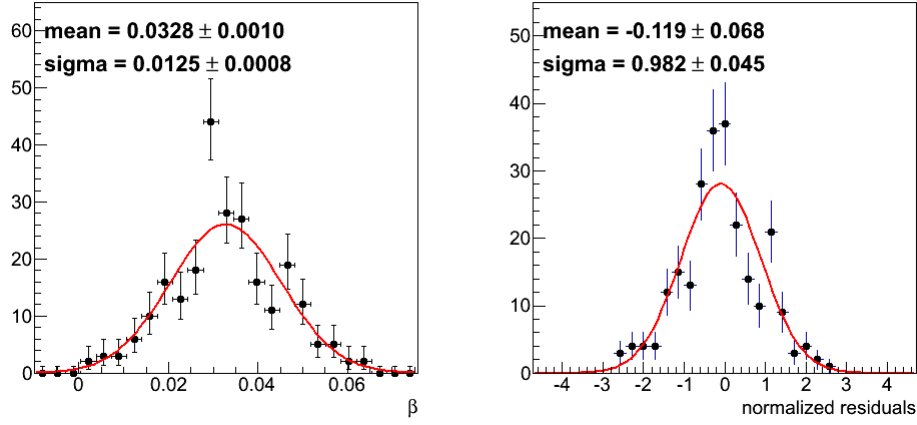
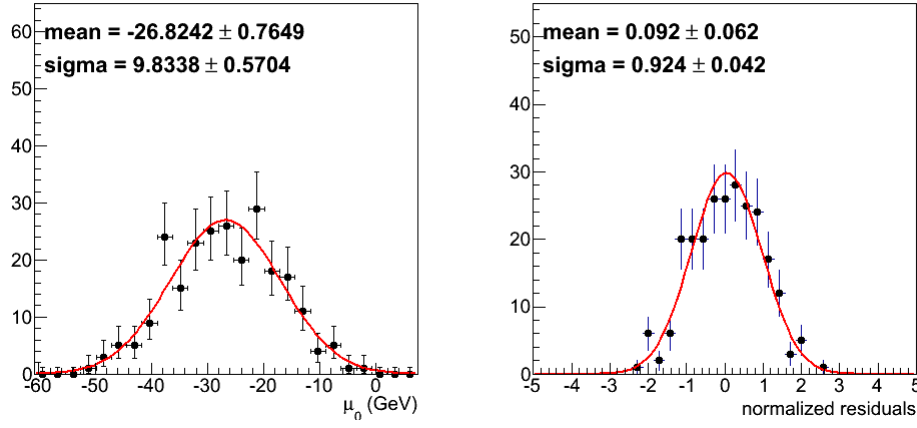
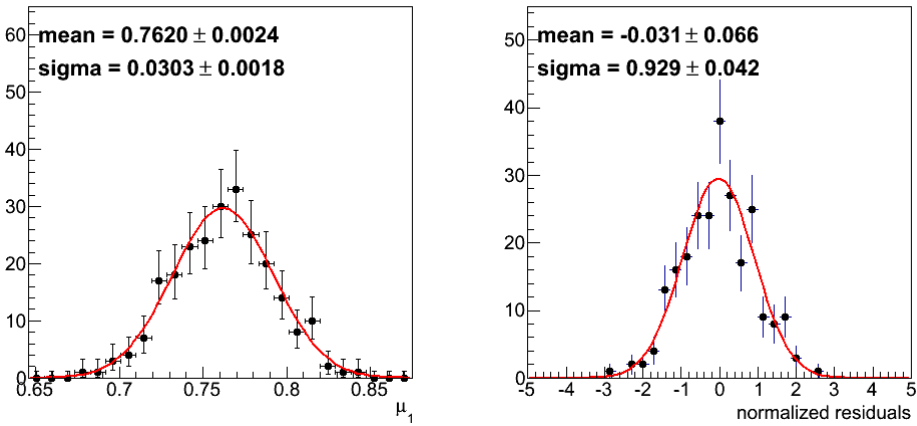
(a) β (b) μ_0 (c) μ_1

Figure B.2.: Distribution of the parameters β , μ_0 , μ_1 and their normalized residuals for 250 toy experiments.

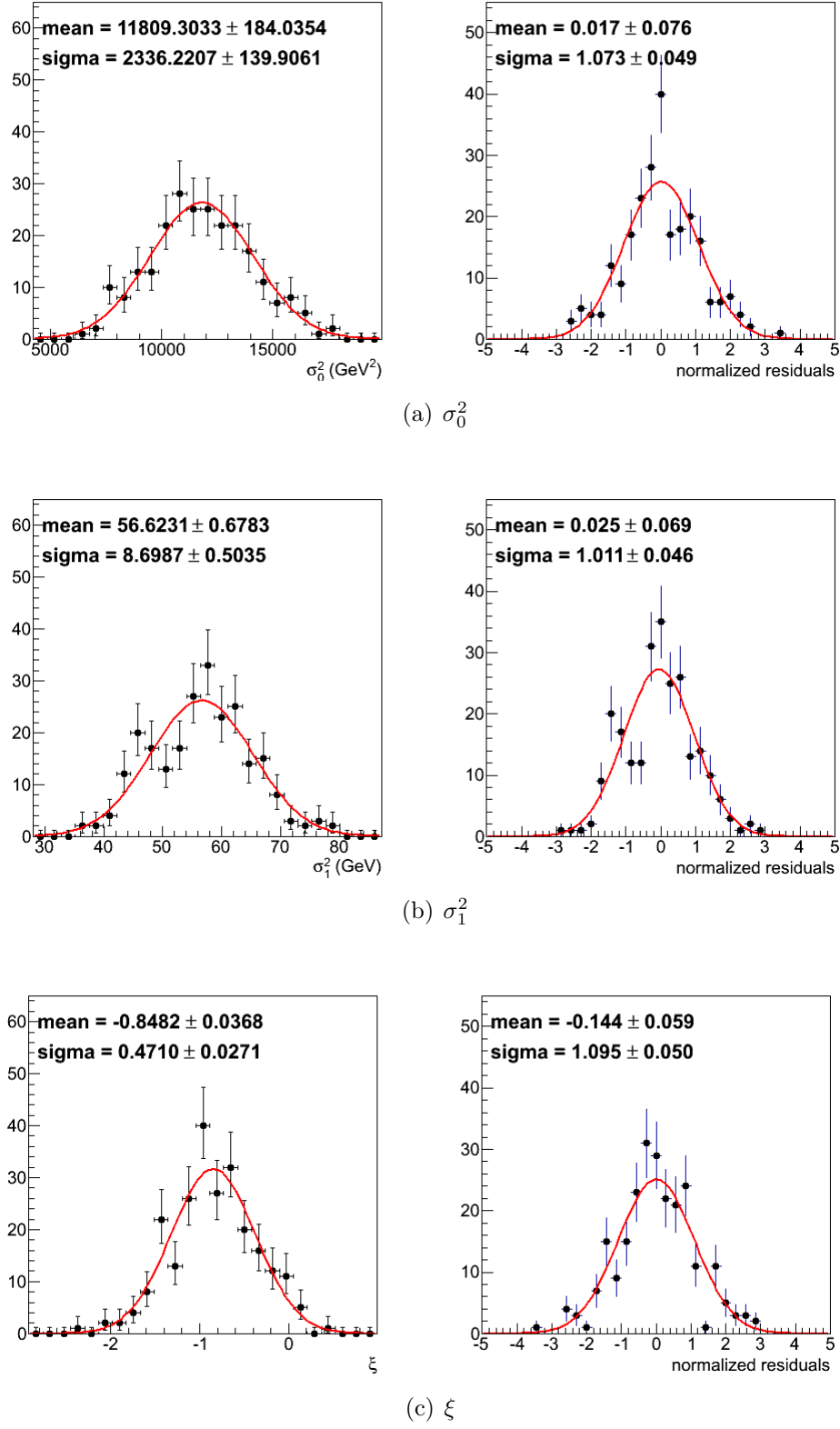


Figure B.3.: Distribution of the parameters σ_0^2 , σ_1^2 , ξ and their normalized residuals for 250 toy experiments.

C. QCD estimation

The estimation of the contribution from QCD multi-jet events to the signal regions considered in this thesis was performed by [126]. Control samples from hadronically triggered data (JetHT dataset) are used, with relaxed requirements on the relative isolation (I_{rel}) of muons and electrons as well as an inversion of the impact parameter (d_{xy}) requirement with respect to the standard selection summarized in Sec. 3.3.1. The distribution of I_{rel} is measured in this QCD enriched control regions and normalized in the sidebands of high relative isolation of the respective signal region. The JetHT dataset is used to avoid a bias from the isolation requirement for electrons at trigger level. The prescale-factors of low- H_T triggers are taken into account by weighting the measured events correspondingly.

Both, the muon and electron control regions require an impact parameter between $0.01 < |d_{xy}| < 0.5 \text{ cm}$ and a minimum of four jets with at least one of them being b -tagged. E_T must be smaller than 150 GeV in the case of muons while for electrons $50 < E_T < 150 \text{ GeV}$ is required. Two examples of I_{rel} control shapes for muon and electron in selected H_T categories are shown in Fig. C.1.

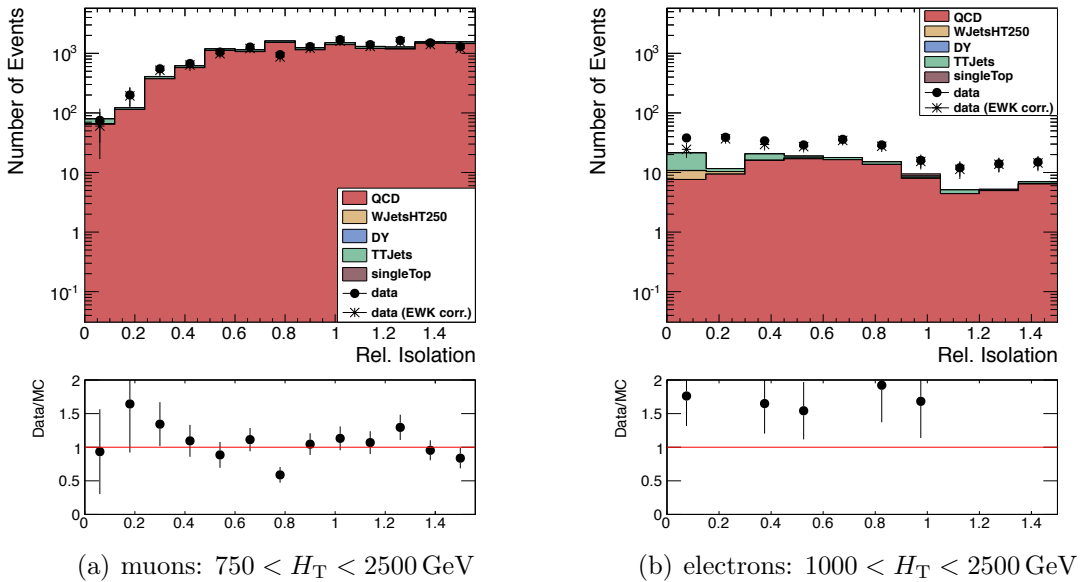


Figure C.1.: Control shape for (a) muons (HLT_HT650) and (b) electrons (HLT_HT750) for two different H_T requirements [126].

For the comparison to the signal regions the I_{rel} shapes from the control regions are normalized in a sideband of the signal regions, defined by inverting the respective I_{rel} selection, thus $0.12 < I_{rel} < 1.5$ is used for muons and $0.15 < I_{rel} < 1.5$ for electrons. Where applicable, the electroweak contribution predicted by simulation is subtracted from the I_{rel} shapes of the signal regions.

This is illustrated for muons and electrons and two selected H_T categories in Fig. C.2. All results are summarized in Tab. C.1 for muons and in Tab. C.2 for electrons.

The electron signal region for $400 < H_T < 750$ GeV and $250 < \cancel{E}_T < 2500$ GeV was estimated inclusively to avoid empty normalization regions. Therefore Tab. C.1 and Tab. C.2 show just one value for this high \cancel{E}_T and low H_T region. Instead of assuming one QCD event, the number of estimated QCD events in the low \cancel{E}_T region ($150 < \cancel{E}_T < 250$ GeV) was scaled with the ratio between the electroweak background from simulation in the high \cancel{E}_T region and that in the low \cancel{E}_T region.

The contribution from QCD multi-jet events to any of the signal regions considered in the analysis is negligible.

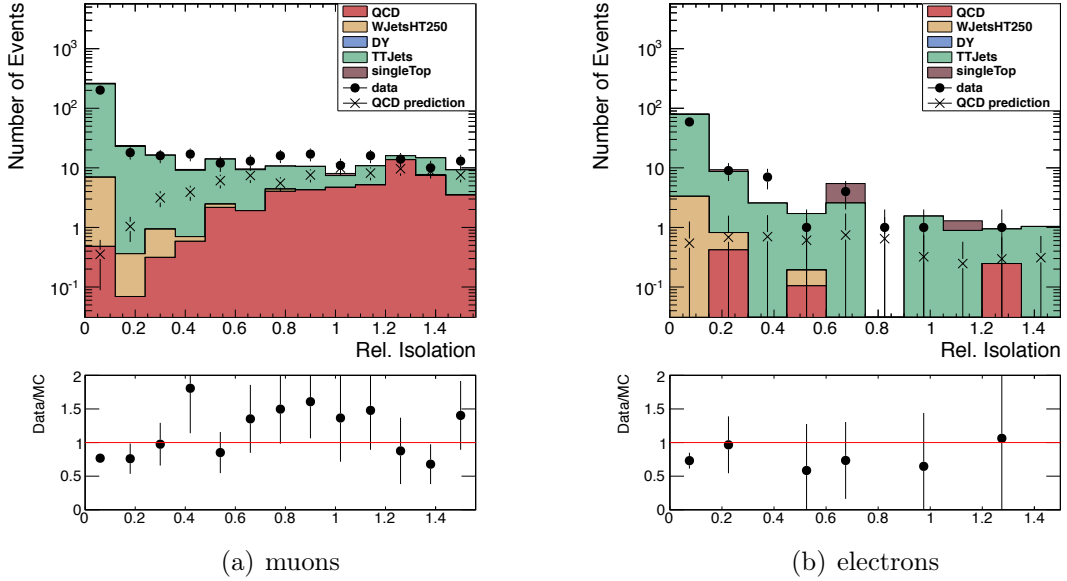


Figure C.2.: Signal regions and normalization sidebands corresponding to the regions shown in C.1: (a) muons, $750 < H_T < 2500$ GeV and $150 < \cancel{E}_T < 250$ GeV; (b) electrons, $1000 < H_T < 2500$ GeV and $150 < \cancel{E}_T < 250$ GeV [126].

Table C.1.: Upper limit on the QCD contribution in the ≥ 1 b-tag bin for the muon channel [126].

≥ 1 b-tags	$400 < H_T < 750$ GeV		
$150 < \cancel{E}_T < 250$ GeV	0.191	\pm	0.186
$250 < \cancel{E}_T < 350$ GeV	0.004	\pm	0.019
$350 < \cancel{E}_T < 450$ GeV	0.011	\pm	0.013
$450 < \cancel{E}_T < 2500$ GeV	0.003	\pm	0.005
≥ 1 b-tags	$750 < H_T < 2500$ GeV		
$150 < \cancel{E}_T < 250$ GeV	0.25	\pm	0.232
$250 < \cancel{E}_T < 350$ GeV	0.012	\pm	0.024
$350 < \cancel{E}_T < 450$ GeV	0.011	\pm	0.012
$450 < \cancel{E}_T < 2500$ GeV	0.0	\pm	0.004
≥ 1 b-tags	$1000 < H_T < 2500$ GeV		
$150 < \cancel{E}_T < 250$ GeV	0.025	\pm	0.04
$250 < \cancel{E}_T < 350$ GeV	0.007	\pm	0.012
$350 < \cancel{E}_T < 450$ GeV	0.002	\pm	0.003
$450 < \cancel{E}_T < 2500$ GeV	0.0	\pm	0.001

Table C.2.: Upper limit on the QCD contribution in the ≥ 1 b-tag bin for the electron channel. The low H_T electron signal region (marked with *) corresponds to the inclusive bin $250 < \cancel{E}_T < 2500$ GeV [126].

≥ 1 b-tags	$400 < H_T < 750$ GeV		
$150 < \cancel{E}_T < 250$ GeV	0.88	\pm	2.158
$250 < \cancel{E}_T < 350$ GeV	0.099*	\pm	0.242
$350 < \cancel{E}_T < 450$ GeV	0.099*	\pm	0.242
$450 < \cancel{E}_T < 2500$ GeV	0.099*	\pm	0.242
≥ 1 b-tags	$750 < H_T < 2500$ GeV		
$150 < \cancel{E}_T < 250$ GeV	3.633	\pm	9.608
$250 < \cancel{E}_T < 350$ GeV	0.0	\pm	0.217
$350 < \cancel{E}_T < 450$ GeV	0.0	\pm	0.217
$450 < \cancel{E}_T < 2500$ GeV	0.0	\pm	0.217
≥ 1 b-tags	$1000 < H_T < 2500$ GeV		
$150 < \cancel{E}_T < 250$ GeV	2.089	\pm	0.879
$250 < \cancel{E}_T < 350$ GeV	0.087	\pm	0.093
$350 < \cancel{E}_T < 450$ GeV	0.087	\pm	0.093
$450 < \cancel{E}_T < 2500$ GeV	0.0	\pm	0.087

D. Results using a fine \cancel{E}_T binning

Table D.1.: Predicted and measured event counts in data for 2 b -tag and different \cancel{E}_T and H_T signal regions. Uncertainties are statistical.

2 b -tag	750 < H_T < 2500 GeV						
	obs.	pred.	stat.	b-tag	sys.	total	
250 < \cancel{E}_T < 275 GeV	12	14.72	± 1.44	± 0.08	± 1.65	± 2.19	
275 < \cancel{E}_T < 300 GeV	2	10.52	± 1.12	± 0.03	± 1.57	± 1.93	
300 < \cancel{E}_T < 350 GeV	12	12.63	± 1.52	± 0.10	± 1.75	± 2.32	
350 < \cancel{E}_T < 450 GeV	9	9.42	± 1.43	± 0.06	± 2.68	± 3.04	
450 < \cancel{E}_T < 2500 GeV	1	3.08	± 0.71	± 0.03	± 1.48	± 1.64	
2 b -tag	1000 < H_T < 2500 GeV						
	obs.	pred.	stat.	b-tag	sys.	total	
250 < \cancel{E}_T < 275 GeV	5	5.53	± 0.86	± 0.04	± 0.89	± 1.24	
275 < \cancel{E}_T < 300 GeV	1	4.15	± 0.67	± 0.02	± 0.91	± 1.13	
300 < \cancel{E}_T < 350 GeV	5	5.44	± 0.93	± 0.05	± 1.16	± 1.49	
350 < \cancel{E}_T < 450 GeV	4	4.73	± 0.92	± 0.02	± 1.47	± 1.73	
450 < \cancel{E}_T < 2500 GeV	1	2.03	± 0.54	± 0.02	± 1.14	± 1.27	

Table D.2.: Predicted and measured event counts in data for ≥ 3 b-tag and different E_T and H_T signal regions. Uncertainties are statistical.

≥ 3 b-tag	$400 < H_{\text{T}} < 2500$ GeV									
	obs.	pred.	stat.		b-tag		sys.		total	
$150 < \cancel{E}_{\text{T}} < 175$ GeV	41	42.07	\pm	2.05	\pm	7.15	\pm	0.52	\pm	7.46
$175 < \cancel{E}_{\text{T}} < 200$ GeV	20	26.51	\pm	1.29	\pm	4.11	\pm	0.64	\pm	4.35
$200 < \cancel{E}_{\text{T}} < 225$ GeV	21	15.78	\pm	0.77	\pm	2.39	\pm	0.04	\pm	2.51
$225 < \cancel{E}_{\text{T}} < 250$ GeV	12	8.11	\pm	0.39	\pm	1.41	\pm	0.21	\pm	1.48
$250 < \cancel{E}_{\text{T}} < 275$ GeV	12	6.39	\pm	0.48	\pm	1.54	\pm	0.81	\pm	1.80
$275 < \cancel{E}_{\text{T}} < 300$ GeV	0	4.20	\pm	0.37	\pm	0.93	\pm	0.46	\pm	1.10
$300 < \cancel{E}_{\text{T}} < 350$ GeV	4	3.94	\pm	0.43	\pm	0.99	\pm	0.45	\pm	1.17
$350 < \cancel{E}_{\text{T}} < 450$ GeV	2	2.55	\pm	0.38	\pm	0.56	\pm	0.49	\pm	0.83
$450 < \cancel{E}_{\text{T}} < 2500$ GeV	0	0.77	\pm	0.18	\pm	0.16	\pm	0.34	\pm	0.42
≥ 3 b-tag	$750 < H_{\text{T}} < 2500$ GeV									
	obs.	pred.	stat.		b-tag		sys.		total	
$150 < \cancel{E}_{\text{T}} < 175$ GeV	11	11.74	\pm	0.99	\pm	1.75	\pm	0.08	\pm	2.01
$175 < \cancel{E}_{\text{T}} < 200$ GeV	8	11.06	\pm	0.93	\pm	1.79	\pm	0.42	\pm	2.06
$200 < \cancel{E}_{\text{T}} < 225$ GeV	12	5.64	\pm	0.48	\pm	0.86	\pm	0.06	\pm	0.98
$225 < \cancel{E}_{\text{T}} < 250$ GeV	6	3.39	\pm	0.29	\pm	0.53	\pm	0.07	\pm	0.60
$250 < \cancel{E}_{\text{T}} < 275$ GeV	9	3.43	\pm	0.33	\pm	0.61	\pm	0.39	\pm	0.80
$275 < \cancel{E}_{\text{T}} < 300$ GeV	0	2.42	\pm	0.26	\pm	0.39	\pm	0.37	\pm	0.59
$300 < \cancel{E}_{\text{T}} < 350$ GeV	3	2.67	\pm	0.32	\pm	0.47	\pm	0.39	\pm	0.69
$350 < \cancel{E}_{\text{T}} < 450$ GeV	2	1.90	\pm	0.29	\pm	0.33	\pm	0.54	\pm	0.70
$450 < \cancel{E}_{\text{T}} < 2500$ GeV	0	0.68	\pm	0.16	\pm	0.15	\pm	0.32	\pm	0.39
≥ 3 b-tag	$1000 < H_{\text{T}} < 2500$ GeV									
	obs.	pred.	stat.		b-tag		sys.		total	
$150 < \cancel{E}_{\text{T}} < 175$ GeV	3	4.60	\pm	0.68	\pm	0.80	\pm	0.03	\pm	1.05
$175 < \cancel{E}_{\text{T}} < 200$ GeV	3	2.66	\pm	0.39	\pm	0.44	\pm	0.38	\pm	0.70
$200 < \cancel{E}_{\text{T}} < 225$ GeV	6	3.15	\pm	0.46	\pm	0.47	\pm	0.12	\pm	0.68
$225 < \cancel{E}_{\text{T}} < 250$ GeV	2	0.73	\pm	0.11	\pm	0.14	\pm	0.02	\pm	0.18
$250 < \cancel{E}_{\text{T}} < 275$ GeV	4	1.43	\pm	0.22	\pm	0.38	\pm	0.23	\pm	0.50
$275 < \cancel{E}_{\text{T}} < 300$ GeV	0	1.03	\pm	0.17	\pm	0.23	\pm	0.23	\pm	0.37
$300 < \cancel{E}_{\text{T}} < 350$ GeV	0	1.10	\pm	0.19	\pm	0.32	\pm	0.23	\pm	0.44
$350 < \cancel{E}_{\text{T}} < 450$ GeV	1	0.91	\pm	0.18	\pm	0.23	\pm	0.28	\pm	0.40
$450 < \cancel{E}_{\text{T}} < 2500$ GeV	0	0.47	\pm	0.13	\pm	0.10	\pm	0.27	\pm	0.31

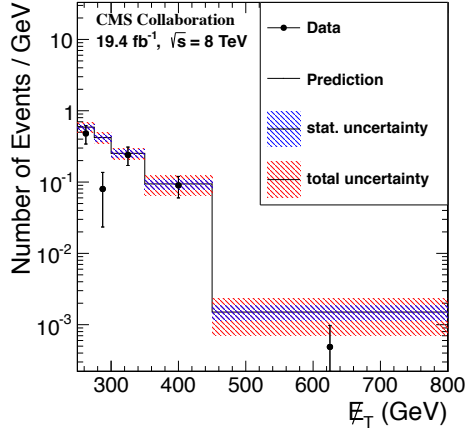
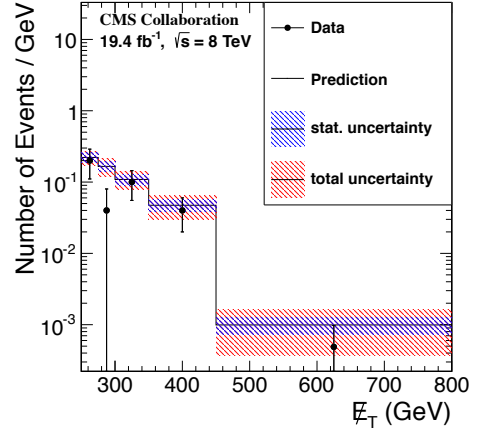
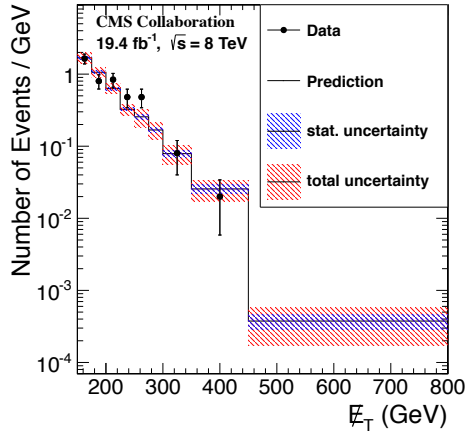
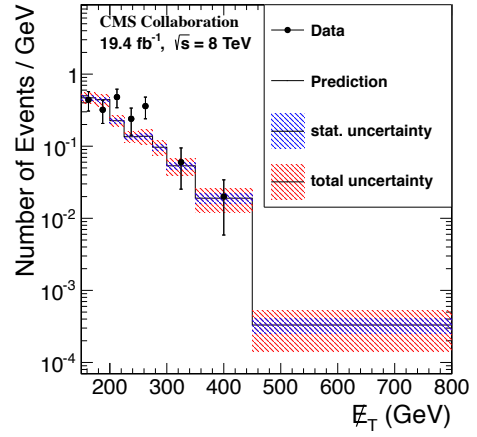
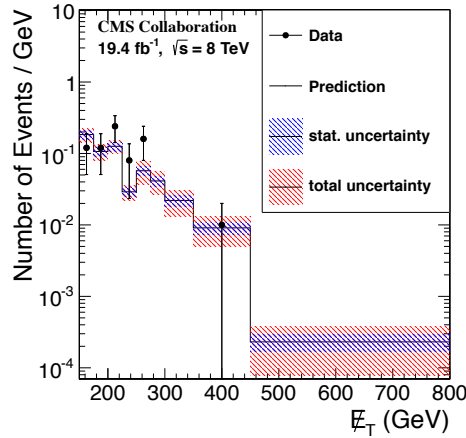
(a) 2 b -tags, $750 < H_T < 2500$ GeV(b) 2 b -tags, $1000 < H_T < 2500$ GeV(c) ≥ 3 b -tags, $400 < H_T < 2500$ GeV(d) ≥ 3 b -tags, $750 < H_T < 2500$ GeV(e) ≥ 3 b -tags, $1000 < H_T < 2500$ GeV

Figure D.1.: Predicted and measured event counts in data. The 2 b -tag categories are (a) $750 < H_T < 2500$ GeV and (b) $1000 < H_T < 2500$ GeV. The ≥ 3 b -tag categories are (c) $400 < H_T < 2500$ GeV, (d) $750 < H_T < 2500$ GeV and (e) $1000 < H_T < 2500$ GeV.

E. Signal contamination, efficiencies and acceptance uncertainties

E.1. Signal contamination

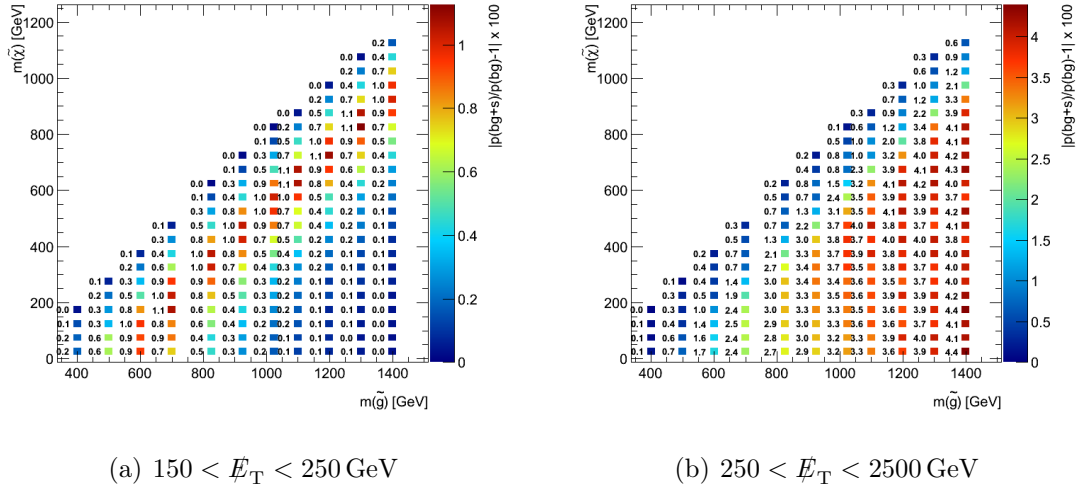


Figure E.1.: Signal contamination for $T1ttttt$ evaluated at a cross-section corresponding to $m_{\tilde{g}} = 1100$ GeV for $400 < H_T < 750$ GeV.

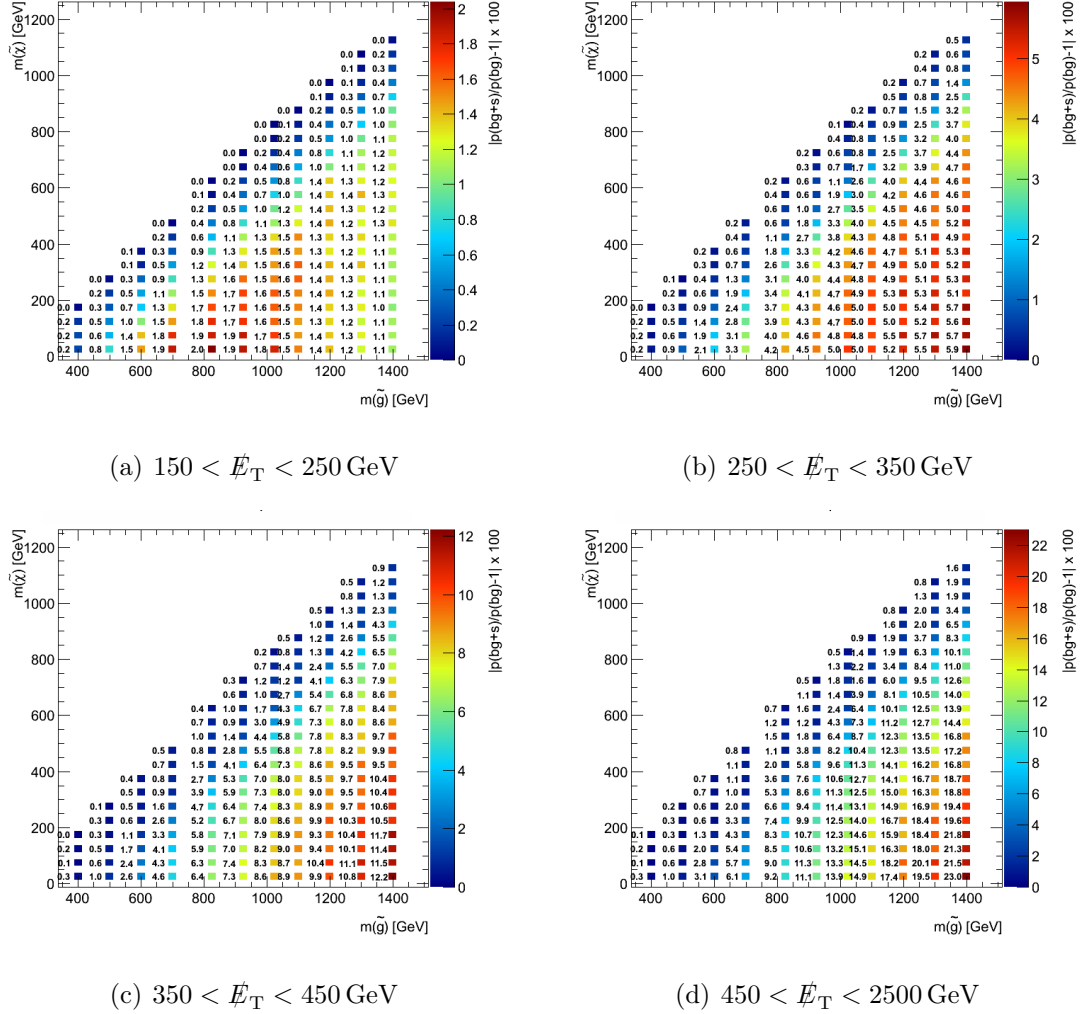


Figure E.2.: Signal contamination for T1ttttt evaluated at a cross-section corresponding to $m_{\tilde{g}} = 1100 \text{ GeV}$ for $750 < H_T < 2500 \text{ GeV}$.

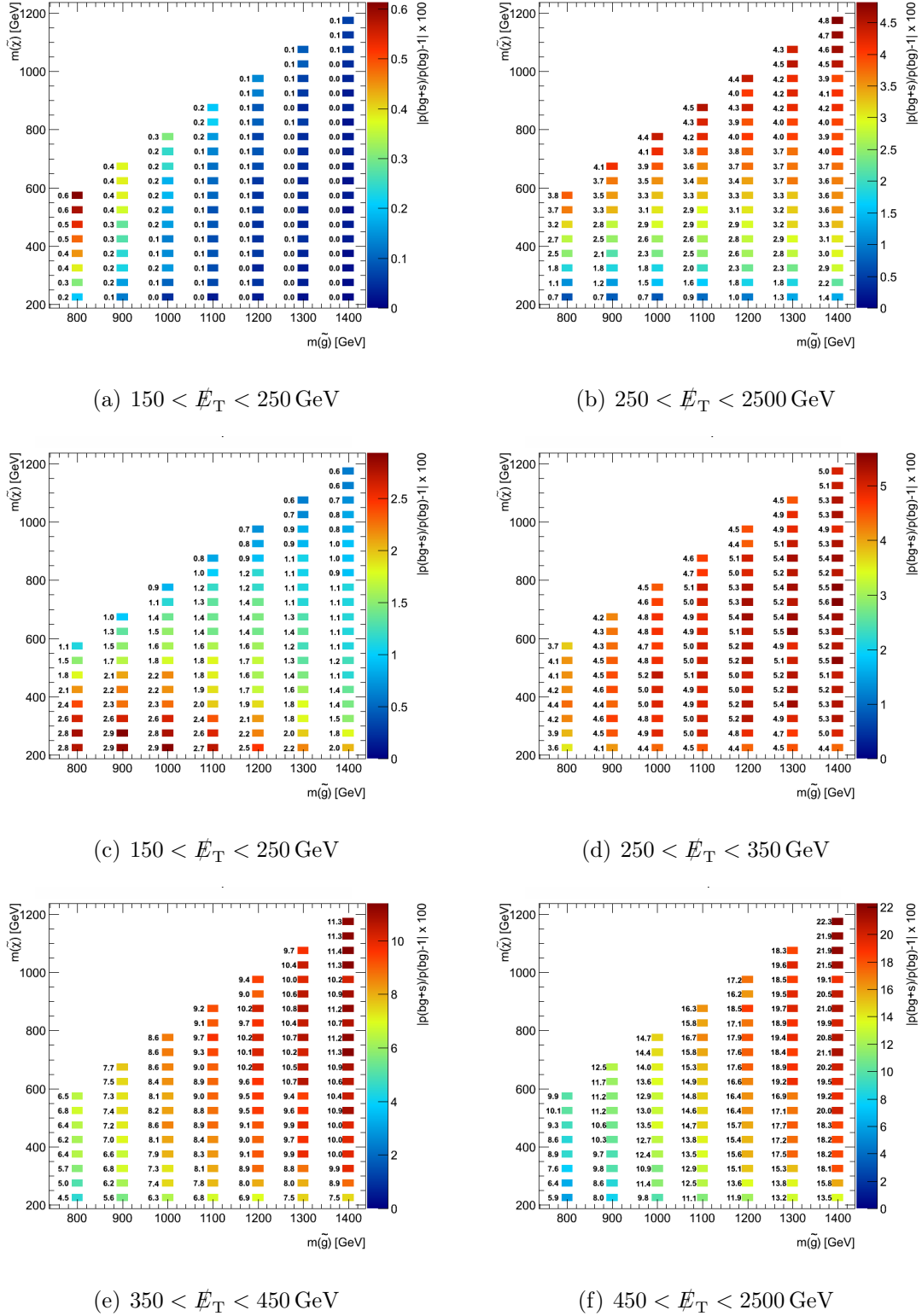


Figure E.3.: Signal contamination for T5ttttt evaluated at a cross-section corresponding to $m_{\tilde{g}} = 1100$ GeV for $400 < H_T < 750$ GeV (a), (b) and $750 < H_T < 2500$ GeV (c)-(f).

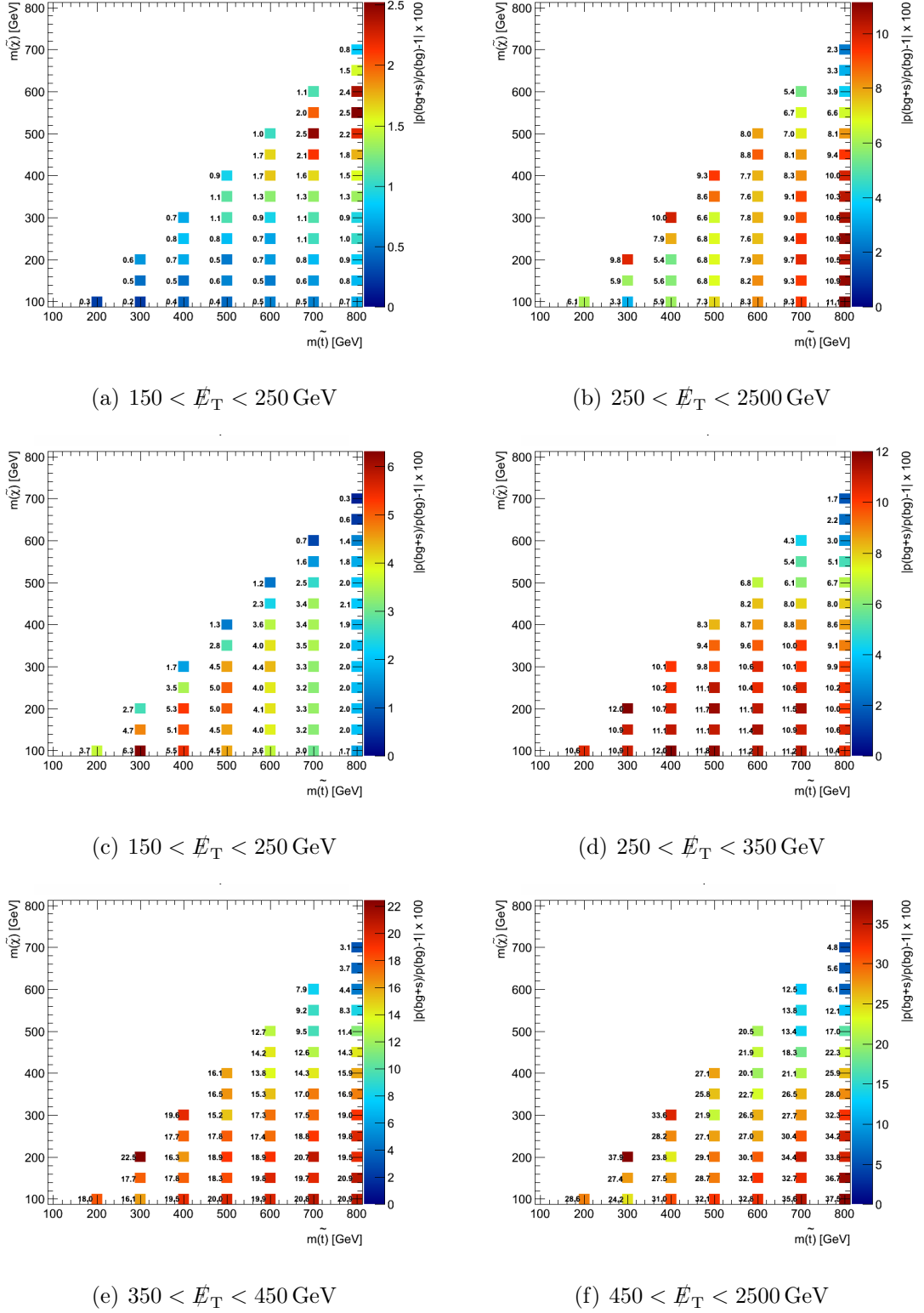


Figure E.4.: Signal contamination for $T1t1t$ evaluated at a cross-section corresponding to $m_{\tilde{g}} = 1000$ GeV for $400 < H_T < 750$ GeV (a), (b) and $750 < H_T < 2500$ GeV (c)-(f).

E.2. Signal efficiency

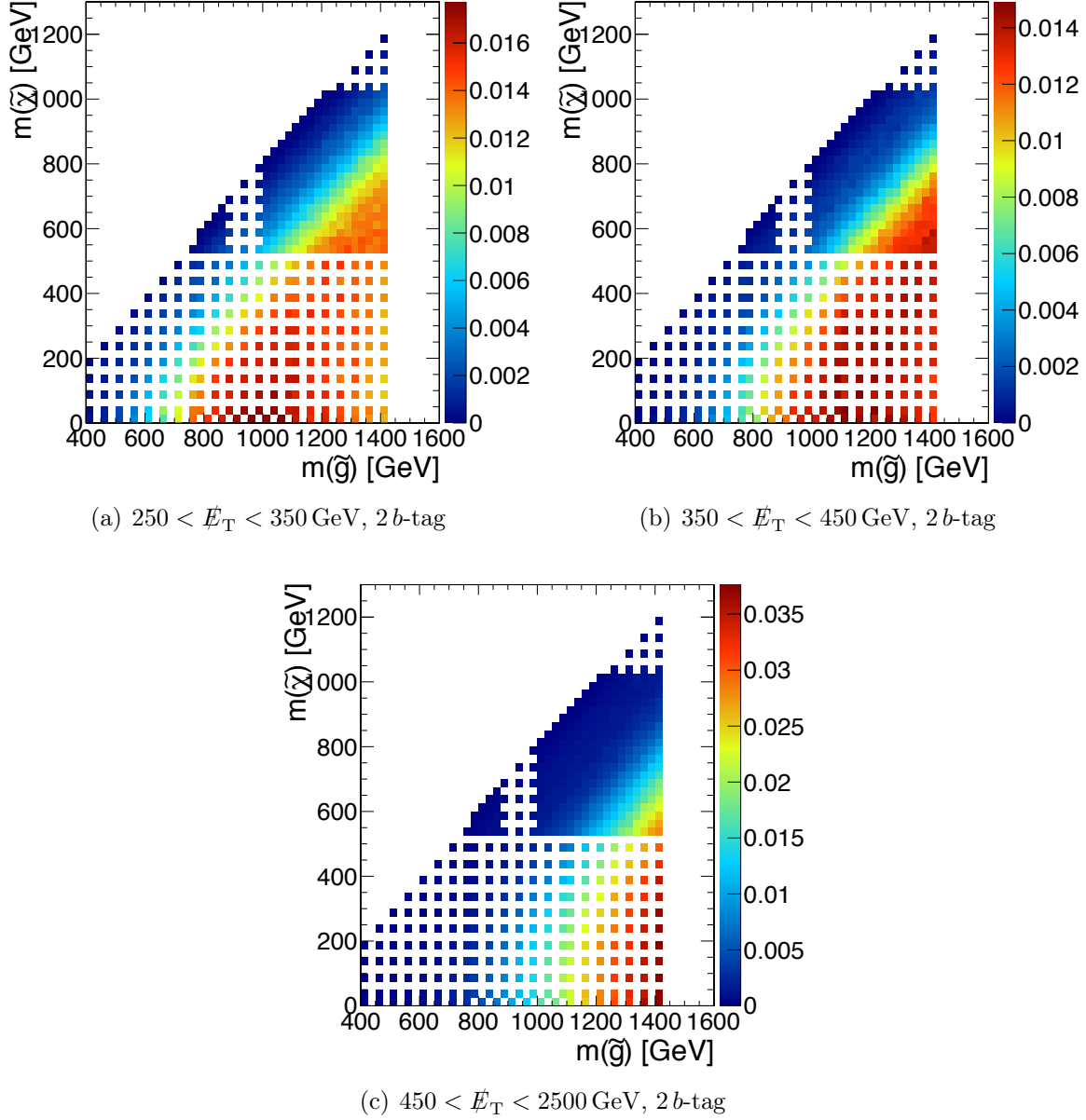


Figure E.5.: Efficiency for $T1ttttt$ for signal regions with $750 < H_T < 2500$ GeV in the 2 b -tag category.

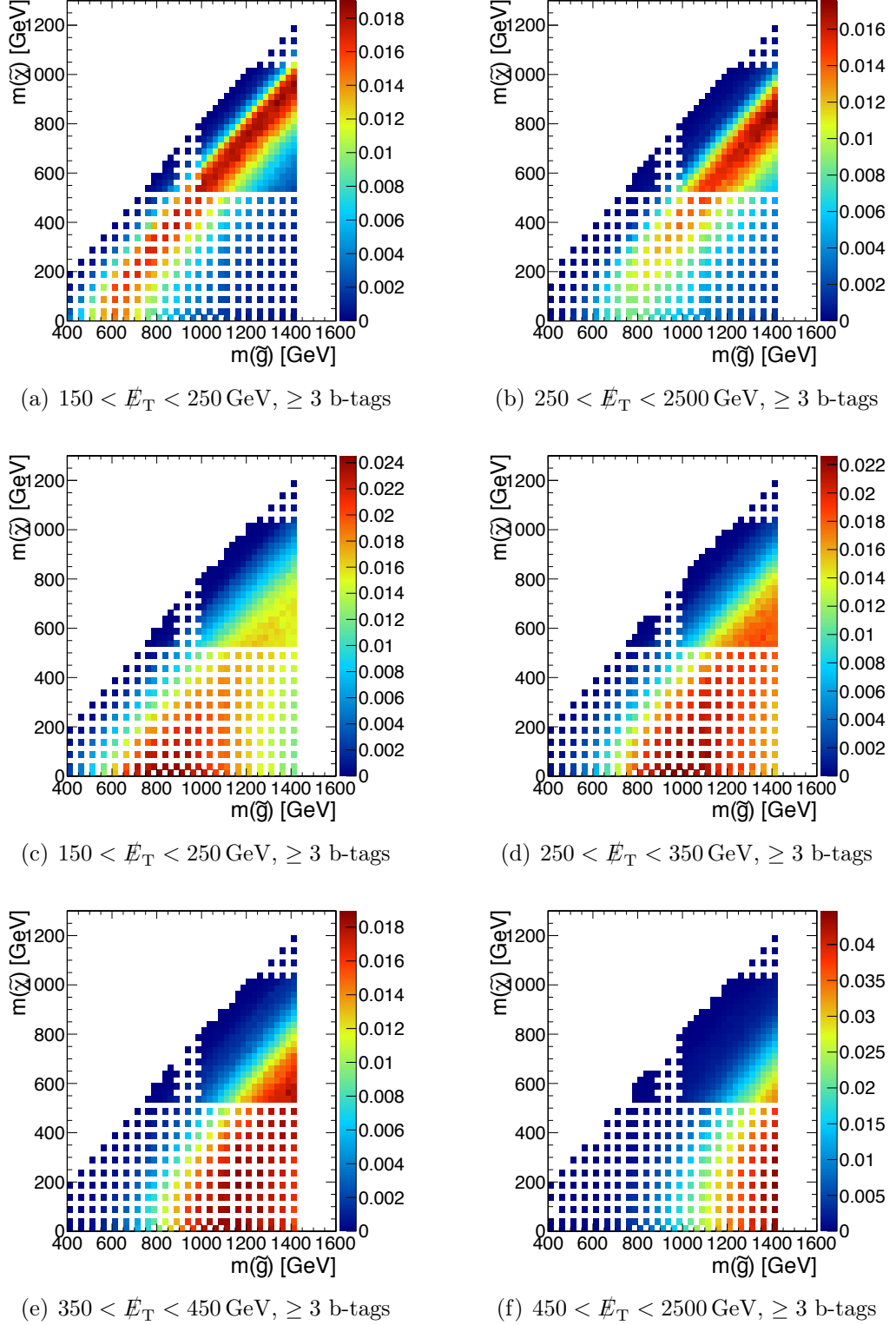


Figure E.6.: Efficiency for T1ttttt for signal regions with $400 < H_T < 750 \text{ GeV}$ (a), (b) and $750 < H_T < 2500 \text{ GeV}$ (c)-(f) in the $\geq 3 \text{ b-tag}$ category.

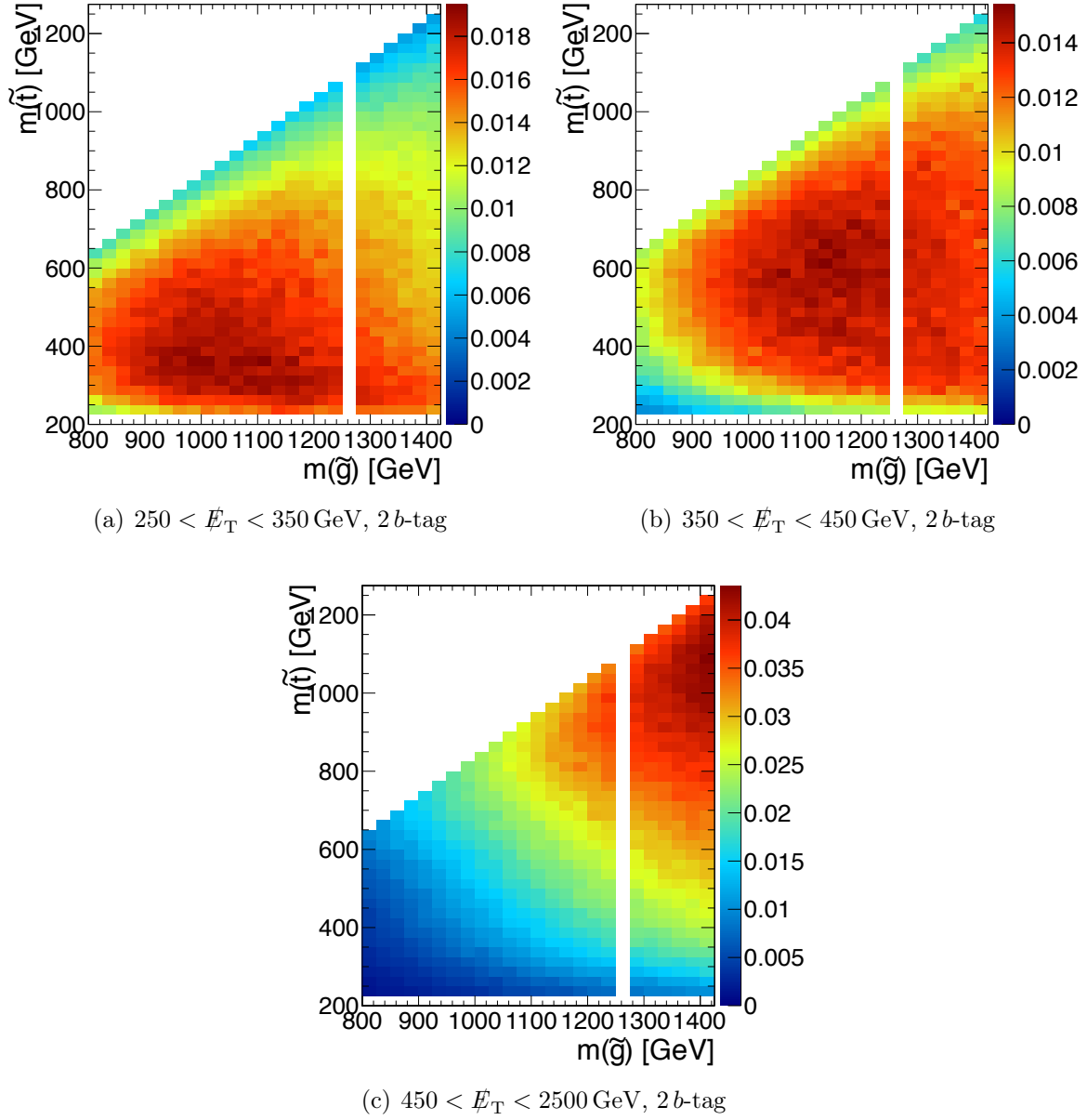


Figure E.7.: Efficiency for T5ttttt for signal regions with $750 < H_T < 2500$ GeV in the 2 b -tag category.

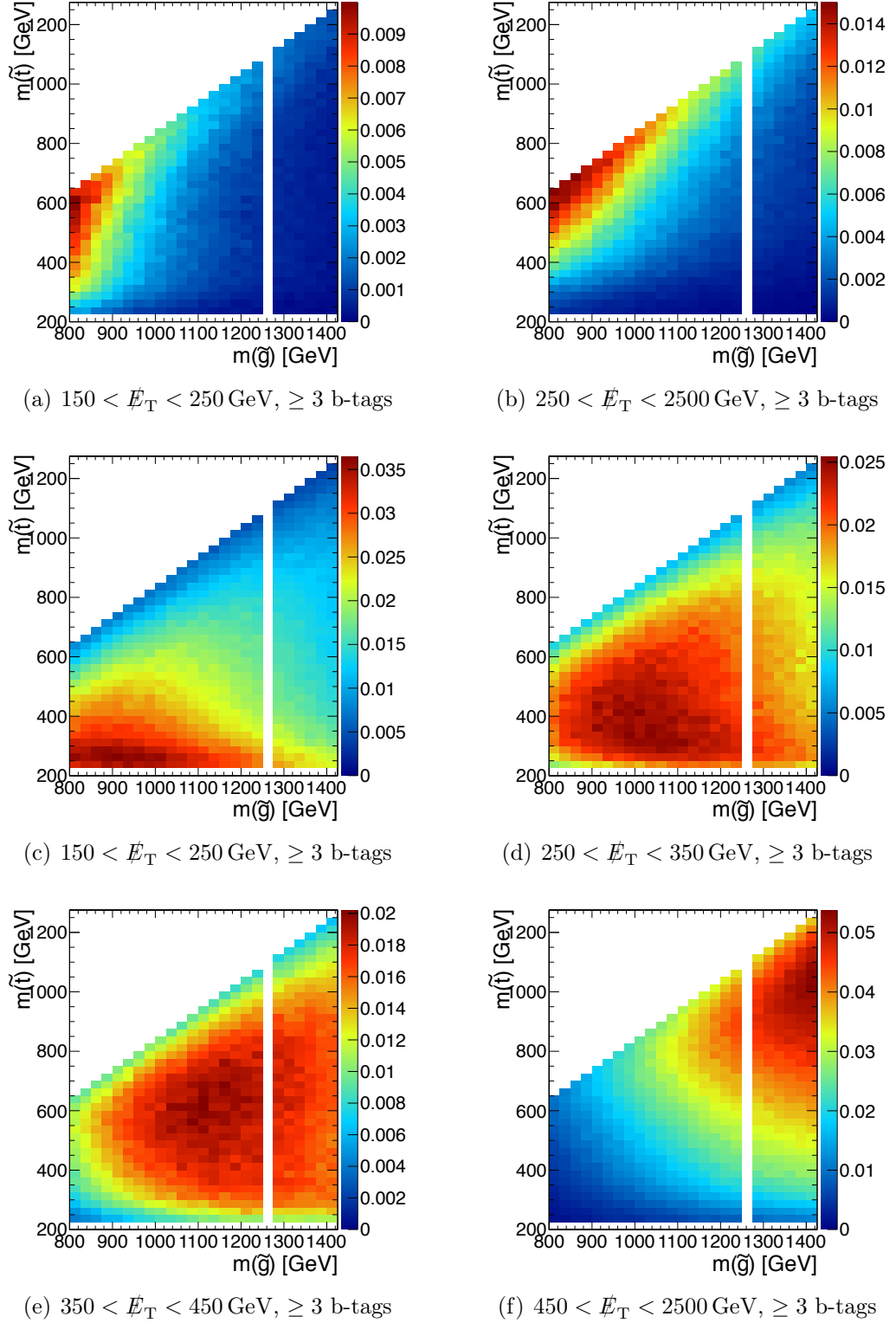


Figure E.8.: Efficiency for T5ttttt for signal regions with $400 < H_T < 750$ GeV (a), (b) and $750 < H_T < 2500$ GeV (c)-(f) in the ≥ 3 b-tag category.

E.3. b -tagging efficiency uncertainty

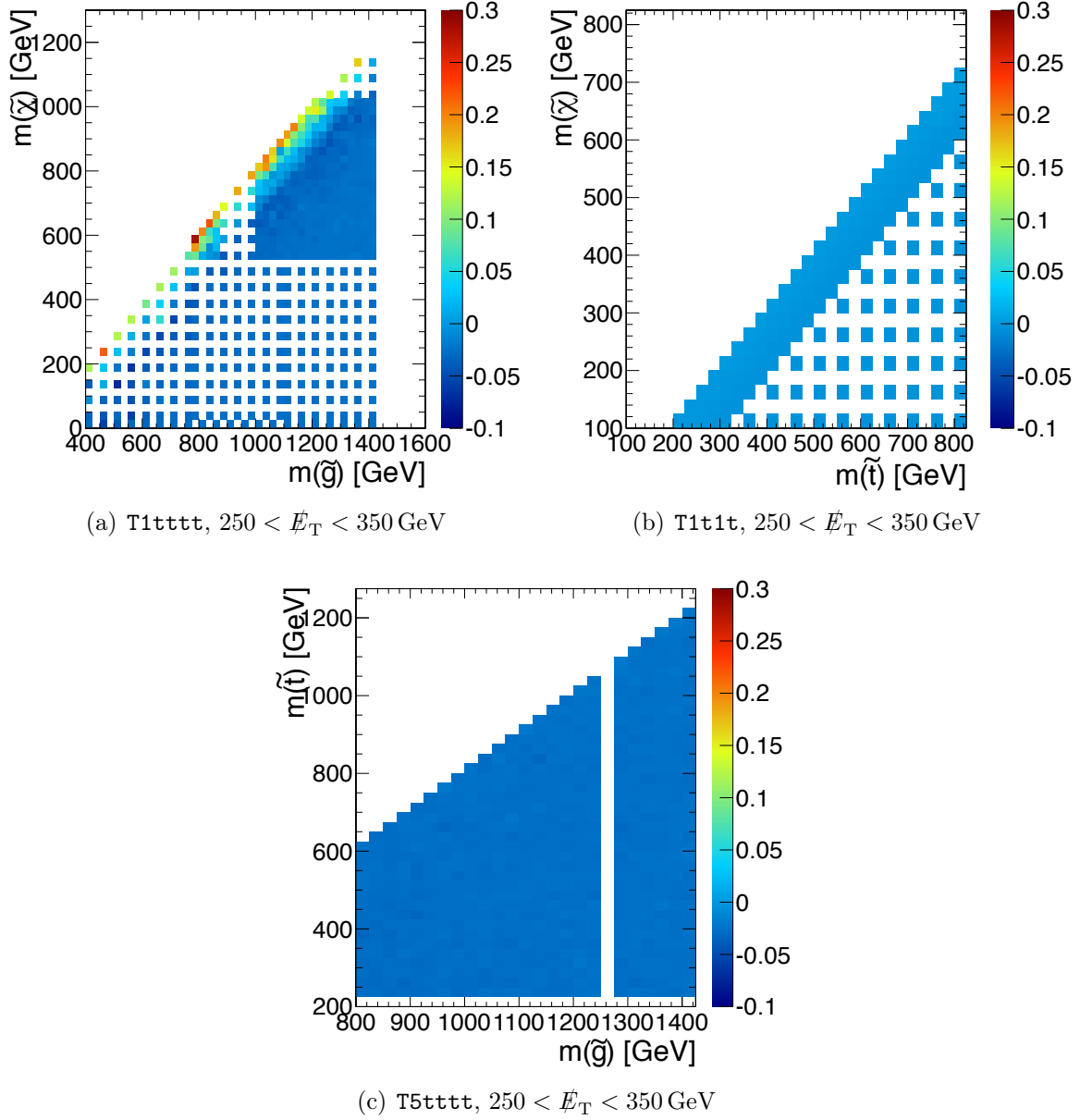


Figure E.9.: Acceptance uncertainties related to the light jet tagging scale-factor in the 2 b -tag category for $750 \text{ GeV} < H_T$ and $250 < \cancel{E}_T < 350 \text{ GeV}$.

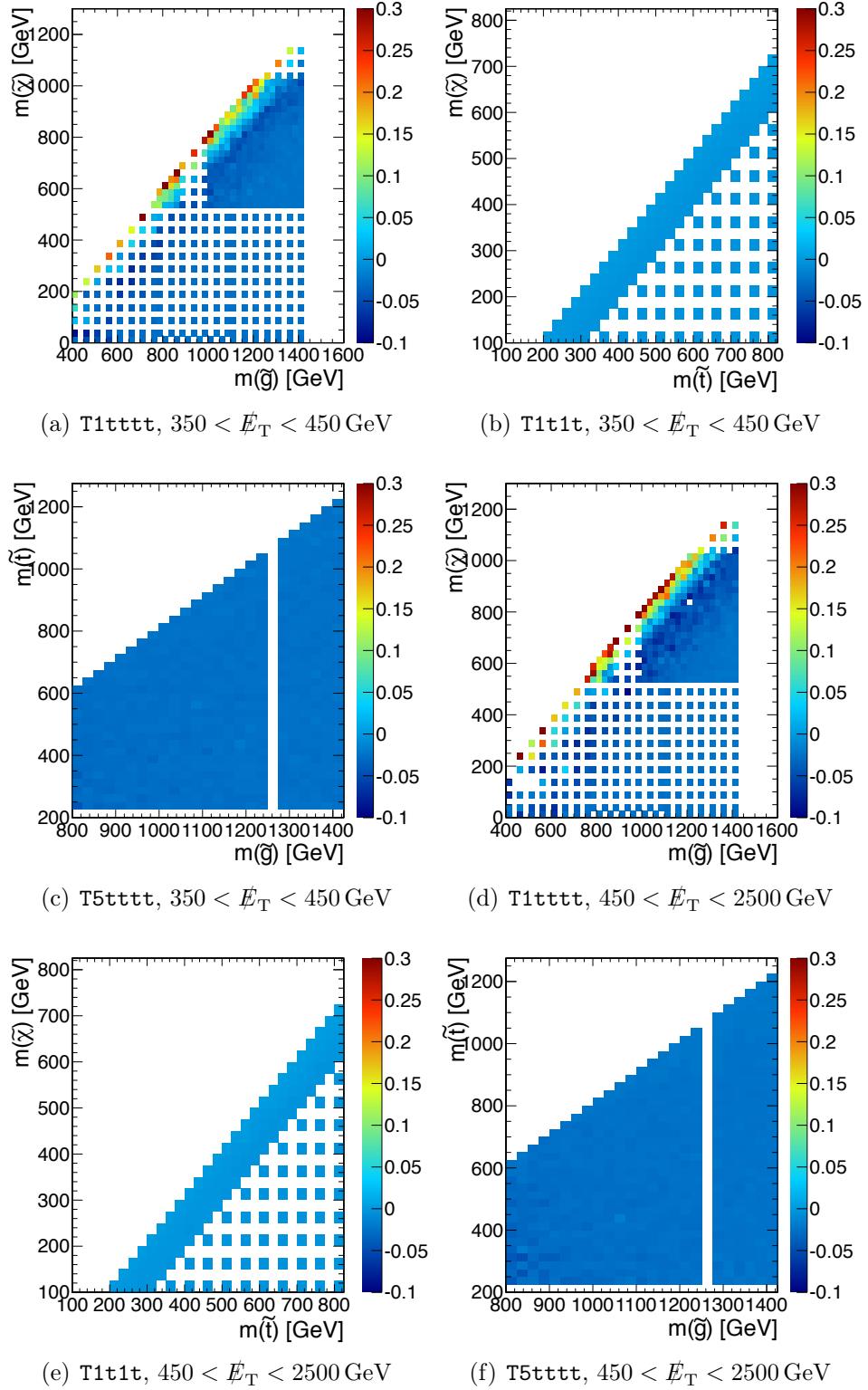


Figure E.10.: Acceptance uncertainties related to the light jet tagging scale-factor in the 2 b -tag category for $750 \text{ GeV} < H_T$.

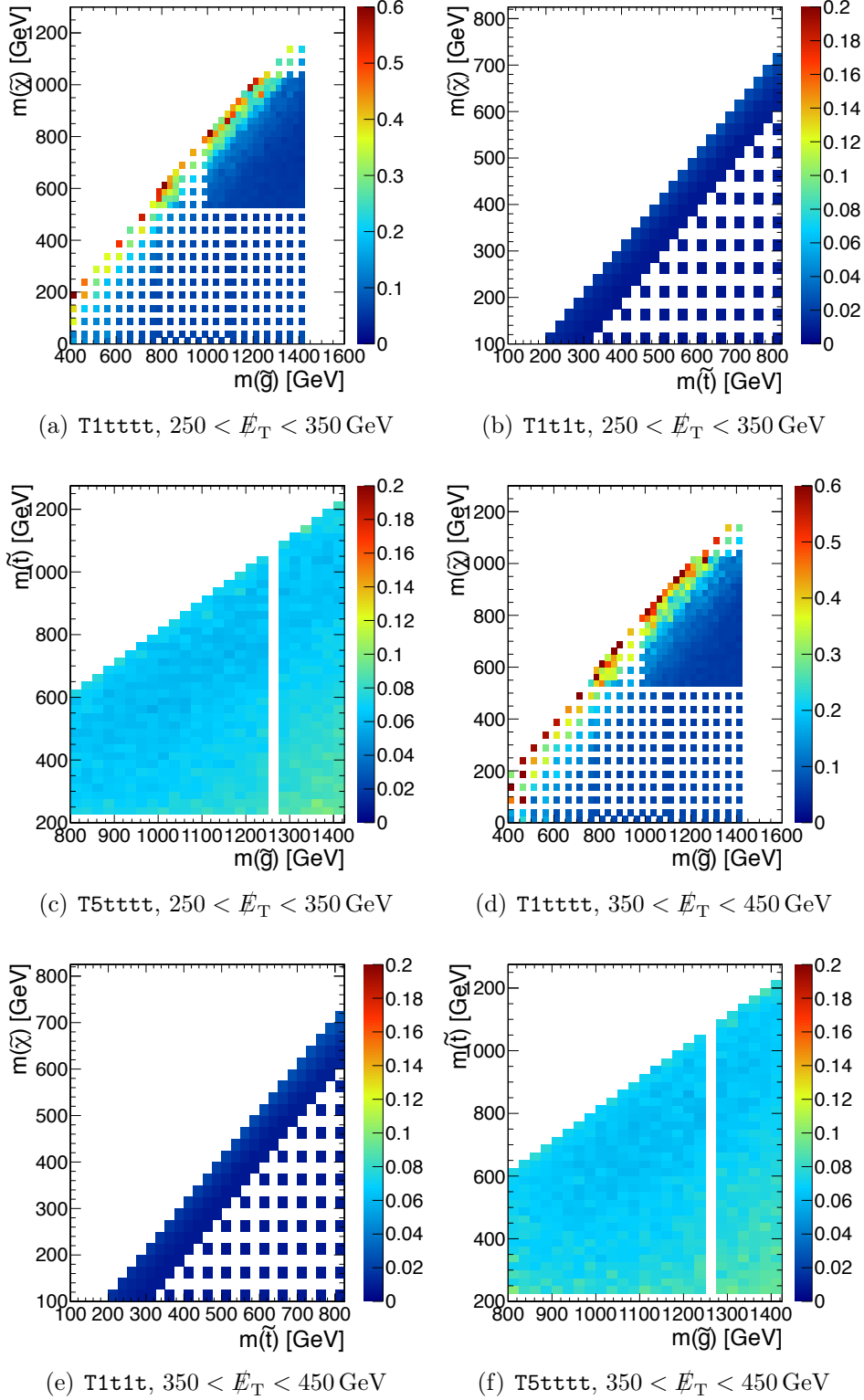


Figure E.11.: Acceptance uncertainties related to the light jet tagging scale-factor in the ≥ 3 b -tag category for $750 \text{ GeV} < H_T$ and $250 < \cancel{E}_T < 350 \text{ GeV}$.

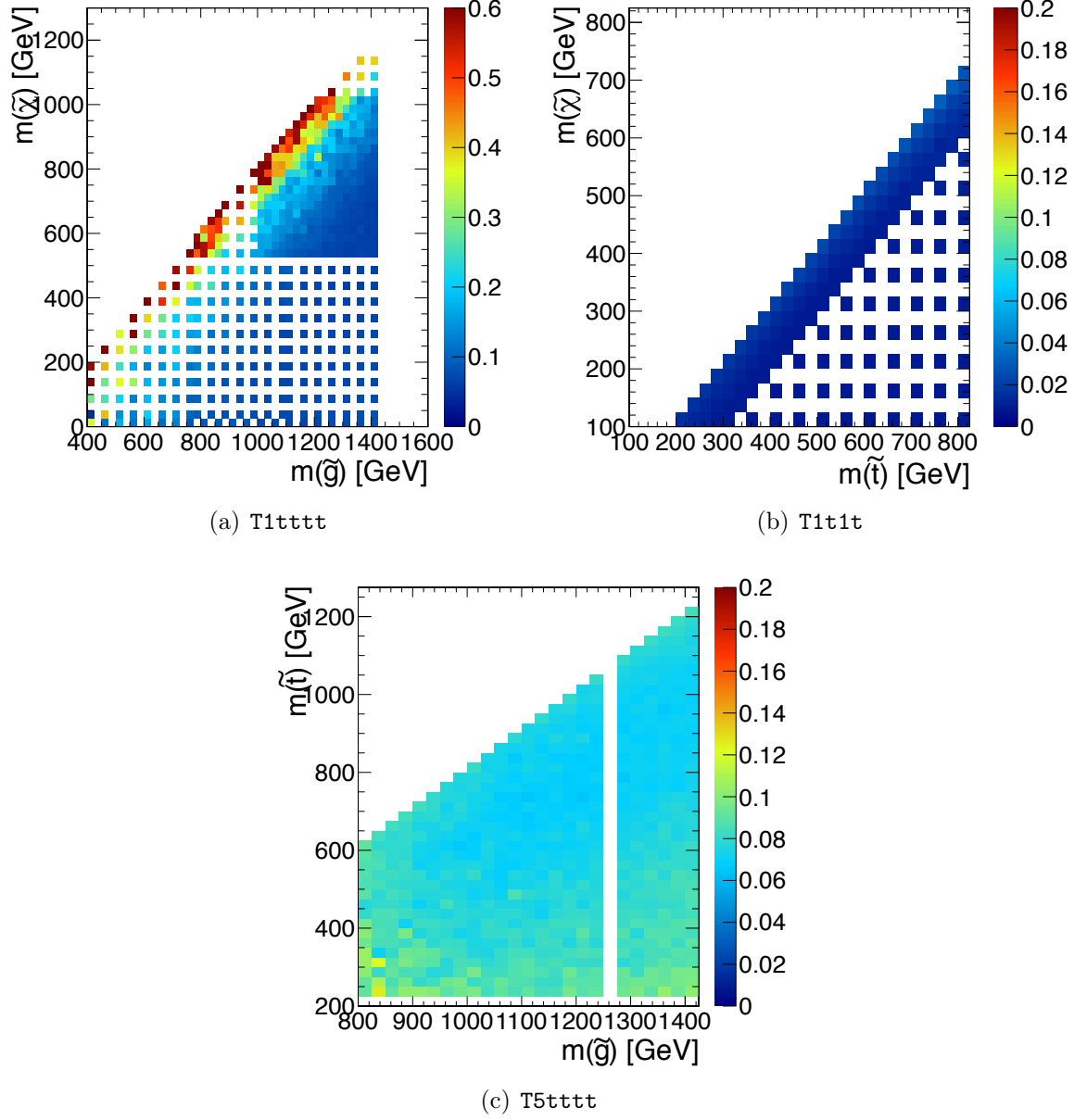


Figure E.12.: Acceptance uncertainties related to the light jet tagging scale-factor in the ≥ 3 b -tag category for $750 \text{ GeV} < H_T$ and $450 < \cancel{E}_T < 2500 \text{ GeV}$.

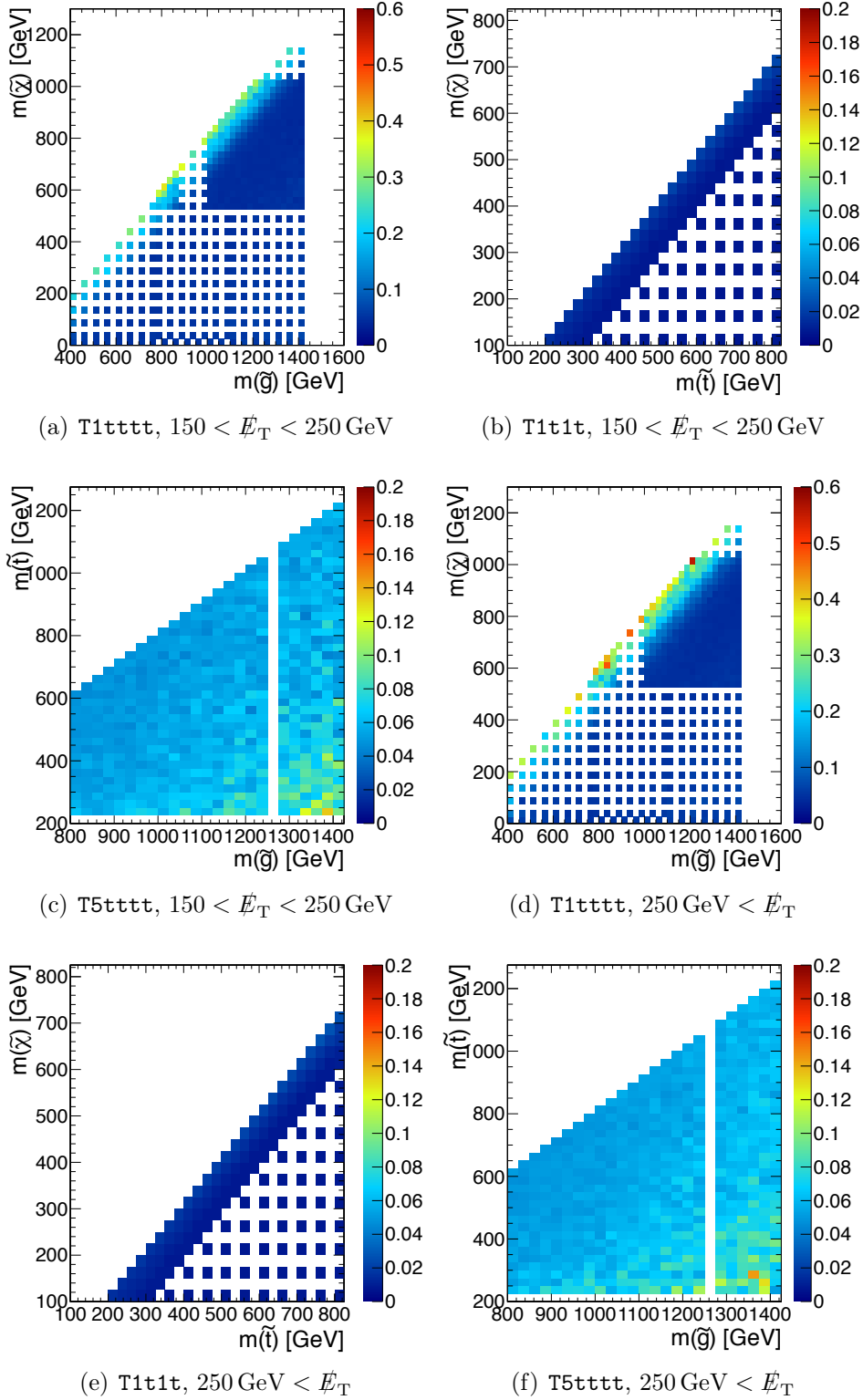


Figure E.13.: Acceptance uncertainties related to the light jet tagging scale-factor in the ≥ 3 b -tag category for $400 \text{ GeV} < H_T < 750 \text{ GeV}$.

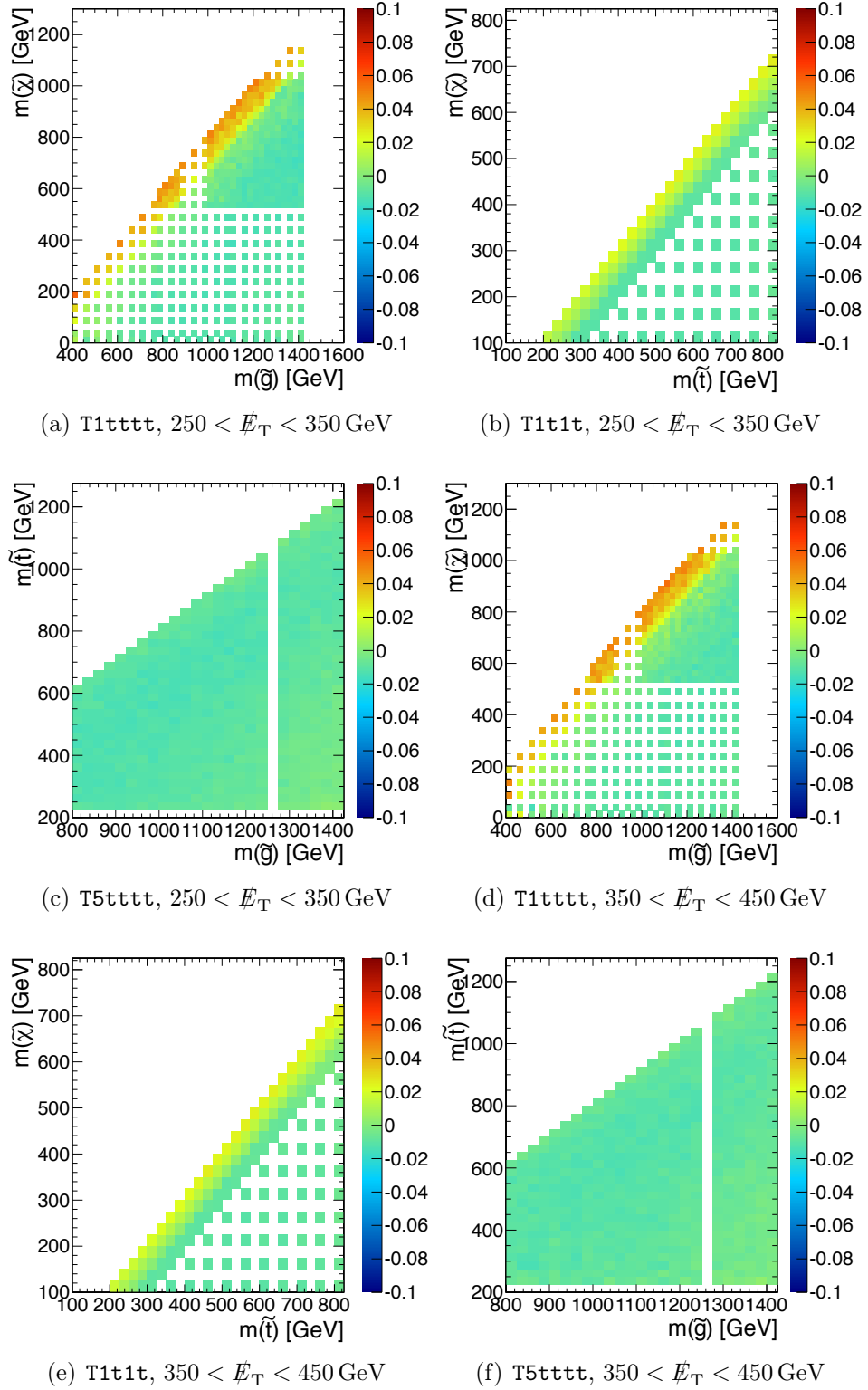


Figure E.14.: Acceptance uncertainties related to the b-tagging scale-factor in the 2 b -tag category for $750 \text{ GeV} < H_T$.

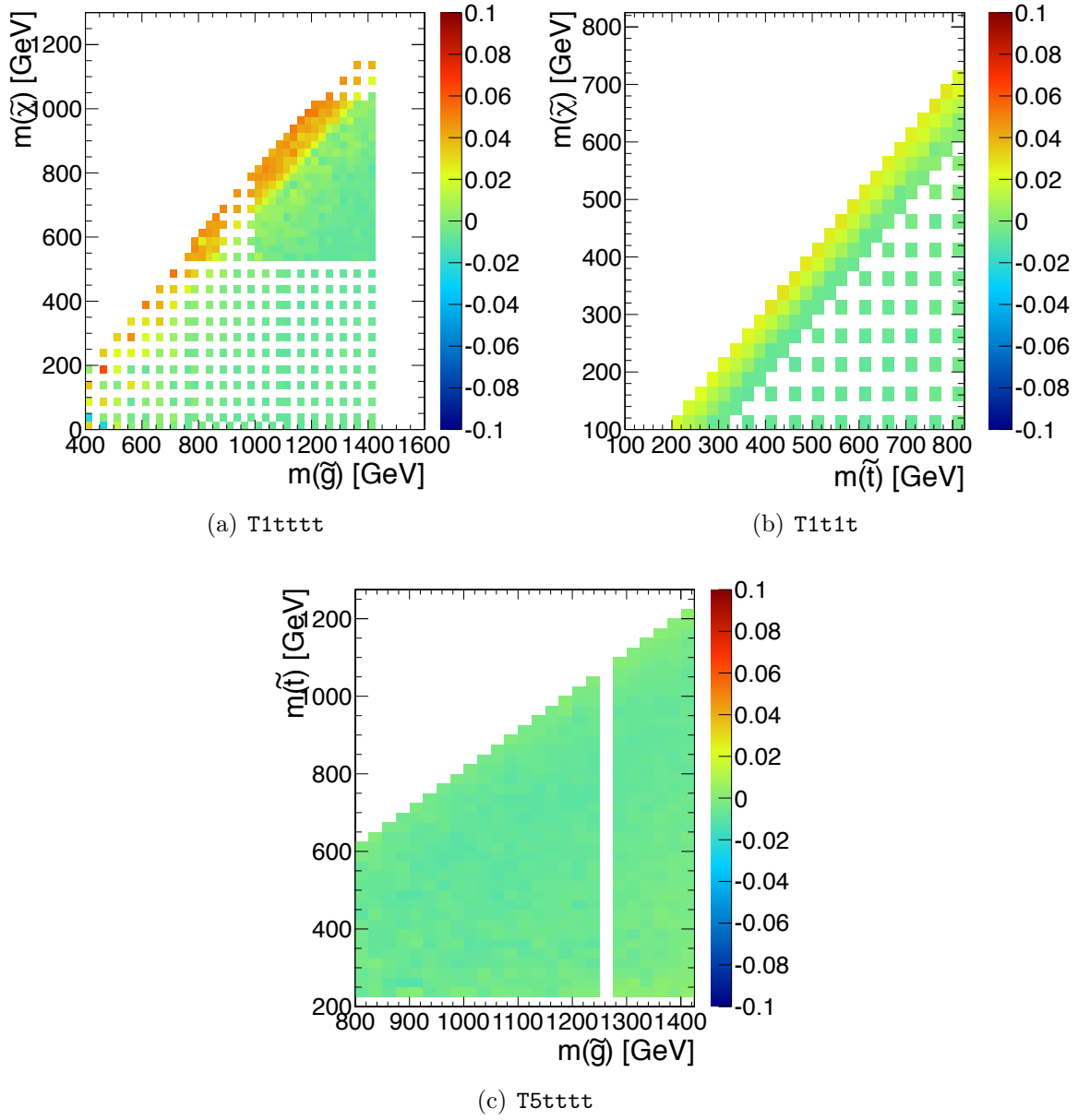


Figure E.15.: Acceptance uncertainties related to the b -tagging scale-factor in the 2 b -tag category for $750 \text{ GeV} < H_T$ and $450 < \cancel{E}_T < 2500 \text{ GeV}$.

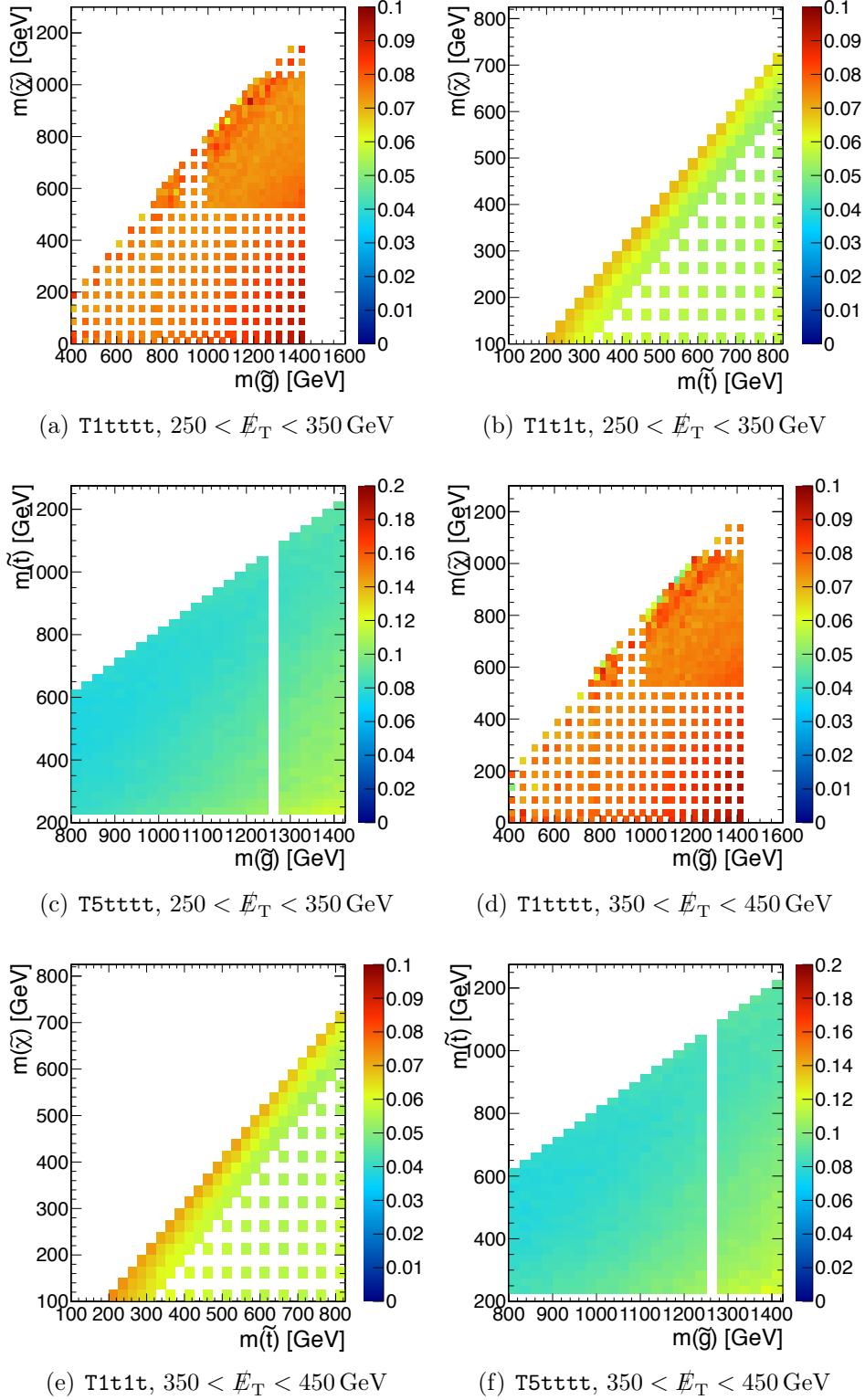


Figure E.16.: Acceptance uncertainties related to the b -tagging scale-factor in the ≥ 3 b -tag category for $750 \text{ GeV} < H_T$.

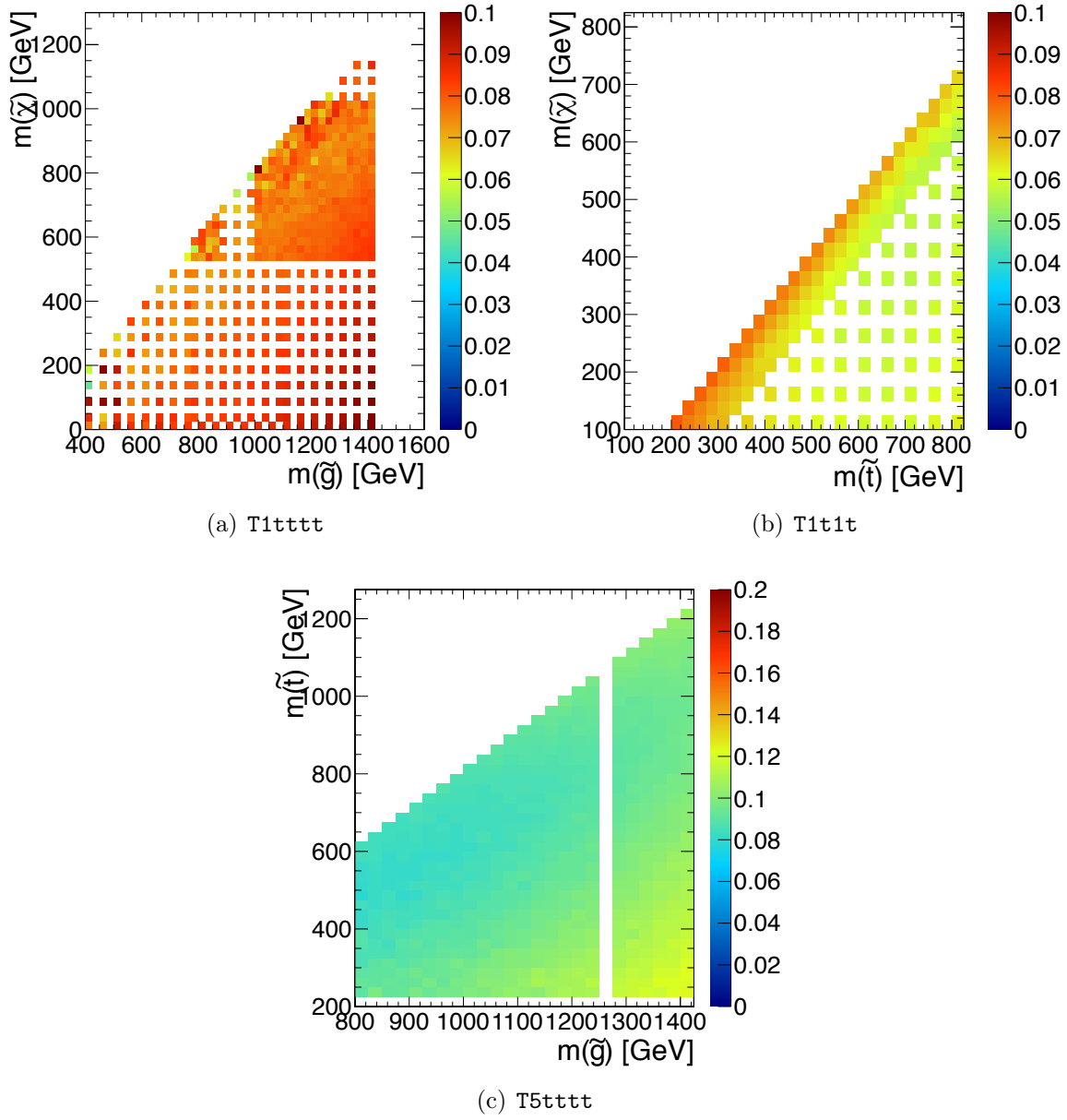


Figure E.17.: Acceptance uncertainties related to the b -tagging scale-factor in the ≥ 3 b -tag category for $750 \text{ GeV} < H_T$ and $450 < \cancel{E}_T < 2500 \text{ GeV}$.

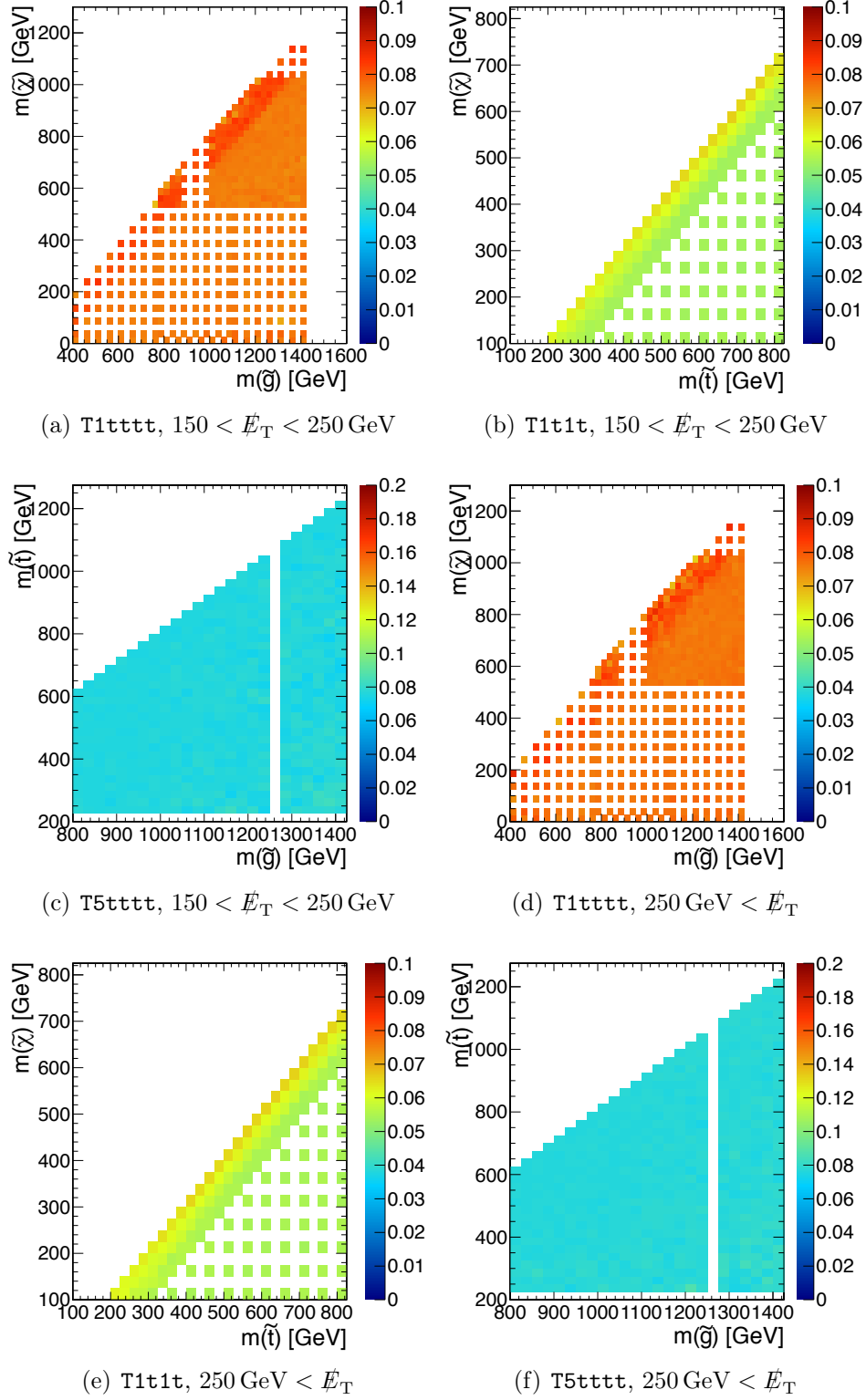


Figure E.18.: Acceptance uncertainties related to the b-tagging scale-factor in the ≥ 3 b-tag category for $400 \text{ GeV} < H_T < 750 \text{ GeV}$.

E.4. Jet energy scale uncertainty

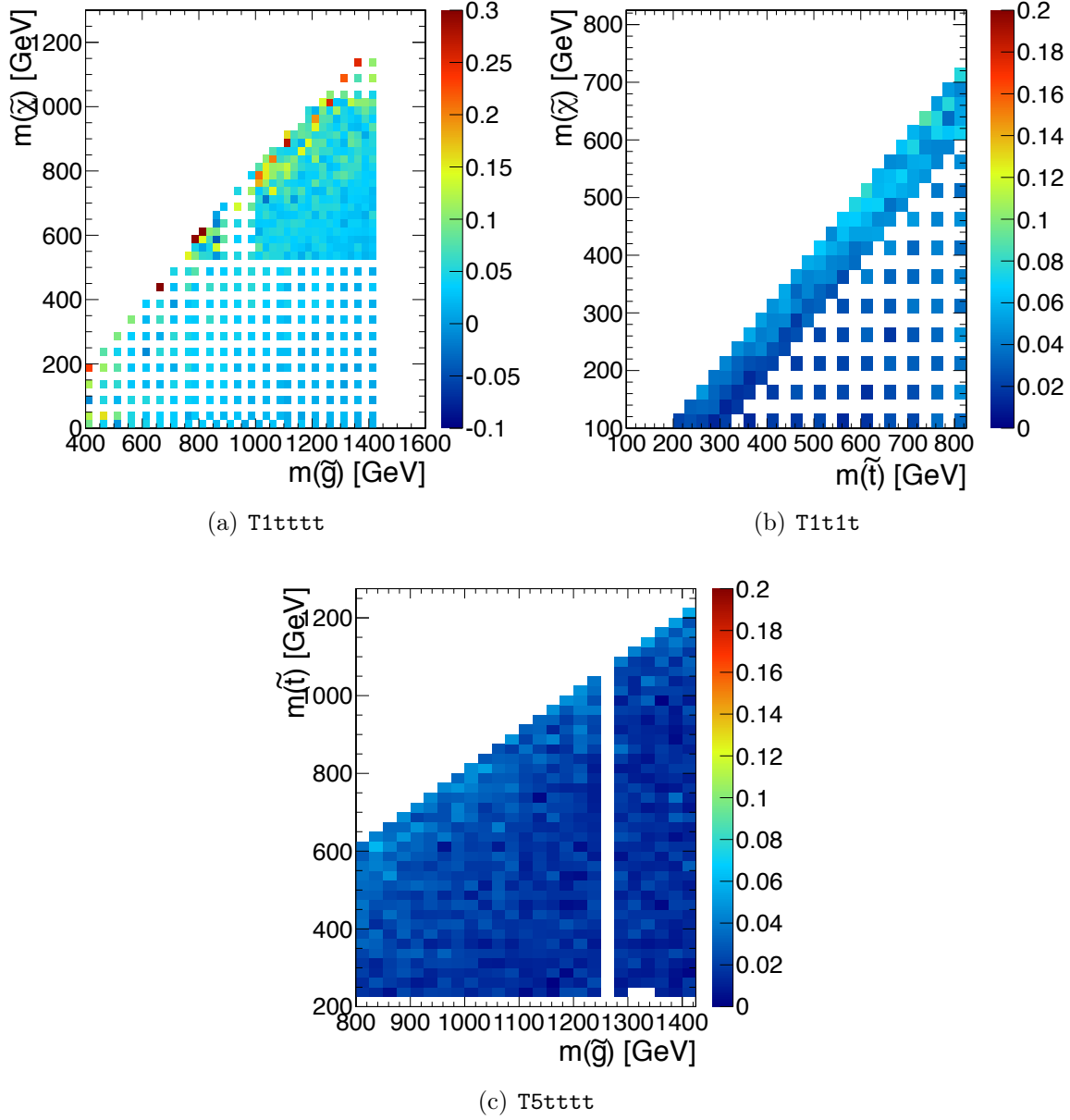


Figure E.19.: Acceptance uncertainties related to the jet energy scale in the 2 b -tag category for $750 \text{ GeV} < H_T$ and $250 < \cancel{E}_T < 350 \text{ GeV}$.

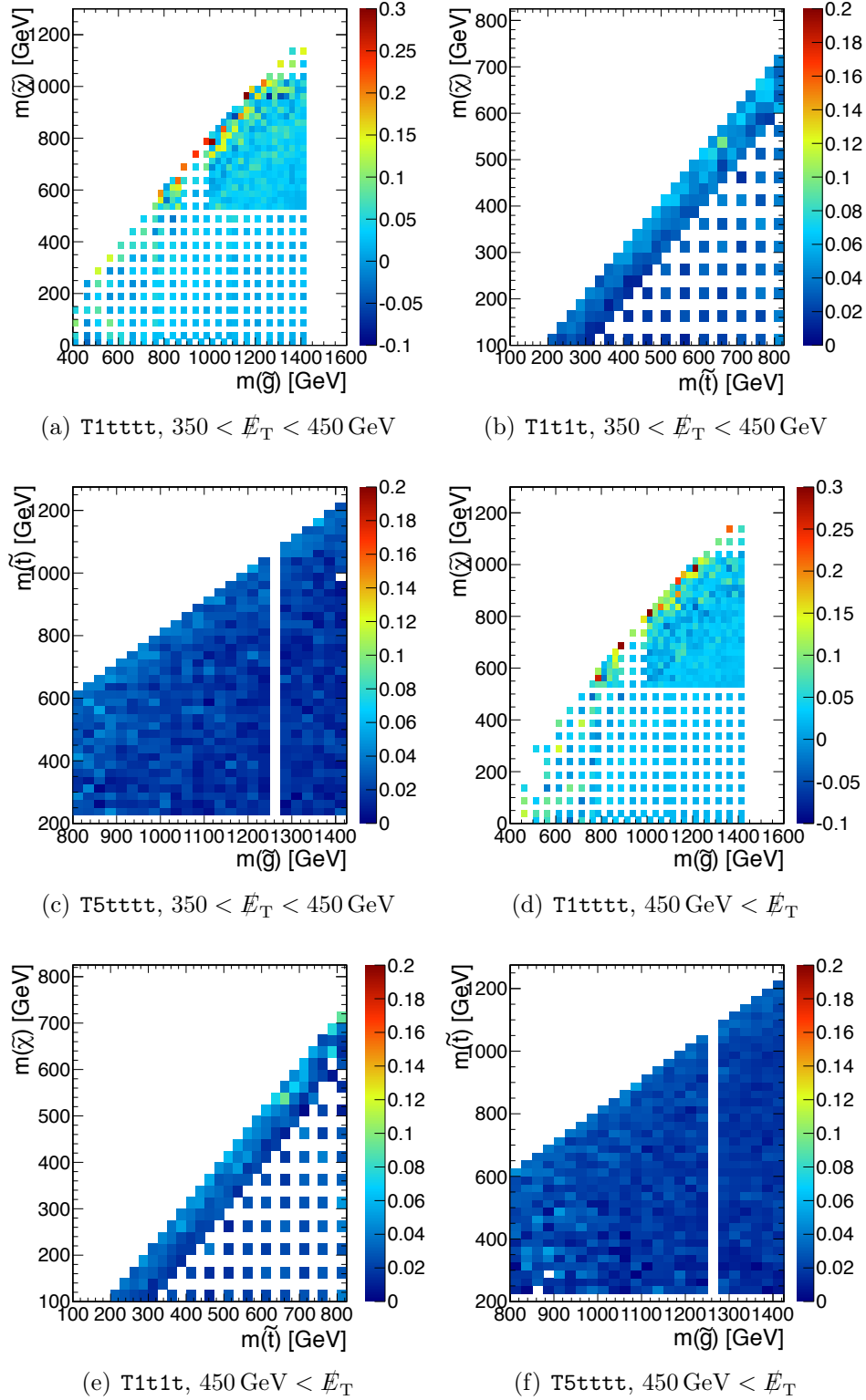


Figure E.20.: Acceptance uncertainties related to the jet energy scale in the 2 b -tag category for $750 \text{ GeV} < H_T$.

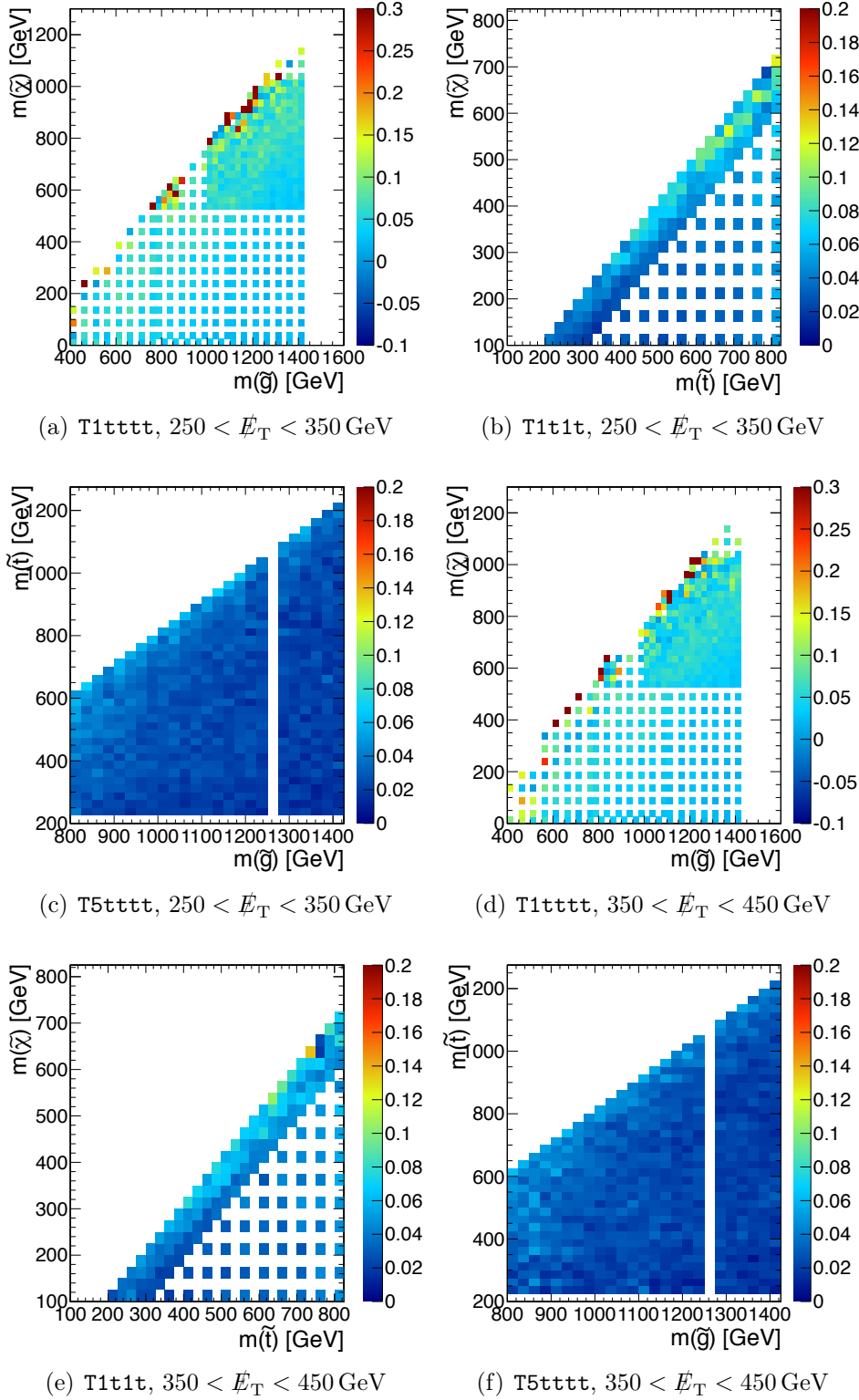


Figure E.21.: Acceptance uncertainties related to the jet energy scale in the ≥ 3 b -tag category for $750 \text{ GeV} < H_T$.

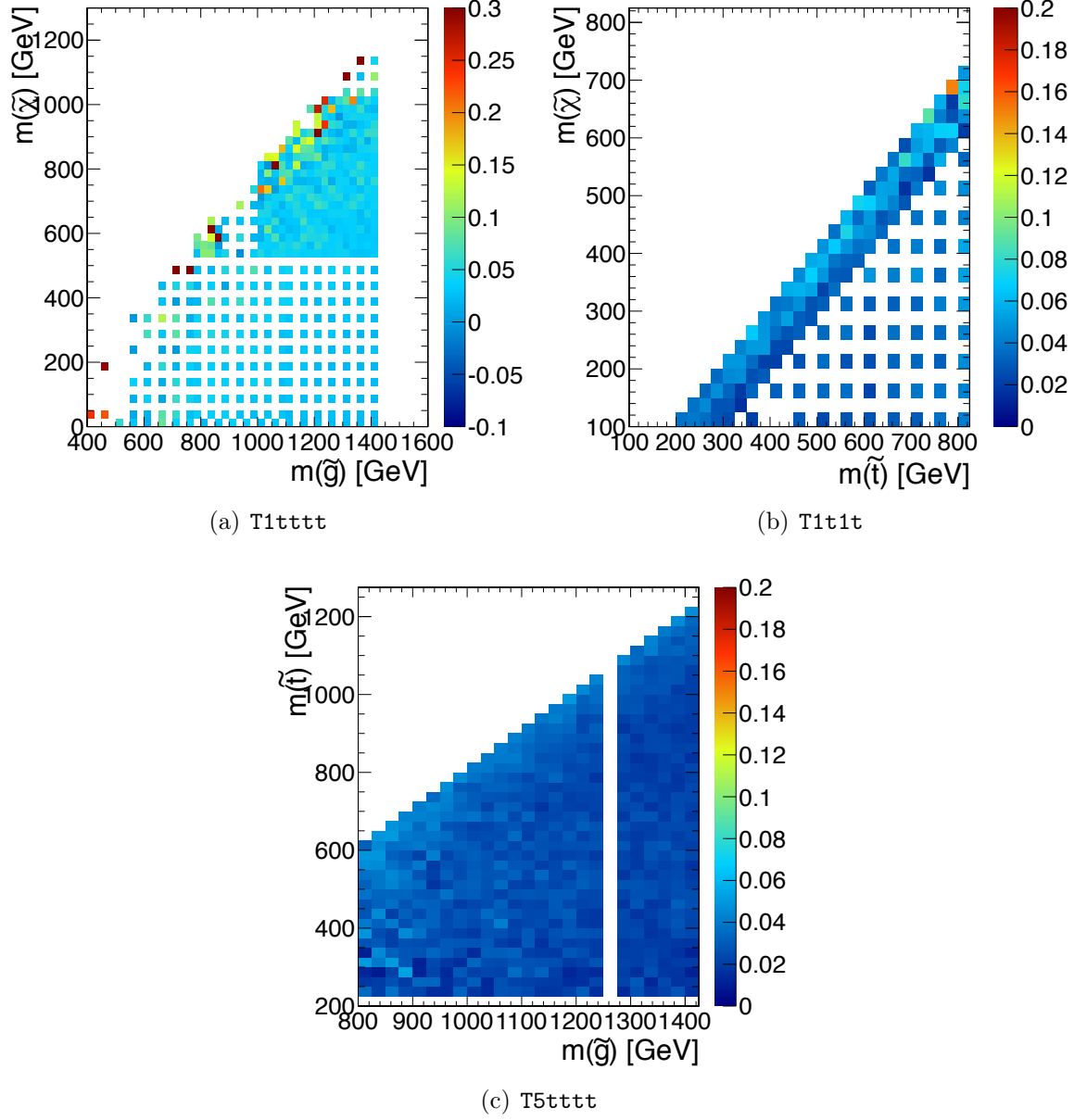


Figure E.22.: Acceptance uncertainties related to the jet energy scale in the ≥ 3 b -tag category for $750 \text{ GeV} < H_T$ and $450 < \cancel{E}_T < 2500 \text{ GeV}$.

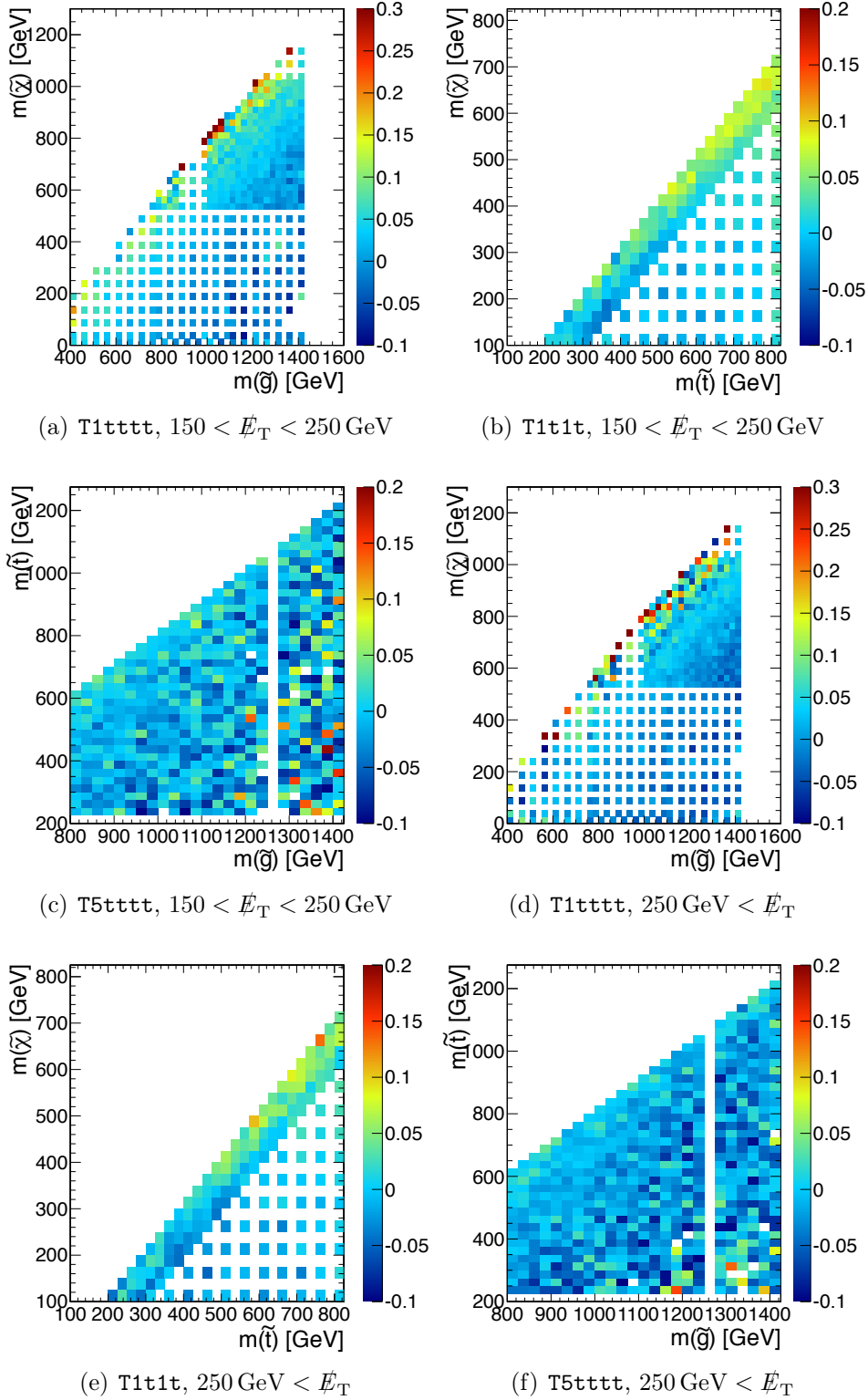


Figure E.23.: Acceptance uncertainties related to the jet energy scale in the ≥ 3 b -tag category for $400 \text{ GeV} < H_T < 750 \text{ GeV}$.

E.5. ISR uncertainty

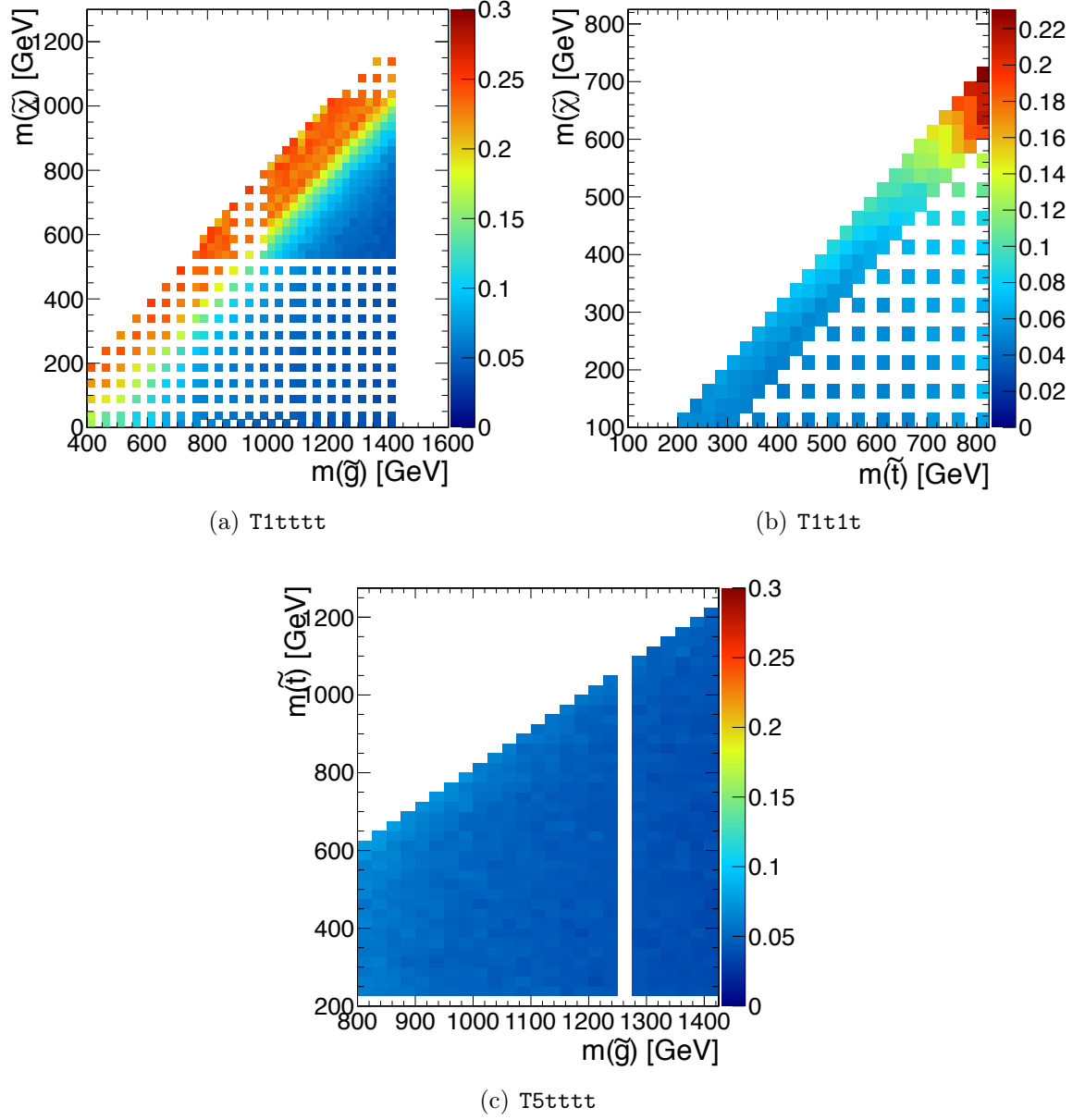


Figure E.24.: Acceptance uncertainties related to the uncertainty on initial state radiation (ISR) in the 2 b -tag category for $750 \text{ GeV} < H_T$ and $250 < \cancel{E}_T < 350 \text{ GeV}$.

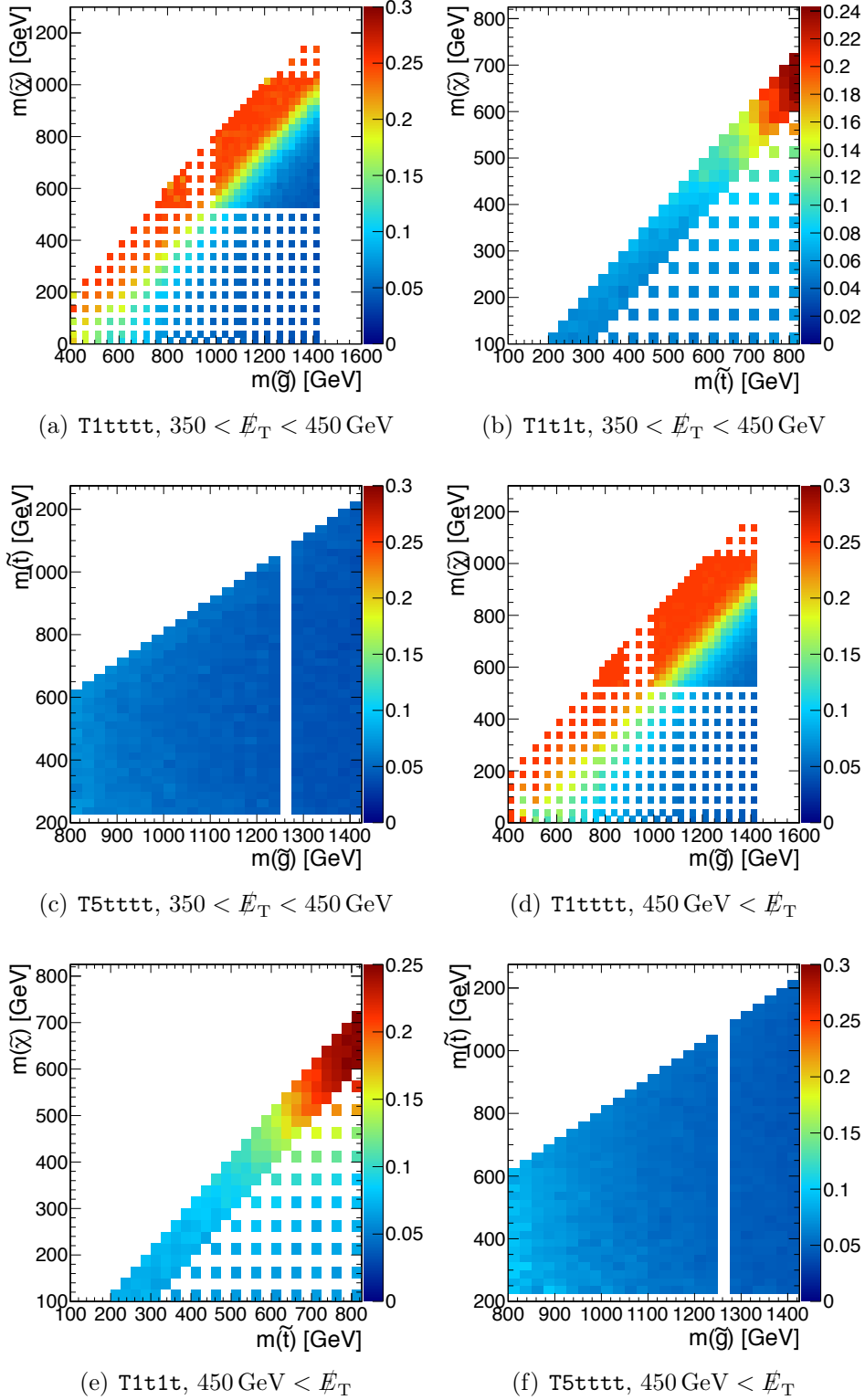


Figure E.25.: Acceptance uncertainties related to the uncertainty on initial state radiation (ISR) in the 2 b -tag category for $750 \text{ GeV} < H_T$.

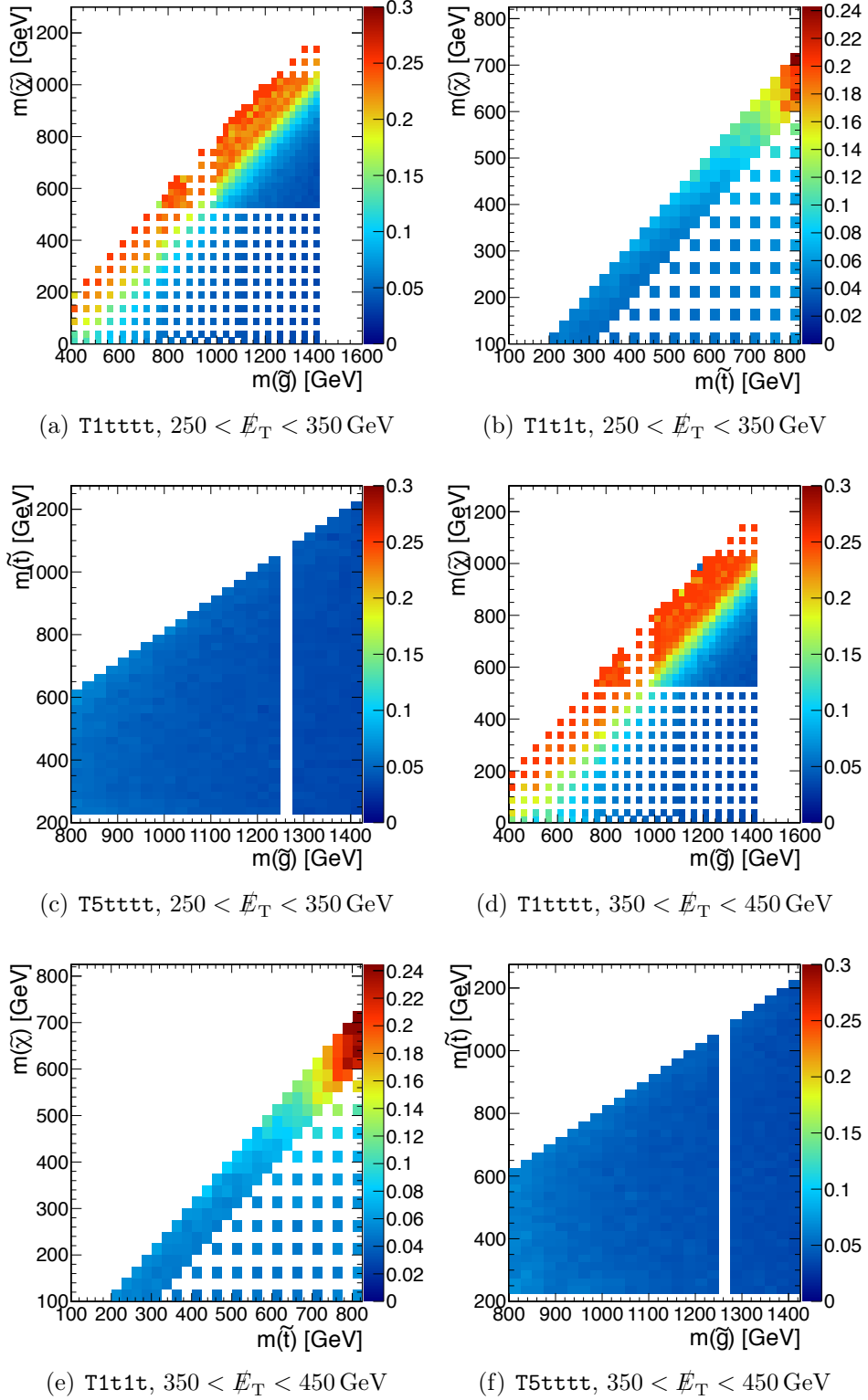


Figure E.26.: Acceptance uncertainties related to the uncertainty on initial state radiation (ISR) in the ≥ 3 b -tag category for $750 \text{ GeV} < H_T$.

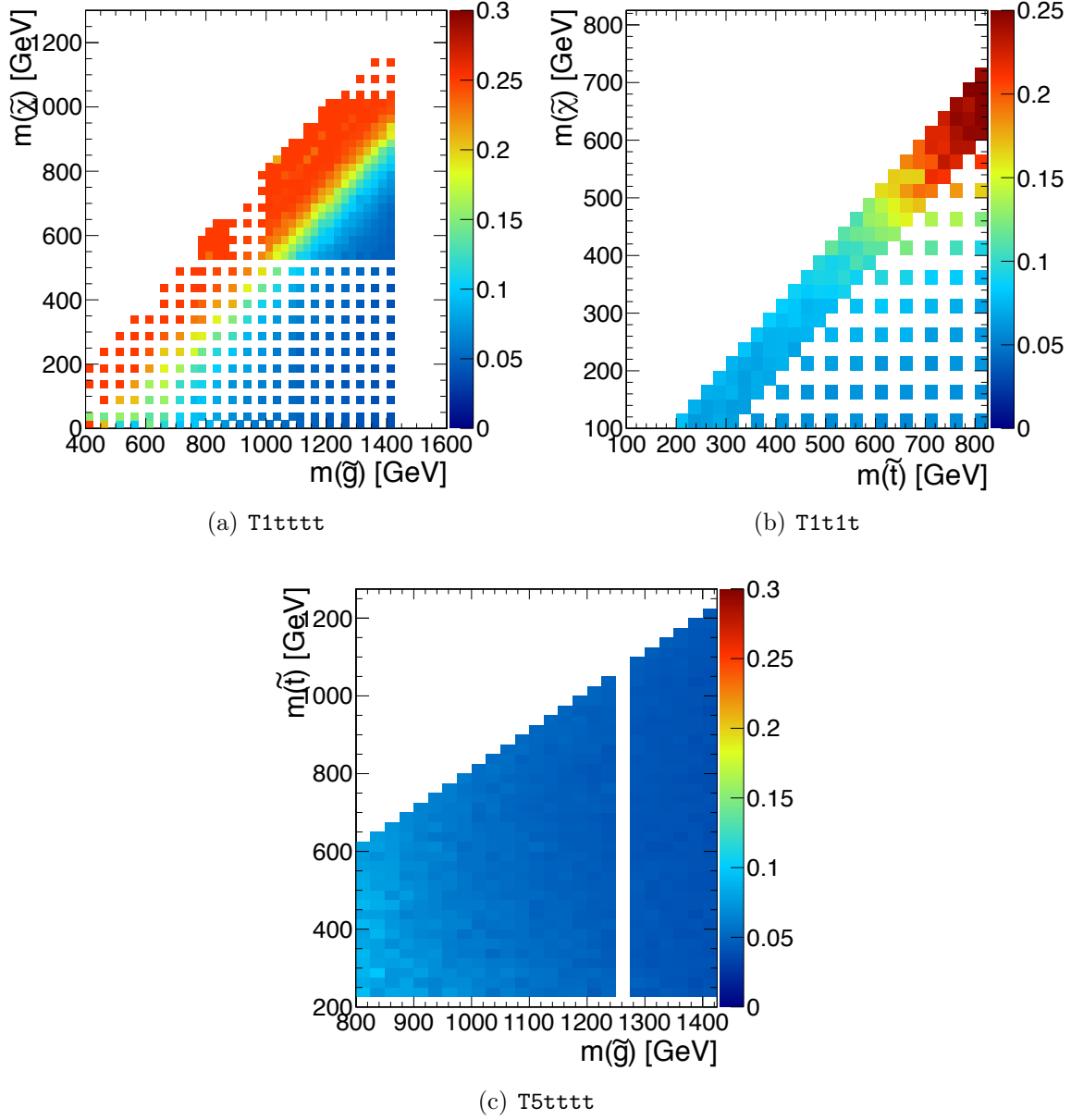


Figure E.27.: Acceptance uncertainties related to the uncertainty on initial state radiation (ISR) in the ≥ 3 b -tag category for $750 \text{ GeV} < H_T$ and $450 < \cancel{E}_T < 2500 \text{ GeV}$.

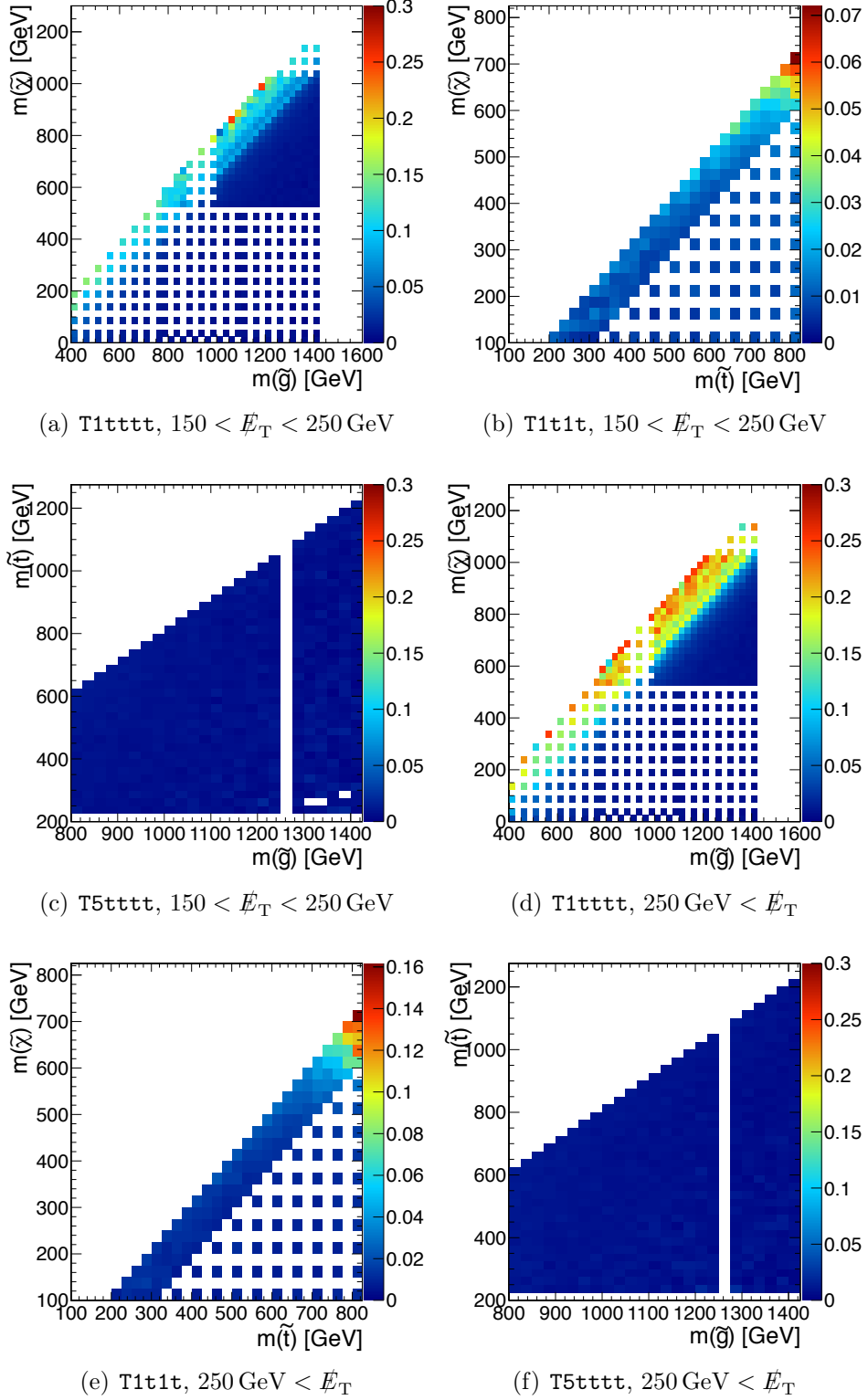


Figure E.28.: Acceptance uncertainties related to the uncertainty on initial state radiation (ISR) in the ≥ 3 b -tag category for $400 \text{ GeV} < H_T < 750 \text{ GeV}$ and $150 < \cancel{E}_T < 250 \text{ GeV}$.

List of Figures

1.1.	Evolution of the inverse gauge couplings $\alpha^{-1}(Q)$. [19]	6
1.2.	One-loop corrections to the Higgs boson mass, for (a) a Dirac fermion f , and (b) a scalar S	7
1.3.	Renormalization group evolution with MSUGRA boundary conditions $m_0 = 200$ GeV, $m_{1/2} = -A_0 = 600$ GeV, $\tan \beta = 10$ and $\mu > 0$. [19] . . .	18
1.4.	Location of the CMS benchmark points in the m_0 vs. $m_{1/2}$ plane of the cMSSM for $\tan \beta = 10$, $A_0 = 0$ and $\mu > 0$. [45]	19
1.5.	Topologies of the simplified models T1ttttt (a) and T1t1t and T5ttttt (b) [51].	20
2.1.	Accelerator complex of CERN [63]	22
2.2.	Integrated luminosity versus time for 2010, 2011, 2012 (p - p collisions only) [66]	24
2.3.	Peak instantaneous luminosity per day for 2010, 2011, 2012 (p - p collisions only) [66]	24
2.4.	The CMS detector [68]	25
2.5.	Schematic cross section through the CMS silicon tracker [57]	26
2.6.	Schematic view of the electromagnetic calorimeter [71]	28
2.7.	Schematic view of the hadronic calorimeter and other subdetectors of CMS [57].	30
2.8.	Muon momentum resolution as function of p . [67]	31
2.9.	Schematic view of the muon system of CMS [67].	32
2.10.	Architecture of the Level-1 Trigger system. [57]	33
2.11.	Architecture of the data acquisition system. [57]	34
3.1.	Distribution for the number of interactions per bunch crossing [66] . . .	39
3.2.	PF E_T distribution for events passing a dijet selection without the 2012 cleaning algorithms applied (open markers), with the 2012 cleaning algorithms applied (filled markers), and simulated events (filled histograms) [109]	45

3.3. CSV discriminator distribution [110].	46
3.4. Misidentification probability vs. b -jet efficiency of several b -tagging algorithms for jets from (a) u -, d - and s -quarks as well as gluons, and (b) c -quarks. [110]	47
3.5. Multiplicity distributions for data and simulation in the ≥ 4 -jet selection, requiring at least one b -tagged jet: (a) number of isolated muons and (b) number of isolated electrons.	48
3.6. Multiplicity distributions for data and simulation: (a) number of reconstructed primary vertices, (b) number of jets, and (c) number of b -tagged jets.	49
3.7. Distributions of (a) p_T of the leading jet, (b) H_T and (c) \cancel{E}_T	49
3.8. Distribution of \cancel{E}_T for a selection of low H_T ($400 < H_T < 750$ GeV) (left) and high H_T ($750 < H_T < 2500$ GeV) (right) and 1 b -tag (a,b), 2 b -tags (c,d) or ≥ 3 b -tags (e,f).	50
3.9. The efficiency ϵ_{ID1} (a,b) and ϵ_{ID2} (c-f). Both efficiencies are shown as a function of p_T for $ \eta < 2.1$ (a, c) and as a function of η for $p_T > 20$ GeV (b, d). Since ϵ_{ID2} includes the relative isolation requirement also the dependence on n_{vtx} (e) and n_{jets} (f) for $p_T > 20$ GeV and $ \eta < 2.1$ is shown.	52
3.10. ϵ_{GSF} as a function of p_T for $ \eta < 2.5$ (left) and η for $p_T > 20$ GeV (right).	53
3.11. Efficiency of the electron identification requirement (including isolation) as a function of p_T for $ \eta < 1.2$ (a) and $1.2 < \eta < 2.5$ (b), as a function of η for $p_T > 20$ GeV (c) and as function of the number of jets ($p_{T,\text{jet}} > 40$ GeV) for $ \eta > 2.5$ and $p_T > 20$ GeV (d).	54
3.12. Efficiency of the *_Mu15_* trigger leg as functions of the muon p_T and η	56
3.13. Efficiency of the *_Ele15_* trigger leg as functions of the muon p_T and η	56
3.14. The H_T turn-on curves for (a) Muon + H_T and for (b) Electron + H_T cross triggers for the run 2012B.	58
3.15. The \cancel{E}_T turn-on curves for the (a) muon + H_T + \cancel{E}_T and (b) electron + H_T + \cancel{E}_T cross triggers for the run 2012B.	58
3.16. Workflow of the estimation of the \cancel{E}_T spectrum to predict SM background yields in signal regions shown in 3.17.	59
3.17. Graphical representation of the different regions in \cancel{E}_T and H_T for events with (a) two and (b) at least three b -tagged jets.	60
3.18. Genuine- \cancel{E}_T distribution of simulated $t\bar{t}$ events with at least 2 jets (a), 3 jets (b), 4 jets (c) and 5 jets (d), with a fit of the generalized Pareto distribution (Eq. 3.9).	62

3.19. (a) Genuine- \cancel{E}_T distribution of simulated $t\bar{t}$ events with at least 6 jets and a fit of the Parteto distribution (Eq. 3.9). (b) Corresponding likelihood scan of the scale and shape parameters α and β	63
3.20. Ratio of the genuine- \cancel{E}_T spectrum for simulated $t\bar{t}$ events after requiring (a) $400 < H_T < 500$ GeV, (b) $700 < H_T < 800$ GeV, (c) $900 < H_T < 1000$ GeV and (d) $1000 < H_T < 1200$ GeV.	65
3.21. Evolution of the error function parameters (a) μ' , (b) σ' and (c) ξ with H_T in simulated $t\bar{t}$ events.	66
3.22. Ratio of the genuine- \cancel{E}_T spectrum for simulated $t\bar{t}$ events and the ≥ 4 -jet selection after requiring (a) $400 < H_T < 500$ GeV, (b) $700 < H_T < 800$ GeV, (c) $900 < H_T < 1000$ GeV and (d) $1000 < H_T < 1200$ GeV. . .	67
3.23. Evolution of the error function parameters (a) μ' , (b) σ' and (c) ξ with H_T for a selection of at least 4 jets in the 2 b -tag bin compared with simulated $t\bar{t}$ events.	68
3.24. Ratio of the genuine- \cancel{E}_T spectrum in b -jet multiplicity bins with respect to the inclusive spectrum for simulated $t\bar{t}$ events after requiring (a) $400 < H_T < 450$ GeV, (b) $550 < H_T < 600$ GeV, (c) $700 < H_T < 750$ GeV and (d) $1000 < H_T < 750$ GeV.	69
3.25. Distribution of b -tag multiplicity.	72
3.26. Ratio of W +jets to $t\bar{t}$ for (a) 1 b -tag and (b) 2 b -tag as predicted by the fit to b -tag multiplicity in data and simulation.	72
3.27. Comparison of the simulated H_T distributions for W +jets (left) and $t\bar{t}$ (right) simulation for different b -tag multiplicities. Overlaid are the data distributions in the 0 b -tag (left) and 2 b -tag bin (right).	73
3.28. Distribution of H_T obtained from different H_T triggers after correction for the trigger prescale factors.	74
3.29. \cancel{E}_T -resolution templates as measured in the QCD control region (dots) and $\cancel{E}_T^{\text{fake}}$ in the single lepton channel for different H_T bins (left, center, right) and the 0 b -tag (top) and ≥ 1 b -tag (bottom) bin.	76
3.30. Addition of $\cancel{E}_T^{\text{gen}}$ and $\cancel{E}_T^{\text{fake}}$ and the shift $\langle \cancel{E}_{T,\parallel}^{\text{fake}} \rangle$ to correct for the effects from the hadronic recoil.	76
3.31. Distribution of $\Delta\phi$ in the single-lepton selection of the simulated $t\bar{t}$ sample before and after correcting for the bias introduced by the recoiling jet system.	77
3.32. (a) Evolution of the shift $\langle \cancel{E}_{T,\parallel}^{\text{fake}} \rangle$ with H_T due to the recoiling jet system. (b) Distribution of $\cancel{E}_T^{\text{fake}}$ in bins of $\cancel{E}_T^{\text{gen}}$ in $t\bar{t}$ events for $H_T > 400$ GeV.	78
3.33. Values of the parameter (a) α and (b) β of the Pareto distribution describing the \cancel{E}_T spectrum for control regions with two to five jets and a lepton p_T threshold of 30 GeV.	79

3.34. Comparison of the predicted event yields with the counts from simulation for regions defined by (left) $750 < H_T < 2500$ GeV and (right) $1000 < H_T < 2500$ GeV, two b -tagged jets and (top) $250 < \cancel{E}_T < 2500$ GeV, (centre) $350 < \cancel{E}_T < 2500$ GeV and (bottom) $450 < \cancel{E}_T < 2500$ GeV. . .	82
3.35. Results from fits to simulation for the (left) 1 b -tag and (right) 2 b -tag bins with (top) $H_T > 400$ GeV, (middle) $H_T > 750$ GeV and (bottom) $H_T > 1000$ GeV.	83
3.36. Results from fits to data for the (left) 1 b -tag and (right) 2 b -tag bins with (top) $H_T > 400$ GeV, (middle) $H_T > 750$ GeV and (bottom) $H_T > 1000$ GeV.	84
3.37. The ≥ 3 b -tag to 2 b -tag scale factors R_{32} for events with (a) $3 \leq n_{jet} \leq 5$ and $150 < \cancel{E}_T < 250$ GeV, (b) $3 \leq n_{jet} \leq 5$ and $250 < \cancel{E}_T < 350$ GeV, (c) $n_{jet} == 5$ and 150 GeV $< \cancel{E}_T$ and (d) $6 \leq n_{jet}$ and 150 GeV $< \cancel{E}_T$. .	92
3.38. Data/MC comparison of the estimation of the probability to find a third b -jet in the event for (a) $250 \leq \cancel{E}_T \leq 350$ GeV and (b) $350 \leq \cancel{E}_T \leq 450$ GeV and $3 \leq n_{jets} \leq 5$	93
4.1. Predicted and measured event counts in data for the 2 b -tag signal regions (a) $750 < H_T < 2500$ GeV and (b) $1000 < H_T < 2500$ GeV. . . .	97
4.2. Predicted and measured event counts in data for the ≥ 3 b -tag signal regions (a) $400 < H_T < 2500$ GeV, (b) $750 < H_T < 2500$ GeV and (c) $1000 < H_T < 2500$ GeV.	98
4.3. Upper limits on the production cross section for $T1tttt$ as function of $m_{\tilde{g}}$ and $m_{\tilde{\chi}^0}$	103
4.4. Upper limits on the production cross section for (a) $T1t1t$ as function of $m_{\tilde{t}}$ and $m_{\tilde{\chi}^0}$ and for (b) $T5tttt$ as function of $m_{\tilde{g}}$ and $m_{\tilde{t}}$	104
4.5. Exclusion limits at 95% C.L. in the $m_{1/2}$ vs. m_0 cMSSM plane for $\tan \beta = 10$, $A_0 = 0$ and $\mu > 0$ using NLO cross sections and the multi-channel approach.	107
4.6. Signal efficiencies (left) and exclusion limits at 95% CL (right) as a function of the two mass parameters of the $T1tttt$ model.	108
B.1. Distribution of the parameter α and its normalized residuals for 250 toy experiments.	115
B.2. Distribution of the parameters β , μ_0 , μ_1 and their normalized residuals for 250 toy experiments.	116
B.3. Distribution of the parameters σ_0^2 , σ_1^2 , ξ and their normalized residuals for 250 toy experiments.	117

C.1. Control shape for (a) muons (HLT_HT650) and (b) electrons (HLT_HT750) for two different H_T requirements [126].	118
C.2. Signal regions and normalization sidebands corresponding to the regions shown in C.1: (a) muons, $750 < H_T < 2500$ GeV and $150 < \cancel{E}_T < 250$ GeV; (b) electrons, $1000 < H_T < 2500$ GeV and $150 < \cancel{E}_T < 250$ GeV [126].	119
D.1. Predicted and measured event counts in data. The 2 b -tag categories are (a) $750 < H_T < 2500$ GeV and (b) $1000 < H_T < 2500$ GeV. The ≥ 3 b -tag categories are (c) $400 < H_T < 2500$ GeV, (d) $750 < H_T < 2500$ GeV and (e) $1000 < H_T < 2500$ GeV.	123
E.1. Signal contamination for $T1tttt$ evaluated at a cross-section corresponding to $m_{\tilde{g}} = 1100$ GeV for $400 < H_T < 750$ GeV.	124
E.2. Signal contamination for $T1tttt$ evaluated at a cross-section corresponding to $m_{\tilde{g}} = 1100$ GeV for $750 < H_T < 2500$ GeV.	125
E.3. Signal contamination for $T5tttt$ evaluated at a cross-section corresponding to $m_{\tilde{g}} = 1100$ GeV for $400 < H_T < 750$ GeV (a), (b) and $750 < H_T < 2500$ GeV (c)-(f).	126
E.4. Signal contamination for $T1t1t$ evaluated at a cross-section corresponding to $m_{\tilde{g}} = 1000$ GeV for $400 < H_T < 750$ GeV (a), (b) and $750 < H_T < 2500$ GeV (c)-(f).	127
E.5. Efficiency for $T1tttt$ for signal regions with $750 < H_T < 2500$ GeV in the 2 b -tag category.	128
E.6. Efficiency for $T1tttt$ for signal regions with $400 < H_T < 750$ GeV (a), (b) and $750 < H_T < 2500$ GeV (c)-(f) in the ≥ 3 b -tag category.	129
E.7. Efficiency for $T5tttt$ for signal regions with $750 < H_T < 2500$ GeV in the 2 b -tag category.	130
E.8. Efficiency for $T5tttt$ for signal regions with $400 < H_T < 750$ GeV (a), (b) and $750 < H_T < 2500$ GeV (c)-(f) in the ≥ 3 b -tag category.	131
E.9. Acceptance uncertainties related to the light jet tagging scale-factor in the 2 b -tag category for $750 \text{ GeV} < H_T$ and $250 < \cancel{E}_T < 350$ GeV.	132
E.10. Acceptance uncertainties related to the light jet tagging scale-factor in the 2 b -tag category for $750 \text{ GeV} < H_T$	133
E.11. Acceptance uncertainties related to the light jet tagging scale-factor in the ≥ 3 b -tag category for $750 \text{ GeV} < H_T$ and $250 < \cancel{E}_T < 350$ GeV.	134
E.12. Acceptance uncertainties related to the light jet tagging scale-factor in the ≥ 3 b -tag category for $750 \text{ GeV} < H_T$ and $450 < \cancel{E}_T < 2500$ GeV.	135

E.13. Acceptance uncertainties related to the light jet tagging scale-factor in the ≥ 3 b -tag category for $400 \text{ GeV} < H_T < 750 \text{ GeV}$	136
E.14. Acceptance uncertainties related to the b -tagging scale-factor in the 2 b -tag category for $750 \text{ GeV} < H_T$	137
E.15. Acceptance uncertainties related to the b -tagging scale-factor in the 2 b -tag category for $750 \text{ GeV} < H_T$ and $450 < \cancel{E}_T < 2500 \text{ GeV}$	138
E.16. Acceptance uncertainties related to the b -tagging scale-factor in the ≥ 3 b -tag category for $750 \text{ GeV} < H_T$	139
E.17. Acceptance uncertainties related to the b -tagging scale-factor in the ≥ 3 b -tag category for $750 \text{ GeV} < H_T$ and $450 < \cancel{E}_T < 2500 \text{ GeV}$	140
E.18. Acceptance uncertainties related to the b -tagging scale-factor in the ≥ 3 b -tag category for $400 \text{ GeV} < H_T < 750 \text{ GeV}$	141
E.19. Acceptance uncertainties related to the jet energy scale in the 2 b -tag category for $750 \text{ GeV} < H_T$ and $250 < \cancel{E}_T < 350 \text{ GeV}$	142
E.20. Acceptance uncertainties related to the jet energy scale in the 2 b -tag category for $750 \text{ GeV} < H_T$	143
E.21. Acceptance uncertainties related to the jet energy scale in the ≥ 3 b -tag category for $750 \text{ GeV} < H_T$	144
E.22. Acceptance uncertainties related to the jet energy scale in the ≥ 3 b -tag category for $750 \text{ GeV} < H_T$ and $450 < \cancel{E}_T < 2500 \text{ GeV}$	145
E.23. Acceptance uncertainties related to the jet energy scale in the ≥ 3 b -tag category for $400 \text{ GeV} < H_T < 750 \text{ GeV}$	146
E.24. Acceptance uncertainties related to the uncertainty on initial state radiation (ISR) in the 2 b -tag category for $750 \text{ GeV} < H_T$ and $250 < \cancel{E}_T < 350 \text{ GeV}$	147
E.25. Acceptance uncertainties related to the uncertainty on initial state radiation (ISR) in the 2 b -tag category for $750 \text{ GeV} < H_T$	148
E.26. Acceptance uncertainties related to the uncertainty on initial state radiation (ISR) in the ≥ 3 b -tag category for $750 \text{ GeV} < H_T$	149
E.27. Acceptance uncertainties related to the uncertainty on initial state radiation (ISR) in the ≥ 3 b -tag category for $750 \text{ GeV} < H_T$ and $450 < \cancel{E}_T < 2500 \text{ GeV}$	150
E.28. Acceptance uncertainties related to the uncertainty on initial state radiation (ISR) in the ≥ 3 b -tag category for $400 \text{ GeV} < H_T < 750 \text{ GeV}$ and $150 < \cancel{E}_T < 250 \text{ GeV}$	151

List of Tables

1.1. Partices of the SM.	2
1.2. Chiral supermultiplets in the MSSM.	10
1.3. Gauge supermultiplets in the MSSM.	10
3.1. Muon efficiencies in the kinematic region $p_T > 20$ GeV and $ \eta < 2.4$. . .	52
3.2. Muon efficiencies in the kinematic region $p_T > 20$ GeV and $ \eta < 2.4$. . .	52
3.3. Electron efficiencies in the kinematic region $p_T > 20$ GeV and $ \eta < 2.5$ for data and full simulation.	55
3.4. Electron efficiencies in the kinematic region $p_T > 20$ GeV and $ \eta < 2.5$ for data and fast simulation.	55
3.5. The lepton efficiencies for single-lepton cross-channel trigger paths with online trigger threshold of $p_T > 5$ GeV or $p_T > 15$ GeV, in events that pass the hadronic trigger selection.	57
3.6. The averaged efficiency plateau values by trigger types.	57
3.7. Parameters determining the evolution of the skew error functions accord- ing to Eq 3.14: values obtained from simulation in the ≥ 6 jet selection (second column) and a comparison of results from simulation and data for the ≥ 4 jet control region (last two columns).	64
3.8. Certification files and primary data sets used for the determination of \cancel{E}_T -resolution templates, together with the run ranges and integrated luminosities for the data-taking periods.	75
3.9. Triggers and H_T binning used for fake- \cancel{E}_T templates.	75
3.10. Fit results for data and simulation for the parameters of the general- ized Pareto function describing the genuine \cancel{E}_T shape and of the error functions describing the effect of a selection in H_T on the \cancel{E}_T shape. . .	80
3.11. Predicted and true event counts in simulation for 2 b -tags and different \cancel{E}_T and H_T signal regions. Uncertainties are statistical.	81
3.12. Parameters used for the evaluation of uncertainties due to variations of the lepton efficiencies.	88

3.13. Systematic uncertainties for the background estimation in different \cancel{E}_T regions defined for $400 < H_T < 750$ GeV, $750 < H_T < 2500$ GeV and $1000 < H_T < 2500$ GeV.	90
3.14. Systematic uncertainties for the impact of residual differences in the kinematics of light jets.	93
3.15. Predicted and true event counts in simulation for different \cancel{E}_T and H_T signal regions and for ≥ 3 b-tags.	95
4.1. Predicted and measured event counts in data for the 2 b -tag signal regions.	96
4.2. Predicted and measured event counts in data for the ≥ 3 b -tag signal regions.	97
4.3. Overview of the predicted and observed yields with statistical and systematical uncertainties for different signal regions from the analysis of the 7 TeV dataset collected in 2011.	106
A.1. Certification files and primary data sets used for the muon and electron channels, together with the run ranges and integrated luminosities for the <i>rereco</i> and <i>prompt reco</i> periods.	112
A.2. Simulated event samples.	113
A.3. HLT trigger path names for the signal selection (muon and electron channel) and for the fake \cancel{E}_T templates.	114
C.1. Upper limit on the QCD contribution in the ≥ 1 b-tag bin for the muon channel [126].	120
C.2. Upper limit on the QCD contribution in the ≥ 1 b-tag bin for the electron channel. [126]	120
D.1. Predicted and measured event counts in data for 2 b -tag and different \cancel{E}_T and H_T signal regions.	121
D.2. Predicted and measured event counts in data for ≥ 3 b-tag and different \cancel{E}_T and H_T signal regions.	122

Bibliography

- [1] S. Glashow. *Partial Symmetries of Weak Interactions*. Nucl.Phys. **22**, pp. 579–588 (1961)
- [2] J. Goldstone, A. Salam, S. Weinberg. *Broken Symmetries*. Phys. Rev. **127**, pp. 965–970 (1962)
- [3] S. Weinberg. *A Model of Leptons*. Phys. Rev. Lett. **19**, pp. 1264–1266 (1967)
- [4] The ALEPH, CDF, D0, DELPHI, L3, OPAL and SLD Collaborations, the LEP Electroweak Working Group, the Tevatron Electroweak Working Group and the SLD electroweak and heavy flavour groups. *Precision Electroweak Measurements and Constraints on the Standard Model* (2010), arXiv:1012.2367
- [5] T. Aoyama, M. Hayakawa, T. Kinoshita, M. Nio. *Revised value of the eighth-order QED contribution to the anomalous magnetic moment of the electron*. Phys.Rev. **D77**, p. 053012 (2008), arXiv:0712.2607
- [6] B. C. Odom, D. Hanneke, B. D’Urso, G. Gabrielse. *New Measurement of the Electron Magnetic Moment Using a One-Electron Quantum Cyclotron*. Phys.Rev.Lett. **97**, p. 030801 (2006)
- [7] K. Kodama, et al. (DONUT Collaboration). *Observation of tau neutrino interactions*. Phys.Lett. **B504**, pp. 218–224 (2001), arXiv:hep-ex/0012035
- [8] G. Aad, et al. (ATLAS Collaboration). *Observation of a new particle in the search for the Standard Model Higgs boson with the ATLAS detector at the LHC*. Phys.Lett. **B716**, pp. 1–29 (2012), arXiv:1207.7214
- [9] S. Chatrchyan, et al. (CMS Collaboration). *Observation of a new boson at a mass of 125 GeV with the CMS experiment at the LHC*. Phys.Lett. **B716**, pp. 30–61 (2012), arXiv:1207.7235
- [10] D. J. Griffiths. *Introduction to Elementary Particles (2nd ed.)*. Wiley-VCH. ISBN ISBN 3-527-40601-8 (2008)
- [11] G. Zweig. *An SU_3 model for strong interaction symmetry and its breaking; Part II*, CERN-TH-412, p. 80 p (1964)
- [12] M. Gell-Mann. *Symmetries of Baryons and Mesons*. Phys. Rev. **125**, pp. 1067–1084 (1962)
- [13] Y. Ne’eman. *Derivation of strong interactions from a gauge invariance*. Nuclear Physics **26**, 2, pp. 222 – 229. ISSN 0029-5582 (1961)

- [14] D. Gross, F. Wilczek. *Ultraviolet Behavior of Nonabelian Gauge Theories*. Phys.Rev.Lett. **30**, pp. 1343–1346 (1973)
- [15] F. Englert, R. Brout. *Broken Symmetry and the Mass of Gauge Vector Mesons*. Phys. Rev. Lett. **13**, pp. 321–323 (1964)
- [16] P. W. Higgs. *Broken Symmetries and the Masses of Gauge Bosons*. Phys. Rev. Lett. **13**, pp. 508–509 (1964)
- [17] G. S. Guralnik, C. R. Hagen, T. W. B. Kibble. *Global Conservation Laws and Massless Particles*. Phys. Rev. Lett. **13**, pp. 585–587 (1964)
- [18] D. B. Chitwood, et al. (MuLan Collaboration). *Improved Measurement of the Positive-Muon Lifetime and Determination of the Fermi Constant*. Phys. Rev. Lett. **99**, p. 032001 (2007)
- [19] S. P. Martin. *A Supersymmetry primer* (1997), arXiv:hep-ph/9709356
- [20] N. Seiberg. *Naturalness versus supersymmetric nonrenormalization theorems*. Phys.Lett. **B318**, pp. 469–475 (1993), arXiv:hep-ph/9309335
- [21] P. Ade, et al. (Planck Collaboration). *Planck 2013 results. I. Overview of products and scientific results* (2013), arXiv:1303.5062
- [22] J. Wess, B. Zumino. *Supergauge transformations in four dimensions*. Nucl. Phys **B70**, p. 39 (1974)
- [23] H. P. Nilles. *Supersymmetry, Supergravity and Particle Physics*. Phys. Reports **110**, p. 1 (1984)
- [24] H. E. Haber, G. L. Kane. *The Search for Supersymmetry: Probing Physics Beyond the Standard Model*. Phys. Reports **117**, p. 75 (1987)
- [25] R. Barbieri, S. Ferrara, C. A. Savoy. *Gauge Models with Spontaneously Broken Local Supersymmetry*. Phys. Lett. **B119**, p. 343 (1982)
- [26] S. Dawson, E. Eichten, C. Quigg. *Search for Supersymmetric Particles in Hadron - Hadron Collisions*. Phys. Rev. **D31**, p. 1581 (1985)
- [27] S. Coleman, J. Mandula. *All Possible Symmetries of the S Matrix*. Phys. Rev. **159**, pp. 1251–1256 (1967)
- [28] R. Haag, J. T. Lopuszanski, M. Sohnius. *All possible generators of supersymmetries of the S-matrix*. Nuclear Physics B **88**, 2, pp. 257 – 274. ISSN 0550-3213 (1975)
- [29] A. Djouadi, et al. (MSSM Working Group). *The Minimal supersymmetric standard model: Group summary report* (1998), arXiv:hep-ph/9901246
- [30] H. E. Haber. *The Status of the minimal supersymmetric standard model and beyond*. Nucl.Phys.Proc.Suppl. **62**, pp. 469–484 (1998), arXiv:hep-ph/9709450
- [31] M. Kuroda. *Complete Lagrangian of MSSM* (1999), arXiv:hep-ph/9902340

- [32] S. Dimopoulos, D. W. Sutter. *The Supersymmetric flavor problem*. Nucl.Phys. **B452**, pp. 496–512 (1995), arXiv:hep-ph/9504415
- [33] H. Nishino, et al. (Super-Kamiokande Collaboration). *Search for Proton Decay via $p \rightarrow e^+\pi^0$ and $p \rightarrow \mu^+\pi^0$ in a Large Water Cherenkov Detector*. Phys. Rev. Lett. **102**, p. 141801 (2009)
- [34] G. Bhattacharyya. *R-parity violating supersymmetric Yukawa couplings: A Minireview*. Nucl.Phys.Proc.Suppl. **52A**, pp. 83–88 (1997), arXiv:hep-ph/9608415
- [35] G. 't Hooft. *Symmetry Breaking through Bell-Jackiw Anomalies*. Phys. Rev. Lett. **37**, pp. 8–11 (1976)
- [36] G. R. Farrar, P. Fayet. *Phenomenology of the Production, Decay, and Detection of New Hadronic States Associated with Supersymmetry*. Phys.Lett. **B76**, pp. 575–579 (1978)
- [37] N. Sakai, T. Yanagida. *Proton Decay in a Class of Supersymmetric Grand Unified Models*. Nucl.Phys. **B197**, p. 533 (1982)
- [38] S. Dimopoulos, S. Raby, F. Wilczek. *Proton Decay in Supersymmetric Models*. Phys.Lett. **B112**, p. 133 (1982)
- [39] S. Weinberg. *Supersymmetry at Ordinary Energies. 1. Masses and Conservation Laws*. Phys.Rev. **D26**, p. 287 (1982)
- [40] S. Dimopoulos, H. Georgi. *Softly Broken Supersymmetry and SU(5)*. Nucl.Phys. **B193**, p. 150 (1981)
- [41] P. Bechtle, S. Heinemeyer, O. Stal, T. Stefaniak, G. Weiglein, et al. *MSSM Interpretations of the LHC Discovery: Light or Heavy Higgs?* Eur.Phys.J. **C73**, p. 2354 (2013), arXiv:1211.1955
- [42] C. Brust, A. Katz, S. Lawrence, R. Sundrum. *SUSY, the Third Generation and the LHC*. JHEP **1203**, p. 103 (2012), arXiv:1110.6670
- [43] M. Papucci, J. T. Ruderman, A. Weiler. *Natural SUSY Endures* (2011), arXiv:1110.6926
- [44] H. Baer, J. List. *Post LHC8 SUSY benchmark points for ILC physics* (2013), arXiv:1307.0782
- [45] G. L. Bayatian, et al. *CMS Physics: Technical Design Report Volume 2: Physics Performance*. J. Phys. G **34**, CERN-LHCC-2006-021. CMS-TDR-8-2, pp. 995–1579. 669 p. Revised version submitted on 2006-09-22 17:44:47 (2006)
- [46] CMS Collaboration. *Phenomenological MSSM interpretation of the CMS 2011 5fb^{-1} results*. Technical Report, CMS-PAS-SUS-12-030, CERN, Geneva (2013)
- [47] D. Alves, et al. (LHC New Physics Working Group). *Simplified Models for LHC New Physics Searches*. J.Phys. **G39**, p. 105005 (2012), arXiv:1105.2838

- [48] N. Arkani-Hamed, P. Schuster, N. Toro, J. Thaler, L.-T. Wang, et al. *MARMOSET: The Path from LHC Data to the New Standard Model via On-Shell Effective Theories* (2007), arXiv:hep-ph/0703088
- [49] D. S. Alves, E. Izaguirre, J. G. Wacker. *Where the Sidewalk Ends: Jets and Missing Energy Search Strategies for the 7 TeV LHC*. JHEP **1110**, p. 012 (2011), arXiv:1102.5338
- [50] C. Gutschow, Z. Marshall. *Setting limits on supersymmetry using simplified models* (2012), arXiv:1202.2662
- [51] S. Chatrchyan, et al. (CMS Collaboration). *Interpretation of Searches for Supersymmetry with simplified Models* (2013), arXiv:1301.2175
- [52] L. Evans, P. Bryant. *LHC Machine*. Journal of Instrumentation **3**, 08, p. S08001 (2008)
- [53] O. S. Brüning, et al. *LHC Design Report, Vol. 1: The LHC Main Ring*. CERN, Geneva (2004)
- [54] O. S. Brüning, et al. *LHC Design Report, Vol. 2: The LHC Infrastructure*. CERN, Geneva (2004)
- [55] M. Benedikt, et al. *LHC Design Report, Vol. 3. The LHC Injector Chain*. CERN, Geneva (2004)
- [56] ATLAS Collaboration. *The ATLAS Experiment at the CERN Large Hadron Collider*. Journal of Instrumentation **3**, 08, p. S08003 (2008)
- [57] CMS Collaboration. *The CMS experiment at the CERN LHC*. Journal of Instrumentation **3**, 08, p. S08004 (2008)
- [58] ALICE Collaboration. *The ALICE experiment at the CERN LHC*. Journal of Instrumentation **3**, 08, p. S08002 (2008)
- [59] LHCb Collaboration. *The LHCb Detector at the LHC*. Journal of Instrumentation **3**, 08, p. S08005 (2008)
- [60] The LHCf Collaboration. *The LHCf detector at the CERN Large Hadron Collider*. Journal of Instrumentation **3**, 08, p. S08006 (2008)
- [61] The TOTEM Collaboration. *The TOTEM Experiment at the CERN Large Hadron Collider*. Journal of Instrumentation **3**, 08, p. S08007 (2008)
- [62] J. Pinfold, et al. *Technical Design Report of the MoEDAL Experiment*. Technical Report, CERN-LHCC-2009-006. MoEDAL-TDR-001, CERN, Geneva (2009)
- [63] C. Lefèvre. *The CERN accelerator complex*. (2008), <https://cds.cern.ch/record/1260465>
- [64] G. Antchev, et al. (TOTEM Collaboration). *Luminosity-independent measurements of total, elastic and inelastic cross-sections at $\sqrt{s} = 7$ TeV*. Technical Report, TOTEM-2012-004. CERN-PH-EP-2012-353, CERN, Geneva (2012)

- [65] G. Antchev, et al. (TOTEM Collaboration). *A luminosity-independent measurement of the proton-proton total cross-section at $\sqrt{s} = 8$ TeV*. Technical Report, TOTEM-2012-005. CERN-PH-EP-2012-354, CERN, Geneva (2012)
- [66] <https://twiki.cern.ch/twiki/bin/view/CMSPublic/LumiPublicResults>
- [67] G. L. Bayatian, et al. *CMS Physics: Technical Design Report Volume 1: Detector Performance and Software*. Technical Design Report CMS, CERN, Geneva (2006)
- [68] CMS Collaboration. *Detector Drawings*. CMS Collection. (2012), <https://cds.cern.ch/record/1433717>
- [69] CMS Collaboration. *Measurement of Momentum Scale and Resolution of the CMS Detector using Low-mass Resonances and Cosmic Ray Muons*. Technical Report, CMS-PAS-TRK-10-004, CERN, 2010. Geneva (2010)
- [70] P. Adzic. *Energy resolution of the barrel of the CMS Electromagnetic Calorimeter*. Journal of Instrumentation **2**, 04, p. P04004 (2007)
- [71] CMS Collaboration. *Performance and operation of the CMS electromagnetic calorimeter*. Journal of Instrumentation **5**, 03, p. T03010 (2010)
- [72] D. Green. *Calibration of the CMS calorimeters*, FERMILAB-FN-0704 (2001), <http://lss.fnal.gov/archive/test-fn/0000/fermilab-fn-0704.shtml>
- [73] S. Cittolin, A. Rácz, P. Sphicas. *CMS The TriDAS Project: Technical Design Report, Volume 2: Data Acquisition and High-Level Trigger. CMS trigger and data-acquisition project*. Technical Design Report CMS, CERN, Geneva (2002)
- [74] G. L. Bayatyan, et al. *CMS TriDAS project: Technical Design Report, Volume 1: The Trigger Systems*. Technical Design Report CMS
- [75] T. Virdee, A. Petrilli, A. Ball. *CMS High Level Trigger*. Technical Report, LHCC-G-134. CERN-LHCC-2007-021, CERN, Geneva. Revised version submitted on 2007-10-19 16:57:09 (2007)
- [76] CMS Collaboration. *Search for supersymmetry in events with a single lepton and jets using templates*. Technical Report, CMS-PAS-SUS-11-027, CERN, Geneva (2012)
- [77] S. Chatrchyan, et al. (CMS Collaboration). *Search for supersymmetry in final states with a single lepton, b-quark jets, and missing transverse energy in proton-proton collisions at $\sqrt{s} = 7$ TeV*. Phys. Rev. D **87**, p. 052006 (2013)
- [78] CMS Collaboration. *CMS Luminosity Based on Pixel Cluster Counting - Summer 2012 Update*. Technical Report, CMS-PAS-LUM-12-001, CERN, Geneva (2012)
- [79] CMS Collaboration. *Absolute Calibration of the Luminosity Measurement at CMS: Winter 2012 Update*. Technical Report, CMS-PAS-SMP-12-008, CERN, Geneva (2012)

- [80] CMS Collaboration. *Measurement of CMS Luminosity*. Technical Report, CMS-PAS-EWK-10-004, CERN, Geneva (2010)
- [81] T. Sjöstrand, S. Mrenna, P. Z. Skands. *PYTHIA 6.4 Physics and Manual; v6.420, tune D6T*. JHEP **05**, p. 026 (2006), arXiv:hep-ph/0603175
- [82] J. Alwall, M. Herquet, F. Maltoni, O. Mattelaer, T. Stelzer. *MadGraph 5: Going Beyond*. JHEP **1106**, p. 128 (2011), arXiv:1106.0522
- [83] S. Alioli, P. Nason, C. Oleari, E. Re. *A general framework for implementing NLO calculations in shower Monte Carlo programs: the POWHEG BOX*. JHEP **1006**, p. 043 (2010), arXiv:1002.2581
- [84] GEANT4 Collaboration, S. Agostinelli et al. (GEANT4). *GEANT4: A simulation toolkit*. Nucl. Instrum. Meth. **A506**, p. 250 (2003)
- [85] S. Abdullin, P. Azzi, F. Beaudette, P. Janot, A. Perrotta, on behalf of the CMS Collaboration. *The Fast Simulation of the CMS Detector at LHC*. Journal of Physics: Conference Series **331**, 3, p. 032049 (2011)
- [86] Z. Was. *TAUOLA the library for tau lepton decay, and KKMC / KORALB / KORALZ /... status report*. Nucl.Phys.Proc.Suppl. **98**, pp. 96–102 (2001), arXiv:hep-ph/0011305
- [87] J. M. Campbell, R. K. Ellis. *Radiative corrections to $Z b$ anti- b production*. Phys. Rev. **D62**, p. 114012 (2000), arXiv:hep-ph/0006304
- [88] R. Kleiss, W. J. Stirling. *Top quark production at hadron colliders: Some useful formulae*. Z. Phys. **C40**, p. 419 (1988)
- [89] K. Melnikov, F. Petriello. *Electroweak gauge boson production at hadron colliders through $O(\alpha_S^2)$* . Phys. Rev. **D74**, p. 114017 (2006), arXiv:hep-ph/0609070
- [90] M. Kramer, A. Kulesza, R. van der Leeuw, M. Mangano, S. Padhi, et al. *Supersymmetry production cross sections in pp collisions at $\sqrt{s} = 7$ TeV* (2012), arXiv:1206.2892
- [91] CMS Collaboration. *Search for Supersymmetry in pp collisions at 8 TeV in events with a single lepton, multiple jets and b-tags*. Technical Report, CMS-PAS-SUS-13-007, CERN, Geneva (2013)
- [92] CMS Collaboration. *Particle-flow commissioning with muons and electrons from J/Ψ and W events at 7 TeV*. Technical Report, CMS-PAS-PFT-10-003, CERN, 2010. Geneva (2010)
- [93] CMS Collaboration. *Commissioning of the Particle-Flow reconstruction in Minimum-Bias and Jet Events from pp Collisions at 7 TeV*. Technical Report, CMS-PAS-PFT-10-002, CERN, Geneva (2010)
- [94] CMS Collaboration. *Particle-Flow Event Reconstruction in CMS and Performance for Jets, Taus, and MET*. Technical Report, CMS-PAS-PFT-09-001, CERN, 2009. Geneva (2009)

- [95] S. Chatrchyan, et al. (CMS Collaboration). *Performance of CMS muon reconstruction in pp collision events at $\sqrt{s} = 7$ TeV*. JINST **7**, p. P10002 (2012), arXiv:1206.4071
- [96] CMS Collaboration. *Performance of CMS muon reconstruction in cosmic-ray events*. Journal of Instrumentation **5**, 03, p. T03022 (2010)
- [97] R. Fruhwirth. *Application of Kalman filtering to track and vertex fitting*. Nucl.Instrum.Meth. **A262**, pp. 444–450 (1987)
- [98] CMS Collaboration. *Performance of muon identification in pp collisions at $\sqrt{s} = 7$ TeV*. Technical Report, CMS-PAS-MUO-10-002, CERN, 2010. Geneva (2010)
- [99] W. Waltenberger, R. Frühwirth, P. Vanlaer. *Adaptive vertex fitting*. Journal of Physics G: Nuclear and Particle Physics **34**, 12, p. N343 (2007)
- [100] CMS Collaboration. *Electron reconstruction and identification at $\sqrt{s} = 7$ TeV*. Technical Report, CMS-PAS-EGM-10-004, CERN, Geneva (2010)
- [101] W. Adam, R. Frühwirth, A. Strandlie, T. Todorov. *Reconstruction of electrons with the Gaussian-sum filter in the CMS tracker at the LHC*. Journal of Physics G: Nuclear and Particle Physics **31**, 9, p. N9 (2005)
- [102] M. Cacciari, G. P. Salam, G. Soyez. *FastJet User Manual*. Eur.Phys.J. **C72**, p. 1896 (2012), arXiv:1111.6097
- [103] M. Cacciari, G. P. Salam, G. Soyez. *The Anti- $k(t)$ jet clustering algorithm*. JHEP **0804**, p. 063 (2008), arXiv:0802.1189
- [104] CMS Collaboration. *Status of the 8 TeV Jet Energy Corrections and Uncertainties based on 11 fb⁻¹ of data in CMS*. Technical Report, CMS-DP-2013-011, CERN, Geneva (2013)
- [105] CMS collaboration. *Determination of jet energy calibration and transverse momentum resolution in CMS*. Journal of Instrumentation **6**, 11, p. P11002 (2011)
- [106] M. Cacciari, G. P. Salam. *Pileup subtraction using jet areas*. Phys.Lett. **B659**, pp. 119–126 (2008), arXiv:0707.1378
- [107] CMS Collaboration. *Calorimeter Jet Quality Criteria for the First CMS Collision Data*. Technical Report, CMS-PAS-JME-09-008, CERN, 2010. Geneva (2010)
- [108] CMS Collaboration. *Missing transverse energy performance of the CMS detector*. Journal of Instrumentation **6**, p. 9001 (2011), arXiv:1106.5048
- [109] CMS Collaboration. *MET performance in 8 TeV data*. Technical Report, CMS-PAS-JME-12-002, CERN, Geneva (2013)
- [110] S. Chatrchyan, et al. *Identification of b-quark jets with the CMS experiment*. J. Instrum. **8** **P04013**, arXiv:1211.4462. CMS-BTV-12-001. CERN-PH-EP-2012-262, p. P04013. 67 p.

- [111] CMS Collaboration. *Performance of b tagging at $\sqrt{s} = 8$ TeV in multijet, $t\bar{t}$ and boosted topology events*. Technical Report, CMS-PAS-BTV-13-001, CERN, Geneva (2013)
- [112] A. Balkema, L. de Haan. *Residual life time at great age*. Annals of Probability **2**, pp. 792–804 (1974)
- [113] J. Pickands. *Statistical inference using extreme order statistics*. Annals of Statistics **3**, pp. 119–131 (1975)
- [114] CMS Collaboration. *b -Jet Identification in the CMS Experiment*. Technical Report, CMS-PAS-BTV-11-004, CERN, Geneva (2012)
- [115] Pavlunin, V. and Andrews, W. and Wuerthwein, F. *Artificial MET predictions for SUSY searches*. Technical Report, AN-2010/160, CERN, Geneva (2011)
- [116] A. Czarnecki, J. G. Körner, J. H. Piclum. *Helicity fractions of W bosons from top quark decays at next-to-next-to-leading order in QCD*. Phys. Rev. D **81**, p. 111503 (2010)
- [117] T. Aaltonen, et al. (CDF Collaboration). *Measurement of W -Boson Polarization in Top-quark Decay in $p\bar{p}$ Collisions at $\sqrt{s} = 1.96$ TeV*. Phys.Rev.Lett. **105**, p. 042002 (2010), arXiv:1003.0224
- [118] V. M. Abazov, et al. (D0 Collaboration). *Measurement of the W boson helicity in top quark decays using 5.4 fb^{-1} of $p\bar{p}$ collision data*. Phys.Rev. **D83**, p. 032009 (2011), arXiv:1011.6549
- [119] R. G. Miller. *Jackknifing Variances*. Ann. Math. Stat. **39**, 2, p. 567. And references therein (1968)
- [120] T. Junk. *Confidence level computation for combining searches with small statistics*. Nucl.Instrum.Meth. **A434**, pp. 435–443 (1999), arXiv:hep-ex/9902006
- [121] A. L. Read. *Modified frequentist analysis of search results (the CL_s method)*, CERN-OPEN-2000-205 (2000)
- [122] A. L. Read. *Presentation of search results: the CL_s technique*. J. Phys. G: Nucl. Part. Phys. **28**, p. 2693 (2002)
- [123] ATLAS Collaboration, CMS Collaboration and the LHC Higgs Combination Group. *Procedure for the LHC Higgs boson search combination in summer 2011*. ATL-PHYS-PUB-2011-818, CMS NOTE-2011/005 (2011)
- [124] D. Bourilkov, R. C. Group, M. R. Whalley. *LHAPDF: PDF use from the Tevatron to the LHC* (2006), arXiv:hep-ph/0605240
- [125] W. Beenakker, R. Hopker, M. Spira, P. Zerwas. *Squark and gluino production at hadron colliders*. Nucl. Phys. **B492**, p. 51 (1997), arXiv:hep-ph/9610490
- [126] S. Kupstaitis-Dunkler. *A Search for Supersymmetry using the Transverse Mass of the W Boson*. Master thesis, Vienna University of Technology (2013, in preparation)

Lebenslauf

Dipl.-Ing. Wolfgang Kiesenhofer

Schönbrunnerstraße 26/6, 1050 Wien (A)

Geboren am 2. Jänner 1982 in Steyr, Oberösterreich

Ausbildung

seit 03/2010	Doktoratsstudium der technischen Wissenschaften, TU Wien Dissertation: <i>A search for supersymmetry with a single lepton in the final state using hadronic variables</i> , ausgeführt am Institut für Hochenergiephysik der ÖAW
01/2010	Diplomprüfung in Technischer Physik, mit Auszeichnung
10/2001 – 01/2010	Diplomstudium der Technischen Physik, TU Wien Diplomarbeit: <i>Performance studies on Silicon Strip Sensors with 50 μm pitch</i> , ausgeführt am Institut für Hochenergiephysik der ÖAW (2009)
10/2000 – 10/2001	Zivildienst , Bezirksaltenheim Enns
1992 – 2000	Bundesrealgymnasium Steyr, Matura (06/2000)
1988 – 1992	Volksschule Wolfers

Berufliche Tätigkeiten

03/2010 – 10/2013	Wissenschaftlicher Mitarbeiter Institut für Hochenergiephysik der ÖAW, Wien (A)
seit 2010	Mitglied der CMS Collaboration CERN, Genf (CH)
05/2007–10/2007	Research Assistant SUNY Downstate Medical Center, NY (USA)
2004 – 2006	Nachhilfelehrer Nachhilfeinstitut „Lernen mit Pfiff“, Wien (A)

Konferenzen und Workshops

- 08/2012 Cern School of Computing
Universität Uppsala, (SWE)
- 09/2012 *Search for supersymmetry in final states with b-jets with the CMS experiment*, Vortrag, ÖPG Tagung, Karl-Franzens-Universität, Graz (A)
- 06/2012 *Toward commonality of W predictions*,
Vortrag, CMS SUSY Workshop 2012, DESY, Hamburg, (D)
- 05/2011 *SUSY and high- p_T flavor tagging at CMS*,
Vortrag (invited), 9th International Conference on Flavor Physics and CP Violation, Maale HaChamisha, (IL)
- 09/2010 *Muon Reconstruction for SUSY Searches at CMS*,
Vortrag, ÖPG Tagung, Universität Salzburg, Salzburg (A)
- 10/2009 *Beam test results for fine pitched multigeometry silicon strip detectors*,
Vortrag, 11th ICATPP (2009), Como, (I)

Publikationen

**Mehrere Publikationen als Mitglied der CMS Collaboration,
darunter mit signifikantem Beitrag:**

Search for supersymmetry in pp collisions at $\sqrt{s} = 8$ TeV in events with a single lepton, large jet multiplicity and multiple b jets, CMS Collaboration, (2013), in preparation

Search for supersymmetry in final states with a single lepton, b-quark jets, and missing transverse energy in proton-proton collisions at $\sqrt{s} = 7$ TeV, CMS Collaboration, Phys. Rev. D 87, 052006 (2013), arXiv:1211.3143

Search for supersymmetry in pp collisions at $\sqrt{s} = 7$ TeV in events with a single lepton, jets, and missing transverse momentum, CMS Collaboration, J. Hep. 08, 156 (2011), arXiv:1107.1870

Missing transverse energy performance of the CMS detector, CMS Collaboration, J. Inst. 6, 9001 (2011), arXiv:1106.5048.

SUSY and high- p_T flavor tagging at CMS, Conference Proceeding FPCP 2011, CMS-CR-2011-163, arXiv:1109.2085

Weitere Publikationen:

Optimising the strip geometry for very fine pitch silicon strip sensors, M. Dragicic, et al., Nucl. Inst. Meth. A 617 1, 532 (2010)

Beam test results for fine pitched multigeometry silicon strip detectors, Conference Proceeding, ICATPP11, 2009